



Università degli Studi di Cagliari

**PHD DEGREE**  
Physics  
Cycle XXXII

## **ACCESSING THE 3D STRUCTURE OF NUCLEONS THROUGH TMD PHENOMENOLOGY**

Scientific Disciplinary Sector(s)  
FIS/02

PhD Student

CARLO FLORE

Coordinator of the PhD Programme

Prof. PAOLO RUGGERONE

Supervisors

Prof. UMBERTO D'ALESIO  
Prof. FRANCESCO MURGIA

Final exam. Academic Year 2018/2019  
Thesis defence: January-February 2020 Session

Carlo Flore gratefully acknowledges Sardinian Regional Government for the financial support of his PhD scholarship (P.O.R. Sardegna F.S.E. - Operational Programme of the Autonomous Region of Sardinia, European Social Fund 2014-2020 - Axis III Education and training, Thematic goal 10, Investment Priority 10ii), Specific goal 10.5.

To my parents and Giulia.

# Accessing the 3D structure of nucleons through TMD phenomenology

## Abstract

The three-dimensional structure of nucleons and transverse polarisation phenomena at high energy are subjects of very intensive researches. While collinear QCD at leading twist is not able to describe such kind of events, more extended approaches including intrinsic transverse momentum effects have turned out to be more suitable in this context.

In this thesis, phenomenological studies on transverse momentum dependent (TMD) functions are presented. By adopting a TMD approach, we enlighten the current knowledge on some of the leading twist polarised TMD functions, such as the (quark and gluon) Sivers distributions, the transversity and the Collins functions. The role of the underlying choices in phenomenological analyses, together with the assessment of TMD signals in the data, is particularly emphasised.

Indeed, some of the assumptions made on the phenomenological model can influence the outcome of an analysis. In the case of the quark Sivers function, suitable choices on the set of parameters result in a more accurate uncertainty evaluation, while for the TMD transversity relaxing some initial hypothesis eases the tension between phenomenology and lattice QCD estimates of the isovector tensor charge. The poorly known gluon Sivers function (GSF) are also analysed, both in the framework of the Generalised Parton Model (GPM) and its colour gauge invariant extension (CGI-GPM), where two independent GSFs are defined. A first constraint on the size and the sign of these functions, as well as a new GPM extraction, are showed.

The extracted TMDs are also adopted to study the single-spin asymmetries observed in polarised proton-proton and lepton-proton processes. The latter reaction is analysed, highlighting the role of the quasisreal photon exchange in the unpolarised cross sections and in the asymmetries. Theoretical predictions compared against existing data show a very good description of the measured asymmetries. By means of the estimated gluon Sivers functions, single-spin asymmetries for inclusive  $J/\psi$  and photon production in polarised proton-proton reactions are also estimated. At the moment, no clear discrimination between the GPM and the CGI-GPM is possible.

A novel Horizon 2020 project, aiming to create an online platform for hadronic and nuclear physics is also presented. In future, it would represent a valuable tool, and its potential extension to TMD physics could become beneficial also for the TMD community.

New data from colliders and fixed target experiments will come in the future. In the quest for understanding polarisation phenomena, a more agnostic, transparent and thorough approach in phenomenological analyses would help in preparing the TMD community to be ready for the next generation of experiments.

# Contents

<b>1</b>	<b>Introduction</b>	<b>1</b>
1.1	From collinear PDFs to TMDs . . . . .	3
1.2	This thesis . . . . .	4
<b>2</b>	<b>Transverse Momentum Dependent physics</b>	<b>6</b>
2.1	Transverse Momentum Dependent functions . . . . .	6
2.1.1	Properties of $T$ -odd TMDs . . . . .	9
2.1.2	Constraints on TMDs . . . . .	12
2.1.3	A small dictionary . . . . .	12
2.2	Two-scale and single-scale processes . . . . .	13
2.2.1	Semi-Inclusive Deep Inelastic Scattering . . . . .	14
2.2.2	Single inclusive hadron production from hadronic collisions . . . . .	19
2.3	Generalised Parton Model . . . . .	20
2.3.1	Single inclusive hadron production in the GPM . . . . .	21
2.3.2	TMD parametrisation and SIDIS in the GPM . . . . .	26
<b>3</b>	<b>Polarised quark TMD distributions</b>	<b>32</b>
3.1	Available TMD data . . . . .	32
3.2	Quark Sivers function and signals of TMD physics in SIDIS data . . . . .	35
3.2.1	General strategy and new Sivers parametrisation . . . . .	35
3.2.2	Fitting the quark Sivers function . . . . .	37
3.2.3	Signals of scale dependence . . . . .	47
3.3	Transversity distribution and pion Collins fragmentation functions from SIDIS and $e^+e^-$ data . . . . .	51
3.3.1	Azimuthal correlations in $e^+e^- \rightarrow h_1 h_2 X$ processes . . . . .	52
3.3.2	Global fit of transversity and Collins functions and role of the Soffer bound . . . . .	56
3.4	Outlook of the chapter . . . . .	62
<b>4</b>	<b>Pinning down the gluon Sivers function(s)</b>	<b>63</b>
4.1	Colour Gauge Invariant Generalised Parton Model . . . . .	63
4.1.1	Initial and final state interactions: an example . . . . .	64
4.1.2	CGI-GPM and single-spin asymmetries in $p^\uparrow p \rightarrow \pi X$ . . . . .	70
4.2	Gluon Sivers functions from hadronic collisions . . . . .	74
4.2.1	GPM fit of the gluon Sivers function . . . . .	74
4.2.2	First constraints on $f$ - and $d$ -type GSFs . . . . .	76
4.3	Outlook and future developements . . . . .	81
<b>5</b>	<b>Phenomenology of single-spin asymmetries</b>	<b>83</b>
5.1	Single-spin asymmetries in inclusive $\ell p^\uparrow \rightarrow hX$ processes: role of quasireal photon exchange . . . . .	83
5.1.1	Formalism and Weizsäcker-Williams approximation . . . . .	84

5.1.2	Weizsäcker-Williams contribution to $A_N$ for $\ell p^\uparrow \rightarrow hX$ processes . . .	87
5.1.3	Phenomenological results and comparison with data . . . . .	91
5.2	CGI-GPM vs GPM: inclusive quarkonia and photon production in polarised $pp$ processes . . . . .	104
5.3	Summary and outlook . . . . .	107
<b>6</b>	<b>A tool for quarkonia</b>	<b>109</b>
6.1	The NLOAccess project . . . . .	109
6.2	HELAC-Onia and its web realisation . . . . .	110
6.2.1	HELAC-Onia Web . . . . .	111
6.3	Future developements . . . . .	114
<b>7</b>	<b>Conclusions</b>	<b>115</b>
	<b>Appendix A Kinematics and helicity frames</b>	<b>A.1</b>
	<b>Appendix B Helicity formalism</b>	<b>B.1</b>
	<b>Appendix C Colour projectors in CGI-GPM</b>	<b>C.1</b>
	<b>Acknowledgments</b>	<b>T.1</b>
	<b>References</b>	<b>R.1</b>

# 1

## Introduction

Our knowledge on the building blocks of nature and of ourselves keeps evolving with time. Starting from Mendeleev's periodic table of 19<sup>th</sup> century, we now know that all the elements are composite structures of protons and neutrons, forming the atomic nucleus, surrounded by electrons balancing the charge to form neutral atoms.

Protons and neutrons, i.e. the nucleons, are examples of hadrons. Back in the 1960s, Gell-Mann [1, 2] and Zweig [3, 4] developed, based on an SU(3) flavour symmetry, the so-called *constituent quark model*, that helped in classifying the large plethora of hadrons. In the meanwhile, to describe observables for high energy processes, Feynman, Bjorken and Paschos [5, 6] introduced the *parton model*. Thanks to these studies, some of the hadrons already observed in particle detectors, that showed a composite nature, could be identified, and the existence of other hadrons that formed later the “particle zoo” was predicted.

The quark model postulates the existence of elementary particles called quarks, and the underlying SU(3) symmetry brings to three elementary quarks called up, down and strange. Their existence was confirmed later by the SLAC measurements [7, 8], where deep-inelastic scattering of electrons off protons and neutrons revealed the presence of up and down quarks. In the meanwhile, theoretical developments moved on. On one side, the works of Cabibbo [9], Kobayashi and Maskawa [10] predicted a total of six quarks, whose existence was later assessed. On the other side, it was proposed that the quarks are bound together inside hadrons by the strong interaction, mediated by the exchange of gluons, that were indirectly observed at DESY [11–14]. All these theoretical works and experimental findings finally led to the identification of quarks, antiquarks and gluons as *partons*.

The description of nucleons then evolved to the quantum field theory language. In fact, the quantum theory of the strong interaction, called Quantum Chromodynamics (QCD), was developed. This is a non-Abelian (or Yang-Mills) theory, whose bosons, the gluons, carry colour charge. So, differently from Quantum Electrodynamics (QED), where photons are electrically neutral, gluons can interact between each others, thus showing a richer and more extended dynamics with respect to QED.

One of the consequences of the non-Abelian nature of the strong force is that the strength of the interaction between partons increases as the distance between them increases. So, at a certain point, the condition that makes the production of a  $q\bar{q}$  pair favourable is reached, thus resulting in an impossibility of detecting free partons in experiments. Viceversa, this makes

us observe only colourless combinations of partons, i.e. the hadrons, or jets. This behaviour is known as *colour confinement*. On the other hand, if nucleons are probed at an high energy scale  $Q^2 \gg M^2$ , where  $M$  is a typical hadronic mass, one would observe them as a bunch of free, non-interacting partons. The more  $Q^2$  is enhanced, the less partons interact with each other. This behaviour is the so-called *asymptotic freedom* of QCD, described in 1973 by Gross, Wilczek and Politzer [15, 16].

Asymptotic freedom reflects in the behaviour of the QCD coupling constant. In fact, as depicted in Fig. 1.1, the energy dependence of  $\alpha_s$  shows this QCD feature: the lower (higher)  $Q$  is, the more (less) quarks and gluons interact with each other. The asymptotically free regime can be described via perturbation theory, while for the confined regime the perturbative approach cannot be applied, so we have to model the nonperturbative behaviour.

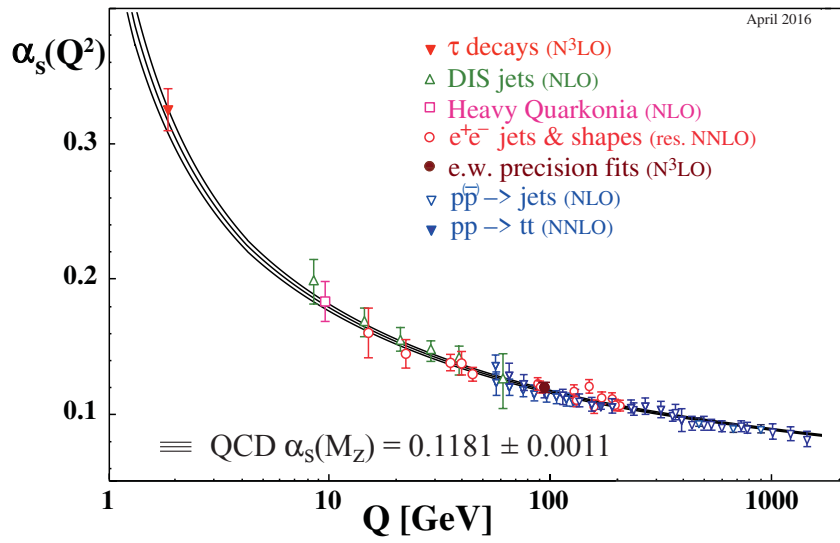


Figure 11: Summary of  $\alpha_s$  measurements as a function of the energy scale  $Q$  (in GeV units), updated to April 2016. Figure is from [17].

QCD relies on factorisation theorems. For a given high-energy collision where at least one hadron is involved (either in the initial or final state), the corresponding cross section is in fact written in terms of perturbatively calculable hard parts and nonperturbative functions that parametrise the hadronic internal structure. These functions are called parton distribution functions (PDFs) for partons inside the hadrons in the initial state of the reaction, and fragmentation functions (FFs) for partons fragmenting into the observed hadrons in the final state, and are both fitted to the data. Historically, they were first introduced by Feynman as collinear PDFs, within the parton model. These distributions encode a one-dimensional information, depending only on  $x$ , the longitudinal momentum fraction of the parent hadron carried by the partons. So,  $f_{i/p}(x)$  describes for example the probability density to find partons of type  $i$  carrying a longitudinal momentum fraction  $x$  inside their parent proton. In this picture, the proton is described as a collection of partons, each of them moving collinearly to the parent hadron, carrying a given fraction of its longitudinal momentum, while the partons intrinsic transverse momentum is integrated over.

PDFs and FFs shapes and values depend also on the energy scale at which they are evaluated. Their  $Q^2$  dependence is nowadays well-known and established: starting from an



initial energy scale  $Q_0^2$ , one can calculate the value of a given PDF or FF at an higher energy  $Q^2$  thanks to the evolution equations developed by Dokshitzer, Gribov, Lipatov, Altarelli and Parisi, now known as DGLAP evolution equations [18–20]. Moreover, as they do not depend on the given hard scattering process, PDFs and FFs are *universal* objects. This implies that they can be extracted from a specific reaction, and used to described another one. Universality of distributions, together with factorisation theorems, renders QCD a predictive theory.

### 1.1 FROM COLLINEAR PDFs TO TMDs

Our knowledge on the nucleon internal structure still keeps evolving. Indeed, even if very successful, collinear QCD phenomenology is not able to describe some of the nucleon properties, such as its spin.

Since the first, pioneering measurements of the EMC Collaboration [21], it is well-known that the intrinsic spin of the valence quarks is not enough to generate the total proton<sup>1</sup> spin. Conversely, we have to take into account contributions coming from both sea quarks and gluons, and also from orbital angular momentum of the partons inside the proton. The latter quantity cannot be described by a simple, one-dimensional collinear framework, but can be accessed indirectly via different kinds of multidimensional partonic functions. Here, we will focus on a specific class of such functions, the so-called transverse momentum dependent distributions and fragmentation functions (TMD-PDFs and TMD-FFs, or more generally TMDs).

TMDs are multidimensional objects that depend on both  $x$  and  $\mathbf{k}_\perp$ , the latter quantity being the intrinsic transverse momentum of partons inside the proton.  $\mathbf{k}_\perp$  is a two-dimensional vector defined on the transverse plane with respect to the direction of motion of the highly energetic parent nucleon, thus TMDs are three-dimensional objects. They encode the correlation between the parton intrinsic transverse momentum and the spin polarisation of partons and/or nucleons, and describe, in momentum space, the azimuthal distribution of partons inside (un)polarised nucleons.

TMDs usually manifest themselves through several angular modulations observed in different processes. Some of them will be analysed later, and belong to a specific class of processes, where two energy scales are detected. Some others, characterised by a single hard scale, can still be ascribed to effects related to the parton intrinsic transverse momenta. Plenty of evidences of nonzero TMD effects are now present, such as the azimuthal modulations in Semi-Inclusive Deep Inelastic Scattering (SIDIS) first measured at HERMES [22] and COMPASS [23, 24], or the transverse single-spin asymmetries (SSA or  $A_N$ ) observed in inclusive hadroproduction from polarised proton-proton collisions. These asymmetries have been observed since the mid 1970s at Argonne [25–27], and confirmed later by the E704 Collaboration [28–31] and, more recently, by measurements at RHIC [32–40] at different center-of-mass energies. The azimuthal modulations in SIDIS give separate access to TMD functions such as the Sivers distribution or the Collins fragmentation function, that also contribute together to generate  $A_N$  in polarised  $pp$  processes.

---

<sup>1</sup>In the following we will mostly cite protons, but all the considerations apply in general to nucleons, i.e. (anti)protons and (anti)neutrons.

As for the collinear case, in order to keep QCD predictive we need factorisation theorems. But, differently from the collinear QCD case, where only a single energy scale is needed to separate the perturbative and nonperturbative phases, TMD factorisation relies on the existence of two energy scales, a small and a large one. This renders TMD-factorisable only a series of processes, namely SIDIS, Drell-Yan and hadron pair production from  $e^+e^-$  annihilation. Moreover, in the expression for a TMD factorised cross section, two quantities are present: a factorisation scale and a rapidity scale, the latter being absent in the collinear case. This reflects also in the evolution of TMDs, whose evolution equations are more involved than the DGLAP ones for collinear PDFs and FFs. Since the last few decades, starting from the original works of Collins, Soper and Sterman [41, 42], a lot of progress has been made on TMD factorisation and evolution. For example, TMD evolution equations are now well established in the language of the Renormalisation Group. More recent works covering these topics can be found in Refs. [43–53].

Another feature that distinguishes collinear PDFs and FFs from TMDs is the fact that, while the former are strictly universal, the latter are not. This is due to the role of Wilson lines (or gauge links), needed to define a proper gauge-invariant TMD. Nonetheless, universality is not completely broken, but is actually modified, leading to a *process dependence* of some TMD functions [54–60]. This dependence is foreseeable, and is one of the key predictions of TMD theory. Its experimental confirmation would be then a milestone for assessing the validity of the TMD approach in terms of factorisation and evolution.

Finally, TMDs are interesting not only for their ultimate role in explaining the proton spin decomposition. In fact, studies at the most powerful hadron colliders can be influenced by considering TMD effects, as for example the impact of intrinsic  $k_\perp$  effects in measuring the electroweak  $W$  boson mass [61], or by looking at some quantities accessible via TMDs like the so-called transversity, whose relative charges are related to beyond Standard Model observables [62–64].

## 1.2 THIS THESIS

This thesis is partly based on the following publications:

1. U. D'Alesio, C. Flore and F. Murgia  
*Transverse single-spin asymmetries in  $\ell p^\uparrow \rightarrow hX$  within a TMD approach: role of quasi-real photon exchange*  
[Phys. Rev. D95 \(2017\) 094002](#) – arXiv:1701.01148 [hep-ph]
2. M. Boglione, U. D'Alesio, C. Flore and J. O. Gonzalez-Hernandez  
*Assessing signals of TMD physics in SIDIS azimuthal asymmetries and in the extraction of the Sivers function*  
[JHEP07 \(2018\) 148](#) – arXiv:1806.10645 [hep-ph]
3. U. D'Alesio, C. Flore, F. Murgia, C. Pisano and P. Taelis  
*Unraveling the Gluon Sivers Function in hadronic collisions at RHIC*  
[Phys. Rev. D99 \(2019\) 036013](#) – arXiv:1811.02970 [hep-ph]

The complete list of publications, including conference proceedings, is available on the [In-Spire database](#).

In the following, we will discuss TMDs from a phenomenological point of view. In order to give the thesis a consistent logic, we do not present the results of the aforementioned papers in chronological order, but we rather start from the last two papers, regarding phenomenological extractions. Throughout the whole thesis, we will try to underline the current actual knowledge on TMDs and what we can really learn from experimental data. By adopting a TMD approach, we will go through some fits of polarised TMDs, and we will then see their impact on other observables, comparing our predictions, when possible, to existent measurements.

In what follows, we will adopt natural units,  $\hbar = c = 1$ . The thesis is organised as follows:

- in Chapter 2, we will introduce TMD physics, giving a brief overview of the most important (un)polarised TMD distributions and fragmentation functions, focussing on the Sivers, transversity and Collins functions. Moreover, we will cover an extension of the parton model that embeds intrinsic transverse momentum effects, the so-called Generalised Parton Model (GPM). We will also give all the expressions for TMD observables and TMD functions parametrisations within the chosen model.
- Chapter 3 will illustrate a thorough updated study of the quark Sivers function, together with a preliminary study on the transversity and Collins extraction. The role of different choices in phenomenological analyses and their impact on other observables will be particularly emphasised.
- In Chapter 4, the less known gluon Sivers function (GSF) will be carefully analysed, both in the GPM framework and in its colour gauge invariant extension, where two independent GSFs are defined. First bounds on these functions, together with an updated GPM fit of the GSF will be presented.
- Chapter 5 will present the results of some phenomenological analyses for single-spin asymmetries in inclusive processes.  $A_N$  inclusive lepton-proton scattering and the role of the exchanged photon will be analysed, together with the inclusive production of a photon or a  $J/\psi$  in polarised  $pp$  processes.
- In Chapter 6 we will introduce a new project, so far not directly related to TMD physics (but easily extendable to it), developed in the framework of an Horizon 2020 proposal called STRONG-2020.
- Finally, conclusions will be drawn in Chapter 7.

# 2

## Transverse Momentum Dependent physics

The three-dimensional structure of the proton is nowadays the subject of very intensive research. Even if very successful, collinear QCD at leading twist fails in explaining transverse polarisation phenomena in hadronic processes. Since the pioneering works of Feynman and collaborators [65, 66], the inclusion of intrinsic transverse momentum effects in the description of such observables helped to shed light on the internal three-dimensional structure of nucleons. Transverse momentum dependent functions have now a pivotal role in describing the rich and involved dynamics of the confined quarks and gluons. At variance with collinear partonic distributions, TMDs are multidimensional objects, encoding, in momentum space, the information about the three-dimensional structure of the nucleon. Their interesting properties can be studied in experimental measurements and phenomenological analyses.

This Chapter is organised as follows. In Section 2.1 we will introduce TMD functions and give more details on some specific functions, while in Section 2.2 we will analyse some processes related to TMD physics, enlighting the existence of different classes sensitive to TMD effects. Finally, in Section 2.3, we will focus on a particular phenomenological model, the Generalised Parton Model (GPM), which will be used throughout all this thesis.

### 2.1 TRANSVERSE MOMENTUM DEPENDENT FUNCTIONS

This Section is devoted to the Transverse Momentum Dependent functions, which are the subject of analysis all through this thesis. In collinear QCD, looking at the possible different polarisations of partons and nucleons, we have only three independent partonic distributions:  $f_1(x)$ ,  $g_1(x)$  (or  $g_{1L}(x)$ ) and  $h_1(x)$  (*unpolarised*, *helicity* and *transversity* respectively), that correspond to an unpolarised, longitudinally or transversely polarised parton inside an unpolarised, longitudinally or transversely polarised nucleon. These three functions encode one-dimensional information. In fact, besides their scale dependence, they depend only on  $x$ , the longitudinal momentum fraction of the hadron carried by the parton. Including the intrinsic motion of partons inside the nucleon, i.e. being sensitive to their intrinsic transverse momentum  $\mathbf{k}_\perp$  (defined on the transverse plane with respect to the direction of motion of the nucleon), allow us to introduce new functions that depend on  $x$  and  $\mathbf{k}_\perp$ , the *TMD distributions* (also indicated as TMD-PDFs or simply TMDs). These functions encode

information on the three-dimensional structure (in momentum space) of protons and neutrons. A generic TMD distribution, e.g. the unpolarised quark TMD, is usually indicated as  $f_{q/p}(x, k_\perp)$ , where  $k_\perp = |\mathbf{k}_\perp|$ , and is related to its collinear counterpart upon integration over  $\mathbf{k}_\perp$ :

$$f_{q/p}(x) = \int d^2\mathbf{k}_\perp f_{q/p}(x, \mathbf{k}_\perp). \quad (2.1)$$

At leading order and leading twist<sup>1</sup>, we have a total of eight independent quark TMDs:

Quark \ Nucl.	U	L	T
U	$f_1$		$h_1^\perp$
L		$g_{1L}$	$h_{1L}^\perp$
T	$f_{1T}^\perp$	$g_{1T}$	$h_1, h_{1T}^\perp$

Table 2.1: The eight independent leading twist quark TMDs. The indices U, L, T correspond to unpolarised, longitudinally or transversely polarised quarks (columns) and nucleons (rows) respectively. Functions in blue are the ones that survive upon integration over  $\mathbf{k}_\perp$ , and are  $T$ -even along with the ones in black. Functions in red are  $T$ -odd.

According to the possible combinations of quark and nucleon polarisation, we have different TMDs with different properties. The three functions in blue in Table 2.1 are the ones that survive in the collinear limit, i.e. upon integration over  $\mathbf{k}_\perp$ , while the ones dyed in red, the *Sivers function* [69, 70],  $f_{1T}^\perp(x, \mathbf{k}_\perp)$ , and the *Boer-Mulders (BM) function* [71],  $h_1^\perp(x, \mathbf{k}_\perp)$ , are  $T$ -odd objects, so that they change sign upon a time-reversal transformation. The Sivers function describes the asymmetry in the azimuthal distribution on the transverse plane of unpolarised quark inside a transversely polarised proton, while the Boer-Mulders function is related to the net transverse polarisation of quarks inside an unpolarised proton. The black functions in Table 2.1 are  $T$ -even objects;  $h_{1T}^\perp$  is called *pretzelosity*, and is somehow related to the non-sphericity of the nucleon shape [72]. The two other functions are related to transversely polarised quarks in a longitudinally polarised nucleon ( $h_{1L}^\perp$ ), and to longitudinally polarised quarks inside a transversely polarised nucleon ( $g_{1T}$ ); they are often referred to as *worm-gear functions*.

Among the eight independent leading twist TMDs we also have the *transversity function*,  $h_1(x, \mathbf{k}_\perp)$ , often referred to as  $\Delta_T q(x, \mathbf{k}_\perp)$ . This chiral-odd function is one of the three TMDs that survive when integrated over  $\mathbf{k}_\perp$ , and is related to a transversely polarised quark inside a transversely polarised proton. Its corresponding collinear counterpart is subject to the so-called *Soffer bound* [73]. This bound relates the three nucleon collinear distributions, i.e. the collinear counterparts of the three TMDs in blue in Table 2.1, and reads:

$$|h_1(x)| \leq \frac{1}{2} [f_1(x) + g_{1L}(x)]. \quad (2.2)$$

<sup>1</sup>Twist is defined in the Operator Product Expansion as  $t = d - s$ , where  $d$  is the dimension of the operator and  $s$  its spin [67]. A working definition of *twist* for a matrix element of a bi-local operator can be found in [68]: it is the order in  $M/Q$  at which the element contributes to the cross section of deep inelastic processes. A generic twist- $t$  matrix element contributes as  $(M/Q)^{t-2}$ .

The last inequality can be also used to put a bound on the *tensor charge*,  $\delta q$ , defined as

$$\delta q = \int_0^1 \left[ h_1^q(x) - h_1^{\bar{q}}(x) \right] dx. \quad (2.3)$$

This quantity is related to another important quantity, the *isovector* or *nucleon tensor charge*

$$g_T = \delta u_v - \delta d_v, \quad (2.4)$$

with  $\delta u_v$  and  $\delta d_v$  being respectively the tensor charge for valence  $u$ - and  $d$ -quark, and whose magnitude can put limits on observables related to beyond Standard Model (BSM) physics [62–64].

As in the quark case, we have eight independent, leading-twist gluon TMDs:

Nucl. \ Gluon			
	U	Circ.	Lin.
U	$f_1^g$		$h_1^{\perp g}$
L		$g_{1L}^g$	$h_{1L}^{\perp g}$
T	$f_{1T}^{\perp g}$	$g_{1T}^{\perp g}$	$h_1^g, h_{1T}^{\perp g}$

Table 2.2: The eight independent leading twist gluon TMDs. The indices U, L, T correspond to unpolarised, longitudinally or transversely polarised nucleons respectively. U, Circ. and Lin. correspond to unpolarised, circularly or linearly polarised gluons. As in Table 2.1, functions in blue are the ones with a collinear counterpart, and are  $T$ -even along with the ones in black, while functions in red are  $T$ -odd.

Likewise to what happens for quark TMDs, we have  $T$ -odd and  $T$ -even functions, and some of them have a collinear counterpart. Differently from the quark case, here we have only two functions that survive under  $k_\perp$ -integration, the unpolarised and the helicity distributions, and the number of  $T$ -odd gluon TMDs is twice the quarks ones. The gluon transversity-like function, although sharing a similar name to the quark one, has not a corresponding collinear function, and is also  $T$ -odd. Again, we have a *gluon Sivers function* (GSF),  $f_{1T}^{\perp g}$ , still a  $T$ -odd object, and a *gluon Boer-Mulders function*,  $h_1^{\perp g}$ , now a  $T$ -even quantity. These functions have an analogous physical interpretation as for the quarks ones, upon considering the proper polarisation for the gluon (e.g. the gluon BM function describes the azimuthal asymmetry in the distribution of linearly polarised gluons inside an unpolarised proton).

It is worth noticing that these gluon distributions are much less known with respect to the quark TMDs. Nonetheless, they currently attract huge interest. In fact, it has been shown that they can be accessed in high-energy collisions at the LHC [74, 75], and especially at future experimental facilities like the Electron-Ion Collider (EIC) [60, 76, 77] or the proposed fixed-target experiments at the LHC [78–81], that will help us to improve our knowledge on gluon TMDs.

So far, we have focussed only on TMD functions in the distribution sector, but one can be also sensitive to transverse momentum effects in the fragmentation sector, i.e. the one describing the hadronisation of a parton into a colourless hadron. For spin- $\frac{1}{2}$  hadrons, we have eight independent quark TMD fragmentation functions (FF):



Nucl. \ Quark	U	L	T
	U	L	T
U	$D_1$		$H_1^\perp$
L		$G_{1L}$	$H_{1L}^\perp$
T	$D_{1T}^\perp$	$G_{1T}$	$H_1, H_{1T}^\perp$

Table 2.3: The eight independent leading twist quark TMD-FFs. The indices U, L, T correspond to unpolarised, longitudinally or transversely polarised quarks (columns) and nucleons (rows) respectively. As in Table 2.1, functions in blue are the ones with a collinear counterpart, and are  $T$ -even along with the ones in black, while functions in red are  $T$ -odd.

Table 2.3 has the same colour code as the previous tables. Here, we recognize the unpolarised fragmentation function,  $D_1(z, p_\perp)$ , that describes the fragmentation of an unpolarised quark into an unpolarised hadron, and the *Collins function* [82],  $H_1^\perp(z, p_\perp)$ , that is related to the fragmentation of a transversely polarised quark into an unpolarised hadron, and the *polarising fragmentation function*,  $D_{1T}^\perp$ , which can be viewed as the analogue of the Sivers function in the fragmentation sector.

### 2.1.1.1 PROPERTIES OF $T$ -ODD TMDs

The TMD functions introduced in Section 2.1 come from proper projections of unintegrated quark and gluon correlators, that satisfy QCD properties (see for example [71, 83], or [84] for a comprehensive review). Moreover, as already mentioned in Section 2.1, they have different properties upon time-reversal transformation, and they are subject to some bounds, coming from a theoretical request of positivity of the spin density matrix eigenvalues [85] (see Section 2.1.2).

Here we focus on some interesting aspects of  $T$ -odd TMD distributions and fragmentation functions, namely the Sivers and Boer-Mulders functions in the distribution sector, and the Collins function in the fragmentation sector.

Let us start from the two  $T$ -odd distributions. The probability to find an unpolarised quark with light-cone momentum fraction  $x$  and transverse momentum  $\mathbf{k}_\perp$  inside a transversely polarised nucleon is given by [86, 87]:

$$f_{q/N^\uparrow}(x, \mathbf{k}_\perp) = f_1(x, k_\perp^2) - \frac{(\hat{\mathbf{P}} \times \mathbf{k}_\perp) \cdot \mathbf{S}_T}{M} f_{1T}^\perp(x, k_\perp^2), \quad (2.5)$$

where  $\hat{\mathbf{P}} \equiv \mathbf{P}/|\mathbf{P}|$  is a unit vector,  $\mathbf{P}$  is the nucleon momentum,  $M$  its mass and  $\mathbf{S}_T$  its spin transverse component. The asymmetric azimuthal distribution of quarks in the transverse plane with respect to the direction of motion of the nucleon is then

$$\begin{aligned} f_{q/N^\uparrow}(x, \mathbf{k}_\perp) - f_{q/N^\downarrow}(x, \mathbf{k}_\perp) &\equiv f_{q/N^\uparrow}(x, \mathbf{k}_\perp) - f_{q/N^\uparrow}(x, -\mathbf{k}_\perp) \\ &= -2 \frac{(\hat{\mathbf{P}} \times \mathbf{k}_\perp) \cdot \mathbf{S}_T}{M} f_{1T}^\perp(x, k_\perp^2), \end{aligned} \quad (2.6)$$

so it is proportional to the Sivers function  $f_{1T}^\perp$ . A nonzero Sivers function means that unpolarised quarks inside a transversely polarised nucleon have a preferred direction of motion.

More specifically, considering a nucleon moving along  $+\hat{z}$  with a transverse polarisation in the  $+\hat{y}$  direction,  $f_{1T}^\perp > 0$  signals right moving unpolarised quarks, that is towards  $-\hat{x}$ .

Likewise the Sivers case, the distribution of a transversely polarised quark inside an unpolarised nucleon is [86, 87]

$$f_{q^\uparrow/N}(x, \mathbf{k}_\perp) = \frac{1}{2} \left[ f_1(x, k_\perp^2) - \frac{(\hat{\mathbf{P}} \times \mathbf{k}_\perp) \cdot \mathbf{S}_{qT}}{M} h_1^\perp(x, k_\perp^2) \right], \quad (2.7)$$

where  $\mathbf{S}_{qT}$  is the quark spin transverse component. The relative asymmetry is

$$f_{q^\uparrow/N}(x, \mathbf{k}_\perp) - f_{q^\downarrow/N}(x, \mathbf{k}_\perp) = -\frac{(\hat{\mathbf{P}} \times \mathbf{k}_\perp) \cdot \mathbf{S}_{qT}}{M} h_1^\perp(x, k_\perp^2) \quad (2.8)$$

and is proportional to the Boer-Mulders (BM) function,  $h_1^\perp$ .

The  $T$ -odd nature of the Sivers and Boer-Mulders functions comes respectively from the correlations  $(\hat{\mathbf{P}} \times \mathbf{k}_\perp) \cdot \mathbf{S}_T$  and  $(\hat{\mathbf{P}} \times \mathbf{k}_\perp) \cdot \mathbf{S}_{qT}$ . This time-reversal property implies a so-called *modified universality* or *process dependence*. This feature comes from the important role of gauge links in the operatorial definition of TMDs. Without entering into details, we mention that it is possible to write an operator definition of the Sivers function:

$$f_{1T}^\perp(x, k_\perp^2) \sim \int d\bar{\xi}^- \int d^2\xi_T e^{i(xP^+\bar{\xi}^- - \mathbf{k}_\perp \cdot \bar{\xi}_T)} \times \langle P, S_T | \bar{\psi}(0) \gamma^+ \mathcal{W}[0, \bar{\xi}] \psi(\bar{\xi}) | P, S_T \rangle |_{\bar{\xi}^+ = 0}. \quad (2.9)$$

Here, light-front coordinates are used:  $\bar{\xi}^\pm = (\bar{\xi}^0 \pm \bar{\xi}^3) / \sqrt{2}$  and  $\bar{\xi}_T^\mu = (0, \bar{\xi}_T, 0)$ . The quantity  $\mathcal{W}[0, \bar{\xi}]$  is the *gauge link* or *Wilson line*. This object is used to ensure a proper gauge invariant definition of the matrix element. If the Wilson line is set to unity, the Sivers operatorial definition, Eq. (2.9), changes sign upon time reversal, therefore the Sivers function itself would be zero [82]. On the other hand, by properly considering the gauge link in Eq. (2.9), it has been shown that the Sivers function is nonvanishing [56]. More specifically, since  $\mathcal{W}[0, \bar{\xi}]$  contains transverse links to infinity that do not reduce to unity in the light-cone gauge, and since time reversal changes a future-pointing Wilson line into a past-pointing one,  $T$ -invariance gives a relation between the gauge links probed in different processes, the Semi-Inclusive Deep Inelastic Scattering (SIDIS) and the Drell-Yan (DY) process (see Section 2.2). In these reactions, the probed Wilson lines point in opposite time directions, and this indicates the existence of *initial* and *final state interactions* (ISI and FSI). In SIDIS the Sivers asymmetry is generated by a final state interaction between the outgoing quark and the remnants in the final state, while in DY production an initial state interaction between the spectator and an incoming quark takes place. This difference in the gauge link structure induces the following relation between the Sivers function probed in SIDIS and DY:

$$f_{1T}^\perp(x, k_\perp^2)_{\text{SIDIS}} = -f_{1T}^\perp(x, k_\perp^2)_{\text{DY}}. \quad (2.10)$$

This is the so-called process dependence or modified universality of the Sivers function, and its experimental confirmation is one of the goals of TMD physics. Very recently, some first hints of the Sivers sign change have been observed in DY Single Spin Asymmetries [88, 89], but more data and with higher accuracy are necessary to verify this important relation. Note



that a relation like Eq. (2.10) holds for the Boer-Mulders function [56] as well.

Differently to what happens with the  $T$ -odd distributions (Sivers and Boer-Mulders), there seems to be no modified universality for the Collins fragmentation function: this TMD is expected to be universal [90, 91]. The Collins function, a chiral-odd one, is probably the most noteworthy TMD FF appearing in Table 2.3. As said before, it describes the fragmentation of a transversely polarised quark into an unpolarised hadron. The relative asymmetry is given by [86, 87]:

$$D_{h/q^\uparrow}(z, \mathbf{p}_\perp) - D_{h/q^\uparrow}(z, -\mathbf{p}_\perp) = 2 \frac{(\hat{\mathbf{p}}_q \times \mathbf{p}_\perp) \cdot \mathbf{s}_q}{zm_h} H_1^\perp(z, p_\perp^2), \quad (2.11)$$

where  $\mathbf{p}_q$  and  $\mathbf{s}_q$  are the quark momentum and spin, respectively,  $m_h$  is the mass of the produced hadron with momentum  $\mathbf{p}_h \simeq z\mathbf{p}_q + \mathbf{p}_\perp$ . A positive  $H_1^\perp$  corresponds to hadrons that prefer to be emitted on the left side of the jet if the quark spin points upwards. This function usually couples to other chiral-odd functions, originating the so-called Collins asymmetries. For example, it allows to measure the TMD transversity distribution (not measurable in DIS processes due to its chiral-odd nature) in the SIDIS azimuthal modulation  $F_{UT}^{\sin(\phi_h + \phi_S)}$  (see Section 2.2). Moreover, two coupled Collins functions are accessible in the azimuthal modulations measured in  $e^+e^- \rightarrow h_1 h_2 X$  processes [92].

#### MOMENTS OF TMDs

Before focussing on some useful constraints on TMDs, we introduce the  $k_\perp(p_\perp)$ -moments of TMD distributions (fragmentation functions). Generally, we define a  $k_\perp(p_\perp)$ -moment as

$$\begin{aligned} f^{(n)}(x) &= \int d^2 \mathbf{k}_\perp \left( \frac{k_\perp^2}{2M^2} \right)^n f(x, k_\perp^2), \\ D^{(n)}(z) &= z^2 \int d^2 \mathbf{p}_\perp \left( \frac{p_\perp^2}{2m_h^2} \right)^n D(z, z^2 p_\perp^2). \end{aligned} \quad (2.12)$$

Note that these definitions only hold up to renormalisation.

Starting from these last expressions, we can construct the  $n$ -th moment of every TMD. Here we focus only on the first moments of the Sivers and the Collins functions.

The first moment of the Sivers function,  $f_{1T}^{\perp(1)}(x)$ , is defined as

$$f_{1T}^{\perp(1)}(x) = \int d^2 \mathbf{k}_\perp \frac{k_\perp^2}{2M^2} f_{1T}^\perp(x, k_\perp^2), \quad (2.13)$$

while the Collins first moment,  $H_1^{\perp(1)}(z)$ , is given by

$$H_1^{\perp(1)}(z) = z^2 \int d^2 \mathbf{p}_\perp \frac{p_\perp^2}{2m_h^2} H_1^\perp(z, z^2 p_\perp^2). \quad (2.14)$$

It is worth mentioning that these moments are intimately related to collinear twist-3 functions. The first moment of the Sivers function, Eq. (2.13), is proportional to the Qiu-Sterman

(QS) function [93–97] via a model-independent relation [58], while the first moment of the Collins function is related to a twist-3 fragmentation function (see e.g. [98]). As first noted in [58], the relation between the Sivers first moment and QS functions implies that, if one of them is nonzero, then also the other is.

### 2.1.2 CONSTRAINTS ON TMDs

The TMD functions introduced in Section 2.1 are subject to useful constraints given in terms of *positivity bounds* and *sum rules*. The bounds come from a theoretical request of positivity of the spin-matrix eigenvalues [85], while the sum rules come as usual from conservation laws.

Apart from the Soffer bound for the transversity distribution, Eq. (2.2), we have two positivity bounds for the (quark and gluon) Sivers function and the Collins function:

$$\frac{k_{\perp}}{M} \left| f_{1T}^{\perp q(g)}(x, k_{\perp}^2) \right| \leq f_1^{q(g)}(x, k_{\perp}^2), \quad \frac{p_{\perp}}{zm_h} \left| H_1^{\perp}(z, p_{\perp}^2) \right| \leq D_1(z, p_{\perp}^2). \quad (2.15)$$

These bounds hold for every value of  $x(z)$  and  $k_{\perp}(p_{\perp})$ , and put a constraint on the size of these functions. They have been widely used in phenomenological analyses, but it is also interesting to test them while analysing experimental data, as we will see in Chapter 3.

At the same time, we can constrain these TMDs using sum rules. A sum rule for the Sivers function was first derived by Burkardt [99, 100], who showed that, at leading order, the sum of all contributions (quarks, antiquarks and gluons) to the average transverse momentum of unpolarised partons inside a transversely polarised nucleon must vanish:

$$\sum_{a=q,\bar{q},g} \langle \mathbf{k}_{\perp}^a \rangle |_{\text{Sivers}} = 0, \quad (2.16)$$

that, in terms of the Sivers first moment, Eq. (2.13), becomes [101]

$$\sum_{a=q,\bar{q},g} \int_0^1 dx f_{1T}^{\perp(1)a}(x) = 0. \quad (2.17)$$

A similar constraint on the Collins function, derived by Schäfer and Terayev [102], comes from the request of intrinsic transverse momentum conservation in the quark fragmentation process. It is written in terms of the Collins first moment, Eq. (2.14), and is given by

$$\sum_h \int_0^1 dz z^2 H_1^{\perp(1)}(z) = 0. \quad (2.18)$$

### 2.1.3 A SMALL DICTIONARY

So far, we have used a specific notation, called “*Amsterdam*” notation. This notation is probably the most widely used in literature. But, another equivalent notation exists, and is usually referred to as “*Torino-Cagliari*” notation. The latter has been widely used, especially in the context of the Generalised Parton Model, and will also be used in a very large part of this thesis. Luckily enough, a dictionary that brings from one notation to the other one has been devel-

oped, the so-called “*Trento conventions*” [103]. It is then worth to report some expressions for the polarised TMDs we have seen so far that relate the two notations.

For example, we can either refer to  $f_{1T}^{\perp q}$  or  $\Delta^N f_{q/p\uparrow}$  as the “Sivers function”. The relation between the two functions is

$$\Delta^N f_{q/p\uparrow}(x, k_\perp^2) = -\frac{2k_\perp}{M} f_{1T}^{\perp q}(x, k_\perp^2). \quad (2.19)$$

Similarly, the Boer-Mulders function in the Torino-Cagliari notation can be related to the one in the Amsterdam notation as

$$\Delta^N f_{q\uparrow/p}(x, k_\perp^2) = -\frac{k_\perp}{M} h_1^{\perp q}(x, k_\perp^2), \quad (2.20)$$

while for the Collins fragmentation function we have:

$$\Delta^N D_{h/q\uparrow}(z, p_\perp^2) = \frac{2p_\perp}{zm_h} H_1^{\perp q}(z, p_\perp^2). \quad (2.21)$$

Using these equations, we find that the bounds on TMDs, Eq. (2.15), can be rewritten as

$$\begin{aligned} \left| \Delta^N f_{q(g)/p\uparrow}(x, k_\perp^2) \right| &\leq 2 f_1^{q(g)}(x, k_\perp^2), \\ \left| \Delta^N D_{h/q\uparrow}(z, p_\perp^2) \right| &\leq 2 D_1^q(z, p_\perp^2), \end{aligned} \quad (2.22)$$

and, regarding the first  $k_\perp$ -moment of the Sivers function, a very simple relation between the two notations holds:

$$\Delta^N f_{q/p\uparrow}^{(1)}(x) = \int d^2 \mathbf{k}_\perp \frac{k_\perp}{4M} \Delta^N f_{q/p\uparrow}(x, k_\perp^2) = -f_{1T}^{\perp(1)q}(x). \quad (2.23)$$

In the rest of this Chapter we will use both notations. Particularly, in Section 2.2, we will give the expressions in terms of TMDs in the Amsterdam notation, while in Section 2.3 the expressions for the TMD parametrisations will be given using both representations.

## 2.2 TWO-SCALE AND SINGLE-SCALE PROCESSES

In this Section we will take a look at some of the processes sensitive to TMD physics. In particular, we will examine two different classes of processes, categorised according to the number of different energy or momentum scales.

TMD factorisation has been proven for a specific class of processes, in which we detect a soft and a hard energy (or momentum) scale [41–53]. These processes are the *Semi-Inclusive Deep Inelastic Scattering* (SIDIS), a lepton-nucleon scattering with the observation of a produced hadron and the scattered lepton in the final state, the *Drell-Yan* (DY) process, lepton pair production from quark-antiquark annihilation (with the quark-antiquark pair coming from two colliding hadrons), and  $e^+e^- \rightarrow h_1 h_2 X$ , where the two hadrons are produced almost back-to-back. In this class of processes, the intrinsic transverse momentum of partons,  $k_\perp$ , and the observed hadron (or lepton pair) transverse momentum,  $P_T$ , are small (of order

$\Lambda_{\text{QCD}}$ ), and the virtuality of the exchanged vector boson,  $Q^2$ , is large. That is, we can observe an ordering of the form (e.g. for SIDIS):

$$k_{\perp}^2 \simeq \Lambda_{\text{QCD}}^2 \simeq P_T^2 \ll Q^2. \quad (2.24)$$

It is important to notice that these are electromagnetic processes, meaning that the cross section can always be separated into a convolution of a leptonic tensor and an hadronic tensor. This separation also indicates that the colour flow in the process is well isolated (the leptonic part contains no QCD colour flow), hence TMD factorisation theorems can be applied.

Contrary to these two-scale processes, there are hadronic processes in which only one hard scale (usually the transverse momentum of the produced hadron) is observed. These are single-scale processes, for which a proof of TMD factorisation does not exist. Nonetheless, phenomenological approaches including intrinsic transverse momentum effects (e.g. the Generalised Parton Model, GPM, see Section 2.3) succeeded in describing observables related to inclusive processes. One example of these observables are the transverse single-spin asymmetries (often referred to in literature as TSSAs, SSAs or  $A_N$ ) measured for inclusive hadron production (typically a pion) from polarised proton-proton scattering. Note that, at large hadron transverse momentum, the size of such asymmetries are not explainable in collinear perturbative QCD at leading twist [104].

It is also worth noticing that single-scale processes can be described in the context of collinear twist-3 (CT3) factorisation, where twist-3 parton correlation functions that couples quark fields and gluon field strengths are used [93–97, 105–108]. Even if for these processes only a collinear approach at higher twist in pQCD could be used, it is very important to underline that twist-3 correlation functions and  $k_{\perp}$ -moments of TMD functions are related. Indeed, another interesting link between collinear twist-3 and TMD physics is represented by the so-called Colour Gauge Invariant Generalised Parton Model (CGI-GPM) [109, 110]. Under a one-gluon-exchange approximation (that corresponds to the first order in the perturbative expansion of the gauge link used in TMD definition, Eq. (2.9)) the process dependence of the Sivers function, Eq. (2.10), can be included into GPM and, up to a prefactor associated to initial/final state interactions, the same form of CT3 partonic cross sections can be recovered as well.

In the following, we will take a closer look at two examples, one for a two-scale process, the Semi-Inclusive DIS, for which TMD factorisation applies, and one for a single-scale process, inclusive hadron production in hadronic collisions, for which no proof of TMD factorisation exists, and in principle the collinear twist-3 approach should be used. Another two-scale process, the  $e^+e^-$  annihilation into two hadrons, will be briefly illustrated later in Section 3.3.1.

### 2.2.1 SEMI-INCLUSIVE DEEP INELASTIC SCATTERING

We now briefly take a look at one of the most important processes for TMD physics, the Semi-Inclusive Deep Inelastic Scattering. This process has a historical role in this context. It allows for several kind of measurements, thanks to the existence of different azimuthal modulations that give access to various combinations of TMD functions. For this reason, SIDIS data are widely used in the extraction of TMD functions like the unpolarised, transversity and Sivers functions (in the distribution sector) and the unpolarised and Collins fragmentation functions [111–120].

This process is characterised by the detection of a hadron in the final state, along with the observation of the scattered lepton, while the target nucleon in the initial state could be either polarised or unpolarised. The reaction is:

$$\ell(l) + N(P, S) \rightarrow \ell(l') + h(P_h) + X \quad (2.25)$$

where  $\ell$  denotes the beam lepton,  $N$  the nucleon target with four-momentum  $P$  and polarisation  $S$ , and  $h$  the produced hadron with four-momentum  $P_h$  and transverse momentum  $P_{h\perp} \equiv P_T$ . We denote by  $M$  and  $m_h$  the masses of the nucleon and of the hadron  $h$ , respectively. Moreover, we define  $q = l - l'$  the momentum of the virtual photon, and  $Q^2 = -q^2$ . With these definitions, we can identify the following invariant variables:

$$x = \frac{Q^2}{2P \cdot q}, \quad y = \frac{P \cdot q}{P \cdot l}, \quad z = \frac{P \cdot P_h}{P \cdot q}, \quad \gamma = \frac{2Mx}{Q}. \quad (2.26)$$

where  $x$  is the so-called *Bjorken- $x$* , and it is often indicated as  $x_{Bj}$ .

The cross section for SIDIS processes depends on the variables in Eq. (2.26), and on  $Q^2$ ,  $P_T$  and  $\phi_h$ , the azimuthal angle of the produced hadron in the final state. In the case of a transversely polarised nucleon, it also depends on  $\phi_S$ , the azimuthal angle of the transverse component  $S_T$  (or  $S_\perp$ ) of the nucleon polarisation.

Following the Trento conventions [103], we consider the  $\gamma^* - p$  center of mass frame, with the virtual photon moving along the positive direction  $+\hat{z}$  of the  $z$ -axis, the proton along  $-\hat{z}$ , and the nucleon has transverse polarisation  $S_T$  with azimuthal angle  $\phi_S$  with respect to the lepton plane, as showed in Fig. 2.1.

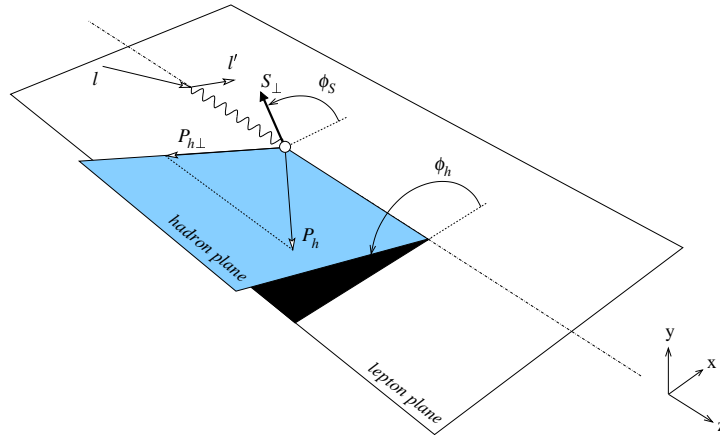


Figure 2.1: Kinematics of polarised Semi-Inclusive DIS according to the Trento conventions [103]. The azimuthal angles are defined in the target rest frame.  $P_{h\perp} \equiv P_T$  and  $S_\perp \equiv S_T$  are the transverse component of  $P_h$  and  $S$  with respect to the photon momentum.

As mentioned before, this process represents a great source of information for TMD physics. The dependence on the two azimuthal angles  $\phi_h$  and  $\phi_S$  generates several azimuthal modulations in the cross section so that, isolating every modulation, we have access to different contributions to the cross section, related to a specific effect. In a single photon exchange approximation, the SIDIS cross section can be written in terms of 18 independent structure

functions as [121]

$$\begin{aligned}
\frac{d\sigma}{dx dy dz d\phi_S d\phi_h dP_T^2} &= \frac{\alpha_{em}^2}{xyQ^2} \frac{y^2}{2(1-\varepsilon)} \left( 1 + \frac{\gamma^2}{2x} \right) \\
&\times \left\{ F_{UU,T} + \varepsilon F_{UU,L} + \sqrt{2\varepsilon(1+\varepsilon)} \cos\phi_h F_{UU}^{\cos\phi_h} + \varepsilon \cos(2\phi_h) F_{UU}^{\cos 2\phi_h} \right. \\
&+ \lambda \sqrt{2\varepsilon(1-\varepsilon)} \sin\phi_h F_{LU}^{\sin\phi_h} \\
&+ S_L \left[ \sqrt{2\varepsilon(1+\varepsilon)} \sin\phi_h F_{UL}^{\sin\phi_h} + \varepsilon \sin(2\phi_h) F_{UL}^{\sin 2\phi_h} \right] \\
&+ S_L \lambda \left[ \sqrt{1-\varepsilon^2} F_{LL} + \sqrt{2\varepsilon(1-\varepsilon)} \cos\phi_h F_{LL}^{\cos\phi_h} \right] \\
&+ S_T \left[ \sin(\phi_h - \phi_S) \left( F_{UT,T}^{\sin(\phi_h - \phi_S)} + \varepsilon F_{UT,L}^{\sin(\phi_h - \phi_S)} \right) \right. \\
&+ \varepsilon \sin(\phi_h + \phi_S) F_{UT}^{\sin(\phi_h + \phi_S)} + \varepsilon \sin(3\phi_h - \phi_S) F_{UT}^{\sin(3\phi_h - \phi_S)} \\
&+ \left. \sqrt{2\varepsilon(1+\varepsilon)} \sin\phi_S F_{UT}^{\sin\phi_S} + \sqrt{2\varepsilon(1+\varepsilon)} \sin(2\phi_h - \phi_S) F_{UT}^{\sin(2\phi_h - \phi_S)} \right] \\
&+ S_T \lambda \left[ \sqrt{1-\varepsilon^2} \cos(\phi_h - \phi_S) F_{LT}^{\cos(\phi_h - \phi_S)} + \sqrt{2\varepsilon(1-\varepsilon)} \cos\phi_S F_{LT}^{\cos\phi_S} \right. \\
&+ \left. \left. \sqrt{2\varepsilon(1-\varepsilon)} \cos(2\phi_h - \phi_S) F_{LT}^{\cos(2\phi_h - \phi_S)} \right] \right\}, \tag{2.27}
\end{aligned}$$

where  $\alpha_{em}$  is the electromagnetic fine structure constant,  $\lambda$  is the helicity of the lepton beam,  $S_T \equiv |\mathbf{S}_T|$  and all the structure functions depend on  $x, z, Q^2$  and  $P_T$ . The subscript of the structure functions are referring to the beam and target polarisation (with respect to the photon direction), respectively, while the third subscript in  $F_{UU,T}$ ,  $F_{UU,L}$  and  $F_{UT,T}^{\sin(\phi_h - \phi_S)}$ ,  $F_{UT,L}^{\sin(\phi_h - \phi_S)}$  corresponds to the polarisation of the exchanged virtual photon.  $\varepsilon$  represents the ratio of the longitudinal and transverse photon fluxes in Eq. (2.27) and is given by

$$\varepsilon = \frac{1 - y - \frac{1}{4}\gamma^2 y^2}{1 - y + \frac{1}{2}y^2 + \frac{1}{4}\gamma^2 y^2}. \tag{2.28}$$

Integrating the master formula, Eq. (2.27), over the outgoing hadron transverse momentum  $P_T$  we than obtain the Semi-Inclusive DIS cross section

$$\begin{aligned}
\frac{d\sigma}{dx dy d\phi_S dz} = & \frac{2\alpha_{em}^2}{xyQ^2} \frac{y^2}{2(1-\varepsilon)} \left(1 + \frac{\gamma^2}{2x}\right) \left[ F_{UU,T} + \varepsilon F_{UU,L} \right. \\
& + S_L \lambda \sqrt{1-\varepsilon^2} F_{LL} \\
& + S_T \sqrt{2\varepsilon(1+\varepsilon)} \sin\phi_S F_{UT}^{\sin\phi_S} \\
& \left. + S_T \lambda \sqrt{2\varepsilon(1-\varepsilon)} \cos\phi_S F_{LT}^{\cos\phi_S} \right],
\end{aligned} \tag{2.29}$$

where the structure functions on the r.h.s. are integrated versions of the previous ones, i.e.

$$F_{UU,T}(x, z, Q^2) = \int d^2\mathbf{P}_T F_{UU,T}(x, z, P_T^2, Q^2) \tag{2.30}$$

and similarly for the other ones.

#### AZIMUTHAL ASYMMETRIES

Starting from the  $P_T$ -dependent SIDIS cross section, Eq. (2.27), we can define weighted ratios of structure functions to construct physical observables, the *azimuthal asymmetries*, that give access to convolutions of transverse momentum dependent distributions and fragmentation functions. Hence, by studying these ratios, we can extract the TMDs we are interested in.

To identify these asymmetries, keeping only terms at leading order in  $1/Q$  we can rewrite Eq. (2.27) as [122]

$$\begin{aligned}
\frac{d\sigma}{dx dy dz d\phi_S d\phi_h dP_T^2} = & \frac{\alpha_{em}^2}{xyQ^2} \left(1 - y + \frac{y^2}{2}\right) F_{UU}(x, z, P_T^2) \\
& \times \left[ 1 + \cos(2\phi_h) p_1 A_{UU}^{\cos(2\phi_h)} + S_L \sin(2\phi_h) p_1 A_{UL}^{\sin(2\phi_h)} + \lambda S_L p_2 A_{LL} \right. \\
& + S_T \sin(\phi_h - \phi_S) A_{UT}^{\sin(\phi_h - \phi_S)} + S_T \sin(\phi_h + \phi_S) p_1 A_{UT}^{\sin(\phi_h + \phi_S)} \\
& \left. + S_T \sin(3\phi_h - \phi_S) p_1 A_{UT}^{\sin(3\phi_h - \phi_S)} + \lambda S_T \cos(\phi_h - \phi_S) p_2 A_{LT}^{\cos(\phi_h - \phi_S)} \right],
\end{aligned} \tag{2.31}$$

where  $F_{UU} \equiv F_{UU,T}$ . The kinematical prefactors are given by

$$p_1 = \frac{1-y}{1-y+\frac{1}{2}y^2}, \quad p_2 = \frac{y\left(1-\frac{1}{2}y\right)}{1-y+\frac{1}{2}y^2}, \tag{2.32}$$

and the asymmetries  $A_{XY}^{W(\phi_h, \phi_S)}$  are defined in terms of structure functions  $F_{XY}^{W(\phi_h, \phi_S)}$  as follows:

$$A_{XY}^{W(\phi_h, \phi_S)} \equiv A_{XY}^{W(\phi_h, \phi_S)}(x, z, P_T) = \frac{F_{XY}^{W(\phi_h, \phi_S)}(x, z, P_T)}{F_{UU}(x, z, P_T)}. \tag{2.33}$$



The first subscript  $X = U(L)$  refers to the unpolarised beam (longitudinally polarised beam with helicity  $\lambda$ ), while the second subscript  $Y = U(L \text{ or } T)$  represents the unpolarised (longitudinally or transversely polarised with respect to the virtual photon) target.  $W(\phi_h, \phi_s)$  denotes the azimuthal dependence; if no  $W(\phi_h, \phi_s)$  is specified, the structure function or the asymmetry are independent of  $\phi_h$ .

The asymmetries defined in Eq. (2.31) are also denoted as “twist-2” asymmetries. On the other hand, subleading asymmetries in  $1/Q$  exist too. The latter contain a factor  $M/Q$  in their definition, and we refer to them as “twist-3” asymmetries. For our purposes, we only consider twist-2 asymmetries, but we notice that the subleading asymmetries can give access to other interesting functions as well, that can play a role in the framework of the collinear twist-3 factorisation, now widely used to describe inclusive production of hadrons in polarised hadronic collisions [106–108].

Throughout this thesis we will particularly concentrate on the following SIDIS azimuthal asymmetries:

$$\begin{aligned} A_{UT}^{\sin(\phi_h - \phi_s)} &= \frac{F_{UT}^{\sin(\phi_h - \phi_s)}}{F_{UU}}, \\ A_{UT}^{\sin(\phi_h + \phi_s)} &= \frac{2(1-y)}{1 + (1-y)^2} \frac{F_{UT}^{\sin(\phi_h + \phi_s)}}{F_{UU}}. \end{aligned} \quad (2.34)$$

The first asymmetry is related to the Sivers effect, while the second asymmetry contains in  $F_{UT}^{\sin(\phi_h + \phi_s)}$  the convolution between the transversity and the Collins functions. More specifically, using the following notation for convolutions [121, 122],

$$\begin{aligned} \mathcal{C}[\omega f D] &= x \sum_{a=q,\bar{q}} e_a^2 \int d^2 \mathbf{k}_\perp d^2 \mathbf{p}_\perp \delta^{(2)}(z \mathbf{k}_\perp + \mathbf{p}_\perp - \mathbf{P}_T) \\ &\times \omega\left(\mathbf{k}_\perp, -\frac{\mathbf{p}_\perp}{z}\right) f_a(x, k_\perp^2) D_a(z, p_\perp^2), \end{aligned} \quad (2.35)$$

we can write the structure functions in Eq. (2.34) as convolutions of TMDs with a proper weight:

$$\begin{aligned} F_{UU} &= \mathcal{C}\left[\omega^{\{0\}} f_1 D_1\right], \\ F_{UT}^{\sin(\phi_h - \phi_s)} &= \mathcal{C}\left[-\omega_A^{\{1\}} f_{1T}^\perp D_1\right], \\ F_{UT}^{\sin(\phi_h + \phi_s)} &= \mathcal{C}\left[\omega_B^{\{1\}} h_1 H_1^\perp\right], \end{aligned} \quad (2.36)$$

where the weights are given by:

$$\omega^{\{0\}} = 1, \quad \omega_A^{\{1\}} = \frac{\hat{\mathbf{P}}_T \cdot \mathbf{k}_\perp}{M}, \quad \omega_B^{\{1\}} = \frac{\hat{\mathbf{P}}_T \cdot \mathbf{p}_\perp}{z m_h}. \quad (2.37)$$

The Collins asymmetry in Eq. (2.34) is defined as the one measured by the HERMES Collaboration. It is important to notice that the COMPASS Collaboration measures  $A_{UT}^{\sin(\phi_h + \phi_s - \pi)} = F_{UT}^{\sin(\phi_h + \phi_s - \pi)} / F_{UU}$ , where the depolarisation factor  $D_{NN} = 2(1-y) / [1 + (1-y)^2]$  is divided out and, due to the extra  $\pi$  factor in the azimuthal phase, the asymmetry has a different sign with respect to the one measured by HERMES.



### 2.2.2 SINGLE INCLUSIVE HADRON PRODUCTION FROM HADRONIC COLLISIONS

In this part we will concentrate on the inclusive production of a single hadron coming from the scattering between two hadrons, that is  $AB \rightarrow CX$ . Let us start considering hadroproduction with a transversely polarised colliding particle. For these processes, a transverse single-spin asymmetry  $A_N$  (often indicated also as single-spin asymmetry or left-right asymmetry) is measured. This asymmetry is defined as

$$A_N = \frac{d\sigma^\uparrow - d\sigma^\downarrow}{d\sigma^\uparrow + d\sigma^\downarrow} = \frac{d\Delta\sigma}{2d\sigma^{\text{unp}}}, \quad (2.38)$$

where the differential cross sections are usually measured as a function of  $P_T$ , the transverse momentum of the produced hadron as well as the only hard scale of the process (typically  $P_T \gtrsim 1$  GeV), and of the Feynman variable  $x_F = 2P_L/\sqrt{s}$ , with  $P_L$  being the longitudinal momentum of the hadron in the final state.

It is well known since very long time that the large single-spin asymmetries observed in polarised  $pp$  collisions at large  $x_F$  cannot be described in the framework of collinear, leading twist perturbative QCD, where  $A_N$  appears only as the imaginary part of interference terms between spin-flip and no-spin-flip partonic scattering amplitudes. These are real quantities at LO, and since helicity is conserved for massless partons, it was naively expected that  $A_N \simeq \alpha_s m/\sqrt{s}$  [104]. That is, in the high-energy regime,  $A_N \simeq 0$ . This result is opposite to the experimental observation, that showed sizeable and persistent asymmetries at high energy and over a large range of  $x_F$  and  $P_T$  [29, 37–40], as showed in Fig. 2.2.

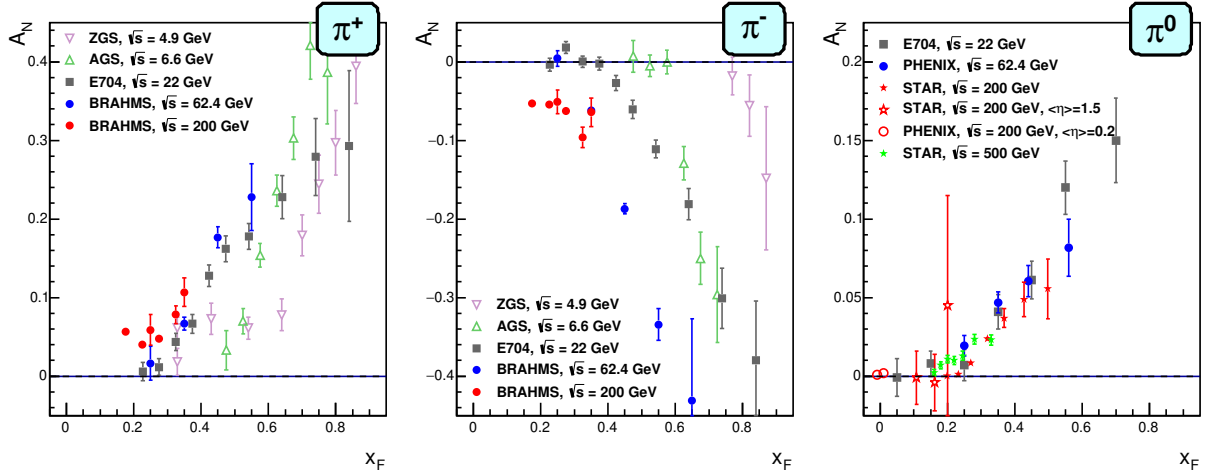


Figure 2.2: Transverse single-spin asymmetry measurements for charged and neutral pions at different center-of-mass energies as a function of Feynman- $x$ ,  $x_F$ .

According to the collinear QCD factorisation theorems [42, 45, 123] the differential cross sections for inclusive production of a single, unpolarised hadron at large  $P_T$  can be written as a convolution of different objects [87]:

$$d\sigma^{(S)} = \sum_{abc} \sum_{\lambda_a \lambda'_a, \lambda_c \lambda'_c} \rho_{\lambda_a \lambda'_a}^{a/A, S} f_{a/A}(x_a) \otimes f_{b/B}(x_b) \otimes d\hat{\sigma}_{\lambda_a \lambda'_a \lambda_c \lambda'_c} \otimes \mathcal{D}_{\lambda_c \lambda'_c}^{C/c}(z). \quad (2.39)$$

In this expression we see the convolution between two distributions,  $f_{a/A}$  and  $f_{b/B}$ , of

parton  $a$  inside hadron  $A$  and parton  $b$  inside hadron  $B$ , respectively, the helicity density matrix  $\rho_{\lambda_a \lambda'_a}^{a/A,S}$  of parton  $a$ , the fragmentation matrix  $\mathcal{D}_{\lambda_c \lambda'_c}^{C/c}$  of parton  $c$  into the unpolarised hadron  $C$  and the partonic cross section  $d\hat{\sigma}$ , that is a perturbatively computable object (at lowest order it represents the cross section for the elementary two-body scattering  $ab \rightarrow cd$ ). The convolutions  $\otimes$  in Eq. (2.39) are on the partonic light-cone momentum fraction  $x_a$ ,  $x_b$  and  $z$ .

In the case under consideration (or when the produced hadron is spinless), the only non-zero elements of  $\mathcal{D}_{\lambda_c \lambda'_c}^{C/c}$  are the diagonal ones, so  $\mathcal{D}_{\lambda_c \lambda'_c}^{C/c} \sim \delta_{\lambda_c \lambda'_c} D^{C/c}(z)$ , with  $D^{C/c}(z)$  being the unpolarised fragmentation function. Moreover, requiring helicity conservation in the partonic process, implies  $\lambda_a = \lambda'_a$ . That is, the differential cross section, Eq. (2.39), is independent of the hadron  $A$  spin, therefore every single-spin asymmetry is zero [104]. So, as said at the beginning of Section 2.2, we need to use other approaches, such as the GPM or the twist-3 approach. In the case of GPM, one is able to probe some of the TMDs defined in Section 2.1, namely the Sivers, Boer-Mulders and transversity distributions and the Collins fragmentation function, while in the framework of CT3 approach the asymmetries are described in terms of various quark-gluon correlators, both in the initial and in the final state. It is important to stress that, differently from SIDIS, where one can isolate specific convolutions of TMDs, here all the allowed effects add up to contribute to  $A_N$ , and so they cannot be disentangled.

### 2.3 GENERALISED PARTON MODEL

We finally go through the phenomenological model that will be used throughout this thesis, the Generalised Parton Model (GPM). This model, first developed during mid 1990s, is an extension of early attempts to deal with the intrinsic motion of partons and with TMD distributions and fragmentation functions [124–127]. This formalism presents its own advantages:

- it is a QCD-improved, generalised parton model approach, with direct inclusion, in the spirit of the parton model itself, of spin and transverse momentum ( $\mathbf{k}_\perp$ ) effects (see Appendix A for the detailed  $\mathbf{k}_\perp$  kinematics);
- the partonic interpretation of all soft, leading twist TMDs is preserved;
- the *helicity formalism* used in the approach plainly shows the connection among polarisation states of the involved particles and the role of spin effects in the soft and hard processes;
- the inclusion of  $\mathbf{k}_\perp$  effects in the kinematics is exact, with no approximation.

Of course, as every theoretical approach, it also has some drawbacks:

- it is somehow used assuming the validity of TMD factorisation for single-scale processes, for which no proof exists;
- it is limited to leading-twist distributions and fragmentation functions, so its application to single-spin asymmetries has to be considered as an effective approach;

- initial and final state interactions, which induce the modified universality of TMDs (e.g. for the Sivers function, Eq. (2.10)) are not taken into account.

Despite these problems, its phenomenological results are still quite remarkable. Let us also note that the GPM is essentially equivalent to the full TMD approach in the limit where neither evolution nor soft factors are taken into account.

### 2.3.1 SINGLE INCLUSIVE HADRON PRODUCTION IN THE GPM

Let us now take a look at the single inclusive hadron production from hadronic collisions in the framework of the Generalised Parton Model. For completeness, let us consider the process in which both hadrons in the initial state could be polarised, that is  $A(S_A) + B(S_B) \rightarrow C + X$ , at high energy and moderately large transverse momentum  $P_T$  of the produced hadron, measured with respect to the direction of the colliding beam. The spin states of the generic hadrons  $A, B, C$  are  $S_A, S_B, S_C$  respectively, and the generic hadron  $h$  can have  $S_h = 0, \frac{1}{2}, 1$ . Using the helicity formalism, we can write down the following *master formula* for the invariant differential cross section for the production of an unpolarised hadron  $C$  in the polarised process  $A(S_A) + B(S_B) \rightarrow C + X$  [86, 125–128]:

$$\begin{aligned}
E_C \frac{d\sigma^{(A,S_A)+(B,S_B) \rightarrow C+X}}{d^3p_C} &= \sum_{a,b,c,d} \sum_{\{\lambda\}} \int \frac{dx_a dx_b dz}{16\pi^2 x_a x_b z^2 s} d^2\mathbf{k}_{\perp a} d^2\mathbf{k}_{\perp b} d^3\mathbf{k}_{\perp C} \\
&\times \delta(\mathbf{k}_{\perp C} \cdot \hat{\mathbf{p}}_C) J(\mathbf{k}_{\perp C}) \delta(\hat{s} + \hat{t} + \hat{u}) \\
&\times \rho_{\lambda_a \lambda'_a}^{a/A, S_A} \hat{f}_{a/A, S_A}(x_a, \mathbf{k}_{\perp a}) \rho_{\lambda_b \lambda'_b}^{b/B, S_B} \hat{f}_{b/B, S_B}(x_b, \mathbf{k}_{\perp b}) \\
&\times \hat{M}_{\lambda_c \lambda_d, \lambda_a \lambda_b} \hat{M}_{\lambda'_c \lambda'_d, \lambda'_a \lambda'_b}^* \hat{D}_{\lambda_c \lambda'_c}^{\lambda_C \lambda'_C}(z, \mathbf{k}_{\perp C}).
\end{aligned} \tag{2.40}$$

Eq. (2.40) is written as a factorised convolution of all possible hard elementary tree-level processes,  $ab \rightarrow cd$ , with soft, spin and  $\mathbf{k}_{\perp}$  dependent distributions and fragmentation functions. In this formula we can recognize the following elements:

- (i)  $A$  and  $B$  are the initial, spin  $\frac{1}{2}$  hadrons in pure spin states denoted by  $S_A$  and  $S_B$  and corresponding polarisation (pseudo)vectors  $\mathbf{P}_A$  and  $\mathbf{P}_B$ , respectively;
- (ii) in the hadronic center-of-mass frame, hadrons  $A$  and  $B$  move respectively along the  $\pm Z_{\text{c.m.}}$ -axis direction, and the hadron  $C$  is produced in the  $(XZ)_{\text{c.m.}}$  plane, with  $(p_C)_{X_{\text{c.m.}}} > 0$ ; transverse polarisations for hadrons  $A$  and  $B$  are along the  $Y_{\text{c.m.}}$  direction, and the following notation is often used:

$$\uparrow \text{ for } P_{Y_{\text{cm}}}^A = 1 \text{ and } P_{Y_{\text{cm}}}^B = -1, \quad \downarrow \text{ for } P_{Y_{\text{cm}}}^A = -1 \text{ and } P_{Y_{\text{cm}}}^B = 1; \tag{2.41}$$

- (iii) the notation  $\{\lambda\}$  refers to a sum over all helicity indices, while

$$x_a = \frac{p_a^+}{p_A^+}, \quad x_b = \frac{p_b^+}{p_B^+}, \quad z = \frac{p_C^+}{p_c^+} \tag{2.42}$$

are the light-cone momentum fractions of partons  $a, b$  inside the initial hadrons  $A, B$  and of hadron  $C$  produced in the fragmentation of parton  $c$ ; the parton transverse momenta are, as usual,  $\mathbf{k}_{\perp a}$  and  $\mathbf{k}_{\perp b}$ , while  $\mathbf{k}_{\perp C}$  is the generic three-momentum of hadron  $C$  in the hadronic c.m. frame. The delta function  $\delta(\mathbf{k}_{\perp C} \cdot \hat{\mathbf{p}}_c)$  in Eq. (2.40) ensures the orthogonality between the transverse momentum of the produced hadron,  $\mathbf{k}_{\perp C}$ , and the parton  $c$  three-momentum,  $\mathbf{p}_c$ ;

- (iv) the factor  $(16\pi^2 x_a x_b s)^{-1}$ , with  $s = (p_A + p_B)^2$  being the hadronic Mandelstam  $s$  variable representing the total energy of the colliding beams, collects phase space factors related to the elementary cross section and the corresponding flux factors for the out of hadronic plane parton scattering process;
- (v) the phase-space factor  $J(\mathbf{k}_{\perp C})/z^2$  is the invariant TMD Jacobian factor for massless particles connecting the parton momentum  $\mathbf{p}_c$  with its parent hadron momentum  $\mathbf{p}_C$  (see for example [126], Appendix A); the Jacobian factor for massless particles is given by:

$$J(\mathbf{k}_{\perp C}) = \frac{(E_C + \sqrt{\mathbf{p}_C^2 + \mathbf{k}_{\perp C}^2})^2}{4(\mathbf{p}_C^2 - \mathbf{k}_{\perp C}^2)}; \quad (2.43)$$

- (vi)  $\rho_{\lambda_a \lambda'_a}^{a/A, S_A}(\rho_{\lambda_b \lambda'_b}^{b/B, S_B})$  is the helicity density matrix of parton  $a(b)$  inside hadron  $A(B)$ , that describes the polarisation state of the particle in its helicity rest frame. In the case of massless particles, no such frame exists, hence the helicity frame is defined as the frame, reached from the hadronic c.m. frame, in which the particle four-momentum is  $p^\mu = (p, 0, 0, p)$  [129];
- (vii)  $\hat{f}_{a/A, S_A}(x_a, \mathbf{k}_{\perp a}) (\hat{f}_{b/B, S_B}(x_b, \mathbf{k}_{\perp b}))$  is the leading-twist TMD-PDF for the unpolarised parton  $a(b)$  inside the polarised hadron  $A(B)$ <sup>2</sup>.
- (viii) the  $\hat{M}$ 's are the helicity amplitudes for the partonic tree-level process  $ab \rightarrow cd$ , and are normalised so that the unpolarised cross section, for a collinear collision, is given by

$$\frac{d\sigma^{ab \rightarrow cd}}{d\hat{t}} = \frac{1}{16\pi\hat{s}^2} \frac{1}{4} \sum_{\lambda_a \lambda_b \lambda_c \lambda_d} |\hat{M}_{\lambda_c \lambda_d, \lambda_a \lambda_b}|^2, \quad (2.44)$$

where again  $\hat{t} = (p_a - p_c)^2$  is a partonic Mandelstam variable. Note that these amplitudes are computed in a natural reference frame, the center-of-mass (c.m.) frame of the colliding hadrons. The collision axis, along with the direction of the produced hadron, forms a plane, the hadronic plane. Due to the inclusion of intrinsic transverse momentum, the hard scattering induce a nonplanar kinematics, out of this hadronic plane. So, the helicity amplitudes are first calculated in the partonic c.m. frame, obtaining the canonical amplitudes  $\hat{M}^{0'}$ 's, and then connected to the one in the hadronic c.m. frame, the  $\hat{M}$ 's, using a proper succession of Lorentz transformations. Hence, the nonplanar geometry of the partonic process and the Lorentz transformations induce

---

<sup>2</sup>The convention used here indicates with a “hat” function with full vectorial dependence on  $\mathbf{k}_{\perp}$ . The ones indicated without a “hat” have a  $k_{\perp} \equiv |\mathbf{k}_{\perp}|$  dependence, with a factorised azimuthal dependence.

nontrivial phases in the distribution and fragmentation matrices (see Appendices A and B for more details).

- (ix)  $\hat{D}_{\lambda_c \lambda'_c}^{\lambda_c \lambda'_c}(z, \mathbf{k}_{\perp C})$  is the product of nonperturbative *fragmentation amplitudes* for the polarised fragmentation process  $c \rightarrow C + X$ .
- (x) when  $C$  is a massless particle or a light hadron (e.g. a pion), a regulator mass  $\mu_0$  is introduced. This is needed to cure the infrared divergences appearing in the propagators when  $k_{\perp}$  effects are included and when  $P_T$  is around 1 – 2 GeV. At larger  $P_T$ , no such problem is present.

The master formula, Eq. (2.40), could be also written in the following condensed form:

$$E_C \frac{d\sigma^{(A,S_A)+(B,S_B) \rightarrow C+X}}{d^3 p_C} = \sum_{a,b,c,d} \int \frac{dx_a dx_b dz}{16\pi^2 x_a x_b z^2 s} d^2 \mathbf{k}_{\perp a} d^2 \mathbf{k}_{\perp b} d^3 \mathbf{k}_{\perp C} \quad (2.45)$$

$$\times \delta(\mathbf{k}_{\perp C} \cdot \hat{\mathbf{p}}_C) J(\mathbf{k}_{\perp C}) \delta(\hat{s} + \hat{t} + \hat{u}) \Sigma(S_A, S_B)^{ab \rightarrow cd},$$

where we have defined the general kernel

$$\Sigma(S_A, S_B)^{ab \rightarrow cd} = \sum_{\{\lambda\}} \rho_{\lambda_a \lambda'_a}^{a/A, S_A} \hat{f}_{a/A, S_A}(x_a, \mathbf{k}_{\perp a}) \rho_{\lambda_b \lambda'_b}^{b/B, S_B} \hat{f}_{b/B, S_B}(x_b, \mathbf{k}_{\perp b}) \quad (2.46)$$

$$\times \hat{M}_{\lambda_c \lambda_d, \lambda_a \lambda_b} \hat{M}_{\lambda'_c \lambda'_d, \lambda'_a \lambda'_b}^* \hat{D}_{\lambda_c \lambda'_c}^{\lambda_c \lambda'_c}(z, \mathbf{k}_{\perp C}).$$

This kernel encodes the complete information about the polarisation states of partons and hadrons. Moreover, upon assigning the proper polarisation to the initial hadrons  $A$  and  $B$ , kernel combinations provide an explicit expression for the numerator and the denominator of the transverse single-spin asymmetry  $A_N$ , Eq. (2.38). For example, considering single inclusive hadroproduction from polarised proton-proton scattering,  $p^{\uparrow} p \rightarrow hX$ , we have, respectively for the numerator and the denominator of  $A_N$

$$d\Delta\sigma \sim \sum_{abcd} \sum_{\{\lambda\}} [\Sigma(\uparrow, 0) - \Sigma(\downarrow, 0)] , \quad (2.47)$$

$$d\sigma^{\text{unp}} \sim \sum_{abcd} \sum_{\{\lambda\}} [\Sigma(\uparrow, 0) + \Sigma(\downarrow, 0)] ,$$

and the sums are extended over all the possible elementary contributions. In this case, eight different partonic processes can take place:

$$\begin{aligned} q_a q_b \rightarrow q_c q_d, \quad & g_a g_b \rightarrow g_c g_d, \quad & g_a g_b \rightarrow q \bar{q}, \quad & q \bar{q} \rightarrow g_c g_d, \\ qg \rightarrow qg, \quad & gq \rightarrow gq, \quad & qg \rightarrow gq, \quad & gq \rightarrow qg, \end{aligned} \quad (2.48)$$

where  $q$  can be either a quark or an antiquark. The subscripts  $a, b, c, d$  for quarks, when necessary, identify the flavour, of course only in processes where different flavours can be present, while for gluons these labels identify the corresponding hadron ( $a \rightarrow A, b \rightarrow B, c \rightarrow C$ ).

As an illustration, let us take a look at two general kernels. The one for the elementary contribution  $q_a q_b \rightarrow q_c q_d$  is given by [127]:

$$\begin{aligned}
\Sigma(S_A, S_B)^{q_a q_b \rightarrow q_c q_d} &= \frac{1}{2} D_{C/c}(z, k_{\perp C}) \hat{f}_{a/S_A}(x_a, \mathbf{k}_{\perp a}) \hat{f}_{b/S_B}(x_b, \mathbf{k}_{\perp b}) \\
&\times \left\{ \left( |\hat{M}_1^0|^2 + |\hat{M}_2^0|^2 + |\hat{M}_3^0|^2 \right) + P_z^a P_z^b \left( |\hat{M}_1^0|^2 - |\hat{M}_2^0|^2 - |\hat{M}_3^0|^2 \right) \right. \\
&\quad + 2\hat{M}_2^0 \hat{M}_3^0 \left[ \left( P_x^a P_x^b + P_y^a P_y^b \right) \cos(\varphi_3 - \varphi_2) \right. \\
&\quad \quad \left. \left. - \left( P_x^a P_y^b - P_y^a P_x^b \right) \sin(\varphi_3 - \varphi_2) \right] \right\} \\
&- \frac{1}{2} \Delta^N D_{C/c^\dagger}(z, k_{\perp C}) \hat{f}_{a/S_A}(x_a, \mathbf{k}_{\perp a}) \hat{f}_{b/S_B}(x_b, \mathbf{k}_{\perp b}) \\
&\times \left\{ \hat{M}_1^0 \hat{M}_2^0 \left[ P_x^a \sin(\varphi_1 - \varphi_2 + \phi_C^H) - P_y^a \cos(\varphi_1 - \varphi_2 + \phi_C^H) \right] \right. \\
&\quad \left. + \hat{M}_1^0 \hat{M}_3^0 \left[ P_x^b \sin(\varphi_1 - \varphi_3 + \phi_C^H) - P_y^b \cos(\varphi_1 - \varphi_3 + \phi_C^H) \right] \right\}, \tag{2.49}
\end{aligned}$$

while the one for  $qg \rightarrow qg$  processes reads

$$\begin{aligned}
\Sigma(S_A, S_B)^{qg \rightarrow qg} &= \frac{1}{2} D_{C/q}(z, k_{\perp C}) \hat{f}_{q/S_A}(x_a, \mathbf{k}_{\perp a}) \hat{f}_{g/S_B}(x_b, \mathbf{k}_{\perp b}) \\
&\times \left\{ \left( |\hat{M}_1^0|^2 + |\hat{M}_2^0|^2 \right) + P_z^q P_z^g \left( |\hat{M}_1^0|^2 - |\hat{M}_2^0|^2 \right) \right\} \\
&- \frac{1}{2} \Delta^N D_{C/q^\dagger}(z, k_{\perp C}) \hat{f}_{q/S_A}(x_a, \mathbf{k}_{\perp a}) \hat{f}_{g/S_B}(x_b, \mathbf{k}_{\perp b}) \\
&\times \left\{ \hat{M}_1^0 \hat{M}_2^0 \left[ P_x^q \sin(\varphi_1 - \varphi_2 + \phi_C^H) - P_y^q \cos(\varphi_1 - \varphi_2 + \phi_C^H) \right] \right\}. \tag{2.50}
\end{aligned}$$

Without entering into details, we can say that Eqs. (2.49) and (2.50) show the explicit dependence on the polarisation states of partons  $a$  and  $b$ , along with the aforementioned nontrivial phase dependences due to the fact that the hard process takes place out of the hadronic plane. Moreover, we see the presence of combinations of canonical helicity amplitudes,  $\hat{M}^0$ 's, the ones calculated in the partonic c.m. frame. Their subscripts refer to helicity amplitudes with different helicity combinations. All the details can be found in Appendix B.

Upon assigning the proper polarisation, one can then construct the contribution to the asymmetry for every partonic channel. As an illustration, we consider the case in which only the initial hadron  $A$  is transversely polarised, while the hadron  $B$  is unpolarised. In such case, the single-spin asymmetry  $A_N$  will receive the contributions, among all the partonic channels, from the two subprocesses  $q_a q_b \rightarrow q_c q_d$  and  $qg \rightarrow qg$ . Here we show explicitly their contributions to the numerator and the denominator of the asymmetry, that respectively read:

$$\begin{aligned}
[\Sigma(\uparrow, 0) - \Sigma(\downarrow, 0)]^{q_a q_b \rightarrow q_c q_d} = & \\
& \frac{1}{2} \Delta \hat{f}_{a/A\uparrow}(x_a, \mathbf{k}_{\perp a}) f_{b/B}(x_b, k_{\perp b}) \left[ |\hat{M}_1^0|^2 + |\hat{M}_2^0|^2 + |\hat{M}_3^0|^2 \right] D_{C/c}(z, k_{\perp C}) \\
& + \left[ \Delta \hat{f}_{s_y/\uparrow}^a(x_a, \mathbf{k}_{\perp a}) \cos(\varphi_1 - \varphi_2 + \phi_C^H) - \Delta \hat{f}_{s_x/\uparrow}^a(x_a, \mathbf{k}_{\perp a}) \sin(\varphi_1 - \varphi_2 + \phi_C^H) \right] \\
& \quad \times f_{b/B}(x_b, k_{\perp b}) \hat{M}_1^0 \hat{M}_2^0 \Delta^N D_{C/c\uparrow}(z, k_{\perp C}) \\
& + 2 \left[ \Delta \hat{f}_{s_y/\uparrow}^a(x_a, \mathbf{k}_{\perp a}) \cos(\varphi_3 - \varphi_2) - \Delta \hat{f}_{s_x/\uparrow}^a(x_a, \mathbf{k}_{\perp a}) \sin(\varphi_3 - \varphi_2) \right] \\
& \quad \times \Delta \hat{f}_{s_y/B}^b(x_b, \mathbf{k}_{\perp b}) \hat{M}_2^0 \hat{M}_3^0 D_{C/c}(z, k_{\perp C}) \\
& + \frac{1}{2} \Delta \hat{f}_{a/A\uparrow}(x_a, \mathbf{k}_{\perp a}) \Delta \hat{f}_{s_y/B}^b(x_b, \mathbf{k}_{\perp b}) \cos(\varphi_1 - \varphi_3 + \phi_C^H) \hat{M}_1^0 \hat{M}_3^0 \Delta^N D_{C/c\uparrow}(z, k_{\perp C}), \tag{2.51}
\end{aligned}$$

$$\begin{aligned}
[\Sigma(\uparrow, 0) - \Sigma(\downarrow, 0)]^{qg \rightarrow qg} = & \\
& \frac{1}{2} \Delta \hat{f}_{q/A\uparrow}(x_q, \mathbf{k}_{\perp q}) f_{g/B}(x_g, k_{\perp g}) \left[ |\hat{M}_1^0|^2 + |\hat{M}_2^0|^2 \right] D_{C/q}(z, k_{\perp C}) \\
& + \left[ \Delta \hat{f}_{s_y/\uparrow}^q(x_q, \mathbf{k}_{\perp q}) \cos(\varphi_1 - \varphi_2 + \phi_C^H) - \Delta \hat{f}_{s_x/\uparrow}^q(x_q, \mathbf{k}_{\perp q}) \sin(\varphi_1 - \varphi_2 + \phi_C^H) \right] \\
& \quad \times f_{g/B}(x_g, k_{\perp g}) \hat{M}_1^0 \hat{M}_2^0 \Delta^N D_{C/q\uparrow}(z, k_{\perp C}), \tag{2.52}
\end{aligned}$$

and

$$\begin{aligned}
[\Sigma(\uparrow, 0) + \Sigma(\downarrow, 0)]^{q_a q_b \rightarrow q_c q_d} = & \\
& f_{a/A}(x_a, k_{\perp a}) f_{b/B}(x_b, k_{\perp b}) \left[ |\hat{M}_1^0|^2 + |\hat{M}_2^0|^2 + |\hat{M}_3^0|^2 \right] D_{C/c}(z, k_{\perp C}) \\
& + 2 \Delta \hat{f}_{s_y/A}^a(x_a, \mathbf{k}_{\perp a}) \Delta \hat{f}_{s_y/B}^b(x_b, \mathbf{k}_{\perp b}) \cos(\varphi_3 - \varphi_2) \hat{M}_2^0 \hat{M}_3^0 D_{C/c}(z, k_{\perp C}) \\
& + \left[ \hat{f}_{a/A}(x_a, k_{\perp a}) \Delta \hat{f}_{s_y/B}^b(x_b, \mathbf{k}_{\perp b}) \cos(\varphi_1 - \varphi_3 + \phi_C^H) \hat{M}_1^0 \hat{M}_3^0 \right. \\
& \quad \left. + \Delta \hat{f}_{s_y/A}^a(x_a, \mathbf{k}_{\perp a}) \hat{f}_{b/B}(x_b, k_{\perp b}) \cos(\varphi_1 - \varphi_2 + \phi_C^H) \hat{M}_1^0 \hat{M}_2^0 \right] \Delta^N D_{C/c\uparrow}(z, k_{\perp C}), \tag{2.53}
\end{aligned}$$

$$\begin{aligned}
[\Sigma(\uparrow, 0) + \Sigma(\downarrow, 0)]^{qg \rightarrow qg} = & \\
& f_{q/A}(x_q, k_{\perp q}) f_{g/B}(x_g, k_{\perp g}) \left[ |\hat{M}_1^0|^2 + |\hat{M}_2^0|^2 \right] D_{C/q}(z, k_{\perp C}) \\
& + \Delta \hat{f}_{s_y/A}^q(x_q, \mathbf{k}_{\perp q}) f_{g/B}(x_g, k_{\perp g}) \cos(\varphi_1 - \varphi_2 + \phi_C^H) \hat{M}_1^0 \hat{M}_2^0 \Delta^N D_{C/q\uparrow}(z, k_{\perp C}). \tag{2.54}
\end{aligned}$$

where again  $q$  can be either a quark or an antiquark.

Let us briefly comment about these last expressions. After having assigned the polarisation in Eqs. (2.49) and (2.50), one can calculate sums and differences of kernels in order to build the expression for the single-spin asymmetry. In doing this, one obtains the “ $\Delta$ ” functions relative to the different effects that can contribute to  $A_N$ . Explicit expressions for these functions and their relations with the TMDs presented in Section 2.1 are given in Appendix B.

Regarding the numerator of the SSA, in the  $q_a q_b \rightarrow q_c q_d$  case, Eq. (2.51), we observe in the



first term the contribution of the Sivers effect, while in the second term we have the Collins effect coupled with the two pieces of the TMD transversity distribution. Moreover, we have two more pieces: the third one is relative to the Boer-Mulders  $\otimes$  TMD transversity distribution; the last one represents a combination of Sivers, Collins and Boer-Mulders effect. In the case of  $qg \rightarrow qg$ , Eq. (2.52), we only have the contribution of the Sivers effect (first term) and of the TMD transversity coupled to the Collins function (second term). Looking now at the contribution to the unpolarised cross section, that enters in the denominator of  $A_N$ , we have a similar overall structure as for the asymmetry numerator. In both cases, Eqs. (2.53) and (2.54), the first piece corresponds to the unpolarised contribution, and the second one to a double Boer-Mulders (or Boer-Mulders-like) effect, respectively. The third and fourth lines of Eq. (2.53) represent a mixed term in which the Boer-Mulders and Collins (or Boer-Mulders-like and Collins-like) effects come out together.

The explicit expressions for the numerator and the denominator of the transverse single-spin asymmetry show their richness in terms of transverse momentum dependent distribution and fragmentation functions. On the other hand, their structure exhibits the composite nature of the single-spin asymmetry in hadronic processes. Differently from Semi-Inclusive DIS, where, thanks to different azimuthal modulation (see Eqs. (2.27) and (2.31)), the convolution of specific pairs of TMDs can be isolated, in the case of single inclusive hadroproduction from hadronic collisions one has to deal with an entangled, complicated structure. The advantage offered by SIDIS processes has always been exploited to extract TMDs from phenomenological analyses. We will see this in the next Section and in Chapter 3. Nonetheless, as we will see in Chapter 4, single inclusive hadron production in hadronic processes can help in estimating, in some particular kinematical region, the size of the less known gluon TMDs, like the gluon Sivers function.

### 2.3.2 TMD PARAMETRISATION AND SIDIS IN THE GPM

In this Section we finally head to TMD parametrisation. Throughout this Section we will see, in the framework of the Generalised Parton Model, how unpolarised and polarised TMD PDFs and FFs are usually modeled and derive the expressions for the azimuthal asymmetries measured in Semi-Inclusive DIS. In particular, we will introduce the standard parametrisation used through the past years in the GPM approach, and we will see how the expressions for the azimuthal asymmetries, Eq. (2.34), can be written in a factorised form under a Gaussian Ansatz (GA). Under this ansatz, we can write a generic TMD PDF or FF with factorised  $x$  and  $\mathbf{k}_\perp$  ( $\mathbf{p}_\perp$ ) dependences as:

$$f(x, k_\perp^2) = f(x) \frac{e^{-k_\perp^2 / \langle k_\perp^2 \rangle}}{\pi \langle k_\perp^2 \rangle}, \quad D(z, p_\perp^2) = D(z) \frac{e^{-p_\perp^2 / \langle p_\perp^2 \rangle}}{\pi \langle p_\perp^2 \rangle}. \quad (2.55)$$

Before diving into the GPM expressions for SIDIS azimuthal asymmetries, is it worth to comment about the Gaussian Ansatz. This approximation became popular for different reasons. One of them is that all convolution integrals of the type in Eq. (2.35) can be solved analytically within the GA. But, it is much more important to underline its good accuracy in many practical phenomenological applications [86, 111, 114, 116, 118, 130–132]. It is obvious that, as any approximation, it can be inconsistent in some cases, e.g. with respect to general



matching expectations at large  $k_\perp$  [133]. Nonetheless, in the appropriate kinematic regime, i.e. the one in which the observed transverse momenta are small with respect to the hard scale in the process, the GA gains quantitatively a good success.

Let us now introduce the parametrisation adopted for five TMD distributions (for quarks inside a proton) and fragmentation functions (of a quark into an unpolarised hadron) that will be used throughout the following Chapters. These five TMDs are the two unpolarised PDF and FF, the transversity function, the Sivers function and the Collins fragmentation function. As mentioned in Section 2.1, Eq. (2.34), these functions show up in the expressions for some specific SIDIS azimuthal asymmetries, namely  $A_{UT}^{\sin(\phi_h - \phi_S)}$  and  $A_{UT}^{\sin(\phi_h + \phi_S)}$ . To begin with, let us remind that, to order  $\mathcal{O}(k_\perp/Q)$ , the following relation between intrinsic transverse momenta and observed transverse momentum holds:

$$\mathbf{P}_T = z\mathbf{k}_\perp + \mathbf{p}_\perp. \quad (2.56)$$

The first structure function in Eq. (2.36),  $F_{UU}$ , can be written within the TMD factorisation scheme as

$$\begin{aligned} F_{UU}(x, z, P_T) &= x \sum_q e_q^2 \int d^2\mathbf{k}_\perp d^2\mathbf{p}_\perp \delta^{(2)}(z\mathbf{k}_\perp + \mathbf{p}_\perp - \mathbf{P}_T) \times f_{q/p}(x, k_\perp^2) D_{h/q}(z, p_\perp^2) \\ &= x \sum_q e_q^2 \int d^2\mathbf{k}_\perp d^2\mathbf{p}_\perp f_{q/p}(x, k_\perp^2) D_{h/q}(z, (\mathbf{P}_T - z\mathbf{k}_\perp)^2), \end{aligned} \quad (2.57)$$

where the sum is both over quarks and antiquarks. Under the GA, the unpolarised TMD distribution and fragmentation functions are written in a factorised form, with separated  $x$  ( $z$ ) and  $k_\perp$  ( $p_\perp$ ) dependences, the latter being assumed to be Gaussian, with the Gaussian width as the only free parameter:

$$f_{q/p}(x, k_\perp^2) = f_{q/p}(x) \frac{e^{-k_\perp^2 / \langle k_\perp^2 \rangle}}{\pi \langle k_\perp^2 \rangle}, \quad (2.58)$$

$$D_{h/q}(z, p_\perp^2) = D_{h/q}(z) \frac{e^{-p_\perp^2 / \langle p_\perp^2 \rangle}}{\pi \langle p_\perp^2 \rangle}. \quad (2.59)$$

In the last expressions, the integrated (collinear) PDF and FF are usually taken from available fits to world data. The Gaussian widths could be in principle functions of  $x$  and  $z$ , and also flavour dependent (see e.g. [84, 119, 132]). In the following, *flavour independence* and constant widths are always used. Under these assumptions, using Eqs. (2.58)–(2.59) into Eq. (2.57), we obtain a simple expression for the structure function  $F_{UU}$ :

$$F_{UU}(x, z, P_T) = x \sum_q e_q^2 f_{q/p}(x) D_{h/q}(z) \frac{e^{-P_T^2 / \langle P_T^2 \rangle}}{\pi \langle P_T^2 \rangle}, \quad (2.60)$$

where  $x \equiv x_{Bj}$ , and where

$$\langle P_T^2 \rangle = \langle p_\perp^2 \rangle + z^2 \langle k_\perp^2 \rangle. \quad (2.61)$$

In order to construct the SIDIS azimuthal asymmetries, we now need to parametrise the polarised TMDs, namely the Sivers and transversity functions, and the Collins fragmentation

function. Here, we meet another assumption usually made within GPM: the  $Q^2$  dependence of the (un)polarised TMDs is only due to the collinear unpolarised distribution and fragmentation functions, that evolve according to the DGLAP equations.

Let us start first with the quark Sivers function. This function is usually parametrised as

$$\begin{aligned}\Delta^N f_{q/p^\uparrow}(x, k_\perp^2) &= -\frac{2k_\perp}{M_p} f_{1T}^{\perp q}(x, k_\perp^2) \\ &= 2\mathcal{N}_q(x) h(k_\perp) f_{q/p}(x, k_\perp^2),\end{aligned}\tag{2.62}$$

where

$$\mathcal{N}_q(x) = N_q x^{\alpha_q} (1-x)^{\beta_q} \frac{(\alpha_q + \beta_q)^{\alpha_q + \beta_q}}{\alpha_q^{\alpha_q} \beta_q^{\beta_q}},\tag{2.63}$$

$$h(k_\perp) = \sqrt{2e} \frac{k_\perp}{M_S} e^{-k_\perp^2/M_S^2},\tag{2.64}$$

and  $M_S$  is a free parameter with mass dimension.

Note that, upon choosing  $|N_q| \leq 1$ , the positivity bound for the Sivers function, Eq. (2.15), is automatically satisfied. Substituting Eqs. (2.58), (2.63) and (2.64) into Eq. (2.62), we get

$$f_{1T}^{\perp q}(x, k_\perp^2) = -\sqrt{2e} \frac{M_p}{M_S} \mathcal{N}_q(x) f_{q/p}(x) \frac{e^{-k_\perp^2/\langle k_\perp^2 \rangle_S}}{\pi \langle k_\perp^2 \rangle_S},\tag{2.65}$$

where  $M_p$  is the proton mass and where we have defined the Sivers width

$$\langle k_\perp^2 \rangle_S = \frac{\langle k_\perp^2 \rangle M_S^2}{\langle k_\perp^2 \rangle + M_S^2}.\tag{2.66}$$

With these expressions, the Sivers first moment becomes [118]

$$\begin{aligned}f_{1T}^{\perp(1)q}(x) &= -\Delta^N f_{q/p^\uparrow}^{(1)}(x) = -\frac{\sqrt{\frac{e}{2}} \langle k_\perp^2 \rangle M_S^3}{M_p (\langle k_\perp^2 \rangle + M_S^2)^2} \mathcal{N}_q(x) f_{q/p}(x) \\ &= -\frac{\sqrt{\frac{e}{2}} \langle k_\perp^2 \rangle_S^2}{M_p M_S \langle k_\perp^2 \rangle} \mathcal{N}_q(x) f_{q/p}(x),\end{aligned}\tag{2.67}$$

where in the last line we have substituted the definition of  $\langle k_\perp^2 \rangle_S$ , Eq. (2.66). The structure function  $F_{UT}^{\sin(\phi_h - \phi_S)}$  can be written in terms of the Sivers first moment as [122]

$$\begin{aligned}F_{UT}^{\sin(\phi_h - \phi_S)}(x, z, P_T) &= -x \frac{2M_p z P_T}{\langle P_T^2 \rangle_S} \sum_q e_q^2 f_{1T}^{\perp(1)q}(x) D_{h/q}(z) \frac{e^{-P_T^2/\langle P_T^2 \rangle_S}}{\pi \langle P_T^2 \rangle_S} \\ &= x \frac{2M_p z P_T}{\langle P_T^2 \rangle_S} \sum_q e_q^2 \Delta^N f_{q/p^\uparrow}^{(1)}(x) D_{h/q}(z) \frac{e^{-P_T^2/\langle P_T^2 \rangle_S}}{\pi \langle P_T^2 \rangle_S},\end{aligned}\tag{2.68}$$

where

$$\langle P_T^2 \rangle_S = z^2 \langle k_\perp^2 \rangle_S + \langle p_\perp^2 \rangle. \quad (2.69)$$

Using now Eqs. (2.60) and (2.68) we can write, under the Gaussian Ansatz, the Sivers azimuthal asymmetry in SIDIS, Eq. (2.34), as

$$\begin{aligned} A_{UT}^{\sin(\phi_h - \phi_S)}(x, z, P_T) &= \frac{F_{UT}^{\sin(\phi_h - \phi_S)}}{F_{UU}} \\ &= -2M_p z P_T \frac{\langle P_T^2 \rangle}{\langle P_T^2 \rangle_S^2} \frac{e^{-P_T^2 / \langle P_T^2 \rangle_S} \sum_q e_q^2 f_{1T}^{\perp(1)q}(x) D_{h/q}(z)}{e^{-P_T^2 / \langle P_T^2 \rangle_S} \sum_q e_q^2 f_{q/p}(x) D_{h/q}(z)} \\ &= 2M_p z P_T \frac{\langle P_T^2 \rangle}{\langle P_T^2 \rangle_S^2} \frac{e^{-P_T^2 / \langle P_T^2 \rangle_S} \sum_q e_q^2 \Delta^N f_{q/p^\uparrow}^{(1)}(x) D_{h/q}(z)}{e^{-P_T^2 / \langle P_T^2 \rangle_S} \sum_q e_q^2 f_{q/p}(x) D_{h/q}(z)}. \end{aligned} \quad (2.70)$$

We can now turn to the second SIDIS azimuthal asymmetry of our interest, the Collins asymmetry  $A_{UT}^{\sin(\phi_h + \phi_S)}$ . Its corresponding polarised structure function  $F_{UT}^{\sin(\phi_h + \phi_S)}$  is written in terms of a convolution of the TMD transversity function and the Collins fragmentation function. Within the GPM and adopting the GA, the  $x$ -dependent part of the transversity function has been usually parametrised in terms of the Soffer bound:

$$h_1^q(x, k_\perp^2) = h_1^q(x) \frac{e^{-k_\perp^2 / \langle k_\perp^2 \rangle_T}}{\pi \langle k_\perp^2 \rangle_T}, \quad (2.71)$$

$$h_1^q(x) = \frac{1}{2} \mathcal{N}_q^T(x) [f_{q/p}(x) + g_{1L}(x)], \quad (2.72)$$

where

$$\mathcal{N}_q^T(x) = N_q^T x^{\alpha_q^T} (1-x)^{\beta_q^T} \frac{(\alpha_q^T + \beta_q^T)^{\alpha_q^T + \beta_q^T}}{\alpha_q^{\alpha_q^T} \beta_q^{\beta_q^T}}. \quad (2.73)$$

The Collins function is also usually parametrised in terms of the corresponding collinear unpolarised fragmentation function:

$$\begin{aligned} \Delta^N D_{h/q^\uparrow}(z, p_\perp^2) &= \frac{2p_\perp}{z m_h} H_1^{\perp q}(z, p_\perp^2) \\ &= 2 \mathcal{N}_q^C(z) h(p_\perp) D_{h/q}(z, p_\perp^2) \end{aligned} \quad (2.74)$$

where  $m_h$  is the mass of the produced hadron, and where

$$\mathcal{N}_{\text{fav,unf}}^C(z) = N_{\text{fav,unf}}^C z^\gamma (1-z)^\delta \frac{(\gamma + \delta)^{\gamma + \delta}}{\gamma^\gamma \delta^\delta}, \quad (2.75)$$

$$h(p_\perp) = \sqrt{2e} \frac{p_\perp}{M_C} e^{-p_\perp^2/M_C^2}, \quad (2.76)$$

and again we have a free mass parameter,  $M_C$ .

In Eq. (2.75) we have introduced the distinction between *favoured* and *unfavoured* Collins fragmentation function. The distinction originates from the definition of favoured and unfavoured unpolarised FFs, that is relative to the flavour content of the different hadrons and is based on isospin symmetry. For example, in the case of charged pions, we have:

$$\begin{aligned} D_{\pi^+/u} &= D_{\pi^+/\bar{d}} = D_{\pi^-/d} = D_{\pi^-/\bar{u}} \equiv D_{\text{fav}}^\pi, \\ D_{\pi^+/d} &= D_{\pi^+/\bar{u}} = D_{\pi^-/u} = D_{\pi^-/\bar{d}} = D_{\pi^\pm/s} = D_{\pi^\pm/\bar{s}} \equiv D_{\text{unf}}^\pi. \end{aligned} \quad (2.77)$$

As in the case of the Sivers function, by choosing  $|N_q^T| \leq 1$  and  $|N_q^C| \leq 1$ , transversity and Collins function automatically satisfy their corresponding bounds, i.e. the Soffer bound and the positivity bound, respectively.

Substituting now Eqs. (2.75) and (2.76) into Eq. (2.74), we get

$$H_1^{\perp q}(z, p_\perp^2) = \sqrt{2e} \frac{zm_h}{M_C} \mathcal{N}_q^C(z) D_{h/q}(z) \frac{e^{-p_\perp^2/\langle p_\perp^2 \rangle_C}}{\pi \langle p_\perp^2 \rangle_C}, \quad (2.78)$$

where we now have defined the Collins width

$$\langle p_\perp^2 \rangle_C = \frac{\langle p_\perp^2 \rangle M_C^2}{\langle p_\perp^2 \rangle + M_C^2}. \quad (2.79)$$

The Collins function can be also expressed in terms of its first moment,  $H_1^{\perp(1)q}(z)$ , as follows:

$$H_1^{\perp q}(z, p_\perp^2) = H_1^{\perp(1)q}(z) \frac{2z^2 m_h^2}{\pi \langle p_\perp^2 \rangle_C^2} e^{-p_\perp^2/\langle p_\perp^2 \rangle_C}, \quad (2.80)$$

where  $H_1^{\perp(1)q}(z)$  is given by [122]

$$\begin{aligned} H_1^{\perp(1)q}(z) &= \frac{\sqrt{e} \langle p_\perp^2 \rangle M_C^3}{zm_h(\langle p_\perp^2 \rangle + M_C^2)^2} \mathcal{N}_q^C(z) D_{h/q}(z) \\ &= \sqrt{\frac{e}{2}} \frac{\langle p_\perp^2 \rangle_C^2}{\langle p_\perp^2 \rangle} \frac{1}{zm_h M_C} \mathcal{N}_q^C(z) D_{h/q}(z). \end{aligned} \quad (2.81)$$

Now, the structure function  $F_{UT}^{\sin(\phi_h+\phi_s)}$  can be written as [122]

$$F_{UT}^{\sin(\phi_h+\phi_s)}(x, z, P_T) = x \frac{2zm_h P_T}{\langle P_T^2 \rangle_C} \sum_q e_q^2 h_1^q(x) H_q^{\perp(1)q}(z) \frac{e^{-P_T^2/\langle P_T^2 \rangle_C}}{\pi \langle P_T^2 \rangle_C}, \quad (2.82)$$

where

$$\langle P_T^2 \rangle_C = z^2 \langle k_\perp^2 \rangle_T + \langle p_\perp^2 \rangle_C. \quad (2.83)$$

So, under the GA, the Collins azimuthal asymmetry (as measured by the HERMES Collaboration, Eq. (2.34)) is given by

$$\begin{aligned}
A_{UT}^{\sin(\phi_h+\phi_S)}(x, z, P_T) &= \frac{2(1-y)}{1+(1-y)^2} \frac{F_{UT}^{\sin(\phi_h+\phi_S)}}{F_{UU}} \\
&= \frac{4 z m_h P_T (1-y)}{1+(1-y)^2} \frac{\langle P_T^2 \rangle}{\langle P_T^2 \rangle_C^2} \frac{e^{-P_T^2/\langle P_T^2 \rangle_C} \sum_q e_q^2 h_1^q(x) H_q^{\perp(1)q}(z)}{e^{-P_T^2/\langle P_T^2 \rangle} \sum_q e_q^2 f_{q/p}(x) D_{h/q}(z)} . \quad (2.84)
\end{aligned}$$

# 3

## Polarised quark TMD distributions

In this Chapter we will go through some phenomenological studies about polarised quark TMDs. In particular, we will focus on some details that affect the various steps while performing a phenomenological analysis. We will see that the assumptions made within a specific chosen model can impact on the interpretation of the results of a fit. Nonetheless, they can also help in assessing signals of TMD physics in the experimental data and in pinning down the actual knowledge about TMDs.

### 3.1 AVAILABLE TMD DATA

We will now take a look at the available TMD data for polarised quark PDFs and FFs, especially for the Sivers and transversity TMD distribution and for the Collins fragmentation function.

It is worth to start by pointing out some important aspects on the available TMD data. Generally speaking, the amount of information on TMD functions at our disposal is less than the one available for collinear PDFs and FFs. If we roughly measure it as the number of datapoints used in a phenomenological extraction of a PDF or a FF, we can instantly notice a difference between the collinear and the TMD cases. In fact, we usually have  $\mathcal{O}(10^3)$  points for fitting collinear PDFs and FFs, while for TMDs, *when data are available*, this number goes down to  $\mathcal{O}(10^1 - 10^2)$  (or also  $\mathcal{O}(10^0)$  in the gluon case, see Chapter 4). So, in principle this means that we have less available information on TMDs.

Actually, we are still at an *early stage* of TMD extractions. Noticeable exceptions to this numbers are surely represented by the Torino 2014 fit [114] (over 6000 datapoints from SIDIS multiplicities data for unpolarised TMD PDFs and FFs), and the first global fit of unpolarised quark TMDs made by Pavia group [119], which used a total amount of 8059 datapoints. Notice that these numbers are finally comparable to the ones used in collinear PDFs extractions.

Obviously, it is not always true that the larger number of datapoints we have, the more we gain in terms of information on TMDs, since this generally depends on the covered kinematical regions (e.g. in  $x$  and  $Q^2$ , see Fig. 3.1 as an example for Sivers asymmetry data) and on the precision of the data. Nevertheless, the fact that wider  $x$  and  $Q^2$  ranges have now been and will be explored in the near future will allow us to better constrain TMDs in some specific regions, currently unconstrained in the phenomenological analyses [76, 134, 135].

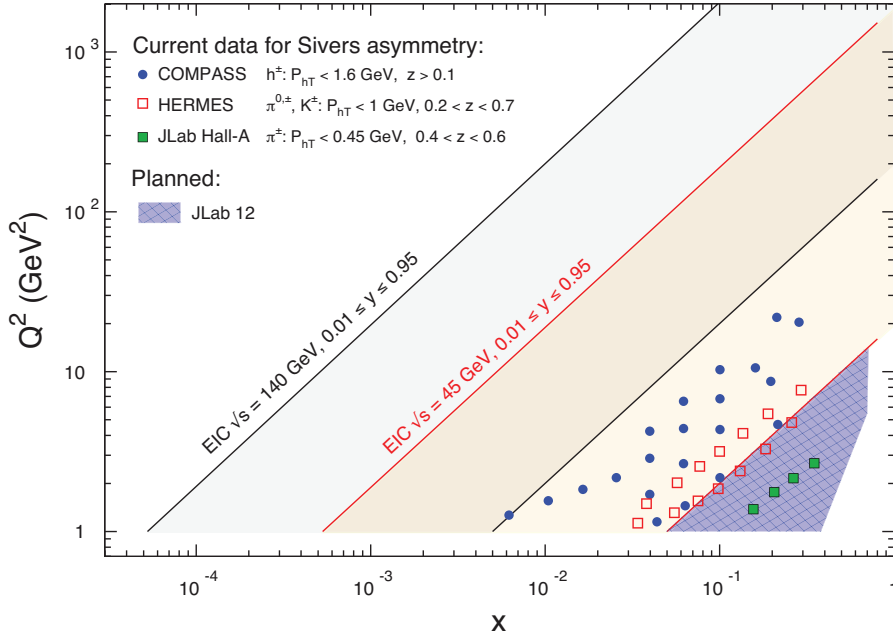


Figure 3.1: Kinematic coverage in  $x$  and  $Q^2$  for the Siverts asymmetry for past, current, and future experiments.  $P_T$  and  $z$  ranges are also shown in the legend. Note that the latest COMPASS data [135] at higher  $Q^2$  is missing. Figure is from [76].

Keeping in mind these preliminary observations, let us now have a look at the measurements we have at our disposal. To start with, let us consider the Siverts asymmetry data. The Siverts effect is accessible in polarised SIDIS and Drell-Yan processes. For the latter, very first preliminary data are available: few points measured by the STAR Collaboration at RHIC for  $A_N$  in  $p^\uparrow p \rightarrow W^\pm/Z^0 + X$  at  $\sqrt{s} = 500$  GeV [88], and some more recent measurements from COMPASS Collaboration at CERN for pion induced Drell-Yan asymmetries with a 190 GeV  $\pi^-$  beam [89]. These first data seem to point towards a confirmation of the predicted sign change of the Siverts function, Eq. (2.10), but much higher statistics is surely needed to claim an experimental validation of the sign change.

Conversely to the Drell-Yan case, the Siverts azimuthal asymmetries in SIDIS have historically represented the only source of information for extracting the quark Siverts function. As seen in the previous Chapter, this TMD is accessible via the  $A_{UT}^{\sin(\phi_h - \phi_s)}$  azimuthal asymmetry (see Eqs. (2.34) and (2.36)). Currently, we have data from the HERMES, COMPASS and the JLab Hall A Collaborations, covering different  $x$ ,  $z$ ,  $P_T$  and  $Q^2$  ranges, as shown in Fig. 3.1. More specifically, let us briefly list the latest data from these Collaborations:

- the HERMES Collaboration measured Siverts asymmetries for  $\pi^\pm$ ,  $\pi^0$  and  $K^\pm$  SIDIS production off a polarised proton target [136];
- the COMPASS Collaboration measured the asymmetries for  $\pi^\pm$ ,  $K^0$  and  $K^\pm$  on LiD (deuterium) [137] and for charged hadron production on  $\text{NH}_3$  targets [135] with  $z > 0.2$ . The latter corresponds to a recent reanalysis of the 2010 COMPASS run, with a novel  $Q^2$  binning, similar to the one used in Drell-Yan measurements [89];
- JLab Hall A data are for  $\pi^\pm$  production off a  $^3\text{He}$  (neutron) target [138].

These data are provided as a function of  $x$ ,  $z$  or  $P_T$ , except for JLab data, whose are only  $x$ -dependent. Note that, in presenting a specific dependence on a kinematical variable, the

other ones are integrated over. The different kinematical coverage and the usage of different targets give access to the Sivers function for different flavours. Due to the flavour content of proton targets, we usually have more information about the  $u$ -quark Sivers function. Neutron data, for isospin symmetry, gives more information on the  $d$ -quark Sivers function, while on a deuterium target the contribution to the azimuthal asymmetries are in principle balanced between  $u$  and  $d$  quarks. Moreover, studying kaon production one could in principle infer the size of the sea quark Sivers function. At the moment, proton data are the most precise ones, while the uncertainties affecting the measured asymmetries off deuterium and neutron targets are still quite large. So, it is expected to have a smaller uncertainty on the fitted  $u$ -quark Sivers function. In future, new proposed runs, as the one for 2021 at COMPASS on deuterium target [139], will certainly help in reducing the uncertainties on the  $d$ -quark Sivers function extraction.

Moving now to the Collins asymmetries, we have two different sources of information: the  $A_{UT}^{\sin(\phi_h+\phi_s)}$  azimuthal asymmetry in SIDIS, Eqs. (2.34) and (2.36), and the azimuthal modulations  $A_0^{UL(C)}$  and  $A_{12}^{UL(C)}$  in  $e^+e^- \rightarrow h_1 h_2 X$  processes. The former gives also access to the TMD transversity distribution, while the latter can be measured with two different methods, namely the “hadronic-plane” ( $A_0^{UL(C)}$ ) and the “thrust-axis” methods ( $A_{12}^{UL(C)}$ ), that are respectively related to the  $\cos(2\phi_0)$  or  $\cos(\phi_1 + \phi_2)$  modulations in the cross section (see Section 3.3.1). At the moment, the latest data come from the HERMES, COMPASS and JLab Hall A Collaborations (for SIDIS) and from the Belle, BaBar and BESIII Collaborations (for  $e^+e^-$ ). More in detail:

- the HERMES Collaboration observed the Collins asymmetries for  $\pi^\pm$ ,  $\pi^0$  and  $K^\pm$  off a polarised proton target [140, 141];
- the COMPASS Collaboration measured  $A_{UT}^{\sin(\phi_h+\phi_s)}$  for  $\pi^\pm$ ,  $K^0$  and  $K^\pm$  off proton [142] and deuteron [137] targets;
- JLab Hall A measurements are performed for  $\pi^\pm$  production off a  $^3\text{He}$  (neutron) target [138];
- the Belle Collaboration measured the azimuthal modulations  $A_0^{UL(C)}$  and  $A_{12}^{UL(C)}$  for  $\pi\pi$  production [143];
- the BaBar Collaboration observed  $A_0^{UL(C)}$  and  $A_{12}^{UL(C)}$  for both  $\pi\pi$ ,  $\pi K$  and  $KK$  production [144];
- the BESIII Collaboration recently measured  $A_0^{UL(C)}$  for  $\pi\pi$  production [145].

SIDIS data for Collins are measured as a function of  $x$ ,  $z$  or  $P_T$  (apart from JLab data, that are only  $x$ -dependent, and again integrating over the two other variables), while  $e^+e^-$  data are obtained by isolating the azimuthal modulation in the cross sections via subsequent ratios. These asymmetries are usually measured as a function of  $z_1$  and  $z_2$ , respectively the two momentum fractions of the produced hadrons  $h_1$  and  $h_2$ , or as a function of  $P_T$ , as in the case of BaBar and BESIII Collaborations. These last sets of data are very interesting, because they give direct access to the transverse momentum dependence of the Collins function. Moreover, they are measured at a different  $Q^2$  values, so in principle they could be used for testing TMD evolution.



### 3.2 QUARK SIVERS FUNCTION AND SIGNALS OF TMD PHYSICS IN SIDIS DATA

In this Section we head to a thorough study on the extraction of the quark Sivers function from SIDIS data within the GPM framework. Specifically, we study the role of an alternative, simpler parametrisation with respect to the one used in previous works, and we assess the visibility of TMD signals in the experimental data. All the results presented here are based on Ref. [120]. In the following, the Torino-Cagliari notation for the TMDs is used, but the relations with the Amsterdam notation can be easily recovered using Eqs. (2.19), (2.65) and (2.67).

#### 3.2.1 GENERAL STRATEGY AND NEW SIVERS PARAMETRISATION

Let us directly start from the new parametrisation. The chosen functional form is very similar to the one adopted in recent works [111, 113, 118, 128] and presented here in Eqs. (2.65) and (2.67), with factorised  $x$  and  $k_\perp$  dependences. The main difference is that here the  $x$ -dependent part of the Sivers function is no more taken to be proportional to the corresponding unpolarised collinear distribution. So, the new parametrisation reads

$$\Delta^N f_{q/p^\uparrow}(x, k_\perp) = 4N_q x^{\alpha_q} (1-x)^{\beta_q} \frac{M_p k_\perp}{\langle k_\perp^2 \rangle_S} \frac{e^{-k_\perp^2 / \langle k_\perp^2 \rangle_S}}{\pi \langle k_\perp^2 \rangle_S}. \quad (3.1)$$

where  $N_q$ ,  $\alpha_q$ ,  $\beta_q$  and  $\langle k_\perp^2 \rangle_S$  are free parameters.

Using this parametrisation makes us renounce to the automatic fulfillment of the positivity bound for the Sivers function, Eq. (2.22). However, using the parametrisation in Eq. (3.1), allow us a realistic determination of the uncertainties that affect the extraction of the Sivers function, and also to test in the most agnostic possible way aspects of the data related to TMD physics, like flavour separation and scale dependence.

Additionally, the new model is directly parametrised in terms of the Sivers width,  $\langle k_\perp^2 \rangle_S$ , and is arranged in such a way that we can study the Sivers function by directly parametrising its first moment. In fact, it is easy to see that, within the model in Eq. (3.1), the Sivers first moment is simply:

$$\Delta^N f_{q/p^\uparrow}^{(1)}(x) = \int d^2 \mathbf{k}_\perp \frac{k_\perp}{4M_p} \Delta^N f_{q/p^\uparrow}(x, k_\perp) = N_q x^{\alpha_q} (1-x)^{\beta_q} = -f_{1T}^{\perp(1)q}(x), \quad (3.2)$$

where on the r.h.s. we have given the relation with the Amsterdam notation.

Regarding the unpolarised TMD PDFs and FFs we adopt the usual functional forms of Eqs. (2.58) and (2.59), choosing as collinear PDFs and FFs the CTEQ6l1 [146, 147] and DSS [148] leading order sets, respectively. The unpolarised PDF and FF widths,  $\langle k_\perp^2 \rangle$  and  $\langle p_\perp^2 \rangle$ , are fixed according to the values extracted in Ref. [114]. As discussed in Section 2.3, the unpolarised TMDs depend on  $Q^2$  only via their collinear parts, that obey the DGLAP evolution equations [18–20]. Therefore, in the following, the structure function  $F_{UU}$  will always evolve in  $Q^2$  via the same evolution equations.

Within this model, by using the definition of the convolution in Eq. (2.35), and recalling that

$$A_{UT}^{\sin(\phi_h - \phi_S)} = \frac{F_{UT}^{\sin(\phi_h - \phi_S)}}{F_{UU}}, \quad (3.3)$$

the Siverts structure functions  $F_{UT}^{\sin(\phi_h - \phi_s)}$  is given by

$$F_{UT}^{\sin(\phi_h - \phi_s)}(x, z, P_T) = x \frac{2M_p z P_T}{\langle P_T^2 \rangle_S} \sum_q e_q^2 \left( N_q x^{\alpha_q} (1-x)^{\beta_q} \right) D_{h/q}(z) \frac{e^{-P_T^2 / \langle P_T^2 \rangle_S}}{\pi \langle P_T^2 \rangle_S}, \quad (3.4)$$

where  $\langle P_T^2 \rangle_S$  is given in Eq. (2.61), and  $F_{UU}$  is written as in Eq. (2.60). Note that this form is exactly the same as in Eq. (2.68), with the Siverts first moment written as in Eq. (3.2); consistently, the asymmetry in Eq. (3.3) then has the same expression as in Eq. (2.70).

In what follows we will analyse different possible scenarios. Particularly, we will build our starting point, a reference best fit, by fixing  $\alpha_q = 0$ , taking a constant  $\langle k_\perp^2 \rangle_S$  in Eq. (3.1), and considering only  $u$  and  $d$  flavour contributions. Then, by modifying some of the starting assumptions, we will address different aspects regarding data sensitivity to some chosen features. In particular, we will study the low- $x$  region and the sensitivity of experimental measurements to  $Q^2$  and  $x$  correlations.

#### DATA SELECTION AND UNPOLARISED WIDTH CHOICE

Before going into the fitting results, it is important to highlight the choices we make on the data selection and on the unpolarised PDF and FF widths.

Regarding the data, we fit all the latest available data on the Siverts SIDIS asymmetries, but excluding some specific data subset. More specifically, we fit all the Siverts SIDIS data listed in Section 3.1, that are the ones coming from HERMES off a proton target [136], COMPASS on LiD [137] and NH<sub>3</sub>, and JLab off a <sup>3</sup>He (neutron) target [138]. Since in our analysis we do not separate valence and sea contributions, we exclude  $K^-$  data, that is mainly driven by the sea contribution itself. Moreover, even if HERMES and COMPASS data are provided as a function of  $x, z$  or  $P_T$  (JLab provides only the  $x$  dependence of  $A_{UT}^{\sin(\phi_h - \phi_s)}$ ), we do not include  $z$ -dependent data, as in our model this dependence is driven only by the FFs, and we do not have any sensitivity to  $z$  in our free parameters. This results in a total of 220 datapoints.

The fit is carried out with a usual  $\chi^2$  minimisation procedure using MINUIT [149], while uncertainties estimation is made by carefully exploring the parameter space and considering a  $2\sigma$  confidence level (CL), that corresponds to a coverage probability of 95.4%. We then accept parameter configurations whose  $\chi^2$ 's lie in the range  $[\chi_{\min}^2, \chi_{\min}^2 + \Delta\chi^2]$ , where  $\Delta\chi^2$  depends on the number of considered parameters. More details on this procedure are given in the Appendix A of Ref. [113].

As mentioned before, for the unpolarised TMD PDFs and FFs we use the values of  $\langle k_\perp^2 \rangle$  and  $\langle p_\perp^2 \rangle$  extracted in Ref. [114]. In that work, SIDIS multiplicities from HERMES and COMPASS were analysed and fitted within the GPM scheme, and it was found that, within the Gaussian Ansatz, the two datasets could be well reproduced, but only if fitted separately: no simultaneous extraction was possible. This results in two different widths pairs for HERMES and COMPASS, respectively. So, we consistently use the results of Ref. [114] for each individual experiment. Moreover, for the JLab data, we adopt the unpolarised widths fitted from HERMES data, as the two experiments were shown to be compatible [114].

In order to support this choice, we first perform simple compatibility tests, where we compute the effects of using different widths for the calculation of  $F_{UU}$  (that is, the unpolarised cross section) for HERMES and COMPASS. In these tests, we compare two hypotheses:

- (i) usage of the same unpolarised widths, namely the ones extracted from HERMES, for both HERMES and COMPASS asymmetries;
- (ii) usage of the corresponding unpolarised widths for each experiment.

In each case, we perform three fits on  $\pi^+$  production from a proton target, considering only the  $u$ -quark Siverson contribution and setting all other flavour contributions to zero: HERMES data only, COMPASS data only, or a simultaneous fit of HERMES and COMPASS data. The results for the correlation between  $N_u$ ,  $\beta_u$  parameters are shown in Fig. 3.2, where scatter plots are at a  $2\sigma$  CL.

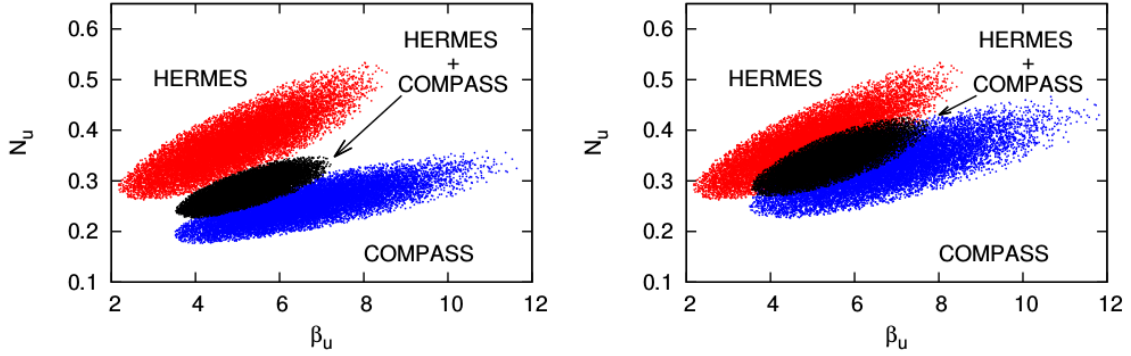


Figure 3.2: Compatibility tests on  $\pi^+$  production from a proton target using only the  $u$ -contribution (all others flavours being set to zero) for the Siverson function, as described in the text. In each panel, we show the scatter plot of the allowed values of  $\beta_u$  and  $N_u$ , corresponding to a  $2\sigma$  CL, for three cases: HERMES data (red), COMPASS data (blue), HERMES+COMPASS (black). Left panel: same unpolarised widths ( $\langle k_\perp^2 \rangle = 0.57 \text{ GeV}^2$  and  $\langle p_\perp^2 \rangle = 0.12 \text{ GeV}^2$  as obtained from HERMES multiplicities). Right panel: different unpolarised widths for each experiment ( $\langle k_\perp^2 \rangle = 0.57 \text{ GeV}^2$  and  $\langle p_\perp^2 \rangle = 0.12 \text{ GeV}^2$  for HERMES data,  $\langle k_\perp^2 \rangle = 0.60 \text{ GeV}^2$  and  $\langle p_\perp^2 \rangle = 0.20 \text{ GeV}^2$  for COMPASS data).

Looking at the red and blue areas on the left panel in Fig. 3.2, we note that the usage of the same unpolarised widths for HERMES and COMPASS data results in a tension between the two sets, as the two fits populate different, well separated regions in the parameter space. Consequently, the joint fit of HERMES and COMPASS data (black area), although still giving a good value of the  $\chi^2$ , has to compromise between the two datasets, rendering values of the normalisation parameter  $N_u$  “half-way” between the red and blue regions. Instead, when we use the corresponding widths for the two experiments (right panel), the explored parameter space overlap, visibly reducing the tension shown on the left panel. This effect can be mostly attributed to the difference in the  $\langle p_\perp^2 \rangle$  values (see Fig. 3.2 caption and Tables below) extracted from HERMES and COMPASS SIDIS multiplicities. Furthermore, this also supports our choice in using the appropriate unpolarised widths for each experimental set in our analysis, and also denotes the importance of having a good knowledge of the unpolarised TMD-PDFs and FFs while analysing any polarised observable. Moreover, as the two datasets cover different  $Q^2$ -ranges, this effect could also be interpreted as a signal of TMD evolution effects. Without getting into it, this is clearly an issue that deserves further investigation.

### 3.2.2 FITTING THE QUARK SIVERS FUNCTION

We now head to the actual different fits that will allow us to assess signals of TMD physics in the SIDIS azimuthal asymmetries and in the extraction of the quark Siverson function. We

recall that our starting point is the Siverson model in Eq. (3.1) with  $\alpha_u = \alpha_d = 0$ . The choice of the two full  $u$  and  $d$  flavours, with no valence/sea separation, is the one that has rendered the lowest value for  $\chi^2_{\min}$ . With these choices, the first moment of the Siverson function reduces to

$$\Delta^N f_{q/p^\uparrow}^{(1)}(x) = N_q(1-x)^{\beta_q}, \quad (3.5)$$

and the full parametrisation reads

$$\Delta^N f_{u/p^\uparrow} = \Delta^N f_{u_v/p^\uparrow} + \Delta^N f_{\bar{u}/p^\uparrow} = 4 N_u(1-x)^{\beta_u} \frac{M_p k_\perp}{\langle k_\perp^2 \rangle_S} \frac{e^{-k_\perp^2 / \langle k_\perp^2 \rangle_S}}{\pi \langle k_\perp^2 \rangle_S}, \quad (3.6)$$

$$\Delta^N f_{d/p^\uparrow} = \Delta^N f_{d_v/p^\uparrow} + \Delta^N f_{\bar{d}/p^\uparrow} = 4 N_d(1-x)^{\beta_d} \frac{M_p k_\perp}{\langle k_\perp^2 \rangle_S} \frac{e^{-k_\perp^2 / \langle k_\perp^2 \rangle_S}}{\pi \langle k_\perp^2 \rangle_S}. \quad (3.7)$$

This results in a fit with a total of 5 free parameters:  $N_u, N_d, \beta_u, \beta_d, \langle k_\perp^2 \rangle_S$ . We refer to these choices as “reference-fit”. In this first, simple extraction, no  $Q^2$  evolution is applied to the Siverson function, and the corresponding plots will be labeled by “no-evolution”; the fitted function will then represent the Siverson function at the average  $Q^2$  scale of the experimental data.

Reference fit - no evolution		
$\chi^2_{\text{tot}} = 212.8$	n. of points = 220	
$\chi^2_{\text{dof}} = 0.99$	n. of free parameters = 5	
$\Delta\chi^2 = 11.3$		
HERMES	$\langle k_{\perp}^2 \rangle = 0.57 \text{ GeV}^2$	$\langle p_{\perp}^2 \rangle = 0.12 \text{ GeV}^2$
COMPASS	$\langle k_{\perp}^2 \rangle = 0.60 \text{ GeV}^2$	$\langle p_{\perp}^2 \rangle = 0.20 \text{ GeV}^2$
$N_u = 0.40 \pm 0.09$	$\beta_u = 5.43 \pm 1.59$	
$N_d = -0.63 \pm 0.23$	$\beta_d = 6.45 \pm 3.64$	
$\langle k_{\perp}^2 \rangle_S = 0.30 \pm 0.15 \text{ GeV}^2$		

Table 3.1: Best fit parameters and  $\chi^2$  values for the reference fit. The parameter errors correspond to a  $2\sigma$  CL. Notice that these errors are well in agreement with the uncertainties on the free parameters shown in the scatter plots of Fig. 3.3.

Table 3.1 shows the best fit values of the parameters, together with the minimal  $\chi^2$  value and the total number of datapoints included. The quoted errors in Table 3.1 are MINUIT errors, and correspond to a  $2\sigma$  CL, that is a coverage probability of 95,4%.

The top panels in Fig. 3.3 show the  $\chi^2_{\text{tot}}$  profiles as functions of the normalisation parameters  $N_u$  and  $N_d$ . In these plots, the correlations between the two parameters are colour-coded, with yellow corresponding to lowest, green to intermediate and purple to highest allowed values of  $N_d$  (top left panel) and  $N_u$  (top right panel). From these plots it is also quite evident that these profiles are well approximated by a quadratic function, confirming that the Hessian method adopted to evaluate the errors on the parameters is reliable. The errors in Table 3.1 are indeed in very good agreement with the uncertainties on the parameters that can easily be inferred by looking at the scatter plots.

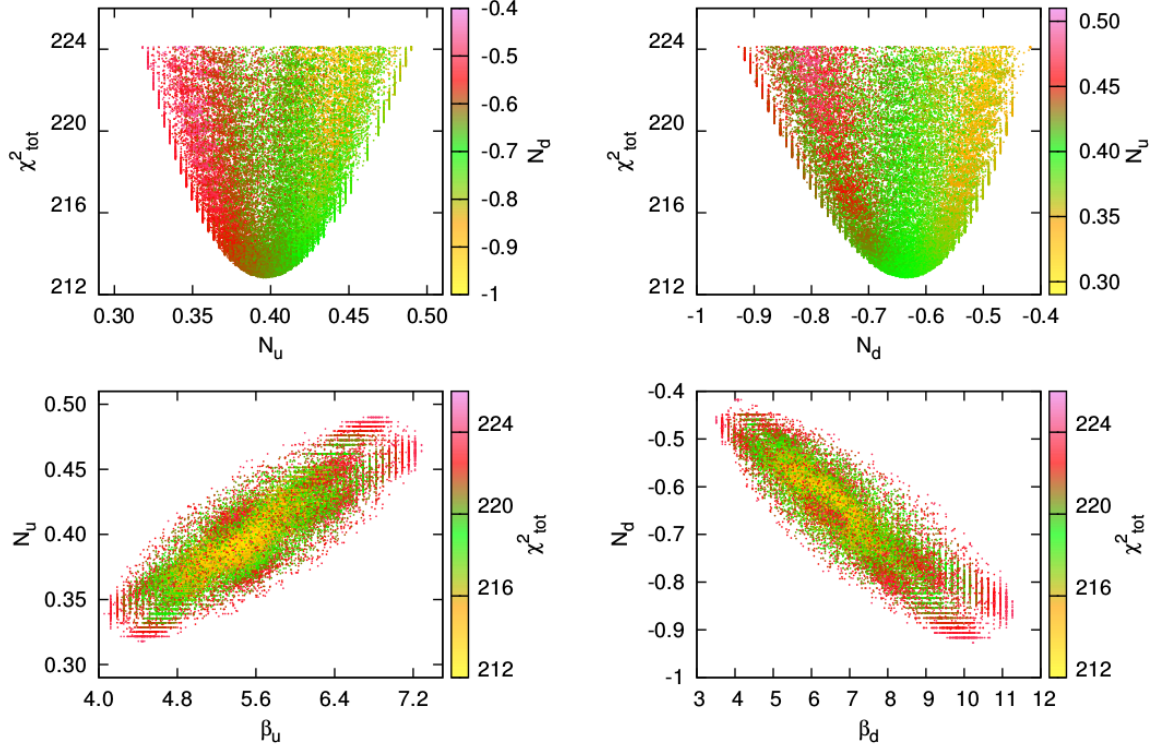


Figure 3.3: Scatter plots representing the parameter space of the reference best fit. The shaded regions correspond to our estimate of the  $2\sigma$  CL error band.

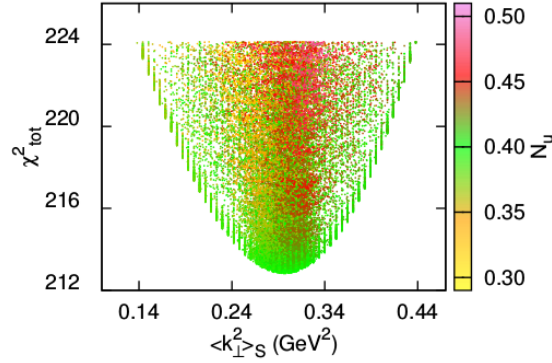


Figure 3.4: Allowed values for the width of the Siverts function  $\langle k_{\perp}^2 \rangle_S$  as a function of  $\chi^2_{\text{tot}}$ . The displayed region corresponds to our estimate of the  $2\sigma$  CL error band.

The lower panels of Fig. 3.3 represent the correlations between the parameters  $N_u$ ,  $\beta_u$  (lower left) and  $N_d$ ,  $\beta_d$  (lower right). Here it is the corresponding  $\chi^2_{\text{tot}}$  which is colour-coded, with yellow corresponding to the lowest, green to intermediate and purple to the highest  $\chi^2_{\text{tot}}$  values. The correlations among parameters shown in these plots cover regions of reasonably regular ellipsoidal shapes, confirming again the consistency of the Hessian approximation used by MINUIT in the  $\chi^2$  minimisation.

Fig. 3.4 shows instead the  $\chi^2_{\text{tot}}$  profile of the Siverts width,  $\langle k_{\perp}^2 \rangle_S$ , and its correlation with  $N_u$ . Colour code is the same as in the top panels of Fig. 3.3. Also in this case the uncertainties indicated by the scatter plots of the parameter space are perfectly consistent with the errors estimated by adopting the Hessian approximation, reported in Table 3.1.

Plots of the extracted Siverts functions and their uncertainty bands will be shown later along with the ones for the second fit, the so-called “ $\alpha$ -fit”, and their differences will be discussed

later as well. Here, we limit ourselves to pointing out that the reference fit, even with a very small number of free parameters, is able to reproduce all the existing SIDIS experimental measurements in a satisfying manner. Furthermore, it provides a successful extraction of the Siverson function as well as a reliable estimate of the uncertainties, over the kinematic region covered by the bulk of experimental data (i.e. approximately  $0.03 < x < 0.3$ ). Below this region, where only very few data points are present, the error bands from the reference fit are at risk of being artificially small.

Even if the reference fit seems to be already quite satisfying, we have to recall that the bulk of experimental measurements lies in a quite narrow region in  $x$ . In order to explore in more detail the low- $x$  kinematic region, we move on performing another fit, the  $\alpha$ -fit, where now we let vary the  $\alpha_q$  parameters in Eq. (3.1). In particular, the only difference with respect to the reference fit is represented by the addition of two more parameters,  $\alpha_u$  and  $\alpha_d$ . The Siverson first moment now generally reads

$$\Delta f_{q/p^\uparrow}^{N_f(1)}(x) = N_q x^{\alpha_q} (1-x)^{\beta_q}. \quad (3.8)$$

$\alpha$ fit - no evolution		
$\chi_{\text{tot}}^2 = 211.5$	n. of points = 220	
$\chi_{\text{dof}}^2 = 0.99$	n. of free parameters = 7	
$\Delta\chi^2 = 14.3$		
HERMES	$\langle k_\perp^2 \rangle = 0.57 \text{ GeV}^2$	$\langle p_\perp^2 \rangle = 0.12 \text{ GeV}^2$
COMPASS	$\langle k_\perp^2 \rangle = 0.60 \text{ GeV}^2$	$\langle p_\perp^2 \rangle = 0.20 \text{ GeV}^2$
$N_u = 0.40 \pm 0.09$	$\beta_u = 5.93 \pm 3.86$	$\alpha_u = 0.073 \pm 0.46$
$N_d = -0.63 \pm 0.23$	$\beta_d = 5.71 \pm 7.43$	$\alpha_d = -0.075 \pm 0.83$
$\langle k_\perp^2 \rangle_S = 0.30 \pm 0.15 \text{ GeV}^2$		

Table 3.2: Best fit parameters and  $\chi^2$  values corresponding to the  $\alpha$ -fit. Notice that, despite the presence of two extra parameters with respect to the reference fit presented in Table 3.1, the value of  $\chi_{\text{tot}}^2$  remains practically unchanged. However, the uncertainty on the free parameters increases considerably. This generates much larger uncertainty bands in the low- $x$  region, as shown in Fig. 3.5.

The results of this new fit are shown in Table 3.2, where we can quickly notice some aspects:

- the  $\chi_{\text{dof}}^2$  is unchanged, so the overall quality of the fit does not improve with respect to the reference fit;
- the values of the  $\alpha$  parameters are compatible with zero, as first guessed in the reference fit;
- the central values of the fitted parameters do not change much with respect to the reference fit, while the parameter errors increase (see Table 3.1).



The last point could suggest that the experimental data currently used are not sensitive to the particular choice of value for  $\alpha_u$  and  $\alpha_d$ , and consequently, further constraining the low- $x$  behaviour of the Siverts function seems at the moment unlikely. However, one can notice that the increase of the parameter errors translates into an effect on the uncertainty bands, as shown in Fig. 3.5, where the light-blue bands correspond to the reference fit, while the wider, grey bands refer to the “ $\alpha$ -fit”.

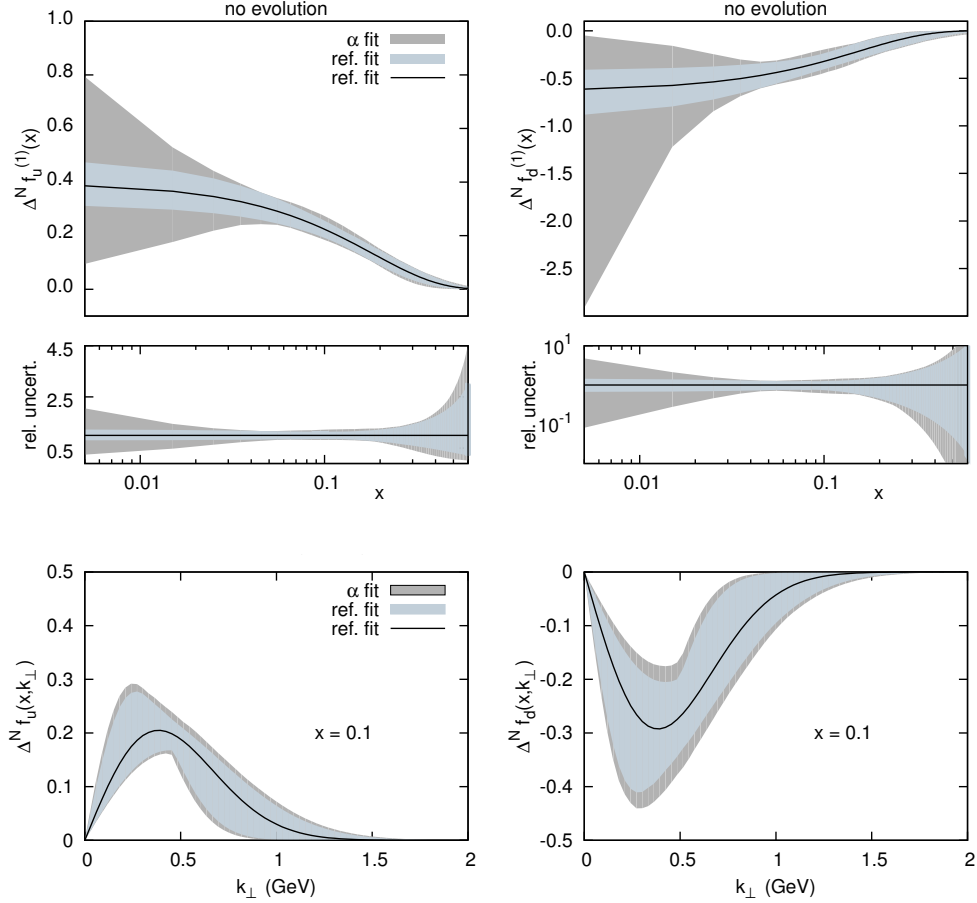


Figure 3.5: The extracted Siverts distributions for  $u = u_v + \bar{u}$  and  $d = d_v + \bar{d}$ . Upper panels: the first moments of the Siverts function, Eqs. (3.5) and (3.8), as a function of  $x$ . Middle panel: relative uncertainties, given by the ratio between the upper/lower border of the uncertainty bands and the best-fit curve for the reference fit. Lower panel:  $k_{\perp}$ -dependence of the Siverts functions, Eq. (3.1), at  $x = 0.1$ . No  $Q^2$  dependence is taken into account here. The shaded bands correspond to our estimate of  $2\sigma$  CL. In all panels, the light blue bands correspond to the uncertainties of the reference fit (only  $N_{u(d)}$  and  $\beta_{u(d)}$  as free parameters), while the large grey bands correspond to the uncertainties for the fit which includes also the  $\alpha_u$  and  $\alpha_d$  parameters.

The inclusion of the  $\alpha$  parameters generates also a modification in the parameter space, as shown in detail in Fig. 3.6. The top panels show the  $\chi^2_{\text{tot}}$  profiles as functions of the parameters  $N_u$  (top-left) and  $N_d$  (top-right), with same colour code as in Fig. 3.3. We instantly notice that the inclusion of the  $\alpha$  parameters generates a significant distortion of these profiles, and therefore, in this case, the Hessian method adopted to evaluate the errors on the parameters cannot be trusted. Indeed, the MINUIT errors reported in Table 3.2 largely underestimate the uncertainties on the free parameter determination: by looking at the plots in Fig. 3.6, it is easy to see that, to  $2\sigma$  CL,  $N_u$  can go as low as 0.1 and as large as 4.0, over a very asymmetric range.



A similar situation happens for  $N_d$ , which can span over an even larger range, from 0 to  $-45$ , on an extremely asymmetric range. Nonetheless, we have a clear indication on the sign of the Siverts function:  $N_u$  is positive and  $N_d$  is negative, therefore the data favour a positive  $u$  and a negative  $d$  Siverts function (in the Torino-Cagliari notation). This confirms the findings of previous works, where the Siverts function was extracted within different approaches [115, 118].

The upper panels of Fig. 3.6 shows also the colour-coded correlations ( $N_u, \alpha_u$ ) and ( $N_d, \alpha_d$ ): the very evident structure in bands of the same colour points to extremely strong correlations. This strong behaviour is even more explicit in the lower panels of Fig. 3.6, where we show  $N_u$  vs.  $\alpha_u$  (bottom left) and  $N_d$  vs.  $\alpha_d$  (bottom right). In these plots we no longer observe any ellipsoidal shape as in the case of the reference fit (see Figs. 3.3 and 3.4), but we can clearly see thin and stretched distributions, indicating that an extremely large number of equally good fits can be obtained provided that the  $N$ ,  $\alpha$  (and  $\beta$ ) parameters are in the appropriate ratio among each others. In other words, if  $N$  is large enough, even very large values of  $\alpha$  and  $\beta$  (for which the function goes much more quickly to zero in the limits  $x \rightarrow 0$  and  $x \rightarrow 1$ ) can result in an acceptable value of the  $\chi^2$ . Conversely, low values of  $\alpha$  and  $\beta$  are also equally appropriate if  $N$  is small enough. So, the strong correlation introduced by  $\alpha$ , in fact, make it cumbersome to find a good fit by a simple minimisation procedure.

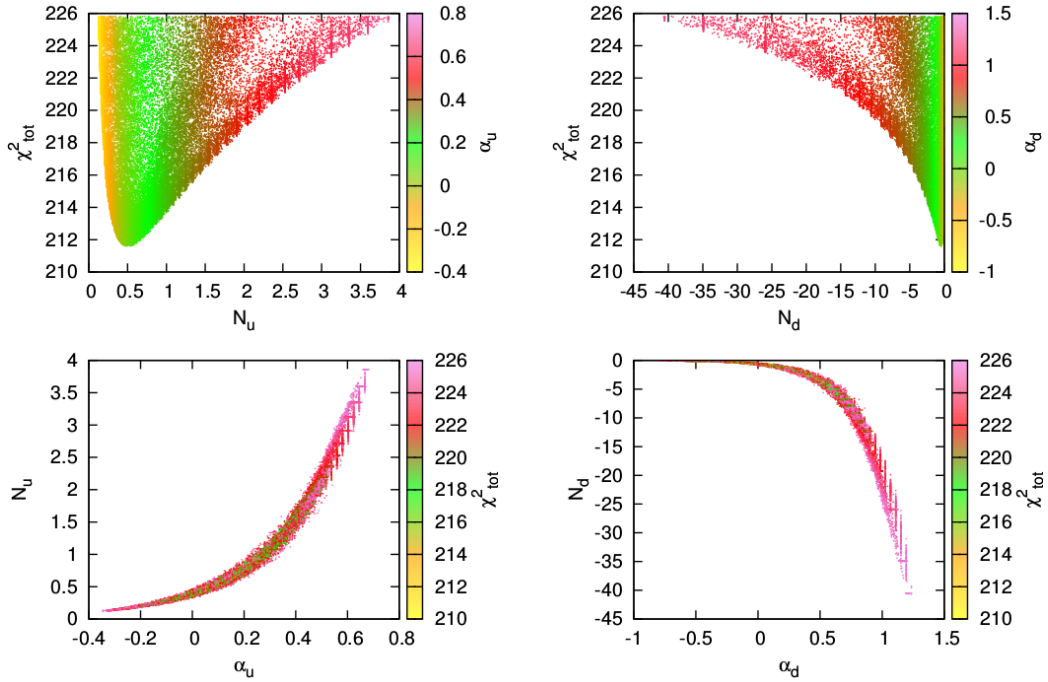


Figure 3.6: Parameter space scatter plots for the  $\alpha$ -fit, which includes the  $\alpha_u$  and  $\alpha_d$  free parameters. The regions displayed correspond to our estimate of the  $2\sigma$  CL error band. Notice that the uncertainties on the parameters which can be inferred from the scatter plots are much larger than the errors reported in Table 3.2.

One can then conclude that the inclusion of  $\alpha$  parameters in the fit represents a high price to pay. It is true that the dramatic changes in the parameter space seem to shuffle and throw the situation into disorder. Nonetheless, as already mentioned before, this also allows for a more realistic estimate of the uncertainty bands in the low- $x$  region, as shown in Fig. 3.5. As expected, the two fits have very similar bands over the region  $0.03 < x < 0.3$ , i.e. the bulk of

experimental data, while the  $\alpha$ -fit uncertainties grow larger outside this range, where very few datapoints are present. Not surprisingly, the Siverson width,  $\langle k_\perp^2 \rangle_S$ , is not significantly affected by the strong broadening of the uncertainty bands. Its central value does not change at all (see Tables 3.1 and 3.2), and the error bands show no significant change, as it is plainly evident in the bottom panels of Fig. 3.5, where the  $k_\perp$  dependence of the  $u$  and  $d$  Siverson function is plotted at  $x = 0.1$ .

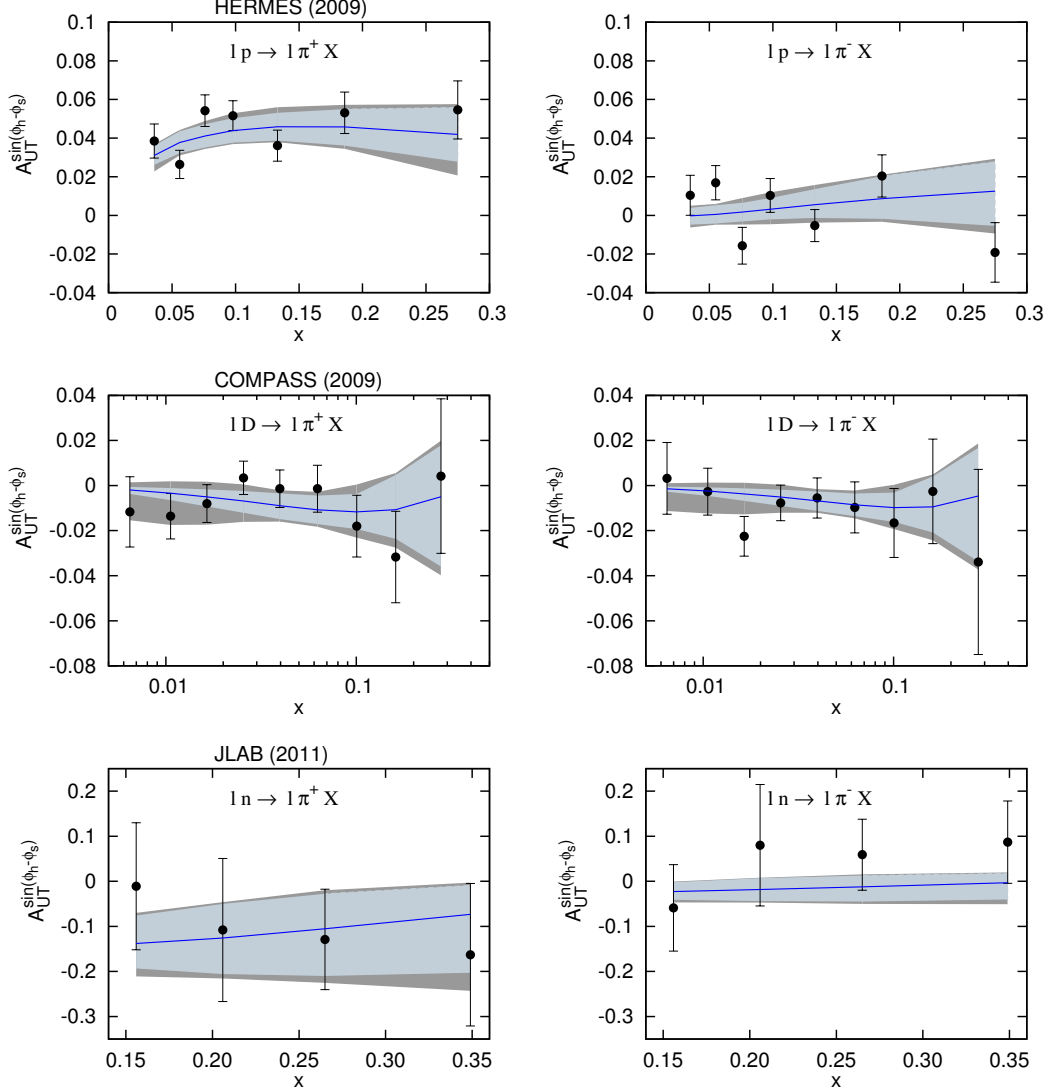


Figure 3.7: The results obtained from the reference fit and the  $\alpha$ -fit are compared to the HERMES measurements of the SIDIS Siverson asymmetry for  $\pi^\pm$  production off a proton target [136] (upper panels), to the COMPASS measurements of the SIDIS Siverson asymmetry on a LiD target [137] for  $\pi^\pm$  production (middle panels), and to the JLab data for  $\pi^\pm$  production on a  $^3\text{He}$  target [138] (bottom panel). Only  $x$  dependence is shown. The shaded regions correspond to our estimate of the  $2\sigma$  CL error bands. As in Fig. 3.5, the light-blue bands correspond to the uncertainties of the reference fit (only  $N_{u(d)}$  and  $\beta_{u(d)}$  free parameters), while the (larger) grey bands correspond to the uncertainties of the  $\alpha$ -fit, which includes also the  $\alpha_{u(d)}$  parameters.

It is also interesting to look at the comparison between the fits and the data. Fig. 3.7 shows the results obtained from the reference fit compared to older data, which have historically been used in previous Torino-Cagliari-JLab group fits (see e.g. [113, 118]). These measurements come from HERMES-proton [136] (top panels), COMPASS-deuterium [137] (middle

panels), and JLab-neutron [138] (bottom panels) analyses. The uncertainty bands are shown as in Fig. 3.5: the light-blue bands and the central lines are related to the reference fit, while the grey bands are the ones for the  $\alpha$ -fit. As for the Sivers function itself, the introduction of the  $\alpha$  parameters provides a more sensible uncertainties at low- $x$ . This is especially clear for COMPASS-deuteron data (middle panels of Fig. 3.7), where we can observe a deterioration of the agreement of the light-blue bands with the data at small values of  $x$ , while the  $\alpha$ -fit bands improve the compatibility with these experimental measurements.

We also note that, since valence/sea separation is not possible with the current data, the effect on the uncertainties introduced by allowing for  $\alpha \neq 0$  also reflects our ignorance about the sea contributions, that are expected to dominate at small  $x$ . This fact supports the need to learn more about the Sivers function in the low- $x$  region and, consequently, its sea contributions. This is one of the main objectives of the future EIC [76], which is planned to be built in the next decade in the USA.

While waiting for new EIC data to get more information about the Sivers sea distribution, let us stress the importance of the deuteron target measurements as those performed by COMPASS [137]. Indeed, proton data are dominated by the  $u$ -quark Sivers contribution, whereas SIDIS Sivers asymmetries on deuteron are also sensitive to the  $d$ -quark Sivers function. Looking at Fig. 3.5, we can clearly note that, for the  $\alpha$ -fit, the uncertainty bands on the extracted  $d$  Sivers function are larger than the  $u$  Sivers ones. So, an improved statistics on deuteron data would bring twofold advantages: it would constrain more the  $d$ -quark Sivers distribution providing, at the same time, a stronger constraint on the size of the sea distributions. Projections for the 2021 COMPASS run on deuteron [139] point in this direction: it is expected to gain a factor of 2 in precision on the  $d$  Sivers function in the region  $x < 0.1$ , as shown in Section 4 of Ref. [120].

Coming back to the comparison with data, we now take a look at Fig. 3.8, where we compare the results obtained from the reference fit, together with the bands for the  $\alpha$ -fit, to a selection of new COMPASS data on the SIDIS Sivers asymmetry for charged hadrons production on a  $\text{NH}_3$  target [135]. In particular, only  $x$  and  $P_T$  dependences are presented, as the  $z$  dependence of the data is not included in the fit. Nonetheless, we have checked that all  $z$ -dependent asymmetries are successfully reproduced. As in Fig. 3.7, the shaded regions correspond to the 95.4% CL error band.

We recall that this new data set comes from a reanalysis of the COMPASS-proton data from the 2010 run, and overcomes the previous published set [142], where no  $Q^2$  binning was present. Conversely, the newly re-analysed data are not only binned in  $x$ ,  $z$  and  $P_T$ , but also in four bins of  $Q^2$ , that are also the same bins used for the Drell-Yan analysis [89]. One can then expect that, the increased degree of information represented by the  $Q^2$  binning could help in the accuracy of the extraction. This is what we slightly observe in Fig. 3.9, where we show a comparison between two sets of extracted Sivers first moments for  $u$  and  $d$ , one in which the old dataset with no  $Q^2$  binning is used (2015) and the other where  $Q^2$  binning is present (2017).

One of the most important features of the new binning is the separation of data in different  $Q^2$  ranges. This allow us, for the first time, to explore the possibility of accessing the scale dependence in the Sivers function, i.e. the visibility of scale dependence in the experimental measurements, as we will see in Section 3.2.3. Before addressing this issue, it is then important to summarise our current knowledge on the Sivers function, to see the impact of some

choices made in building the model, and to look at the large- $x$  uncertainties, i.e. in the region  $x \gtrsim 0.3$ .

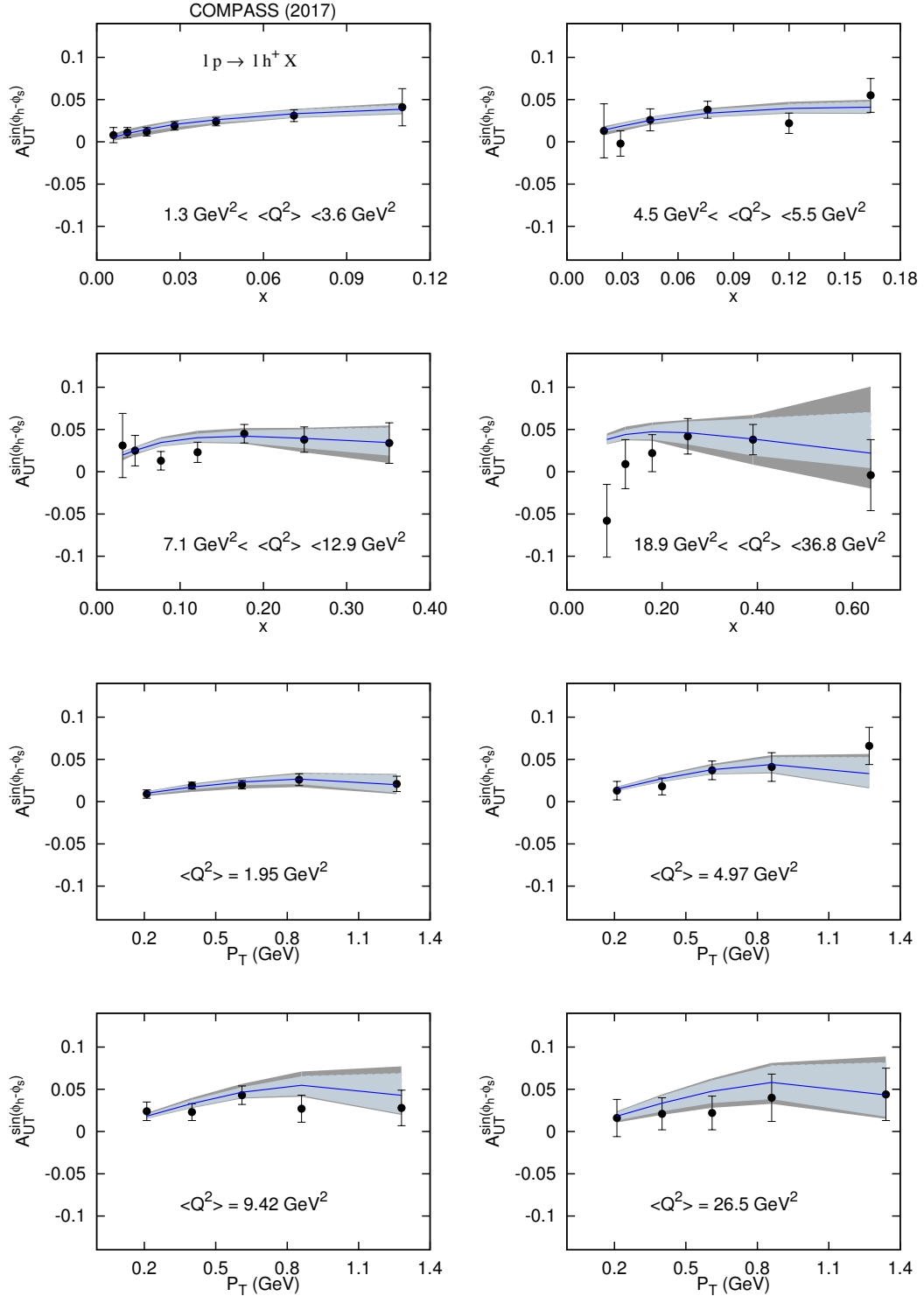


Figure 3.8: The results obtained from the reference fit and the  $\alpha$ -fit are compared to the COMPASS Collaboration measurements of the SIDIS Sivers asymmetry on a  $\text{NH}_3$  target [135] for  $h^+$  production.  $x$  and  $P_T$  dependences are shown. The shaded regions correspond to our estimate of the  $2\sigma$  CL error band. The light-blue bands correspond to the uncertainties of the reference fit (only  $N_{u(d)}$  and  $\beta_{u(d)}$  free parameters), while the (larger) grey bands correspond to the uncertainties of the  $\alpha$ -fit which includes also the  $\alpha_{u(d)}$  parameters.

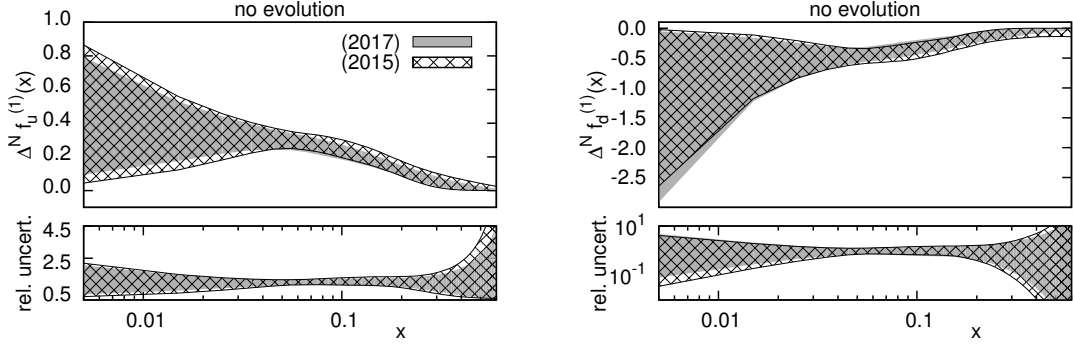


Figure 3.9: Uncertainties on the first moments of the Siverts distribution for  $u = u_v + \bar{u}$  (left panel) and  $d = d_v + \bar{d}$  (right panel). The shaded bands correspond to our estimate of  $2\sigma$  CL error for the  $\alpha$ -fit case. In both panels, the grey bands correspond to the fit which includes the new COMPASS-2017 data [135] for  $h^+$  and  $h^-$  production off  $\text{NH}_3$  target, while the meshed areas correspond to the uncertainties obtained when the COMPASS-2015 data from the older analysis [142] are included. Relative errors, given by the ratio between the upper/lower border of the uncertainty bands and the best-fit curve for the reference fit, are shown in the lower panels. Note the logarithmic scale on the vertical axis of the lower-right panel.

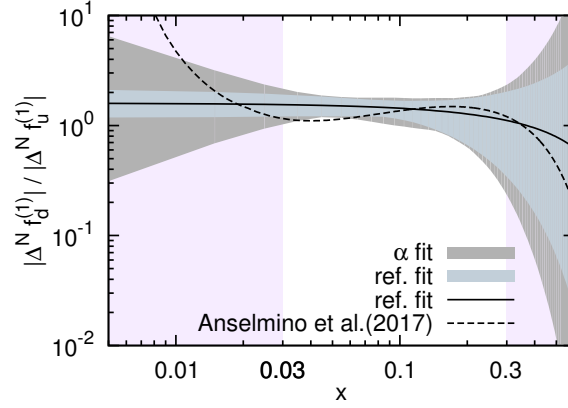


Figure 3.10: Flavour ratio for the first moments of the Siverts TMD distributions,  $|\Delta f_{d/p^+}^{(1)}|/|\Delta f_{u/p^+}^{(1)}|$ , as extracted in the reference fit ( $\alpha = 0$ ) (light-blue bands) and in the  $\alpha$ -fit (grey bands). The solid line shows the central line for the ratio, according to our reference fit. As a comparison, the corresponding central line according to the extraction of Ref. [118] is also shown. The low- $x$  and large- $x$  regions, where experimental information is scarce, are highlighted in purple.

It is worth noticing that in this region the Siverts function should approach zero according to the positivity bound, Eq. (2.22), which should hold at every value of  $x$  and  $k_\perp$  for any partonic flavour. As we have already seen in Fig. 3.5, middle panels, the Siverts function is largely undetermined at large  $x$ . At the same time, also the integrated unpolarised PDFs are largely undetermined in the large- $x$  region, undermining the significance of any phenomenological application of the positivity bound itself.

To render the large- $x$  uncertainties more visible, and to compare different models, we show in Fig. 3.10 the ratio  $|\Delta f_{d/p^+}^{(1)}|/|\Delta f_{u/p^+}^{(1)}|$ , together with the central line of the previous extraction of the Siverts function [118]. As one could expect, in the region where data are present, the agreement between the two fits is acceptable. But, as soon as one moves outside this region, the two extractions exhibit very different behaviours. This is clearly evident in the low- $x$  region, where the central line of the previous Siverts extraction lies outside the error bands of the current fit. This difference is essentially due to the distinct assumptions

made in the fit. In fact, at variance with this study, where the Sivers function is independent of the unpolarised collinear PDF, in the previous extraction the Sivers function was taken proportional to the collinear distribution (see Eqs. (2.62) and (2.65)), so its shape is partially modeled by the unpolarised part itself. This difference is milder in the large- $x$  region, where the two extractions seems to be more compatible. This point is then very important: it is a signal of our early-stage situation in TMDs extractions. More data are definitely needed to have stronger constraints on the TMD distributions and, in turn, to improve our models. Surely, future measurements at JLab at 12 GeV will help in this direction, allowing us to shed light on the large- $x$  behaviour of the unpolarised TMDs and the Sivers function, and giving us a much clearer signature for the flavour separation of the valence contribution.

### 3.2.3 SIGNALS OF SCALE DEPENDENCE

Even if no  $Q^2$  dependence of the Sivers function has been considered yet, the reference fit and the  $\alpha$ -fit seem to be already quite useful to pin down a lot of information from the existent experimental measurements. Nonetheless, thanks to new COMPASS data [135], we now have the possibility to study potential signals of scale dependence in the data and, in turn, see whether this scale dependence can affect the analysis made so far. To do so, we will consider two different approaches:

- a collinear twist-3 evolution scheme, based on Refs. [150–153];
- a TMD-like  $Q^2$  evolution similar to the one described in Ref. [154].

As already mentioned in Section 2.2, in the collinear twist-3 approach, spin and transverse momentum correlations are included in the higher-twist collinear correlators. These functions have no probabilistic interpretation, but they represent quantum interferences between a collinear active quark state in the scattering amplitude and a collinear quark-gluon composite state in its complex conjugate amplitude. Moreover, there is no  $k_\perp$  dependence, since every intrinsic transverse momentum is integrated over. Therefore, twist-3  $Q^2$  evolution affects only the  $x$ -shape of distributions and fragmentation functions.

In the TMD factorisation approach, correlations between spin and intrinsic  $k_\perp$  are encoded in the TMD distributions or fragmentation functions, which preserve their probabilistic interpretation. Therefore,  $Q^2$  evolution affects their  $x$ -dependent part, as well as their  $k_\perp$ -shape.

Even if defined in a different context, TMDs and collinear quark-gluon correlation functions are closely related to each other. As we already mentioned in Section 2.1.1, the first  $k_\perp$  moment of the Sivers function is proportional to the collinear twist-3 quark-gluon correlation function  $T_{q,F}(x, x)$  [153], via a model independent relation [58]. Moreover, the evolution equations for the QS function are known. So, by adopting them in our study, it is possible to investigate possible signals of scale dependence in the Sivers data. Specifically, in the following we will adopt as initial scale for the evolution  $Q_0^2 = 1.2 \text{ GeV}^2$ , which coincides with the lowest  $Q^2$  value of the fitted experimental measurements.

The implementation of the collinear twist-3 evolution is made via the Higher Order Perturbative Parton Evolution Toolkit (HOPPET) code [155], properly modified to include the kernels corresponding to the Sivers function [156], that read [150–153]

$$\begin{aligned}
\frac{\partial T_{q,F}(x, x, \mu)}{\partial \log \mu^2} = & \frac{\alpha_s}{2\pi} \int_x^1 \frac{d\tilde{\xi}}{\tilde{\xi}} \left\{ P_{qq}(z) T_{q,F}(\tilde{\xi}, \tilde{\xi}, \mu) \right. \\
& + \frac{N_c}{2} \left[ \frac{1+z^2}{1-z} (T_{q,F}(\tilde{\xi}, x, \mu) - T_{q,F}(\tilde{\xi}, \tilde{\xi}, \mu)) + z T_{q,F}(\tilde{\xi}, x, \mu) + T_{\Delta q,F}(x, \tilde{\xi}, \mu) \right] \\
& - N_c \delta(1-z) T_{q,F}(x, x, \mu) \\
& \left. + \frac{1}{2N_c} [(1-2z) T_{q,F}(x, x - \tilde{\xi}, \mu) + T_{\Delta q,F}(x, x - \tilde{\xi}, \mu)] \right\}.
\end{aligned} \tag{3.9}$$

where  $z = x/\tilde{\xi}$  and  $T_{\Delta q,F}(x, x)$  is defined in Eq. (16) of Ref. [150]. We underline that we do not include off-diagonal terms in the twist-3 evolution case, as the QS function  $T_{q,F}(x_1, x_2)$  is not known for  $x_1 \neq x_2$ . This approximation should be enough for our purposes, since we will test whether current data can distinguish between a no-evolution approach (as in the reference fit) and another in which a scale dependence is included for the Siverts first moment.

The results of this “CT3-evolution fit” are presented in Table 3.3, where we can immediately notice a slight improvement of the  $\chi^2_{\min}$ , while Fig. 3.11 shows the comparison between the  $u$  and  $d$  Siverts first moments extracted in the reference best fit with no  $Q^2$  evolution (solid, black lines) and those extracted in the CT3-evolution fit (blue lines). The latter are plotted at three different values of  $Q^2$ :  $Q^2 = 1.2 \text{ GeV}^2$  (long-dashed) and  $Q^2 = 40 \text{ GeV}^2$  (dotted), that represent the lowest and largest  $Q^2$  values of the COMPASS measurements, and  $Q^2 = 3.5 \text{ GeV}^2$  (short-dashed), which is approximately the mean  $Q^2$  value of the full data sample.

Collinear twist-3 evolution		
$\chi^2_{\text{tot}} = 201.5$	n. of points = 220	
$\chi^2_{\text{dof}} = 0.94$	n. of free parameters = 5	
$\Delta\chi^2 = 11.3$		
HERMES	$\langle k_{\perp}^2 \rangle = 0.57 \text{ GeV}^2$	$\langle p_{\perp}^2 \rangle = 0.12 \text{ GeV}^2$
COMPASS	$\langle k_{\perp}^2 \rangle = 0.60 \text{ GeV}^2$	$\langle p_{\perp}^2 \rangle = 0.20 \text{ GeV}^2$
$N_u = 0.39 \pm 0.08$	$\beta_u = 3.55 \pm 1.26$	
$N_d = -0.65 \pm 0.27$	$\beta_d = 4.77 \pm 3.41$	
$\langle k_{\perp}^2 \rangle_S = 0.33 \pm 0.14 \text{ GeV}^2$		

Table 3.3: Best fit parameters and  $\chi^2$  values for the collinear twist-3 evolution case. The parameter errors correspond to  $2\sigma$  CL. Notice the reduced value of  $\chi^2_{\text{tot}}$  with respect to that of the reference fit in Table 3.1.

By looking at Fig. 3.11, we can notice that the central value of the functions extracted in the reference fit are quite analogous to those obtained using the collinear twist-3 evolution scheme at the experimental average value  $Q^2 = 3.5 \text{ GeV}^2$ . They are indeed very similar in the region that represents the bulk of data,  $0.03 < x < 0.3$ , while they grow progressively



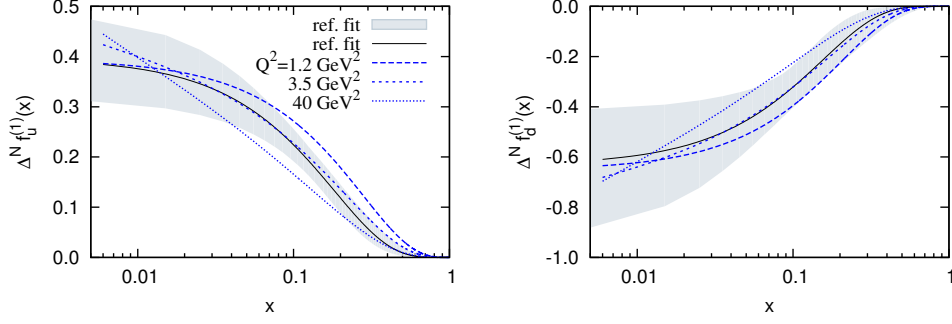


Figure 3.11: Extracted first moments of the Siverson function for  $u = u_v + \bar{u}$  (left panel) and  $d = d_v + \bar{d}$  (right panel). The results corresponding to the reference fit with no  $Q^2$  evolution (solid, black line) are compared to those obtained by applying a collinear twist-3 evolution (blue lines), as described in the text, for three values of  $Q^2$ :  $1.2 \text{ GeV}^2$  (long-dashed),  $3.5 \text{ GeV}^2$  (short-dashed) and  $40 \text{ GeV}^2$  (dotted). The bands correspond to the uncertainty on the reference fit with no  $Q^2$  evolution.

apart when  $Q^2$  varies to reach its lowest and largest values.

Bearing in mind that the whole  $Q^2$  dependence occurs only through  $x$ , leaving the  $k_\perp$  part of the Siverson function unchanged, we can draw some conclusions about signals of evolution in the data. As we see in Fig. 3.11, for the  $u$  flavour, we observe that the  $Q^2$  variation of the first moment due to the CT3 evolution is larger than the uncertainty band coming from the no-evolution reference fit. This could then represent a possible signal of evolution effects in the data, and it is a positive message about the precision of the data, specifically about the new binning of COMPASS asymmetries. We then observe an opposite situation for the  $d$  flavour which, as already observed in Section 3.2.2, is affected by a larger uncertainty. In fact, the  $Q^2$  variation of  $\Delta N_{f_{d/p^\uparrow}}^{(1)}$  lies into the error band of the reference fit. Again, an improved precision on the deuteron data by COMPASS would certainly help in exploring evolution effects for the  $d$ -quark Siverson function.

We can finally focus on TMD evolution effects. A proper Siverson extraction within a full TMD scheme is made by exploiting an “input function”, that is the value of the Siverson function at the initial scale  $Q_0^2$ . Then, a TMD factorisation scheme as the one described in in Ref. [46], and successively implemented in Refs. [154, 157], can be applied to compute the Siverson function at any larger value of  $Q^2$ .

Within this approach, the shape of TMD-PDFs and FFs changes in  $k_\perp$  as  $Q^2$  varies: more precisely, their  $k_\perp$ -distributions broaden and dilute as  $Q^2$  increases. While the TMDs themselves (and their first moments) experience variations in their  $x$ - and  $k_\perp$ -distributions as  $Q^2$  increases, these effects are expected to partially reduce in the azimuthal asymmetries, as they are essentially ratios of TMDs. Another complication of this type of analysis is the limited knowledge of the unpolarised functions in the kinematic region of the available Siverson asymmetries. In fact, recent studies have suggested that the errors of factorisation, at these kinematics, may not be under control [158–162]. This may affect all of the SIDIS analyses.

While waiting for further studies to clarify this situation, one may ask to what extent TMD-evolution effects are visible in the data. To pin down this issue, we slightly modify our model, giving a scale dependence to the width of the Siverson function,  $\langle k_\perp^2 \rangle_S$ , according to

$$\langle k_\perp^2 \rangle_S = g_1 + g_2 \ln \frac{Q^2}{Q_0^2}, \quad (3.10)$$



where  $g_1$  and  $g_2$  are two free parameters to be determined by a fit, and  $Q_0 = 1 \text{ GeV}$ .

This particular choice is a minimal attempt to mimick the mean feature of TMDs scale dependence, i.e. the broadening of the  $k_\perp$ -distribution with varying  $Q^2$ . Within the full TMD scheme, this feature is partly regulated by the non-perturbative, universal function  $g_K$  (see, for instance, Eq. (44) in Ref. [46]). Here we just use Eq. (3.10) as a proxy to study the sensitivity of the data to TMD effects, without making any precise correspondence between  $g_K$  and our parameter  $g_2$ . Indeed, a full implementation of evolution would require to go beyond a pure Gaussian dependence.

The values of the  $\chi^2$  and of the best fit parameters obtained within this “TMD-like fit” are presented in Table 3.4. We can instantly notice that the value of  $\chi^2_{\text{tot}}$  presents *no* reduction with respect to the reference fit one in Table 3.1, although one extra parameter has been added to the fit. So, we do not expect to see any major difference with respect to the results of the reference fit.

TMD-like fit		
$\chi^2_{\text{tot}} = 212.8$		n. of points = 220
$\chi^2_{\text{dof}} = 0.99$		n. of free parameters = 6
$\Delta\chi^2 = 12.9$		
HERMES	$\langle k_{\perp}^2 \rangle = 0.57 \text{ GeV}^2$	$\langle p_{\perp}^2 \rangle = 0.12 \text{ GeV}^2$
COMPASS	$\langle k_{\perp}^2 \rangle = 0.60 \text{ GeV}^2$	$\langle p_{\perp}^2 \rangle = 0.20 \text{ GeV}^2$
$N_u = 0.40 \pm 0.09$		$\beta_u = 5.42 \pm 1.70$
$N_d = -0.63 \pm 0.26$		$\beta_d = 6.45 \pm 3.89$
$\langle k_{\perp}^2 \rangle_s = g_1 + g_2 \log (Q^2/Q_0^2)$		
$g_1 = 0.28 \pm 0.29 \text{ GeV}^2$		$g_2 = 0.01 \pm 0.20 \text{ GeV}^2$

Table 3.4: Best fit parameters and  $\chi^2$  values for the TMD-like fit, in which our reference model is modified according to Eq. (3.10). The parameter errors correspond to  $2\sigma$  CL. Notice that there is *no* reduction in the value of  $\chi^2_{\text{tot}}$  with respect to that of the reference fit in Table 3.1.

It is interesting to take a look at the correlation between the  $g_1$  and  $g_2$  parameters. This is shown in Fig. 3.12, where we have the same colour-code as in the lower panels of Figs. 3.3 and 3.6. As it is clear both from this plot and the results in Table 3.4,  $g_1$  and  $g_2$  are both affected by a rather large uncertainty. Moreover, we note that the central value of  $g_1$  is quite close to the fitted value of the constant  $\langle k_\perp^2 \rangle_s$  of the reference fit, while its error is significantly increased. The correlation between the two parameters is strong and, provided that  $g_1$  is small enough, equally good descriptions of the data can be achieved by using very large and positive values of  $g_2$ . Paradoxically, even negative values of  $g_2$  are acceptable if  $g_1$  is allowed to grow large and positive, in such a way that the combination in Eq. (3.10) remains overall positive.

The situation described so far for the TMD-like fit is also confirmed by looking at the effects of TMD-like evolution on the  $k_\perp$ -distributions of the Sivers functions for  $u$  and  $d$  flavours. Fig. 3.13 shows indeed the two fitted Sivers functions at  $x = 0.1$ , with blue lines representing the Sivers function at three different  $Q^2$  values (the same used in Fig. 3.11 for the CT3-

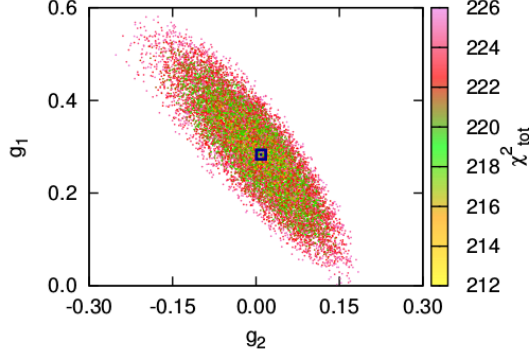


Figure 3.12: Scatter plots showing the correlation between the  $g_1$  and  $g_2$  free parameters of Eq. (3.10). The  $\chi^2_{\text{tot}}$  corresponding to this fit is colour-coded: yellow corresponds to its lowest values while red and purple to the highest accepted values. The black square corresponds to the fitted values of  $g_1$  and  $g_2$  of Table 3.4.

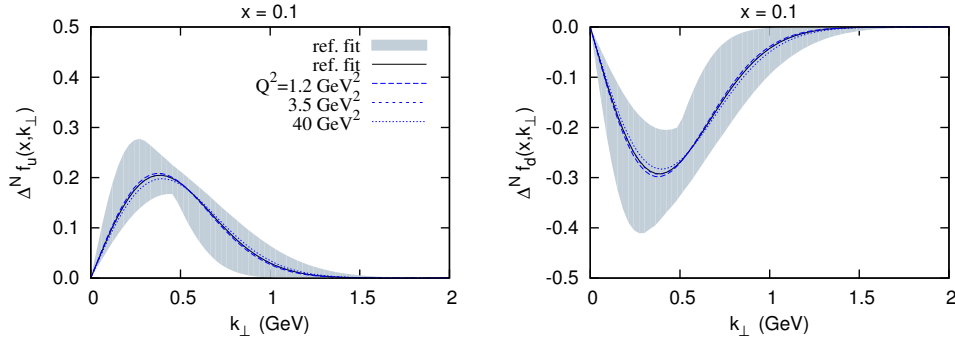


Figure 3.13: Extracted Sivers distributions for  $u = u_v + \bar{u}$  (left panel) and  $d = d_v + \bar{d}$  (right panel). The central line of our reference fit (solid black), is compared the Sivers function, extracted with the modified model according to Eq. (3.10), at a fixed value of  $x = 0.1$  (blue lines), for three values of  $Q^2$ :  $1.2 \text{ GeV}^2$  (long-dashed),  $3.5 \text{ GeV}^2$  (short-dashed) and  $40 \text{ GeV}^2$  (dotted). For comparison, we show the error bands corresponding to the reference fit with no  $Q^2$  evolution.

evolution fit). As expected, the small best fit value of  $g_2$  renders virtually no visible effect in the Sivers function. So, as partially expected, we can conclude that at the moment we do not observe in the data any TMD-like evolution effect for the Sivers function. Moreover, these results suggest that in a full TMD analysis, the current Sivers asymmetries will probably not constrain strongly the function  $g_K$ . On the other hand, due the large uncertainties on  $g_2$ , good compatibility between the Sivers asymmetries and the values of  $g_K$  extracted from other observables are likely to be achieved.

### 3.3 TRANSVERSITY DISTRIBUTION AND PION COLLINS FRAGMENTATION FUNCTIONS FROM SIDIS AND $e^+e^-$ DATA

In this Section we move to some *preliminary* results obtained in fits for the TMD transversity distribution and the Collins fragmentation functions for pions. Here we will particularly emphasise the role of the underlying assumptions, that represent, together with the choice of the model, the basis of every phenomenological analysis. Furthermore, we will concentrate on the impact of the outcome of a fit on other observables, that connect TMD physics to other areas of Particle Physics.

As already done in the previous Section, we will work in the GPM framework, using the Torino-Cagliari notation for the TMDs. The relations with the TMDs in Amsterdam notation

can be easily reobtained, e.g. for the Collins function, via Eqs. (2.21), (2.74) and (2.78). All the details that will be presented have as touchstone the global fit of pion Collins functions from SIDIS and  $e^+e^-$  data published in Ref. [116].

### 3.3.1 AZIMUTHAL CORRELATIONS IN $e^+e^- \rightarrow h_1 h_2 X$ PROCESSES

Before presenting some preliminary results, it is useful to take a look at the GPM expressions for the azimuthal correlations in  $e^+e^- \rightarrow h_1 h_2 X$  processes. We recall that, contrary to the Sivers case, where essentially we have only SIDIS data, independent information on the Collins functions can be obtained in unpolarised  $e^+e^-$  processes, by looking at the azimuthal correlations of hadrons produced in opposite jets [92]. As we have seen in Section 3.1, we have data from the Belle [143], BaBar [144] and BESIII [145] Collaborations, which have measured azimuthal hadron-hadron correlations for inclusive charged pion production in  $e^+e^- \rightarrow \pi\pi X$  processes. These correlations involve the convolution of two Collins function, and therefore can be interpreted as a direct measurement of the Collins effect.

Two different methods have been adopted in the experimental analysis of the  $e^+e^- \rightarrow h_1 h_2 X$  data [92, 143, 144, 163, 164]:

- (i) the “*thrust-axis method*”;
- (ii) the “*hadronic-plane method*”.

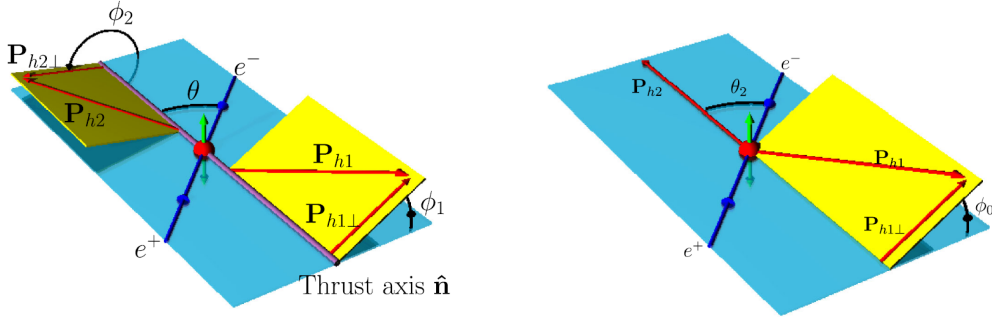


Figure 3.14: Kinematics of  $e^+e^- \rightarrow h_1 h_2 X$  processes. Left: thrust-axis method; right: hadronic-plane method. Figures are from Ref. [143].

In the thrust-axis method the jet thrust axis, in the  $e^+e^-$  c.m. frame, fixes the  $\hat{z}$  direction and the  $e^+e^- \rightarrow q\bar{q}$  scattering defines the  $\hat{x}\hat{z}$  plane; here,  $\phi_1$  and  $\phi_2$  ( $\phi_1$  and  $\phi_2$  in Fig. 3.14, respectively) are the azimuthal angles of the two hadrons around the thrust axis, while  $\theta$  is the angle between the lepton direction and the thrust axis. At leading order, in this simplified reference frame, and with unpolarised leptons, the cross section can be written as [116, 163]:

$$\begin{aligned}
 & \overline{d\sigma^{e^+e^- \rightarrow h_1 h_2 X}} \\
 & dz_1 dz_2 p_{\perp 1} dp_{\perp 1} p_{\perp 2} dp_{\perp 2} d\cos\theta d(\phi_1 + \phi_2) = \\
 & \frac{3\pi^2 \alpha_{em}^2}{s} \sum_q e_q^2 \left\{ (1 + \cos^2\theta) D_{h_1/q}(z_1, p_{\perp 1}) D_{h_2/\bar{q}}(z_2, p_{\perp 2}) \right. \\
 & \left. + \frac{1}{4} \sin^2\theta \Delta^N D_{h_1/q^\uparrow}(z_1, p_{\perp 1}) \Delta^N D_{h_2/\bar{q}^\uparrow}(z_2, p_{\perp 2}) \cos(\phi_1 + \phi_2) \right\}.
 \end{aligned} \tag{3.11}$$

By normalising Eq. (3.11) to the azimuthal averaged cross section,

$$\begin{aligned}\langle d\sigma \rangle &\equiv \frac{1}{2\pi} \frac{d\sigma^{e^+e^- \rightarrow h_1 h_2 X}}{dz_1 dz_2 p_{\perp 1} dp_{\perp 1} p_{\perp 2} dp_{\perp 2} d\cos\theta} \\ &= \frac{3\pi^2 \alpha_{em}^2}{s} \sum_q e_q^2 (1 + \cos^2\theta) D_{h_1/q}(z_1, p_{\perp 1}) D_{h_2/\bar{q}}(z_2, p_{\perp 2}),\end{aligned}\quad (3.12)$$

one can define a first ratio:

$$\begin{aligned}R_{12}(z_1, z_2, p_{\perp 1}, p_{\perp 2}, \theta, \varphi_1 + \varphi_2) \\ \equiv \frac{1}{\langle d\sigma \rangle} \frac{d\sigma^{e^+e^- \rightarrow h_1 h_2 X}}{dz_1 dz_2 p_{\perp 1} dp_{\perp 1} p_{\perp 2} dp_{\perp 2} d\cos\theta d(\varphi_1 + \varphi_2)} \\ = 1 + \frac{1}{4} \frac{\sin^2\theta}{1 + \cos^2\theta} \cos(\varphi_1 + \varphi_2) \frac{\sum_q e_q^2 \Delta^N D_{h_1/q^\uparrow}(z_1, p_{\perp 1}) \Delta^N D_{h_2/\bar{q}^\uparrow}(z_2, p_{\perp 2})}{\sum_q e_q^2 D_{h_1/q}(z_1, p_{\perp 1}) D_{h_2/\bar{q}}(z_2, p_{\perp 2})}.\end{aligned}\quad (3.13)$$

To eliminate false asymmetries, i.e. to correct for acceptance effects, one then takes the ratio of unlike-sign ( $\pi^+\pi^- + \pi^-\pi^+$ ) to like-sign ( $\pi^+\pi^+ + \pi^-\pi^-$ ) or charged ( $\pi^+\pi^+ + \pi^+\pi^- + \pi^-\pi^+ + \pi^-\pi^-$ ) pion pair production, denoted respectively with indices  $U$ ,  $L$  and  $C$ . For instance, in the case of unlike- to like-pair production, one has

$$\begin{aligned}\frac{R_{12}^U}{R_{12}^L} &= \frac{1 + \frac{1}{4} \cos(\varphi_1 + \varphi_2) \frac{\sin^2\theta}{1 + \cos^2\theta} P_U}{1 + \frac{1}{4} \cos(\varphi_1 + \varphi_2) \frac{\sin^2\theta}{1 + \cos^2\theta} P_L} \\ &\simeq 1 + \frac{1}{4} \cos(\varphi_1 + \varphi_2) \frac{\sin^2\theta}{1 + \cos^2\theta} (P_U - P_L) \\ &\equiv 1 + \cos(\varphi_1 + \varphi_2) A_{12}^{UL}(z_1, z_2, p_{\perp 1}, p_{\perp 2}, \theta),\end{aligned}\quad (3.14)$$

where

$$\begin{aligned}P_U &\equiv \frac{(P_U)_N}{(P_U)_D} = \\ &\frac{\sum_q e_q^2 [\Delta^N D_{\pi^+/q^\uparrow}(z_1, p_{\perp 1}) \Delta^N D_{\pi^-/\bar{q}^\uparrow}(z_2, p_{\perp 2}) + \Delta^N D_{\pi^-/q^\uparrow}(z_1, p_{\perp 1}) \Delta^N D_{\pi^+/\bar{q}^\uparrow}(z_2, p_{\perp 2})]}{\sum_q e_q^2 [D_{\pi^+/q}(z_1, p_{\perp 1}) D_{\pi^-/\bar{q}}(z_2, p_{\perp 2}) + D_{\pi^-/q}(z_1, p_{\perp 1}) D_{\pi^+/\bar{q}}(z_2, p_{\perp 2})]},\end{aligned}\quad (3.15)$$

$$\begin{aligned}P_L &\equiv \frac{(P_L)_N}{(P_L)_D} = \\ &\frac{\sum_q e_q^2 [\Delta^N D_{\pi^+/q^\uparrow}(z_1, p_{\perp 1}) \Delta^N D_{\pi^+/\bar{q}^\uparrow}(z_2, p_{\perp 2}) + \Delta^N D_{\pi^-/q^\uparrow}(z_1, p_{\perp 1}) \Delta^N D_{\pi^-/\bar{q}^\uparrow}(z_2, p_{\perp 2})]}{\sum_q e_q^2 [D_{\pi^+/q}(z_1, p_{\perp 1}) D_{\pi^+/\bar{q}}(z_2, p_{\perp 2}) + D_{\pi^-/q}(z_1, p_{\perp 1}) D_{\pi^-/\bar{q}}(z_2, p_{\perp 2})]},\end{aligned}\quad (3.16)$$

and the asymmetry reads

$$A_{12}^{UL}(z_1, z_2, p_{\perp 1}, p_{\perp 2}, \theta) = \frac{1}{4} \frac{\sin^2 \theta}{1 + \cos^2 \theta} (P_U - P_L). \quad (3.17)$$

Similarly, for  $A_{12}^{UC}(z_1, z_2, p_{\perp 1}, p_{\perp 2}, \theta)$  we have

$$A_{12}^{UC}(z_1, z_2, p_{\perp 1}, p_{\perp 2}, \theta) = \frac{1}{4} \frac{\sin^2 \theta}{1 + \cos^2 \theta} (P_U - P_C), \quad (3.18)$$

where

$$P_C = \frac{(P_U)_N + (P_L)_N}{(P_U)_D + (P_L)_D}. \quad (3.19)$$

In order to obtain the  $z_1, z_2$ -dependent asymmetries, in Eqs. (3.15) and (3.16), one has first to integrate separately numerators and denominators over  $p_{\perp 1}$  and  $p_{\perp 2}$ , and *then* calculate the ratios.

Differently from the thrust-axis method, in the hadronic-plane method one of the produced hadrons, e.g.  $h_2$ , identifies the  $\hat{z}$  direction, and the  $\hat{x}\hat{z}$  plane is determined by the lepton and the  $h_2$  directions; the other relevant plane is determined by  $\hat{z}$  and the direction of the other observed hadron,  $h_1$ , at an angle  $\phi_1$  ( $\phi_0$  in Fig. 3.14) with respect to the  $\hat{x}\hat{z}$  plane. Here  $\theta_2$  is the angle between  $h_2$  and the  $e^+e^-$  direction. In this reference frame, the elementary process  $e^+e^- \rightarrow q\bar{q}$  does not occur in the  $\hat{x}\hat{z}$  plane, and thus the helicity scattering amplitudes involve an azimuthal phase  $\varphi_2$  [116, 163]. The analogue of Eq. (3.11) now reads

$$\begin{aligned} \frac{d\sigma^{e^+e^- \rightarrow h_1 h_2 X}}{dz_1 dz_2 d^2\mathbf{p}_{\perp 1} d^2\mathbf{p}_{\perp 2} d\cos\theta_2} = & \\ \frac{3\pi\alpha_{em}^2}{2s} \sum_q e_q^2 \left\{ (1 + \cos^2\theta_2) D_{h_1/q}(z_1, p_{\perp 1}) D_{h_2/\bar{q}}(z_2, p_{\perp 2}) \right. & \\ \left. + \frac{1}{4} \sin^2\theta_2 \Delta^N D_{h_1/q^\dagger}(z_1, p_{\perp 1}) \Delta^N D_{h_2/\bar{q}^\dagger}(z_2, p_{\perp 2}) \cos(2\varphi_2 + \phi_q^{h_1}) \right\}, & \end{aligned} \quad (3.20)$$

where  $\phi_q^{h_1}$  is the azimuthal angle of the detected hadron  $h_1$  around the direction of the parent fragmenting quark,  $q$ . That is,  $\phi_q^{h_1}$  is the azimuthal angle of  $\mathbf{p}_{\perp 1}$  in the helicity frame of  $q$ . It can be expressed in terms of the following integration variables,  $\mathbf{p}_{\perp 2}$  and  $\mathbf{P}_{1T}$ , the transverse momentum of the  $h_1$  hadron. At lowest order in  $p_{\perp}/(z\sqrt{s})$  we have [116]

$$\begin{aligned} \cos\phi_q^{h_1} &= \frac{P_{1T}}{p_{\perp 1}} \cos(\phi_1 - \varphi_2) - \frac{z_1}{z_2} \frac{p_{\perp 2}}{p_{\perp 1}}, \\ \sin\phi_q^{h_1} &= \frac{P_{1T}}{p_{\perp 1}} \sin(\phi_1 - \varphi_2). \end{aligned} \quad (3.21)$$

The integration over  $\mathbf{p}_{\perp 2}$  is performed explicitly, using the parametrisation of the Collins function given in Eq. (6) of Ref. [116]. Moreover, as  $\mathbf{p}_{\perp 1} = \mathbf{P}_1 - z_1 \mathbf{q}_1$ , we can replace  $d^2\mathbf{p}_{\perp 1}$  with  $d^2\mathbf{P}_{1T}$ . We then obtain

$$\frac{d\sigma^{e^+e^- \rightarrow h_1 h_2 X}}{dz_1 dz_2 d^2 \mathbf{P}_{1T} d \cos \theta_2} = \frac{3\pi\alpha_{em}^2}{2s} \left\{ D_{h_1 h_2} + N_{h_1 h_2} \cos 2\phi_1 \right\}, \quad (3.22)$$

where

$$D_{h_1 h_2} = (1 + \cos^2 \theta_2) \sum_q e_q^2 D_{h_1/q}(z_1) D_{h_2/\bar{q}}(z_2) \frac{e^{-P_{1T}^2 / \langle \tilde{p}_\perp^2 \rangle}}{\pi \langle \tilde{p}_\perp^2 \rangle}, \quad (3.23)$$

$$N_{h_1 h_2} = \frac{1}{4} \frac{z_1 z_2}{z_1^2 + z_2^2} \sin^2 \theta_2 \sum_q e_q^2 \tilde{\Delta}^N D_{h_1/q^\uparrow}(z_1) \tilde{\Delta}^N D_{h_2/\bar{q}^\uparrow}(z_2) \\ \times \frac{2e P_{1T}^2}{\tilde{M}_C^2 + \langle \tilde{p}_\perp^2 \rangle} \frac{e^{-P_{1T}^2 (1/\tilde{M}_C^2 + 1/\langle \tilde{p}_\perp^2 \rangle)}}{\pi \langle \tilde{p}_\perp^2 \rangle}, \quad (3.24)$$

and

$$\tilde{M}_C^2 = M_C^2 \frac{(z_1^2 + z_2^2)}{z_2^2}, \quad \langle \tilde{p}_\perp^2 \rangle = \langle p_\perp^2 \rangle \frac{(z_1^2 + z_2^2)}{z_2^2}. \quad (3.25)$$

Note that the function  $\tilde{\Delta}^N D_{h/q^\uparrow}(z)$  is given by [116]

$$\tilde{\Delta}^N D_{h/q^\uparrow}(z, Q^2) = 2 \mathcal{N}_q^C(z, Q^2) D_{h/q}(z, Q^2), \quad (3.26)$$

and it is easy to verify, using the parametrisation of the Collins function in Eq. (2.78), together with Eq. (2.81), that

$$\tilde{\Delta}^N D_{h/q^\uparrow}(z) = 2 H_{1h/q}^\perp(z) = \frac{2z m_h M_C \langle p_\perp^2 \rangle}{\sqrt{\frac{e}{2}} \langle p_\perp^2 \rangle_C} H_{1h/q}^{\perp(1)}(z), \quad (3.27)$$

with  $H_{1h/q}^\perp(z)$  as defined in Eq. (A.10) of Ref. [122].

Again, to eliminate false asymmetries, unlike, like and charged combinations are built:

$$\begin{aligned} D^U &= D_{\pi^+ \pi^-} + D_{\pi^- \pi^+} & N^U &= N_{\pi^+ \pi^-} + N_{\pi^- \pi^+} \\ D^L &= D_{\pi^+ \pi^+} + D_{\pi^- \pi^-} & N^L &= N_{\pi^+ \pi^+} + N_{\pi^- \pi^-} \\ D^C &= D^U + D^L & N^C &= N^U + N^L, \end{aligned} \quad (3.28)$$

so that

$$P_0^{U,L,C} = \frac{N^{U,L,C}}{D^{U,L,C}}, \quad (3.29)$$

and finally

$$R_0^{U,L,C} = 1 + P_0^{U,L,C} \cos(2\phi_1). \quad (3.30)$$

As in the thrust-axis method case, ratios of unlike/like and unlike/charged asymmetries are built:

$$\begin{aligned}
\frac{R_0^U}{R_0^{L(C)}} &= \frac{1 + P_0^U \cos(2\phi_1)}{1 + P_0^{L(C)} \cos(2\phi_1)} \\
&\simeq 1 + (P_0^U - P_0^{L(C)}) \cos(2\phi_1) \\
&\equiv 1 + \cos(2\phi_1) A_0^{UL(C)},
\end{aligned} \tag{3.31}$$

and  $A_0^{UL(C)}$  is the quantity measured by the experimental Collaborations to which we directly compare with.

### 3.3.2 GLOBAL FIT OF TRANSVERSITY AND COLLINS FUNCTIONS AND ROLE OF THE SOFFER BOUND

We now head towards presenting a selection of preliminary results from a global fit of TMD transversity and pion Collins functions from SIDIS and  $e^+e^-$  data. We will see that, without making any major modification to the model, but just relaxing some initial assumptions, we can learn more about the data we are fitting, and we can also observe some interesting outcomes, that have an impact on the predictions for quantities like the isovector tensor charge, Eq. (2.4).

To completely set the ground, we underline that, with respect to Ref. [116], some slight modifications on the dataset and on collinear PDFs and FFs have been done. Specifically, the dataset is represented by all the available data for pions mentioned in Section 3.1, namely SIDIS azimuthal asymmetries from HERMES off a proton target [140] and COMPASS off proton [142] and deuteron [137] targets, and Belle [143], Babar [144] and BESIII [145] data for  $e^+e^- \rightarrow \pi\pi X$   $A_0^{UL(C)}$  azimuthal correlations. Moreover, in order to compute the Soffer bound, we adopt the most recent extraction of the collinear helicity distributions, namely the NLO DSSV set of Ref. [165]. For consistency, for the collinear PDFs and FFs we adopt the NLO CTEQ66 PDFs set [166] and the NLO DSS 2014 pion FFs set [167].

It is useful to briefly recall the parametrisation for the TMDs involved in this analysis. As usual, unpolarised TMD PDFs and FFs are parametrised according Eqs. (2.58) and (2.59). The corresponding Gaussian widths are fixed to the value obtained by fitting HERMES multiplicities in Ref. [114]:

$$\langle k_\perp^2 \rangle = 0.57 \text{ GeV}^2, \quad \langle p_\perp^2 \rangle = 0.12 \text{ GeV}^2. \tag{3.32}$$

For the TMD transversity function the functional form in Eqs. (2.71) and (2.72) is adopted. The transversity width is taken equal to the unpolarised one, i.e.  $\langle k_\perp^2 \rangle_T \equiv \langle k_\perp^2 \rangle$ , and, at the initial scale  $Q_0^2$ , the collinear part of transversity is parametrised in terms of the Soffer bound (SB), Eq. (2.2), as

$$\begin{aligned}
h_1^q(x, Q_0^2) &= \mathcal{N}_q^T(x, Q_0^2) SB(x, Q_0^2) \\
&= \mathcal{N}_q^T(x, Q_0^2) \frac{1}{2} \left[ f_{q/p}(x, Q_0^2) + g_{1L}^q(x, Q_0^2) \right].
\end{aligned} \tag{3.33}$$

Then, a transversity DGLAP kernel is employed to carry out the evolution up to the proper value of  $Q^2$ , by using an appropriately modified version of HOPPET [155]. The Soffer bound is built in by using the CTEQ66 and the DSSV helicity distributions at the input scale  $Q_0^2 =$



1.69 GeV<sup>2</sup>, with  $\alpha_s(M_Z) \simeq 0.118$  according to the CTEQ66 scheme. The  $\mathcal{N}_q^T(x)$  factor in Eq. (3.33) is now given by

$$\mathcal{N}_q^T(x) = N_q^T x^\alpha (1-x)^\beta \frac{(\alpha + \beta)^{\alpha + \beta}}{\alpha^\alpha \beta^\beta} \quad (q = u_v, d_v) \quad (3.34)$$

with the same  $\alpha$  and  $\beta$  parameters for  $u_v$  and  $d_v$  transversity functions. Thus, the transversity distributions depend on a total of four parameters:  $N_u^T, N_d^T, \alpha$  and  $\beta$ .

The Collins function is parametrised as in Eq. (2.74). More specifically, the  $\mathcal{N}^C(z)$  factors, Eq. (2.75), are the following: the favoured contribution reads

$$\mathcal{N}_{\text{fav}}^C(z) = N_{\text{fav}}^C z^\gamma (1-z)^\delta \frac{(\gamma + \delta)^{\gamma + \delta}}{\gamma^\gamma \delta^\delta}, \quad (3.35)$$

while the unfavoured contribution is simply

$$\mathcal{N}_{\text{unf}}^C(z) = N_{\text{unf}}^C. \quad (3.36)$$

The complete favoured and unfavoured pion Collins functions can be found in Eqs. (24), (25) of Ref. [116]. By adopting  $-1 \leq N_{\text{fav}}^C, N_{\text{unf}}^C \leq 1$ , the positivity bound for the Collins function is automatically satisfied. Furthermore, notice that the Collins functions evolve in  $Q^2$  through the collinear FFs. The free parameters for the Collins functions are then  $N_{\text{fav}}^C, N_{\text{unf}}^C, \gamma, \delta$  and  $M_C$ , the latter related to the Collins width via Eq. (2.79).

#### ROLE OF THE SOFFER BOUND AND ITS IMPACT ON THE TENSOR CHARGE

By requiring  $|N_{u_v(d_v)}^T| \leq 1$ , the transversity functions automatically satisfy the Soffer Bound. This choice has been always adopted in the past, e.g. in Refs. [116, 163, 164]. Relaxing this initial hypothesis allow us to test whether we do really observe the fulfillment of the Soffer bound in the data, as well as what is the impact of this choice on the tensor charge and the isovector tensor charge, Eqs. (2.3) and (2.4) respectively.

In order to tackle these issues, we performed two different extractions of transversity and Collins functions from a global fit of SIDIS and  $e^+e^-$  data, via usual  $\chi^2$  minimisation using MINUIT [149]. Numerical integration for  $e^+e^- z_1 z_2$ -dependent data is performed using the CUBA library [168]. These two fits have as basis the model presented at the beginning of the Section. The only difference is that in one we assume that transversity automatically fulfills the SB, with the constraint  $|N_{u_v(d_v)}^T| \leq 1$ , while in the other one no such constraint is imposed. That is, we assume that the transversity distribution is proportional to its SB at the initial scale  $Q_0^2$ , but we no longer ensure the automatic fulfillment when the function is evolved to higher values of  $Q^2$ . We stress that the results we are going to present are purely *preliminary*, and this issue should be pinned down in future studies.

Given its preliminary character, we do not present any numerical value of the fitted parameters. Moreover, we will not show any result on the Collins functions, as we checked that the extracted functions are completely compatible between the two fits and with respect to the latest one reported in Ref. [116]. This agreement is largely expected, since the only difference in the dataset is the addition of the latest BESIII data [145], that does not imply a change in the  $z$ - and  $p_\perp$ -shape of the Collins function. In the following, the results related to



the fit where the SB is automatically fulfilled are labeled as “using SB”, while the ones related to the fit with the relaxed assumption are labeled as “no SB”.

Fig. 3.15 shows the results of the two estimates. The extracted transversity functions for  $u_v$  and  $d_v$  flavours, together with their  $2\sigma$  CL uncertainty bands, are plotted at  $Q^2 = 2.4 \text{ GeV}^2$ . As in the Sivers fit case (see Section 3.2.1), the bands are computed according to the procedure described in the Appendix A of Ref. [113]. The Soffer bound at  $Q^2 = 2.4 \text{ GeV}^2$  for the two flavours is also shown, with a  $\pm 10\%$  variation representing an uncertainty estimate on their central values, while the grey areas are the ones outside the bulk of the data, that lies in the range  $0.035 < x < 0.278$ .

First of all, let us observe that, since the helicity distribution for the  $d_v$  quark flavour is negative, the corresponding SB results much more stringent with respect to the  $u_v$  one. So, in a fit, there is less room for the parameters to vary for giving the best fit shape. We also mention that, in the previous fits,  $N_{d_v}^T$  was basically always saturating its lower bound [116, 164]. On the left panel of Fig. 3.15, as expected, we observe two extracted functions that respect their SB, while on the right panel we can note the following:

- (i) while relaxing the constraint on  $N_{d_v}^T$ , the corresponding transversity function does not essentially change with respect to the one in the left panel;
- (ii) conversely, the transversity function for  $d_v$  flavour seems to violate its Soffer bound, especially in the region where data are present;
- (iii) while the uncertainty bands of the two extracted  $h_1^{u_v}$  are quite similar, there is a huge difference between the ones relative to  $h_1^{d_v}$ .

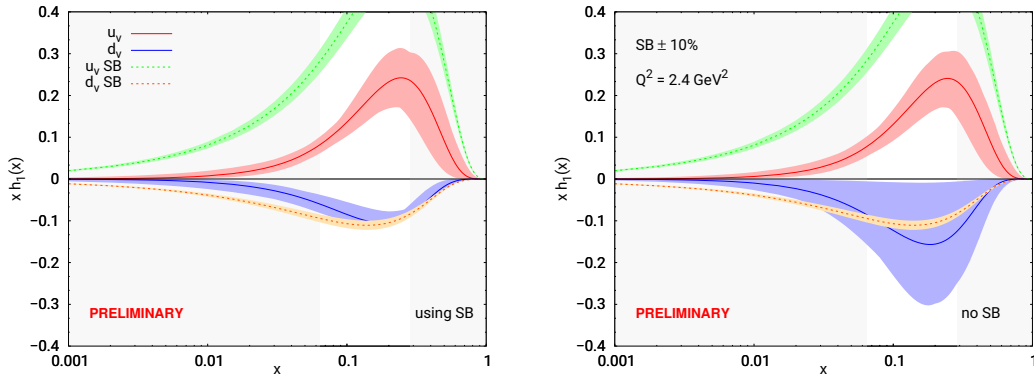


Figure 3.15: *Preliminary* results for transversity functions for  $u_v$  (red) and  $d_v$  (blue) flavours from a global fit to SIDIS and  $e^+e^-$  data at  $Q^2 = 2.4 \text{ GeV}^2$ . Left panel: results with automatic fulfillment of the Soffer Bound ( $|N_{u_v(d_v)}^T| \leq 1$ ). Right panel: results with no constraints on  $N_{u_v(d_v)}^T$ . Error bands on the fitted functions are at  $2\sigma$  CL. The corresponding Soffer bound, built with CTEQ66 [166] and DSSV [165], is also shown for  $u_v$  (green) and  $d_v$  (orange), together with a  $\pm 10\%$  variation. The white area represents the bulk of the data; outside that region no datapoints is present in the fit.

One may now wonder whether we are really observing a violation of the SB in the data. To have a rough quantitative estimate of this apparent violation, we can use a simple z-score to measure whether we are observing a statistically significant deviation from our zero hypothesis, i.e. the fulfillment of the SB by the  $d_v$  transversity function. The z-score is generally defined as

$$z = \frac{x - \mu}{\sigma}, \quad (3.37)$$

and tells us how many standard deviations  $\sigma$  we are far from the mean  $\mu$  for the point  $x$ . In the case of the extracted  $d_v$  transversity function, the  $z$  score is less than  $1\sigma$  (especially in the region where the uncertainty is large). Thus, statistically speaking, *no* violation of the Soffer bound is observed in the data. In other words, data are compatible with the hypothesis of fulfillment of the SB.

Furthermore, the huge difference in the uncertainty bands for the two  $d_v$  transversity functions is probably teaching us that the automatic imposition of the SB does not allow the minimiser to explore some configurations in the parameter space that are potentially compatible with the  $2\sigma$  CL we adopt, thus rendering an artificially small uncertainty band on the fitted function.

What is the effect of these extraction on the tensor charge? We recall that, upon integrating over the whole  $x$  range the collinear transversity function, we obtain the tensor charge  $\delta q$ , Eq. (2.3). Moreover, the difference between  $\delta u_v$  and  $\delta d_v$  represent an important quantity for BSM physics, the isovector tensor charge  $g_T$  [62–64]. It is useful to define truncated charges as follows:

$$\overline{\delta q} = \int_{x_{\min}}^{x_{\max}} [h_1^q(x) - h_1^{\bar{q}}(x)] dx, \quad (3.38)$$

$$\overline{g_T} = \overline{\delta u_v} - \overline{\delta d_v}, \quad (3.39)$$

i.e. charges calculated using as lower and upper limits the lowest and largest value of  $x$  in the data,  $x_{\min}$  and  $x_{\max}$  respectively.

The full tensor charges are calculated not only from phenomenology, but also by the lattice QCD community. In lattice QCD, the tensor charge is directly calculated as a matrix element over the full range of  $x$ ,  $0 \leq x \leq 1$ . Without entering into details, it is worth mentioning a tension observed between phenomenology and lattice QCD calculations. In fact,  $\delta u_v$  values from phenomenology seem to be incompatible with lattice ones, and  $g_T$  values calculated on the lattice are found to be higher than the ones in phenomenological analyses [169], approximately in the range  $0.95 \lesssim g_T \lesssim 1.1$ . For a comprehensive review of lattice results, see Ref. [170] and references therein. A summary of the lattice results for  $g_T$  at  $Q^2 = 4 \text{ GeV}^2$ , calculated with different discretisation schemes, lattice spacings and volumes is shown in Fig. 3.16.

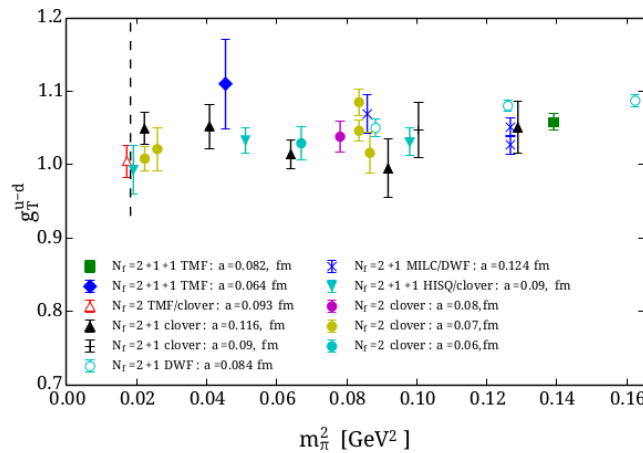


Figure 3.16: Collection of lattice QCD results for the isovector tensor charge  $g_T = \delta u_v - \delta d_v$ , at  $Q^2 = 4 \text{ GeV}^2$ . Note that the values lie approximately in the range  $0.95 \lesssim g_T \lesssim 1.1$ , and are computed with different discretisation schemes, lattice spacings and volumes. Figure is from Ref. [170].

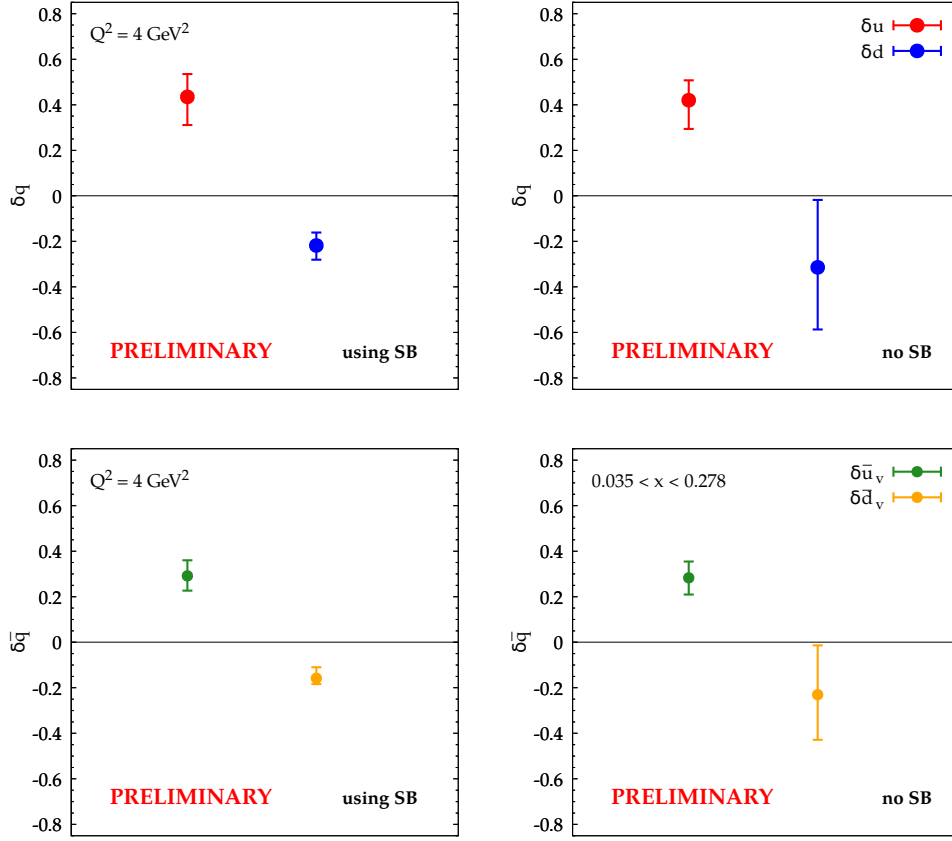


Figure 3.17: *Preliminary* results for tensor charges calculated using the transversity functions in Fig. 3.15 at  $Q^2 = 4 \text{ GeV}^2$ . Top panels: full tensor charges (integrated over the range  $0 < x < 1$ ) for  $u_v$  (red) and  $d_v$  (blue) flavours. Bottom panels: truncated tensor charges, integrated over the experimental  $x$  range ( $0.035 < x < 0.278$ ). Left panels: results based on the fit with automatic fulfillment of the Soffer Bound ( $|N_{u_v(d_v)}^T| \leq 1$ ); right panels: results with no constraints on  $N_{u_v(d_v)}^T$ . Error bars are calculated propagating the error on the fits at  $2\sigma$  CL.

How does the effect of relaxing the automatic fulfillment of the SB translate into the values of the tensor charges and the isovector tensor charge? Fig. 3.17 shows the results for the tensor charge at  $Q^2 = 4 \text{ GeV}^2$  calculated from integrating the extracted transversity functions of Fig. 3.15. The upper panels show the results for the full tensor charges for  $u_v$  (red) and  $d_v$  (blue) flavours, while the lower panels are related to the truncated tensor charges, Eq. (3.38), for  $u_v$  (green) and  $d_v$  (orange). Moreover, the left panels represent the results of the fit with automatic fulfillment of the SB, while the ones on the right are relative to the “no SB” fit. The chosen  $Q^2$  value is intended to be used for a comparison with lattice measurements. We will not show results at different  $Q^2$  values, since this would not add more information to the message we would like to deliver with these tests.

From Fig. 3.17 we can notice that, while the  $u_v$  tensor charge seems not to be affected by the change in the initial hypothesis on the SB,  $\delta d_v$  presents quite a large variation, both for its central value and its error bar. Indeed, the error bar for the “no SB” fit is much larger than the one for the other fit. This huge variation reflects the observed enlargement of the uncertainty affecting the  $d_v$  transversity function.

The difference in the computed values of  $\delta u_v$  and  $\delta d_v$  consequently translates into a different value and, more importantly, a different uncertainty for  $g_T$ . Fig. 3.18 shows the results for

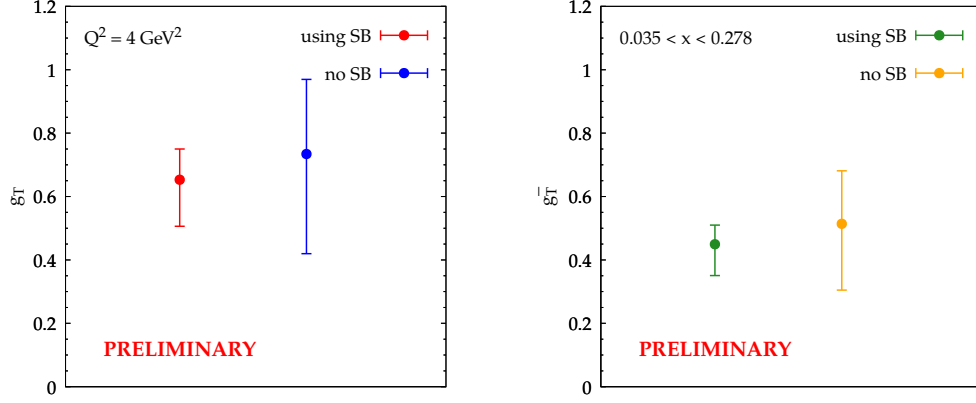


Figure 3.18: *Preliminary* results for the isovector tensor charge calculated using the fitted transversity functions in Fig. 3.15 at  $Q^2 = 4 \text{ GeV}^2$ . Left panel: full isovector tensor charges (calculated over the range  $0 < x < 1$ ) for constrained fit with Soffer Bound (red) and unconstrained fit (blue). Right panel: truncated isovector tensor charges, calculated over the experimental  $x$  range ( $0.035 < x < 0.278$ ); colour code is the same as the left panel. Error bars are calculated propagating the error on the fits at  $2\sigma$  CL.

the isovector tensor charge, calculated over the full  $x$ -range (left panel) and over the range covered by the data used in the fit (right panel). The red (green) point on the left (right) panel is related to the (un)constrained fit, while the blue (orange) one is related to the “no SB” extraction.

As expected, we can note that the larger uncertainty band on  $h_1^{d_v}$  generates a larger error over the isovector tensor charge  $g_T$ , both over the full one and the truncated one. This fact has a twofold meaning: even if the uncertainty grows, we actually get an error band that covers the region where lattice QCD results lie. That is, a larger uncertainty signals a relaxation of the tension between phenomenology and lattice QCD estimates, or in other words, a compatibility between these two results.

A word of caution and some comments are in order. From a certain point of view, all these results seem to be promising. Nonetheless, we need to bear in mind that, since the  $x$  range in which experimental datapoints are present is limited, all the results for the full tensor charges and isovector tensor charge are obtained by performing an *extrapolation* outside this range. Extrapolations depend of course on the model and all the assumptions made at the beginning of any phenomenological analysis. So, again, we see that even a slight modification in the initial hypotheses can lead to very different results and, in turn, very different interpretations. Moreover, let us stress that lattice calculations also need their assumptions, and that are for matrix elements over the full range of  $x$ . Therefore, the comparison between phenomenological and lattice results should be always done prudently.

On the other hand, we showed that, with a more agnostic approach, we can interrogate the data about our theoretical expectations. We know indeed that the Soffer bound should be preserved by the  $Q^2$  evolution at higher orders [171]. Based on our observation, we can say that the expectation seems to be satisfied by the data, at least considering the effect of  $Q^2$  evolution. Of course, in order to stress-test the theory, more data over a broader  $x$ -range are needed. Again, the future EIC [76] would be an ideal tool to pursue this issue, but also an enhanced precision on SIDIS Collins measurements off deuteron targets would help in further constraining the  $d_v$  transversity function and, consequently, would offer stronger constraints on  $g_T$ .

### 3.4 OUTLOOK OF THE CHAPTER

To close this Chapter, let us make some final remarks about the work presented in Sections 3.2 and 3.3.

As we emphasised at the beginning of Section 3.1, we are at a relatively early stage of TMD extractions. So, as we have seen in the past Sections, phenomenological analyses may render some counterintuitive results, making their final interpretation quite involved. Moreover, we have seen that any assumption made for a model can somehow bias the analysis (e.g. the artificially small error bands for transversity, see Fig. 3.15).

We believe that the work presented in Ref. [120] and the preliminary results presented in Section 3.3 can give a more agnostic point of view that, in the spirit of a careful data analysis, would help to test in a deeper way any theoretical expectation we have about TMD effects.

Regarding the quark Sivers function, we have showed that, even with a very small amount of parameters, we are able to describe the current data on SIDIS azimuthal asymmetries. Moreover, we have shown that the usage of datasets that contain a higher amount of information, e.g. a  $Q^2$  binning as in the latest COMPASS data, helps in making more refined studies, that include a scale dependence. Future projections for deuteron data are also promising for reducing the uncertainties on the extracted  $d$ -quark Sivers function. A word of caution is in order: the kinematical range covered at the moment by the experiments is not enough to discriminate between different models. We are anyway confident that, in the future, new data coming from future experiments, such as the future Electron-Ion Collider, COMPASS and JLab at 12 GeV will help us to go further in phenomenological extractions of the Sivers function.

Other interesting results, although preliminary, have also shown that, by relaxing an initial hypothesis on the parametrisation of the transversity distributions, we obtain a more accurate error estimate, reducing the existent tension between phenomenology and lattice calculations for the isovector tensor charge. Moreover, it allow us to further test our theoretical expectations, like the validity of the Soffer bound for transversity at different  $Q^2$  scales. The latter hypothesis is indeed compatible with the current data. Finally, we remark that, while comparing lattice results and calculations made on the basis of phenomenological extractions, it would be useful to stress that extrapolations are present, and that the truncated charges are the only quantities on which we really have information, based on the kinematical coverage of the experiments.

# 4

## Pinning down the gluon Sivers function(s)

Recalling what we stated in Section 2.1, TMD gluon distributions are surely the TMDs on which our knowledge is currently limited the most. Nevertheless, TMD community is very attracted by studying these functions, and future experiments will have a very important role in tackling these distributions [60, 74–77, 79, 80, 172].

In this Chapter we will concentrate only on one of the eight independent gluon TMDs, the poorly known gluon Sivers function (GSF). Specifically, we will see how we can estimate its size by using  $A_N$  data for inclusive  $p^\uparrow p$  processes, measured in a specific kinematic region, where its contribution to the single-spin asymmetries is the dominant one. Moreover, we will also see that, by using an extended version of the GPM, the Colour Gauge invariant GPM [109, 173, 174], where *two* independent GSFs are defined, one can constrain their size by using two or more independent datasets, trying also to discriminate between the two GPM versions.

### 4.1 COLOUR GAUGE INVARIANT GENERALISED PARTON MODEL

In this Section we briefly review the so-called *Colour Gauge Invariant Generalised Parton Model*. This GPM modification has been introduced in Ref. [109] for quarks, and then extended to the gluon case in Refs. [110, 175] for inclusive hadron and photon production in  $p^\uparrow p$  collisions.

In this model, initial- and final-state interactions (ISIs and FSIs) between the struck quark and the spectators from the polarised proton are taken into account via a single, eikonal gluon exchange approximation, i.e. the leading order contribution, in an expansion in the coupling constant  $g$ , to the gauge link used in the definition of a gauge invariant TMD-PDF. It is then the imaginary part of the eikonal propagator that provides the phase needed to generate the asymmetry. In doing this, the process dependence of the Sivers function, Eq. (2.10), is recovered. One then can keep it formally in the function itself, defining a process dependent Sivers function,  $f_{1T}^{\perp a, ab \rightarrow cd}$ , or shift it to the partonic cross sections, that are then modified with proper colour factors.

It is worth noticing that, within the CGI-GPM, quark and gluon cases present some differences. While the process dependence of the Sivers function can be absorbed into the partonic hard functions in both cases, the number of independent Sivers functions is different. In fact, in the quark case, we still have one independent quark Sivers function, that is assumed to

be the one from SIDIS data. However, in the gluon case, one has to introduce *two* universal, totally independent Sivvers functions, because of the two different ways of forming a colour-singlet state for three coloured gluons. Specifically, there are the totally antisymmetric colour combination, even under charge conjugation, that is commonly referred to as an *f*-type state, while the symmetric combination, odd under C-parity, is referred to as a *d*-type state. Correspondingly, an *f*-type and a *d*-type GSFs are introduced. Note that these two independent GSFs are related, at least at tree level, to the two distinct twist-3 trigluon Qiu-Sterman functions  $T_G^{(f/d)}$  [176, 177], from which they inherit their name. For a comprehensive review illustrating the properties of these GSFs, we refer the reader to Ref. [172].

#### 4.1.1 INITIAL AND FINAL STATE INTERACTIONS: AN EXAMPLE

All the details regarding the quark case can be found in Ref. [109]. Here, to illustrate the way these two independent GSFs emerge, we minimally report the outline of the calculations for the simpler  $p^\uparrow p \rightarrow \gamma X$  process, where we will see that only ISIs contribute. To do that, we follow the computation outlined in Refs. [109, 110].

For  $p^\uparrow p \rightarrow \gamma X$ , the only partonic process sensitive to the gluon Sivvers effect is

$$g(p_a) + q(p_b) \rightarrow \gamma(p_c) + q(p_d), \quad (4.1)$$

where the particles four-momenta are given between brackets. At leading order in perturbative QCD, this process is described by the Feynman diagrams in Figs. 4.1a–4.1d. All these diagrams have the same colour structure and contribute to the unpolarised cross section, that is the denominator of the Sivvers contribution to  $A_N$ , with the same colour factor

$$C_U = \frac{1}{2N_c}, \quad (4.2)$$

with  $N_c$  being the number of colours.

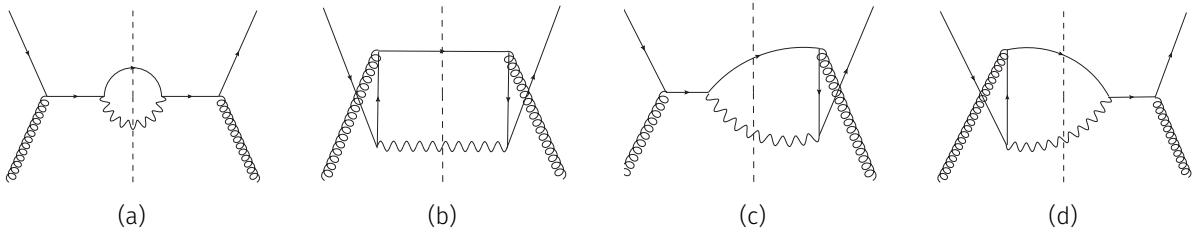


Figure 4.1: Cut diagrams for the partonic process  $gq \rightarrow \gamma q$  at LO in perturbative QCD. Feynman diagrams are made with Jaxodraw [178, 179].

In order to show how the ISIs and FSIs are taken into account within the CGI-GPM, let us consider for instance the ISIs for the diagram in Fig. 4.1a. The gauge link is approximated by an insertion of a single, eikonal gluon. This insertion is represented by a longitudinally polarised gluon  $A^+$ , with momentum  $k^\mu \approx k^+$  and colour index  $c$ , as depicted in Fig. 4.2a. The corresponding amplitude, assuming massless fermions, is calculated from the Born one, by making the following replacement for the spinor of parton  $b$ ,  $u(p_b)$ :



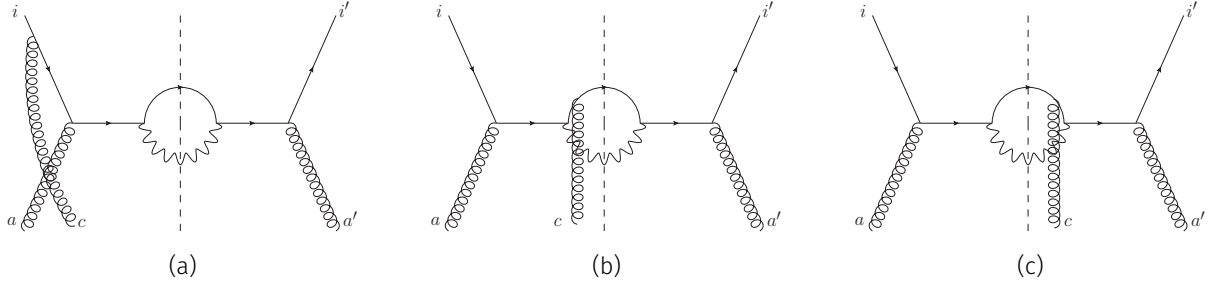


Figure 4.2: Initial and final state interactions in  $gq \rightarrow \gamma q$  for the cut diagram in Fig. 4.1a: (a) initial state interactions, (b)-(c) final state interactions for the undetected parton  $d$ . Colour indices are shown. Feynman diagrams are made with Jaxodraw [178, 179].

$$\begin{aligned}
u(p_b) &\rightarrow -ig \frac{i(\not{p}_b + \not{k})}{(p_b + k)^2 + i\epsilon} \gamma^- t^c u(p_b) \\
&\approx g \frac{\not{p}_b}{2p_b^- k^+ + i\epsilon} \gamma^- t^c u(p_b) \\
&\approx g \frac{-\gamma^- \not{p}_b + 2p_b^-}{2p_b^- k^+ + i\epsilon} t^c u(p_b) \\
&= g \left[ \frac{1}{k^+ + i\epsilon} \right] t^c u(p_b),
\end{aligned} \tag{4.3}$$

where  $t^c$  are the generators of  $SU(N_c)$  in the fundamental representation. Since we are interested in the pole of the propagator at  $k^+ = 0$ , in the second line of Eq. (4.3) we have neglected the term  $\not{k} \approx k^+ \gamma^-$ . Furthermore, in the last step of the calculation, we have used the Dirac equation for massless fermions  $\not{p}_b u(p_b) = 0$ . By using the following relation

$$\frac{1}{k^+ \pm i\epsilon} = \text{P} \frac{1}{k^+} \mp i\pi\delta(k^+), \tag{4.4}$$

where P refers to the principal value, we find that the imaginary part of the quark propagator,  $1/(k^+ + i\epsilon)$ , is given by  $-i\pi\delta(k^+)$ . While calculating the full diagram, such term is multiplied by the Born amplitude, taken with a different colour factor because of the extra gluon attachment. The new colour factor can be computed by adopting the methods described in Refs. [176, 177, 180], that have been developed in the collinear twist-3 framework for the three-gluon correlation functions.

Recalling that, since we have two ways to neutralise the colour, i.e. with symmetric and antisymmetric structure constants of the colour group  $SU(N_c)$ , two different kinds of modified colour factors will emerge, corresponding to the two independent gluon Sivers functions, the  $f$ - and  $d$ -type ones. For the  $f$ -type GSF, the colour is neutralised by  $(T^c)_{aa'} = -if_{caa'}$ , where  $f_{caa'}$  are the fully antisymmetric structure constants for  $SU(N_c)$ , and the corresponding colour factor is computed by contracting the colour indices of the diagram in Figs. 4.2a–4.2c with the colour projector (see Appendix C for the colour rules for the projectors)

$$\mathcal{T}_{aa'}^c = \mathcal{N}_{\mathcal{T}} (T^c)_{aa'}, \tag{4.5}$$



where the normalisation factor  $\mathcal{N}_{\mathcal{T}}$  is given by [181]

$$\mathcal{N}_{\mathcal{T}} = \frac{1}{\text{Tr}(T^c T^c)} = \frac{1}{N_c (N_c^2 - 1)}. \quad (4.6)$$

Therefore, the modified  $f$ -type colour factor for Fig. 4.2a is given by [175]

$$\begin{aligned} C_I^{(f)} &= \mathcal{T}_{aa'}^c (t^c)_{ji} (t^a)_{kj} (t^{a'})_{i'k} \frac{\delta^{ii'}}{N_c} \\ &= \frac{1}{N_c (N_c^2 - 1)} (T^c)_{aa'} \text{Tr}(t^c t^{a'} t^a) \\ &= -\frac{1}{4N_c^2 (N_c^2 - 1)} \text{Tr}(T^c T^c) \\ &= -\frac{1}{4N_c}. \end{aligned} \quad (4.7)$$

In deriving the last result, Eq. (4.7), the following relations have been used [181]:

$$\text{Tr}(t^a t^b t^c) = \frac{1}{4} [(D^a)_{bc} - (T^a)_{bc}], \quad \text{Tr}(T^a D^b) = 0, \quad \text{Tr}(T^a T^b) = N_c \delta^{ab}, \quad (4.8)$$

where  $(D^a)_{bc} = d_{abc}$  are the symmetric structure constants of  $SU(N_c)$  and  $\delta^{ab}$  is the Kronecker delta.

To calculate the modified colour factor for the  $d$ -type GSF, we need to contract the colour indices of the same Feynman diagram with another projector:

$$\mathcal{D}_{aa'}^c = \mathcal{N}_{\mathcal{D}} (D^c)_{aa'}, \quad (4.9)$$

where now [181]

$$\mathcal{N}_{\mathcal{D}} = \frac{1}{\text{Tr}(D^c D^c)} = \frac{N_c}{(N_c^2 - 4) (N_c^2 - 1)}. \quad (4.10)$$

The corresponding colour factor is then [175]

$$\begin{aligned} C_I^{(d)} &= \mathcal{D}_{aa'}^c (t^c)_{ji} (t^a)_{kj} (t^{a'})_{i'k} \frac{\delta^{ii'}}{N_c} \\ &= \frac{N_c}{(N_c^2 - 4) (N_c^2 - 1)} (D^c)_{aa'} \text{Tr}(t^c t^{a'} t^a) \\ &= \frac{N_c}{4 (N_c^2 - 4) (N_c^2 - 1)} \text{Tr}(D^c D^c) \\ &= \frac{1}{4N_c}. \end{aligned} \quad (4.11)$$

It is easy to verify that, by repeating the same calculation for all the other Born diagrams in Figs. 4.1b–4.1d, the same colour factors  $C_I^{(f/d)}$  are obtained.

What about the final state interactions in Figs. 4.2b–4.2c? One can show that, in the case of  $p^\uparrow p \rightarrow \gamma X$ , no FSI contribution to the polarised cross section is present. In fact, since the photon does not interact with the remnant of the polarised hadron, i.e. the eikonal gluon, trivially  $C_{F_c}^{(f/d)} = 0$ . Moreover, parton  $d$  is not observed, and so it also holds  $C_{F_d}^{(f/d)} = 0$ . This last point is actually a general property of inclusive processes. For instance, it can be explained noticing that in the computation one has to take into account both diagrams in Figs. 4.2b–4.2c, that have the same topology apart from the fact that, in one of them, parton  $d$  is on shell with  $p_d^2 = m_d^2$ , while in the other one  $d$  is off shell with  $(p_d - k)^2 = m_d^2$ . Since  $d$  is undetected, one should consider both cases. It turns out that the pole contributions of the two diagrams cancel [109, 176, 177]. To see it explicitly, we have respectively from Figs. 4.2b–4.2c that:

$$\begin{aligned} -ig t^c \bar{u}(p_d) \gamma^- \frac{i(\not{p}_d - \not{k})}{(p_d - k)^2 + i\epsilon} \delta(p_d^2) &\approx g t^c \bar{u}(p_d) \left[ \frac{1}{-k^+ + i\epsilon} \right] \delta(p_d^2) \\ &\rightarrow -i\pi \delta(p_d^2) \delta(k^+) \times \frac{C_{F_d}^{(f/d)}}{C_U} \times [\text{BornAmplitude}], \end{aligned} \quad (4.12)$$

and

$$\begin{aligned} -ig \frac{i\not{p}_d}{p_d^2 - i\epsilon} \gamma^- t^c u(p_d - k) \delta((p_d - k)^2) &\approx g \left[ \frac{1}{p_d^2 - i\epsilon} \right] t^c u(p_d) \delta(k^+) \\ &\rightarrow +i\pi \delta(p_d^2) \delta(k^+) \times \frac{C_{F_d}^{(f/d)}}{C_U} \times [\text{BornAmplitude}], \end{aligned} \quad (4.13)$$

with

$$C_{F_d}^{(f)} = C_{F_d}^{(d)} = \frac{1}{4N_c}. \quad (4.14)$$

So, they cancel out as expected.

Moving now to the  $g\bar{q} \rightarrow \gamma\bar{q}$  process, whose corresponding Feynman diagrams are obtainable by reversing the arrows direction in Figs. 4.1a–4.1d, we can compute as before the colour factors for initial and final state interactions,  $C_I^{(f/d)}$  and  $C_{F_d}^{(f/d)}$ , by reversing the fermion lines in the diagrams in Figs. 4.2a–4.2b, respectively. This leads to an important consequence: the pole contributions to the imaginary part will have opposite signs with respect to the quark case. So, it can be shown that [175]

$$C_I^{(f)} = \frac{1}{4N_c} \quad C_I^{(d)} = -\frac{1}{4N_c} \quad C_{F_d}^{(f)} = -\frac{1}{4N_c} \quad C_{F_d}^{(d)} = -\frac{1}{4N_c}, \quad (4.15)$$

which all have opposite signs as compared to the  $gq \rightarrow \gamma q$  case.

As a cross check, it is useful to calculate the *gluonic pole strengths* defined as [182]

$$C_G = \frac{C_I + C_{F_c} + C_{F_d}}{C_U} = \frac{C_I + C_{F_d}}{C_U} \quad (4.16)$$

and compare them with the ones given in Table B.4 of Ref. [183] for  $gq \rightarrow \gamma q$ .

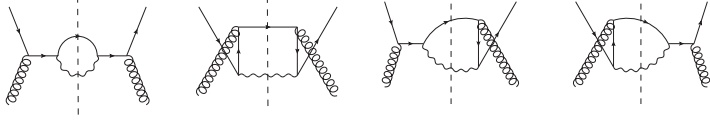
$D$	$C_U$	$C_I^{(f)}$	$C_{F_d}^{(f)}$	$C^{\text{Inc}(f)}$	$C_I^{(d)}$	$C_{F_d}^{(d)}$	$C^{\text{Inc}(d)}$
	$\frac{1}{2N_c}$	$-\frac{1}{4N_c}$	$\frac{1}{4N_c}$	$-\frac{1}{4N_c}$	$\frac{1}{4N_c}$	$\frac{1}{4N_c}$	$\frac{1}{4N_c}$

Table 4.1: Colour factors for the LO diagrams contributing to the process  $gq \rightarrow \gamma q$  [175].  $C_U$  is the unpolarised colour factor for the diagram  $D$ , while  $C_I$ ,  $C_{F_c}$  and  $C_{F_d}$ , respectively for the  $f$ - and  $d$ -type, are the colour factors obtained when an extra gluon is attached in  $D$  to parton  $b$  ( $C_I$ ), parton  $c$  ( $C_{F_c}$ ) or parton  $d$  ( $C_{F_d}$ ). Furthermore,  $C^{\text{Inc}} = C_I + C_{F_c}$ .  $C_{F_c}$  factors are not presented, as they are all zero in this case (no interaction between the photon and the polarised proton remnants). For the  $g\bar{q} \rightarrow \gamma\bar{q}$  process, the  $f$ -type colour factors are the same, while the  $d$ -ones have an overall minus sign.

The two calculations, while adopting two different methods<sup>1</sup> agree, giving

$$C_G^{(f)} = 0, \quad C_G^{(d)} = 1. \quad (4.17)$$

This shows that the one-gluon approximation is enough to recover the exact gluonic pole strengths in any partonic process calculated at leading order in perturbative QCD [182].

All the colour factors for the  $gq \rightarrow \gamma q$  process are listed in Table 4.1. For the partonic subprocess involving antiquarks,  $g\bar{q} \rightarrow \gamma\bar{q}$ , the  $f$ -type colour factors are the same, while the  $d$ -ones have an overall minus sign.

#### HARD FACTORS AND SINGLE-SPIN ASYMMETRIES IN $p^\uparrow p \rightarrow \gamma X$

After having computed the modified colour factors, we can now present the results obtained for the hard factors and the numerator of  $A_N$  related to the gluon Siverts effect. Schematically, the latter quantity for an inclusive process is generally written in the GPM as [110, 175, 184]

$$d\Delta\sigma \propto \sum_{abcd} \left( -\frac{k_{\perp a}}{M_p} \right) f_{1T}^{\perp a}(x_a, k_{\perp a}) \cos \phi_a \otimes f_{b/p}(x_b, \mathbf{k}_{\perp b}) \otimes H_{ab \rightarrow cd}^U \otimes D_{h/c}(z, \mathbf{p}_{\perp}), \quad (4.18)$$

where, as seen in Section 2.3.1,  $\otimes$  indicates a convolution over light-cone momentum fractions and over transverse momenta. In the case of inclusive photoproduction,  $D_{h/c}(z, \mathbf{p}_{\perp})$  is replaced by  $\delta(1-z)\delta^2(\mathbf{p}_{\perp})$  in Eq. (4.18). The hard functions  $H_{ab \rightarrow cd}^U$  are related to the usual unpolarised partonic cross section for  $ab \rightarrow cd$  subprocesses, and can be calculated perturbatively.

Formally, when parton  $a$  inside the polarised proton is either a quark or an antiquark ( $a = q$ ), the numerator of  $A_N$  in the CGI-GPM is obtained from Eq. (4.18) by performing the following substitution [109]:

$$f_{1T}^{\perp q} \otimes H_{qb \rightarrow cd}^U \rightarrow f_{1T}^{\perp q} \otimes H_{qb \rightarrow cd}^{\text{Inc}}, \quad (4.19)$$

where the modified partonic functions, denoted by  $H_{qb \rightarrow cd}^{\text{Inc}}$  are obtained by using the tech-

<sup>1</sup>Results in Ref. [183], have been derived by looking at the full gauge link structure and taking the derivative of the gauge link.

niques presented in Ref. [109].

As already mentioned, when parton  $a$  is a gluon, we have two independent gluon Sivers functions, the  $f$ - and  $d$ -type GSFs. Differently from Eq. (4.19), here the GSF contribution of the GPM is replaced by a linear combination of the  $f_{1T}^{\perp g(f/d)}$ , as [110, 175, 184]

$$f_{1T}^{\perp g} \otimes H_{gb \rightarrow cd}^U \rightarrow f_{1T}^{\perp g(f)} \otimes H_{gb \rightarrow cd}^{\text{Inc}(f)} + f_{1T}^{\perp g(d)} \otimes H_{gb \rightarrow cd}^{\text{Inc}(d)}. \quad (4.20)$$

The  $H_{ab \rightarrow cd}^{\text{Inc}(f/d)}$  are the hard factors with modified colour factors, calculated following the rules presented in Section 4.1. In the case of inclusive processes, they are related to the unpolarised hard factors  $H_{ab \rightarrow cd}^U$  by

$$H_{ab \rightarrow cd}^{\text{Inc}(f/d)} = \frac{C^{\text{Inc}(f/d)}}{C_U} H_{ab \rightarrow cd}^U \equiv \frac{C_I^{(f/d)} + C_{F_c}^{(f/d)}}{C_U} H_{ab \rightarrow cd}^U. \quad (4.21)$$

Using the modified hard functions, we can then write more explicitly the cross section in Eq. (4.18) as [175]

$$\begin{aligned} d\Delta\sigma^{\text{CGI-GPM}} &= \frac{E_\gamma d\sigma^\uparrow}{d^3\mathbf{p}_\gamma} - \frac{E_\gamma d\sigma^\downarrow}{d^3\mathbf{p}_\gamma} \simeq \frac{2\alpha_{em}\alpha_s e_q^2}{s} \sum_{abd} \int \frac{dx_a dx_b}{x_a x_b} d^2\mathbf{k}_{\perp a} d^2\mathbf{k}_{\perp b} \\ &\times \left( -\frac{k_{\perp a}}{M_p} \right) f_{1T}^{\perp a}(x_a, k_{\perp a}) \cos\phi_a f_{b/p}(x_b, k_{\perp b}) \\ &\times H_{ab \rightarrow \gamma d}^{\text{Inc}}(x_a, x_b, \hat{s}, \hat{t}, \hat{u}) \delta(\hat{s} + \hat{t} + \hat{u}), \end{aligned} \quad (4.22)$$

where  $a = q, \bar{q}, g$ . As we have showed that, in the case of inclusive  $\gamma$  production there is no FSI contribution (see Eqs. (4.12)–(4.14)), the modified hard functions are simply

$$H_{ab \rightarrow \gamma d}^{\text{Inc}(f/d)} = \frac{C_I^{(f/d)}}{C_U} H_{ab \rightarrow \gamma d}^U, \quad (4.23)$$

where  $C_U$  and the  $C_I^{(f/d)}$ 's are presented in Table 4.1 for the gluon case [175], while the quark and antiquark ones were derived in Ref. [109]. The unpolarised hard factors are normalised so that the partonic cross sections read

$$\frac{d\hat{\sigma}}{d\hat{t}} = \frac{\pi\alpha_{em}\alpha_s e_q^2}{\hat{s}^2} H_{gq \rightarrow \gamma q}^U. \quad (4.24)$$

Having now all the elements at our disposal, we can calculate the modified hard factors  $H_{ab \rightarrow \gamma d}^{\text{Inc}(f/d)}$ . First, we recall that, in the case of unpolarised scattering, one has the well-known results:

$$H_{qg \rightarrow \gamma q}^U = \frac{1}{N_c} \left( -\frac{\hat{t}}{\hat{s}} - \frac{\hat{s}}{\hat{t}} \right) \quad H_{q\bar{q} \rightarrow \gamma g}^U = \frac{N_c^2 - 1}{N_c^2} \left( \frac{\hat{t}}{\hat{u}} + \frac{\hat{u}}{\hat{t}} \right) \quad (4.25)$$

$$H_{gq \rightarrow \gamma q}^U = H_{g\bar{q} \rightarrow \gamma \bar{q}}^U = \frac{1}{N_c} \left( -\frac{\hat{u}}{\hat{s}} - \frac{\hat{s}}{\hat{u}} \right), \quad (4.26)$$

where  $\hat{s}$ ,  $\hat{t}$ ,  $\hat{u}$  are the usual Mandelstam variables. For the Siverts effect in gluon initiated subprocesses, we have that the  $f$ - and  $d$ -type GSF contributions are respectively given by [175, 185]

$$\begin{aligned} H_{gq \rightarrow \gamma q}^{\text{Inc}(f)} &= H_{g\bar{q} \rightarrow \gamma \bar{q}}^{\text{Inc}(f)} = -\frac{1}{2} H_{gq \rightarrow \gamma q}^U, \\ H_{gq \rightarrow \gamma q}^{\text{Inc}(d)} &= -H_{g\bar{q} \rightarrow \gamma \bar{q}}^{\text{Inc}(d)} = \frac{1}{2} H_{gq \rightarrow \gamma q}^U, \end{aligned} \quad (4.27)$$

The modified hard factors for quark initiated subprocesses were calculated in Ref. [109]. We present them below again for completeness:

$$\begin{aligned} H_{qg \rightarrow \gamma q}^{\text{Inc}} &= -H_{\bar{q}g \rightarrow \gamma \bar{q}}^{\text{Inc}} = -\frac{N_c^2 - 1}{N_c^2} \left( -\frac{\hat{t}}{\hat{s}} - \frac{\hat{s}}{\hat{t}} \right), \\ H_{q\bar{q} \rightarrow \gamma g}^{\text{Inc}} &= -H_{\bar{q}q \rightarrow \gamma g}^{\text{Inc}} = \frac{1}{N_c^2} \left( \frac{\hat{t}}{\hat{u}} + \frac{\hat{u}}{\hat{t}} \right). \end{aligned} \quad (4.28)$$

#### 4.1.2 CGI-GPM AND SINGLE-SPIN ASYMMETRIES IN $p^\uparrow p \rightarrow \pi X$

As they will be used in the following Section, we present here the results obtained in Ref. [175] for inclusive pion production in polarised  $pp$  collisions. These results will be then used in Section 4.2 to put some constraints on the size of the two independent gluon Siverts functions. Within the framework of the CGI-GPM, the numerator of  $A_N$  for the  $p^\uparrow p \rightarrow \pi X$  process is

$$\begin{aligned} d\Delta\sigma^{\text{CGI-GPM}} &\equiv \frac{E_\pi d\sigma^\uparrow}{d^3\mathbf{p}_\pi} - \frac{E_\pi d\sigma^\downarrow}{d^3\mathbf{p}_\pi} \\ &\simeq \frac{2\alpha_s^2}{s} \sum_{abcd} \int \frac{dx_a dx_b dz}{x_a x_b z^2} d^2\mathbf{k}_{\perp a} d^2\mathbf{k}_{\perp b} d^3\mathbf{k}_{\perp \pi} \delta(\mathbf{k}_{\perp \pi} \cdot \hat{\mathbf{p}}_c) J(k_{\perp \pi}) \\ &\quad \times \left( -\frac{k_{\perp a}}{M_p} \right) f_{1T}^{\perp a}(x_a, k_{\perp a}) \cos \phi_a f_{b/p}(x_b, k_{\perp b}) \\ &\quad \times H_{ab \rightarrow cd}^{\text{Inc}}(x_a, x_b, \hat{s}, \hat{t}, \hat{u}) \delta(\hat{s} + \hat{t} + \hat{u}) D_{\pi/c}(z, k_{\perp \pi}), \end{aligned} \quad (4.29)$$

where  $a = q, \bar{q}, g$ ,  $J(k_{\perp \pi})$  is the kinematical factor introduced in Section 2.3.1, Eq. (2.43), and  $\hat{s}$ ,  $\hat{t}$ ,  $\hat{u}$  are again the usual Mandelstam variables for the partonic subprocess  $ab \rightarrow cd$ .  $f_{b/p}(x_b, k_{\perp b})$  is the unpolarised TMD-PDF for parton  $b$ , while  $D_{\pi/c}(z, k_{\perp \pi})$  is the fragmentation function of an unpolarised parton  $c$  into a pion. Again,  $H_{ab \rightarrow cd}^{\text{Inc}}$  are the perturbatively calculable hard scattering functions; the ones for which  $a$  is a quark or an antiquark, are well-known and can be found in Ref. [109], while the remaining ones, when  $a$  is a gluon, have been evaluated for the first time in Ref. [175], along the lines of Ref. [110].

Differently from the inclusive  $\gamma$  production case, in the case of  $\pi$  production parton  $c$  can interact with the polarised quark remnants, and so one has also final state interaction contributions. Moreover, we have now that the  $C_{F_d}$  factors sum up to zero, so as before they do not play any role in the single-inclusive hadron production.

Specifically, with  $q$  being either a quark or an antiquark, the gluon initiated subprocesses are now

$$gq \rightarrow gq \quad gg \rightarrow q\bar{q}, \quad gg \rightarrow gg. \quad (4.30)$$

The explicit results for the colour factors calculated within CGI-GPM for these subprocesses are shown respectively in Tables 4.2–4.4. All the tables present the same structure as Table 4.1, with the only difference represented by the presence of the nonzero  $C_{F_c}^{(f/d)}$  factors.

For each process, the sum of all diagrams, taken with the new colour factors  $C_I^{(f/d)}$  and  $C_{F_c}^{(f/d)}$ , gives  $H_I^{(f/d)}$  and  $H_{F_c}^{(f/d)}$ , respectively, and we have that

$$H^{\text{Inc}(f/d)} = H_I^{(f/d)} + H_{F_c}^{(f/d)}. \quad (4.31)$$

Alternatively,  $H^{\text{Inc}(f/d)}$  can be obtained directly by summing the diagrams with the colour factors

$$C^{\text{Inc}(f/d)} \equiv C_I^{(f/d)} + C_{F_c}^{(f/d)}. \quad (4.32)$$

Finally, we have checked that, for each diagram  $D$ , the gluonic pole strengths defined by

$$C_G^{(f/d)} = \frac{C_I^{(f/d)} + C_{F_c}^{(f/d)} + C_{F_d}^{(f/d)}}{C_U}, \quad (4.33)$$

are in full agreement with the ones given in Ref. [182] for less inclusive processes like  $p^\uparrow p \rightarrow \pi \pi X$ , for which the FSI of parton  $d$  need to be taken into account as well.

Using the calculated colour factors, the explicit leading order expressions for the hard functions corresponding to the gluon Sivers distribution  $f_{1T}^{\perp g(f)}$  read

$$H_{gq \rightarrow gq}^{\text{Inc}(f)} = H_{g\bar{q} \rightarrow g\bar{q}}^{\text{Inc}(f)} = -\frac{\hat{s}^2 + \hat{u}^2}{4\hat{s}\hat{u}} \left( \frac{\hat{s}^2}{\hat{t}^2} + \frac{1}{N_c^2} \right), \quad (4.34)$$

$$H_{gq \rightarrow qg}^{\text{Inc}(f)} = H_{g\bar{q} \rightarrow \bar{q}g}^{\text{Inc}(f)} = -\frac{\hat{s}^4 - \hat{t}^4}{4\hat{s}\hat{t}\hat{u}^2}, \quad (4.35)$$

$$H_{gg \rightarrow q\bar{q}}^{\text{Inc}(f)} = H_{gg \rightarrow \bar{q}q}^{\text{Inc}(f)} = -\frac{N_c}{4(N_c^2 - 1)} \frac{\hat{t}^2 + \hat{u}^2}{\hat{t}\hat{u}} \left( \frac{\hat{t}^2}{\hat{s}^2} + \frac{1}{N_c^2} \right), \quad (4.36)$$

$$H_{gg \rightarrow gg}^{\text{Inc}(f)} = \frac{N_c^2}{N_c^2 - 1} \left( \frac{\hat{t}}{\hat{u}} - \frac{\hat{s}}{\hat{u}} \right) \frac{(\hat{s}^2 + \hat{s}\hat{t} + \hat{t}^2)^2}{\hat{s}^2\hat{t}^2}, \quad (4.37)$$

where  $N_c$  is, as usual, the number of colours. For the other gluon Sivers function  $f_{1T}^{\perp g(d)}$ , one has

$$H_{gq \rightarrow gq}^{\text{Inc}(d)} = -H_{g\bar{q} \rightarrow g\bar{q}}^{\text{Inc}(d)} = \frac{\hat{s}^2 + \hat{u}^2}{4\hat{s}\hat{u}} \left( \frac{\hat{s}^2 - 2\hat{u}^2}{\hat{t}^2} + \frac{1}{N_c^2} \right), \quad (4.38)$$

$$H_{gq \rightarrow qg}^{\text{Inc}(d)} = -H_{g\bar{q} \rightarrow \bar{q}g}^{\text{Inc}(d)} = -\frac{\hat{s}^2 + \hat{t}^2}{4\hat{s}\hat{t}} \left( \frac{\hat{s}^2 + \hat{t}^2}{\hat{u}^2} - \frac{2}{N_c^2} \right), \quad (4.39)$$

$$H_{gg \rightarrow q\bar{q}}^{\text{Inc}(d)} = -H_{gg \rightarrow \bar{q}q}^{\text{Inc}(d)} = -\frac{N_c}{4(N_c^2 - 1)} \frac{\hat{t}^2 + \hat{u}^2}{\hat{t}\hat{u}} \left( \frac{\hat{t}^2 - 2\hat{u}^2}{\hat{s}^2} + \frac{1}{N_c^2} \right), \quad (4.40)$$

$$H_{gg \rightarrow gg}^{\text{Inc}(d)} = 0. \quad (4.41)$$

$D$	$C_U$	$C_I^{(f)}$	$C_{F_c}^{(f)}$	$C_{F_d}^{(f)}$	$C^{\text{Inc}(f)}$	$C_I^{(d)}$	$C_{F_c}^{(d)}$	$C_{F_d}^{(d)}$	$C^{\text{Inc}(d)}$
	$\frac{1}{2}$	$-\frac{1}{8}$	$\frac{1}{4}$	$\frac{1}{8}$	$\frac{1}{8}$	$\frac{1}{8}$	0	$\frac{1}{8}$	$\frac{1}{8}$
	$\frac{N_c^2-1}{4N_c^2}$	$\frac{1}{8N_c^2}$	$\frac{1}{8}$	$\frac{N_c^2-1}{8N_c^2}$	$\frac{N_c^2+1}{8N_c^2}$	$-\frac{1}{8N_c^2}$	$-\frac{1}{8}$	$\frac{N_c^2-1}{8N_c^2}$	$-\frac{N_c^2+1}{8N_c^2}$
	$\frac{N_c^2-1}{4N_c^2}$	$-\frac{N_c^2-1}{8N_c^2}$	$\frac{1}{8}$	$-\frac{1}{8N_c^2}$	$\frac{1}{8N_c^2}$	$\frac{N_c^2-1}{8N_c^2}$	$\frac{1}{8}$	$-\frac{1}{8N_c^2}$	$\frac{2N_c^2-1}{8N_c^2}$
	$\frac{1}{4}$	$-\frac{1}{8}$	$\frac{1}{8}$	0	0	$\frac{1}{8}$	$\frac{1}{8}$	0	$\frac{1}{4}$
	$\frac{1}{4}$	$-\frac{1}{8}$	$\frac{1}{8}$	0	0	$\frac{1}{8}$	$\frac{1}{8}$	0	$\frac{1}{4}$
	$-\frac{1}{4N_c^2}$	$\frac{1}{8N_c^2}$	0	$-\frac{1}{8N_c^2}$	$\frac{1}{8N_c^2}$	$-\frac{1}{8N_c^2}$	0	$-\frac{1}{8N_c^2}$	$-\frac{1}{8N_c^2}$
	$-\frac{1}{4N_c^2}$	$\frac{1}{8N_c^2}$	0	$-\frac{1}{8N_c^2}$	$\frac{1}{8N_c^2}$	$-\frac{1}{8N_c^2}$	0	$-\frac{1}{8N_c^2}$	$-\frac{1}{8N_c^2}$
	$-\frac{1}{4}$	0	$-\frac{1}{8}$	$-\frac{1}{8}$	$-\frac{1}{8}$	0	$\frac{1}{8}$	$-\frac{1}{8}$	$\frac{1}{8}$
	$-\frac{1}{4}$	0	$-\frac{1}{8}$	$-\frac{1}{8}$	$-\frac{1}{8}$	0	$\frac{1}{8}$	$-\frac{1}{8}$	$\frac{1}{8}$

Table 4.2: Colour factors for the LO diagrams contributing to the process  $gq \rightarrow gq$ .  $C_U$  denotes the unpolarised colour factor for the diagram  $D$ , while  $C_I$ ,  $C_{F_c}$  and  $C_{F_d}$ , respectively for the  $f$ - and  $d$ -type, are the colour factors obtained when an extra gluon is attached in  $D$  to parton  $b$  ( $C_I$ ), parton  $c$  ( $C_{F_c}$ ) or parton  $d$  ( $C_{F_d}$ ). Furthermore,  $C^{\text{Inc}} = C_I + C_{F_c}$ .

For comparison, we also show here the corresponding, well-known unpolarised hard functions,

$$H_{gq \rightarrow gq}^U = -\frac{\hat{s}^2 + \hat{u}^2}{2\hat{s}\hat{u}} \left( \frac{\hat{s}^2 + \hat{u}^2}{\hat{t}^2} - \frac{1}{N_c^2} \right), \quad (4.42)$$

$$H_{gg \rightarrow q\bar{q}}^U = \frac{N_c}{N_c^2 - 1} \frac{\hat{t}^2 + \hat{u}^2}{2\hat{t}\hat{u}} \left( \frac{\hat{t}^2 + \hat{u}^2}{\hat{s}^2} - \frac{1}{N_c^2} \right), \quad (4.43)$$

$$H_{gg \rightarrow gg}^U = \frac{N_c^2}{N_c^2 - 1} \frac{(\hat{s}^4 + \hat{t}^4 + \hat{u}^4)(\hat{s}^2 + \hat{t}^2 + \hat{u}^2)}{\hat{s}^2 \hat{t}^2 \hat{u}^2}, \quad (4.44)$$

defined in such a way that the partonic cross section, which appear in the denominators of the asymmetries, reads

$$\frac{d\hat{\sigma}}{d\hat{t}} = \frac{\pi\alpha_s^2}{\hat{s}^2} H_{ab \rightarrow cd}^U. \quad (4.45)$$

All the results presented here for inclusive pion production, along with the results for  $D$ -meson obtained in Ref. [110], will be used in Section 4.2 to put a constraint on the size and the sign of the two independent gluon Sivers functions,  $f_{1T}^{\perp g(f/d)}$ . Moreover, using the results of Refs. [110, 175], predictions for inclusive  $\gamma$  production, along with comparisons and predictions for future experiments for inclusive  $J/\psi$  production will be presented in Chapter 5.



$D$	$C_U$	$C_I^{(f)}$	$C_{F_c}^{(f)}$	$C_{F_d}^{(f)}$	$C^{\text{Inc}(f)}$	$C_I^{(d)}$	$C_{F_c}^{(d)}$	$C_{F_d}^{(d)}$	$C^{\text{Inc}(d)}$
	$\frac{1}{4N_c}$	$-\frac{N_c}{8(N_c^2-1)}$	$\frac{1}{8N_c}$	$-\frac{1}{8N_c(N_c^2-1)}$	$-\frac{1}{8N_c(N_c^2-1)}$	$\frac{N_c}{8(N_c^2-1)}$	$\frac{1}{8N_c}$	$\frac{1}{8N_c(N_c^2-1)}$	$\frac{2N_c^2-1}{8N_c(N_c^2-1)}$
	$\frac{1}{4N_c}$	$-\frac{N_c}{8(N_c^2-1)}$	$-\frac{1}{8N_c(N_c^2-1)}$	$\frac{1}{8N_c}$	$-\frac{N_c^2+1}{8N_c(N_c^2-1)}$	$-\frac{N_c}{8(N_c^2-1)}$	$-\frac{1}{8N_c(N_c^2-1)}$	$-\frac{1}{8N_c}$	$-\frac{N_c^2+1}{8N_c(N_c^2-1)}$
	$\frac{N_c}{2(N_c^2-1)}$	$-\frac{N_c}{4(N_c^2-1)}$	$\frac{N_c}{8(N_c^2-1)}$	$\frac{N_c}{8(N_c^2-1)}$	$-\frac{N_c}{8(N_c^2-1)}$	0	$\frac{N_c}{8(N_c^2-1)}$	$-\frac{N_c}{8(N_c^2-1)}$	$\frac{N_c}{8(N_c^2-1)}$
	$\frac{N_c}{4(N_c^2-1)}$	$-\frac{N_c}{8(N_c^2-1)}$	$\frac{N_c}{8(N_c^2-1)}$	0	0	$\frac{N_c}{8(N_c^2-1)}$	$\frac{N_c}{8(N_c^2-1)}$	0	$\frac{N_c}{4(N_c^2-1)}$
	$\frac{N_c}{4(N_c^2-1)}$	$-\frac{N_c}{8(N_c^2-1)}$	$\frac{N_c}{8(N_c^2-1)}$	0	0	$\frac{N_c}{8(N_c^2-1)}$	$\frac{N_c}{8(N_c^2-1)}$	0	$\frac{N_c}{4(N_c^2-1)}$
	$-\frac{N_c}{4(N_c^2-1)}$	$\frac{N_c}{8(N_c^2-1)}$	0	$-\frac{N_c}{8(N_c^2-1)}$	$\frac{N_c}{8(N_c^2-1)}$	$\frac{N_c}{8(N_c^2-1)}$	0	$\frac{N_c}{8(N_c^2-1)}$	$\frac{N_c}{8(N_c^2-1)}$
	$-\frac{N_c}{4(N_c^2-1)}$	$\frac{N_c}{8(N_c^2-1)}$	0	$-\frac{N_c}{8(N_c^2-1)}$	$\frac{N_c}{8(N_c^2-1)}$	$\frac{N_c}{8(N_c^2-1)}$	0	$\frac{N_c}{8(N_c^2-1)}$	$\frac{N_c}{8(N_c^2-1)}$
	$-\frac{1}{4N_c(N_c^2-1)}$	0	$-\frac{1}{8N_c(N_c^2-1)}$	$-\frac{1}{8N_c(N_c^2-1)}$	$-\frac{1}{8N_c(N_c^2-1)}$	0	$-\frac{1}{8N_c(N_c^2-1)}$	$\frac{1}{8N_c(N_c^2-1)}$	$-\frac{1}{8N_c(N_c^2-1)}$
	$-\frac{1}{4N_c(N_c^2-1)}$	0	$-\frac{1}{8N_c(N_c^2-1)}$	$-\frac{1}{8N_c(N_c^2-1)}$	$-\frac{1}{8N_c(N_c^2-1)}$	0	$-\frac{1}{8N_c(N_c^2-1)}$	$\frac{1}{8N_c(N_c^2-1)}$	$-\frac{1}{8N_c(N_c^2-1)}$

Table 4.3: Colour factors for the LO diagrams contributing to the process  $gg \rightarrow q\bar{q}$ . Notation is the same as in Table 4.2.

$D$	$C_U$	$C_I^{(f)}$	$C_{F_c}^{(f)}$	$C_{F_d}^{(f)}$	$C^{\text{Inc}(f)}$	$C_I^{(d)}$	$C_{F_c}^{(d)}$	$C_{F_d}^{(d)}$	$C^{\text{Inc}(d)}$
	$\frac{N_c^2}{N_c^2-1}$	$-\frac{N_c^2}{4(N_c^2-1)}$	$\frac{N_c^2}{2(N_c^2-1)}$	$\frac{N_c^2}{4(N_c^2-1)}$	$\frac{N_c^2}{4(N_c^2-1)}$	0	0	0	0
	$\frac{N_c^2}{N_c^2-1}$	$-\frac{N_c^2}{4(N_c^2-1)}$	$\frac{N_c^2}{4(N_c^2-1)}$	$\frac{N_c^2}{2(N_c^2-1)}$	0	0	0	0	0
	$\frac{N_c^2}{N_c^2-1}$	$-\frac{N_c^2}{2(N_c^2-1)}$	$\frac{N_c^2}{4(N_c^2-1)}$	$\frac{N_c^2}{4(N_c^2-1)}$	$-\frac{N_c^2}{4(N_c^2-1)}$	0	0	0	0
	$\frac{N_c^2}{2(N_c^2-1)}$	$-\frac{N_c^2}{4(N_c^2-1)}$	$\frac{N_c^2}{4(N_c^2-1)}$	0	0	0	0	0	0
	$\frac{N_c^2}{2(N_c^2-1)}$	$-\frac{N_c^2}{4(N_c^2-1)}$	$\frac{N_c^2}{4(N_c^2-1)}$	0	0	0	0	0	0
	$-\frac{N_c^2}{2(N_c^2-1)}$	$\frac{N_c^2}{4(N_c^2-1)}$	0	$-\frac{N_c^2}{4(N_c^2-1)}$	$\frac{N_c^2}{4(N_c^2-1)}$	0	0	0	0
	$-\frac{N_c^2}{2(N_c^2-1)}$	$\frac{N_c^2}{4(N_c^2-1)}$	0	$-\frac{N_c^2}{4(N_c^2-1)}$	$\frac{N_c^2}{4(N_c^2-1)}$	0	0	0	0
	$\frac{N_c^2}{2(N_c^2-1)}$	0	$\frac{N_c^2}{4(N_c^2-1)}$	$\frac{N_c^2}{4(N_c^2-1)}$	$\frac{N_c^2}{4(N_c^2-1)}$	0	0	0	0
	$\frac{N_c^2}{2(N_c^2-1)}$	0	$\frac{N_c^2}{4(N_c^2-1)}$	$\frac{N_c^2}{4(N_c^2-1)}$	$\frac{N_c^2}{4(N_c^2-1)}$	0	0	0	0

Table 4.4: Colour factors for the LO diagrams contributing to the process  $gg \rightarrow gg$ . Notation is the same as in Table 4.2. In this case all  $C^{(d)}$  colour factors are zero for symmetry reasons.

## 4.2 GLUON SIVERS FUNCTIONS FROM HADRONIC COLLISIONS

We now move towards a more quantitative analysis of the gluon Sivers functions. Specifically, we will present an updated fit of the GSF within the GPM approach and, by using two independent datasets, we will try to put some constraints on the size and on the sign of the CGI-GPM  $f$ - and  $d$ -type gluon Sivers distributions. The work presented here is based on Ref. [175].

### 4.2.1 GPM FIT OF THE GLUON SIVERS FUNCTION

Let us first take a look at the results obtained for the updated GPM fit of the gluon Sivers function. We recall that a first extraction of the GSF has been published in Ref. [186], using the knowledge on the quark Sivers function at that time, and analysing  $A_N$  data for pion production at midrapidity. Here, by adopting the same approach, we present an update to this extraction.

Notice that, as mentioned in Section 3.1, the available amount of information for polarised quark TMDs is generally limited to, at most, hundreds of datapoints. The situation dramatically worsen when moving to gluon TMDs. This is due to the fact that, in the case of the GSF, the corresponding effect can be accessed in polarised hadronic collisions where, as we showed in Section 2.3.1, a plethora of different effects come into play all together. So, one has to somehow disentangle and magnify the gluon Sivers effect, i.e. by analysing data measured in specific kinematical regions where all the effects but it are negligible. As was already pointed out in Refs. [186, 187], this is the case for the extremely precise and accurate data on SSAs in  $pp$  collisions for inclusive pion production at midrapidity, measured by the PHENIX Collaboration at RHIC, Ref. [40], and used in Ref. [175] to extract the GSF. Although this is the only dataset available, we can use it to put some constraints on the GSF, thanks to its very high precision, with order of per mille errors on the data.

One may wonder why such a reanalysis has been done. We underline that, in Ref. [186], the same value for quark and gluon Gaussian widths,  $\langle k_\perp^2 \rangle = 0.25 \text{ GeV}^2$ , has been used. In this updated analysis, by following the results of Ref. [110], a different value for the unpolarised gluon width, namely  $\langle k_\perp^2 \rangle = 1 \text{ GeV}^2$  is adopted. This, indeed, gives a better account of the unpolarised cross sections for inclusive  $J/\psi$  production in  $pp$  collisions at not so large  $p_T$  values, still allowing a good description, for instance, of the inclusive pion production.

As usually done within the GPM, a Gaussian-like and factorised parametrisation for the GSF is adopted:

$$\Delta^N f_{g/p^\uparrow}(x, k_\perp) = -\frac{2k_\perp}{M_p} f_{1T}^{\perp g}(x, k_\perp) = 2\mathcal{N}_g(x) f_{g/p}(x) h(k_\perp) \frac{e^{-k_\perp^2 / \langle k_\perp^2 \rangle}}{\pi \langle k_\perp^2 \rangle}, \quad (4.46)$$

where  $f_{g/p}(x)$  is the standard unpolarised collinear gluon distribution, the  $\mathcal{N}_g$  factor is

$$\mathcal{N}_g(x) = N_g x^\alpha (1-x)^\beta \frac{(\alpha + \beta)^{(\alpha + \beta)}}{\alpha^\alpha \beta^\beta}, \quad (4.47)$$

with  $|N_g| \leq 1$ , and

$$h(k_\perp) = \sqrt{2e} \frac{k_\perp}{M'} e^{-k_\perp^2/M'^2}. \quad (4.48)$$

Alternatively, one can also define the parameter

$$\rho = \frac{M'^2}{\langle k_\perp^2 \rangle + M'^2}, \quad (4.49)$$

such that  $0 < \rho < 1$ , and then Eq. (4.46) becomes

$$\Delta^N f_{g/p^\uparrow}(x, k_\perp) = 2 \frac{\sqrt{2e}}{\pi} \mathcal{N}_g(x) f_{g/p}(x) \sqrt{\frac{1-\rho}{\rho}} k_\perp \frac{e^{-k_\perp^2/\rho \langle k_\perp^2 \rangle}}{\langle k_\perp^2 \rangle^{3/2}}. \quad (4.50)$$

This results in a total of four parameters for the GSF:  $N_g$ ,  $\alpha$ ,  $\beta$  and  $\rho$ . With these choices, assuming that the unpolarised TMD gluon distribution is given by

$$f_{g/p}(x, k_\perp) = f_{g/p}(x) \frac{e^{-k_\perp^2/\langle k_\perp^2 \rangle}}{\pi \langle k_\perp^2 \rangle}, \quad \langle k_\perp^2 \rangle = 1 \text{ GeV}^2 \quad (4.51)$$

the Siverson function automatically fulfills its proper positivity bound for any  $(x, k_\perp)$  values. Analogously, for the unpolarised TMD fragmentation function (for a parton  $c$ ) we use [111]

$$D_{\pi/c}(z, k_{\perp\pi}) = D_{\pi/c}(z) \frac{e^{-k_{\perp\pi}^2/\langle k_{\perp\pi}^2 \rangle}}{\pi \langle k_{\perp\pi}^2 \rangle}, \quad \langle k_{\perp\pi}^2 \rangle = 0.20 \text{ GeV}^2. \quad (4.52)$$

In this analysis we adopt the CTEQ6l1 LO parametrisation [146] for the unpolarised gluon distribution,  $f_{g/p}(x)$ , with the factorisation scale equal to the pion transverse momentum,  $p_T$ , and the leading order DSS collinear fragmentation function set [148]. As mentioned in Section 2.3.2, within this model all TMDs evolve with the hard scale through the scale dependence of the collinear distributions entering in their parametrisations, that is following a DGLAP evolution [18–20].

Using the parametrisation in Eqs. (4.46) and (4.48), we can write the first  $k_\perp$ -moment of the Siverson function

$$\Delta^N f_{g/p^\uparrow}^{(1)}(x) = \int d^2 \mathbf{k}_\perp \frac{k_\perp}{4M_p} \Delta^N f_{g/p^\uparrow}(x, k_\perp) \equiv -f_{1T}^{\perp(1)g}(x), \quad (4.53)$$

as

$$\begin{aligned} \Delta^N f_{g/p^\uparrow}^{(1)}(x) &= \frac{\sqrt{\frac{e}{2}} \langle k_\perp^2 \rangle M'^3}{M_p (\langle k_\perp^2 \rangle + M'^2)^2} \mathcal{N}_g(x) f_{g/p}(x) \\ &= \sqrt{\frac{e}{2}} \frac{\sqrt{\langle k_\perp^2 \rangle}}{M_p} \sqrt{\rho^3 (1-\rho)} \mathcal{N}_g(x) f_{g/p}(x). \end{aligned} \quad (4.54)$$

This quantity will be used to compare the results for the GPM and the CGI-GPM gluon Siverson functions.

With these choices, the aforementioned dataset has been reanalysed within the GPM approach, getting results very similar to those reported in Ref. [186], although with slightly different parameters:

$$N_g = 0.25, \quad \alpha = 0.6, \quad \beta = 0.6, \quad \rho = 0.1. \quad (4.55)$$

The correlations between these parameters are very strong, hence an equally good description of pion  $A_N$  data can be obtained even with different sets of the above parameters. While this could imply very different  $k_\perp$  dependences of the GSF, as one could expect, its first  $k_\perp$ -moment remains almost unchanged in the range of  $x$  probed by data ( $10^{-3} \leq x \leq 0.4$ ). The results for the first moment of the GSF in the GPM approach will be shown in the next Section, along with the  $f$ - and  $d$ -type GSFs obtained by using the CGI-GPM approach.

#### 4.2.2 FIRST CONSTRAINTS ON $f$ - AND $d$ -TYPE GSFs

As we have seen in Section 4.1, by using a single, eikonal gluon exchange approximation, we can define two independent gluon Siverson functions, according to the two different ways in which colour can be neutralised. As the quantity of independent functions is larger than one, a single dataset would be not enough to simultaneously constrain the  $f$ - and  $d$ -type gluon Siverson distributions. In fact, at least two independent datasets are needed, and possibly sensitive to these two GSFs in a different way. Hence, in addition to the  $A_N$  data for inclusive pion production in  $pp$  collisions at midrapidity [40], we will also use those for  $D$ -meson production [188] measured by the PHENIX Collaboration at RHIC. Notice that they also collected SSA data for  $J/\psi$  production [189], to which we will compare our estimates in Chapter 5. From the phenomenological point of view, it is worth noticing that for the latter process, in the CGI-GPM approach, only the  $f$ -type contribution appears [110]. Therefore, as it will become more clear in the following, it is important to consider additional processes, where also the  $d$ -type GSF plays a role.

We stress that all these processes have a common feature: the gluon initiated subprocesses dominate over the quark ones. The SSA for inclusive pion production in  $pp$  collisions at midrapidity is directly sensitive to the gluon Siverson distribution [186, 187]. In fact, the contribution involving the quark Siverson functions, as extracted from SIDIS azimuthal asymmetries, is totally negligible, and all other effects, like the one driven by the Collins function, are washed out by integrations over the azimuthal phases. Concerning the SSAs in  $D$ -meson production, as discussed in Ref. [110], one has a clear and direct access to the GSF, due to the dominance of the  $gg \rightarrow c\bar{c}$  channel.

Within our strategy, the first issue we address is to which extent the  $f$ - and  $d$ -type contributions are effectively relevant in the process under consideration. More specifically, we observe that the numerators of  $A_N$ , Eqs. (4.22) and (4.29), contain three fundamental quantities: the azimuthal factor of the gluon Siverson function,  $\cos \phi_a$  (with  $\phi_a$  to be integrated over), the perturbatively computable hard functions,  $H_{ab \rightarrow cd}$ , and the unknown GSF,  $f_{1T}^{\perp g}$ . In order to explore the role played by the first two factors, and noticing that the amount of available data do not allow us to extract precise information on the  $x$ - and  $k_\perp$ -dependence of the two GSFs, we adopt, as a first attempt, the same parametrisation for the  $f$ - and  $d$ -type GSFs, Eqs. (4.46) and (4.50). Moreover, in order to maximise the effects of the two functions,

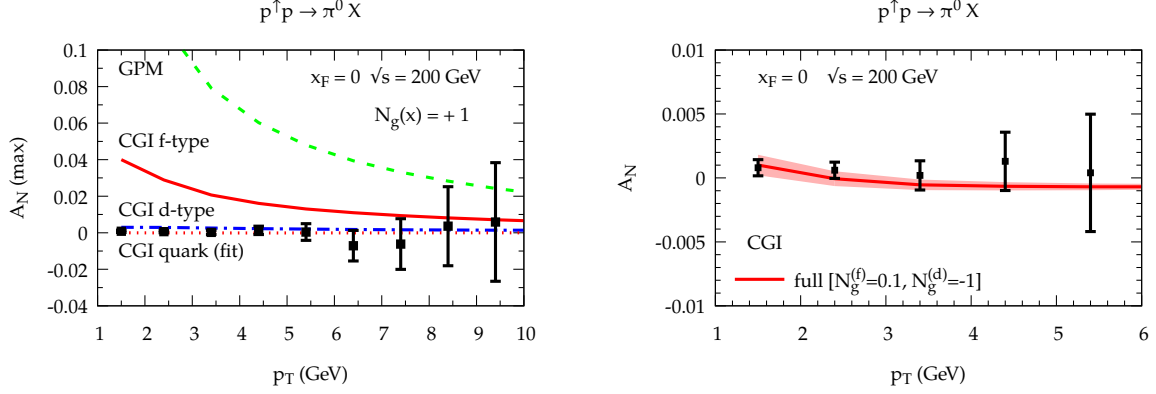


Figure 4.3: Left panel: maximised gluon Siverts contributions ( $\mathcal{N}_g(x) = +1$ ) to  $A_N$  for the process  $p^\uparrow p \rightarrow \pi^0 X$  at  $\sqrt{s} = 200$  GeV and midrapidity as a function of  $p_T$  within the GPM (green dashed line) and the CGI-GPM approaches:  $f$ -type (red solid line) and  $d$ -type (blue dot-dashed line). The quark Siverts contribution within the CGI-GPM scheme, as extracted from SIDIS data, is also shown (red dotted line). Right panel:  $A_N$  estimates, in the moderate  $p_T$  range, obtained adopting a suitably reduced  $f$ -type GSF ( $\mathcal{N}_g^{(f)}(x) = 0.1$ ) and a negative saturated  $d$ -type GSF ( $\mathcal{N}_g^{(d)}(x) = -1$ ). Shaded area corresponds to a  $\pm 20\%$  uncertainty on  $\mathcal{N}_g^{(f)}$ . Notice the different scale on the  $y$ -axis. Data are from Ref. [40].

we saturate the positivity bound for their  $x$ -dependent parts (i.e. we take  $\mathcal{N}_g(x) = \pm 1$ ) and adopt the value  $\rho = \frac{2}{3}$  [190] in Eq. (4.50).

Regarding the  $x$ -dependent part of the GSF, we also introduce the following notation

$$\Delta^N f_{g/p^\uparrow}(x) = 2\mathcal{N}_g(x) f_{g/p}(x), \quad (4.56)$$

which, for  $\mathcal{N}_g(x) = \pm 1$ , implies  $\Delta^N f_{g/p^\uparrow}(x) = \pm 2f_{g/p}(x)$ .

Fig. 4.3 (left panel) presents the maximised ( $\mathcal{N}_g(x) = +1$ ) gluon Siverts contributions to  $A_N$  for the process  $p^\uparrow p \rightarrow \pi^0 X$  at  $\sqrt{s} = 200$  GeV and midrapidity as a function of  $p_T$ , together with PHENIX data [40], for the  $f$ -type (red solid line) and  $d$ -type (blue dot-dashed line) contributions. For completeness we also show the maximised gluon Siverts term in the GPM (green dashed line). As already mentioned, it turns out that the quark Siverts contribution, even within the CGI-GPM scheme and adopting the parametrisation as extracted from SIDIS data [113], is totally negligible (red dotted line). From this plot we realise that while the  $d$ -type contribution, for this process and in this kinematical region, is dynamically suppressed, the  $f$ -type one can be potentially large. This is due to the fact that, for the  $d$ -type term, the hard functions for the processes initiated by  $gq$  and  $g\bar{q}$  pairs enter with a relative sign (see Eqs. (4.38) and (4.39)) and at midrapidity the quark and anti-quark unpolarised TMD PDFs are equally important. On top of that, there is no  $gg \rightarrow gg$  contribution (see Eq. (4.41)), that is the dominant channel at moderate values of  $p_T$ . This is in contrast with the  $f$ -type term, which indeed could be potentially very large. Notice that the corresponding effect in the GPM approach results even larger: the reason is that its partonic contributions are exactly those entering the unpolarised cross section, all positive and unsuppressed.

These first elements allow us to move to the second step of our strategy, i.e. the attempt to describe reasonably well the  $A_N$  data for  $\pi^0$  production at midrapidity within the CGI-GPM approach, by adopting simultaneously the most conservative (that is less stringent) bounds on the  $f$ - and  $d$ -type GSFs. Notice that in the kinematical region where they are

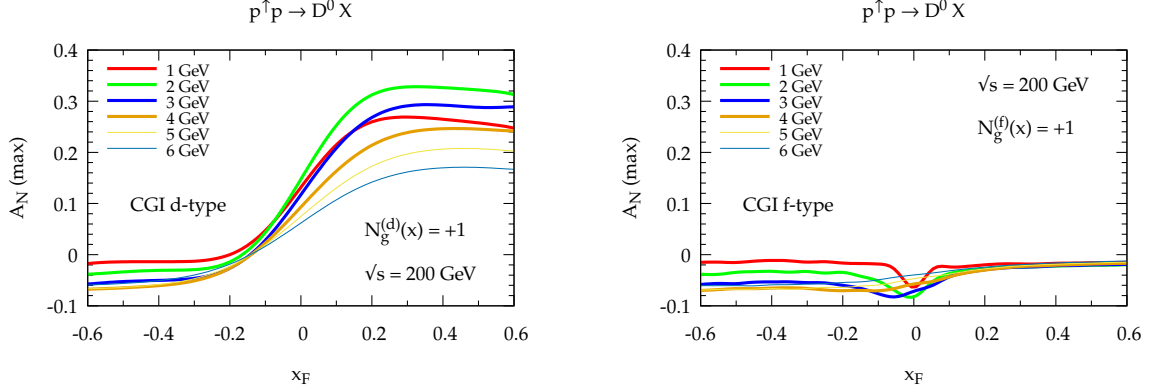


Figure 4.4: Maximised ( $\mathcal{N}_g(x) = +1$ )  $A_N$  for the process  $p^\dagger p \rightarrow D^0 X$  at  $\sqrt{s} = 200$  GeV and different  $p_T$  values (between 1 and 6 GeV) as a function of  $x_F$ , within the CGI-GPM approach:  $d$ -type (left panel) and  $f$ -type (right panel) contributions.

more precise, i.e. the region  $p_T \lesssim 5$  GeV, the data are positive and tiny, with central values of the order of per mille. So, it is clear that the most conservative scenario that could lead us to a good comparison with  $A_N$  data implies a cancellation between the two independent gluon Sivers contributions, with a positive, strongly suppressed  $f$ -type GSF and a saturated, negative  $d$ -type one, which is still supposed totally unknown. Under these hypothesis, the corresponding results, for  $\mathcal{N}_g^{(f)}(x) = +0.1$  and  $\mathcal{N}_g^{(d)}(x) = -1$ , are shown in the right panel of Fig. 4.3, together with an estimated overall uncertainty band of  $\pm 20\%$  on  $\mathcal{N}_g^{(f)}$ . Notice that a smaller  $d$ -type GSF (in size, that is either positive or negative) would imply an even smaller  $f$ -type GSF. This issue will be addressed in the following.

We now consider  $A_N$  for  $D^0$  production at  $\sqrt{s} = 200$  GeV in the kinematical region relevant to carry out the corresponding analysis for its muon decays, for which data from the PHENIX Collaboration are available [188]. To be more general, we consider an even larger region both in  $x_F = 2p_L/\sqrt{s}$  (where  $p_L$  is now the  $D$  meson longitudinal momentum) and  $p_T$ . Fig. 4.4 shows the results for  $A_N$  as a function of  $x_F$  and for different  $p_T$  values, computed by separately maximizing the  $d$ - (left panel) and  $f$ -type (right panel) contributions, as explained above. One can see that in the forward region, differently from the  $\pi^0$  production case, while the  $d$ -type term could be potentially sizeable, the  $f$ -type one is, persistently, relatively small. This is due to the fact that, since for  $D^0$  production at leading order one consistently considers only the dominant fragmentation of the charm quark into the heavy meson, the cancellations between the  $gq$  and  $g\bar{q}$  initiated processes, affecting the  $\pi^0$  case, are not present anymore. Furthermore, the hard parts favour now the  $d$ -type w.r.t. the  $f$ -type term: as one can see from Eq. (41) of Ref. [110], besides some common factors, the hard function for the  $f$ -type GSF contains a factor  $\hat{t}^2/\hat{s}^2$ , whilst that for the  $d$ -type GSF contains a term  $(\hat{t}^2 - 2\hat{u}^2)/\hat{s}^2$ . Since, as  $x_F$  increases,  $|\hat{t}|$  becomes smaller and smaller, the first piece is relatively suppressed with respect to the second one. On the other hand, in the backward region, where the two hard parts are similar, both contributions are relatively suppressed by the integration over the Sivers azimuthal phase, which for  $x_F < 0$  is less effective in the hard parts.

Using now the information extracted from the analysis of the other independent dataset, i.e. the  $\pi^0$   $A_N$  data, the  $f$ -type contribution in Fig. 4.4 should be accordingly reduced by a fac-



tor of about 0.1 (coming from the corresponding GSF), thus becoming essentially negligible. We are then safe in considering the  $d$ -type contribution as the only active one for  $D^0$  production; therefore, it can be constrained by a comparison with the available data. Analogous considerations, within the CGI-GPM approach, apply also to  $\bar{D}^0$  production, as discussed in Ref. [110], where it is shown that the  $f$ -type contribution to  $A_N$  is the same as the one for  $D^0$  production, while the  $d$ -type gets an opposite sign.

At this point, since  $D$ -meson data in Ref. [188] are provided for its relative muon decay products, one has to convert the estimates for  $D$ -meson production to the corresponding  $A_N$  for muon production [191]. It is important to point out that, in this leading order approach, the SSAs for  $D^0$  and  $D^+$  production (leading to the  $\mu^+$  results) are equal; the same happens for those for  $\bar{D}^0$  and  $D^-$  production ( $\mu^-$  results).

Since the amount of muon  $A_N$  datapoints is still quite small, and since they are yet affected by a relatively large uncertainty, we refrain from performing a proper fit, and consider a simple, constant,  $x$ -independent  $\mathcal{N}_g^{(f,d)}(x) \equiv \mathcal{N}_g^{(f,d)}$ . In what follows, in order to put a first constraint on the size and sign of the two independent  $f$ - and  $d$ -type GSFs, we discuss different possible scenarios for these functions, taking into account the information coming from the two independent, complementary dataset on  $\pi^0$  and  $D$ -meson, i.e.  $\mu^\pm$ , single-spin asymmetries. It will turn out that, even from this very conservative approach, we can extract some important information on these two unknown gluon TMDs.

Fig. 4.5 shows that, for both  $\mu^+$  (left panel) and  $\mu^-$  (right panel) production, the data are compatible with zero, with only one datapoint, the one at the largest  $x_F$  value, slightly positive for the  $\mu^+$  case. Clearly, the maximised  $d$ -type GSF contributions (thin red solid line:  $\mathcal{N}_g^{(d)} = +1$ , thin blue dot-dashed line:  $\mathcal{N}_g^{(d)} = -1$ ) largely overestimate the positive  $x_F$  experimental data in size. Notice also that the value  $\mathcal{N}_g^{(d)} = -1$ , together with  $\mathcal{N}_g^{(f)} = +0.1$ , was adopted in order to reasonably reproduce the  $\pi^0$  SSA data (see Fig. 4.3, right panel). On the other hand, to get a fair account of the muon data, one has to take indicatively  $|\mathcal{N}_g^{(d)}| \leq 0.15$ , with a mild preference for positive values, because of the positive  $\mu^+$  data point. As an example, the results obtained adopting  $\mathcal{N}_g^{(d)} = +0.15(-0.15)$  are shown as thick red solid lines (thick blue dot-dashed lines) in Fig. 4.5 both for  $\mu^+$  (left panel) and  $\mu^-$  (right panel) production.

Taking into account this new piece of information on the  $d$ -type GSF, we can reconsider the pion SSA data more accurately. Specifically, we find that by varying  $\mathcal{N}_g^{(d)}$  in the range  $-0.15 \div +0.15$ , while keeping  $\rho = 2/3$ , a very good description of both the  $\mu^\pm$  and  $\pi^0$  data can be obtained by taking  $\mathcal{N}_g^{(f)}$  in the corresponding range  $+0.05 \div -0.01$ ; in other words:

$$\begin{aligned} \mathcal{N}_g^{(d)} = -0.15 &\rightarrow \mathcal{N}_g^{(f)} = +0.05 \\ \mathcal{N}_g^{(d)} = +0.15 &\rightarrow \mathcal{N}_g^{(f)} = -0.01. \end{aligned} \tag{4.57}$$

This means that, a stronger suppression of the  $f$ -type GSF is required by the combined analysis of muon and pion SSA data. On the contrary, in the GPM approach, the extracted value of the parameters from the  $\pi^0$  SSA data, see Eq. (4.55), leads to a gluon Siverts asymmetry for  $\mu^\pm$  leptons in very good agreement with available data, as clear from the green dashed lines in Fig. 4.5. For completeness, in Fig. 4.6 we also show the corresponding  $A_N$  estimates as a function of  $p_T$  in the positive and negative  $x_F$  regions.



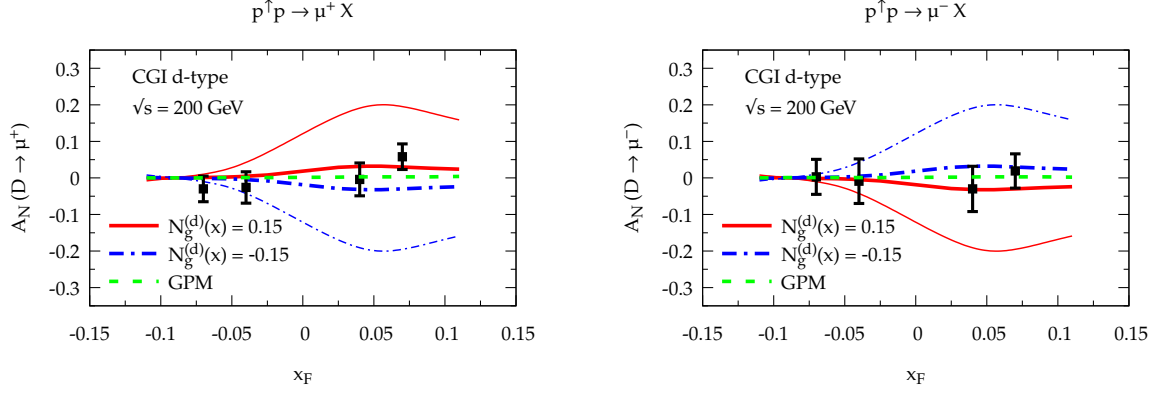


Figure 4.5:  $d$ -type gluon contributions, within the CGI-GPM approach, to  $A_N$  for the process  $p^\uparrow p \rightarrow \mu^+ X$  (left panel) and  $p^\uparrow p \rightarrow \mu^- X$  (right panel) from  $D$ -meson production at  $\sqrt{s} = 200 \text{ GeV}$  as a function of  $x_F$ : maximised effect,  $\mathcal{N}_g^{(d)}(x) = +1$  (thin red solid lines),  $\mathcal{N}_g^{(d)}(x) = -1$  (thin blue dot-dashed lines); reduced (constrained) contribution,  $\mathcal{N}_g^{(d)}(x) = +0.15$  (thick red solid lines),  $\mathcal{N}_g^{(d)}(x) = -0.15$  (thick blue dot-dashed lines). GPM predictions (green dashed lines) are also shown. Data are from Ref. [188].

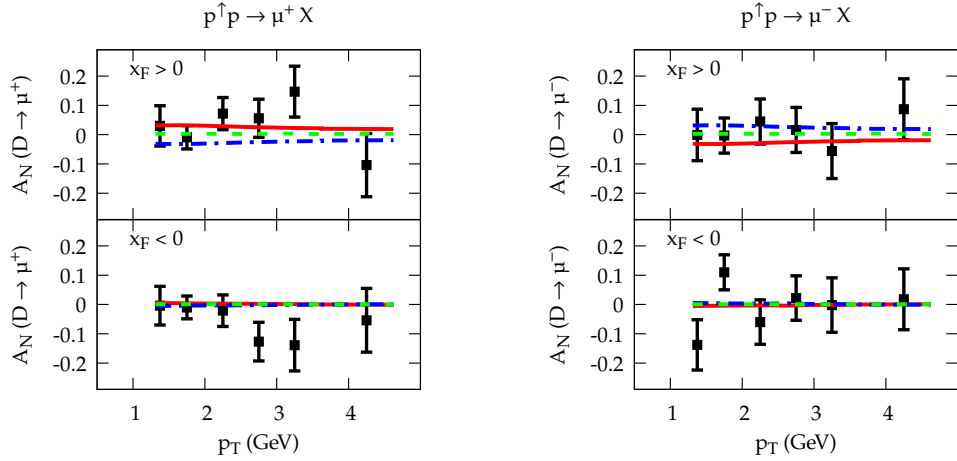


Figure 4.6:  $d$ -type gluon contributions, within the CGI-GPM approach, to  $A_N$  for the process  $p^\uparrow p \rightarrow \mu^+ X$  (left panel) and  $p^\uparrow p \rightarrow \mu^- X$  (right panel) from  $D$ -meson production at  $\sqrt{s} = 200 \text{ GeV}$  as a function of  $p_T$ :  $\mathcal{N}_g^{(d)}(x) = +0.15$  (thick red solid lines),  $\mathcal{N}_g^{(d)}(x) = -0.15$  (thick blue dot-dashed lines). GPM predictions (green dashed lines) are also shown. Data are from Ref. [188].

It is worth recalling that a similar analysis of single-spin asymmetries for  $D$ -meson production, within the collinear twist-three approach, was carried out in Ref. [192], and the corresponding predictions for  $\mu^\pm$  production were compared against the data in Figs. 5 – 7 of Ref. [188], showing a fairly good agreement.

Some comments on the adopted procedure are in order. First of all, using a fixed  $\rho$  value implies a fixed  $k_\perp$  dependence of the GSF, therefore no such information has been extracted within the CGI-GPM approach. On the other hand, the adopted value leaves the size of the GSF practically unconstrained. Then, by tuning the parameter  $N_g$  against the data we can control and estimate its size. We also have to remind that there are strong correlations between these parameters. As already underlined, the scarce amount and the limited precision of available data prevent us from performing a proper fit.

Bearing all of this in mind, in what follows we only present the first  $k_{\perp}$ -moment of the GSF, Eqs. (4.53) and (4.54), which better represents its size in an almost unbiased form (at least in the  $x$  region probed by the data,  $10^{-3} \leq x \leq 0.4$ ), without speculating on its detailed  $k_{\perp}$  or  $x$  dependences. Further studies in this respect will surely be necessary.

Fig. 4.7 shows the results for the absolute value of the first  $k_{\perp}$ -moment of the GSFs as extracted from our analyses for the GPM (parameters in Eq. (4.55), green dashed line) and the CGI-GPM approaches,  $d$ -type ( $|N_g^d| = 0.15$ , blue dot-dashed line) and  $f$ -type ( $N_g^{(f)} = 0.05$ , red solid line), together with the positivity bound (Eq. (2.22), black dotted line). We can observe that the most stringent bound is the one on the extracted GSF in the GPM approach, since in this case there are no relative cancellations between the hard partonic parts, being them all positive. In contrast, within the CGI-GPM scheme, among the two independent GSFs the  $d$ -type one is the less bounded, as it was expectable from the above observations on the size and sign of this function.

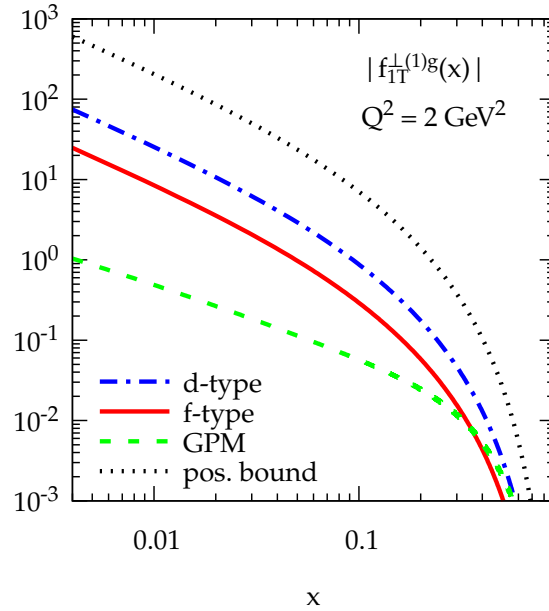


Figure 4.7: Upper values for the first  $k_{\perp}$ -moments of the gluon Sivers functions in different approaches and scenarios at  $Q^2 = 2 \text{ GeV}^2$ : GPM approach (green dashed line), CGI-GPM  $d$ -type (blue dot-dashed line) and  $f$ -type ( $N_g^{(f)} = 0.05$ , red solid line). The positivity bound (black dotted line), Eq. (2.22), is also shown.

### 4.3 OUTLOOK AND FUTURE DEVELOPEMENTS

Before concluding, it is worth commenting on the results presented throughout this Chapter. In Section 4.1 a colour gauge invariant extension of the Generalised Parton Model has been presented. Here, taking into account, in the one-gluon exchange approximation, the initial and final state interactions of the active parton with the remnants of the polarised proton, we were able to recover a process dependent Sivers function. Notice that the work presented in Section 4.1 extends to the gluon sector the computations of the expression for the single-spin asymmetries in inclusive pion and photon production from polarised  $pp$  collisions. In this way, we completed the study of Ref. [109], in which only the corresponding quark-induced subprocesses were analysed. Recalling also that the CGI-GPM and the

collinear twist-3 approach present strong analogies, it is surely worth going deeper while investigating their relationship in future studies.

On the phenomenological side, the combined analysis of  $A_N$  data for the processes  $p^\uparrow p \rightarrow \pi^0 X$  [40] and  $p^\uparrow p \rightarrow D X \rightarrow \mu X$  [188], measured by the PHENIX Collaboration at RHIC, helped us in putting some first, *preliminary* constraints on the two (so far) unknown  $f$ - and  $d$ -type gluon Sivers distributions. As presented in Sections 4.2.1 and 4.2.2, the world data for fitting the GSF is limited to tenths of datapoints, partially affected by relatively large uncertainties, belonging to a specific kinematical regime, where (at least in these approaches) quark contributions can be neglected. Nevertheless, we have shown how PHENIX data on inclusive pion and  $D$ -meson production allow us to partially disentangle and considerably constrain the size of these two GSFs, which could be much smaller than their positivity bounds (see Fig. 4.7). This can be considered the first significant attempt towards a quantitative extraction of these process dependent gluon Sivers functions.

Finally, a last remark. These exploratory studies compared the two GPM approaches, namely the original one and the CGI-GPM. Although the results are encouraging, it is not yet possible to plainly discriminate between the two approaches. As we will see in Chapter 5, we expect that in future new measurements at planned experiments like the EIC and the fixed-target proposals at the LHC will help in shedding light on the poorly known gluon Sivers functions.

# 5

## Phenomenology of single-spin asymmetries

In this Chapter we finally head to some applications of TMDs extractions to transverse single-spin asymmetries. Specifically, we will go through comparisons with data and predictions for ongoing and future experiments, based on the GPM and its CGI version. We will see that, even without using the TMD approach in its full glory, very interesting results can be obtained within the GPM ansatz. In fact, we will focus on single scale processes, i.e. inclusive hadron and photon production in polarised processes, for which single-spin asymmetries will be calculated and compared, when possible, to available data. In Section 5.1 we will analyse a simple inclusive process,  $\ell p \rightarrow hX$ , that represents a bridge between Semi-Inclusive DIS and  $pp \rightarrow hX$  processes. Finally, the asymmetries for inclusive  $J/\psi$  and photon production in polarised  $pp$  reactions will be analysed in Section 5.2, by adopting the gluon Sivers functions presented in Section 4.2.

### 5.1 SINGLE-SPIN ASYMMETRIES IN INCLUSIVE $\ell p^\uparrow \rightarrow hX$ PROCESSES: ROLE OF QUASIREAL PHOTON EXCHANGE

We would like to present here the results of an updated study of transverse single-spin asymmetries for inclusive production of hadrons in polarised lepton-proton scattering. This process represents a sort of bridge between SIDIS and inclusive  $pp$  processes. In fact, it is single inclusive, with a single large energy scale (as the  $pp \rightarrow hX$  process) and, at the same time, at leading order, is controlled by the colour-blind electromagnetic interaction (as the SIDIS process). This should reduce the role of initial and final state interactions, that can lead towards potential factorisation breaking effects. On the other hand, by adopting the relevant TMDs, i.e. Sivers, transversity and Collins functions, as extracted from SIDIS and  $e^+e^-$  data, this reaction represents a test towards a unified TMD scheme.

This process has indeed attracted the interest of various research groups. For instance, it was considered in Refs. [193, 194] in the framework of the collinear twist-3 approach, while inclusive jet production was studied, in the same framework, in Ref. [195]. These single-spin asymmetries were also studied within the GPM formalism in Refs. [196, 197]. Both Refs. [194, 197] tried to describe the asymmetries measured by the HERMES Collaboration [198], and both studies presented results with quite a lot of analogies on the size and sign of the asymmetries. In particular, in Ref. [197] the leading order GPM estimates were

compared with a selection of the experimental data by the HERMES Collaboration, showing a good agreement in sign and size. In spite of this, it was also pointed out that some of the discrepancies still present between theory and experiment could be ascribed to effects neglected in a LO treatment.

In this Section, we present the updated work of Refs. [199, 200], developed in the framework of the GPM. The updated study extends the leading order one by including the contribution from quasireal photon exchange, in the so-called Weizsäcker-Williams approximation, potentially relevant in the small  $Q^2$  kinematical region. In particular, we will provide the complete calculation, within a TMD formalism, of the quasireal photon exchange in  $\ell p \rightarrow h X$  and  $\ell p \rightarrow \text{jet } X$  processes, and compute the unpolarised cross sections and  $A_N$  for various experimental setups.

### 5.1.1 FORMALISM AND WEIZSÄCKER-WILLIAMS APPROXIMATION

Let us start by first recalling some detail about the GPM formalism. We consider the transverse single-spin asymmetry,  $A_N$ , for the process  $p^\uparrow \ell \rightarrow h X$  in the proton-lepton c.m. frame,

$$\begin{aligned} A_N &= \frac{d\sigma^\uparrow(\mathbf{P}_T) - d\sigma^\downarrow(\mathbf{P}_T)}{d\sigma^\uparrow(\mathbf{P}_T) + d\sigma^\downarrow(\mathbf{P}_T)} \\ &= \frac{d\Delta\sigma(\mathbf{P}_T)}{2 d\sigma^{\text{unp}}(\mathbf{P}_T)}, \end{aligned} \quad (5.1)$$

where we used the shorthand notation

$$d\sigma^{\uparrow,\downarrow} \equiv \frac{E_h d\sigma^{p^{\uparrow,\downarrow} \ell \rightarrow h X}}{d^3\mathbf{P}_h} \quad (5.2)$$

and  $\mathbf{P}_h$  and  $\mathbf{P}_T$  are respectively the three-momentum of the final hadron and its vector transverse component. In analogy to what we have seen in Section 2.2.2, the polarised proton (or nucleon) is in a pure transverse spin state  $\mathbf{S}$ , and moves along the positive  $Z_{\text{c.m.}}$  axis, while the lepton is unpolarised. The proton transverse polarisation is along the  $Y_{\text{c.m.}}$  direction, with  $\uparrow$  and  $\downarrow$  respectively for protons polarised parallel or antiparallel to  $Y_{\text{c.m.}}$ , and the  $X_{\text{c.m.}}$  axis is defined in such a way that a hadron  $h$  with  $(P_h)_{X_{\text{c.m.}}} > 0$  is produced *to the left* of the incoming proton, as shown in Fig. 5.1.

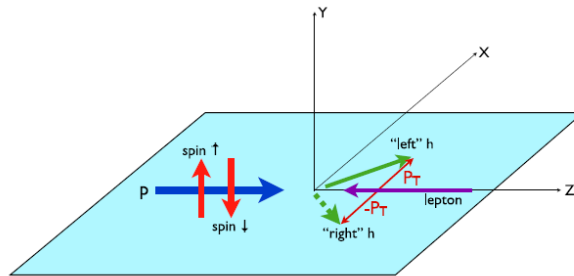


Figure 5.1: Kinematical configuration and conventions for the  $p^\uparrow \ell \rightarrow h X$  process. Figure is from Ref. [196].

Notice that for a generic transverse polarisation,  $\mathbf{S}_T$ , along an azimuthal direction  $\phi_S$  in the

chosen reference frame, in which the  $\uparrow$  direction is given by  $\phi_S = \pi/2$ , one has:

$$A(\phi_S, S_T) = \mathbf{S}_T \cdot (\hat{\mathbf{p}} \times \hat{\mathbf{P}}_T) A_N = S_T \sin \phi_S A_N, \quad (5.3)$$

where  $\mathbf{p}$  is the proton momentum, and  $A_N$  is the quantity in Eq. (5.1) that we will consider in our predictions.

In order to include effects from quasireal photon exchange, we adopt the so-called Weizsäcker-Williams (WW) approximation, and write  $A_N$  as follows:

$$A_N = \frac{d\Delta\sigma^{\text{LO}} + d\Delta\sigma^{\text{WW}}}{2[d\sigma^{\text{LO}} + d\sigma^{\text{WW}}]}, \quad (5.4)$$

where the WW contributions will be presented below, while the LO contributions, to which the elastic scattering  $q\ell \rightarrow q\ell$  is the only partonic subprocess to contribute, were calculated in Refs. [196, 197], and are given by:

$$d\Delta\sigma^{\text{LO}} = \sum_q \int \frac{dx dz}{16 \pi^2 x z^2 s} d^2 \mathbf{k}_\perp d^3 \mathbf{p}_\perp \delta(\mathbf{p}_\perp \cdot \hat{\mathbf{p}}'_q) J(p_\perp) \delta(\hat{s} + \hat{t} + \hat{u}) [\Sigma(\uparrow) - \Sigma(\downarrow)]^{q\ell \rightarrow q\ell} \quad (5.5)$$

$$2 d\sigma^{\text{LO}} = \sum_q \int \frac{dx dz}{16 \pi^2 x z^2 s} d^2 \mathbf{k}_\perp d^3 \mathbf{p}_\perp \delta(\mathbf{p}_\perp \cdot \hat{\mathbf{p}}'_q) J(p_\perp) \delta(\hat{s} + \hat{t} + \hat{u}) [\Sigma(\uparrow) + \Sigma(\downarrow)]^{q\ell \rightarrow q\ell}, \quad (5.6)$$

with  $q = u, \bar{u}, d, \bar{d}, s, \bar{s}$  and the kernels combination are

$$\begin{aligned} [\Sigma(\uparrow) - \Sigma(\downarrow)]^{q\ell \rightarrow q\ell} &= \frac{1}{2} \Delta^N f_{q/p^\uparrow}(x, k_\perp) \cos \phi \left[ |\hat{M}_1^0|^2 + |\hat{M}_2^0|^2 \right] D_{h/q}(z, p_\perp) \\ &\quad + h_{1q}(x, k_\perp) \hat{M}_1^0 \hat{M}_2^0 \Delta^N D_{h/q^\uparrow}(z, p_\perp) \cos(\phi' + \phi_q^h) \\ &\quad - \frac{k_\perp^2}{2M_p^2} h_{1T}^{\perp q}(x, k_\perp) \hat{M}_1^0 \hat{M}_2^0 \Delta^N D_{h/q^\uparrow}(z, p_\perp) \cos(2\phi - \phi' - \phi_q^h) \end{aligned} \quad (5.7)$$

$$\begin{aligned} [\Sigma(\uparrow) + \Sigma(\downarrow)]^{q\ell \rightarrow q\ell} &= f_{q/p}(x, k_\perp) \left[ |\hat{M}_1^0|^2 + |\hat{M}_2^0|^2 \right] D_{h/q}(z, p_\perp) \\ &\quad - \frac{k_\perp}{M_p} h_1^{\perp q}(x, k_\perp) \hat{M}_1^0 \hat{M}_2^0 \Delta^N D_{h/q^\uparrow}(z, p_\perp) \cos(\phi - \phi' - \phi_q^h). \end{aligned} \quad (5.8)$$

Eqs. (5.7) and (5.8) have an analogous structure to the kernels presented in Eqs. (2.51)–(2.54). Proper definition of all functions and variables appearing in the above Equations can be found in Ref. [196] and its Appendices and in Ref. [127]. Here, we just limit ourselves in pointing out the presence of all the elements introduced in Section 2.3.1: the azimuthal phases, that arise from the out of hadronic plane partonic process  $q\ell \rightarrow q\ell$ , the helicity amplitudes  $\hat{M}^0$ 's, calculated in the partonic c.m. frame, and the (un)polarised TMD-PDFs and FFs (see also Appendix B). Regarding the different contributions to the numerator and denominator of the LO parts, we see in Eq. (5.7) the contribution of the Sivers effect (first line), the transversity  $\otimes$  Collins effect (second line) and the convolution of Boer-Mulders and Collins functions (third line). In the denominator for the LO term, Eq. (5.8), we see the usual unpolarised piece, with the unpolarised TMD distribution and fragmentation func-

tion (first line), and again the Boer-Mulders  $\otimes$  Collins contribution (second line). Notice that, even saturating their positivity bounds, due to the integration over the corresponding azimuthal phases, the pieces proportional to the Boer-Mulders functions were all found to be numerically negligible [197].

#### QUASIREAL PHOTON EXCHANGE

In order to include the quasireal photon contribution to the SSA for the process under consideration, we need to find a suitable approximation. As showed in Ref. [201], in a NLO treatment of the inclusive process  $\ell p \rightarrow hX$ , the collinear lepton singularities could be regularised, and opportunely redefined, by introducing a QED parton distribution for the lepton, in strong analogy with the usual nucleon PDFs, where now the photon and the lepton itself are the partons. Without going into details, we underline that, at order  $\alpha_{em}^2 \alpha_s$ , there will be a contribution from the photon acting as a parton inside the parent lepton, that enters into the hard scattering process. This can be represented under the so-called *Weizsäcker-Williams approximation* [202, 203], in which the lepton (more specifically an ultrarelativistic charged lepton) is seen as a source of real photons (see also Refs. [204–206]). Under this approximation, by considering the kinematical configuration in which the angle between the (unobserved) scattered lepton and the emitted photon is small (i.e. when the transverse momentum of the photon is small, and therefore the photon is almost on its mass shell,  $-q^2 = Q^2 \sim 0$  – see Fig. 5.2), one can define a *collinear* leptonic PDF for photons into a lepton, with a partonic-like interpretation.

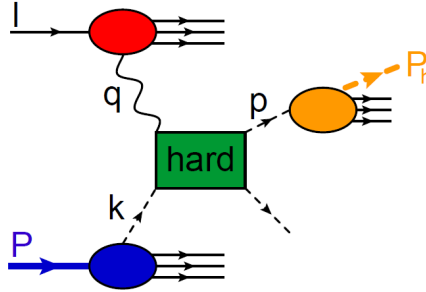


Figure 5.2: Weizsäcker-Williams contribution at  $\mathcal{O}(\alpha_{em}^2 \alpha_s)$ . The quasireal photon with  $-q^2 \equiv Q^2 \sim 0$  enters the hard scattering being treated as a parton inside the parent lepton. Figure is from Ref. [201].

Under the WW approximation, we assume the following factorised expression for the WW contribution to the process  $\ell p \rightarrow hX$

$$\sigma^{WW}(\ell p \rightarrow hX) = \int dy f_{\gamma/\ell}(y) \sigma(\gamma p \rightarrow hX), \quad (5.9)$$

where  $f_{\gamma/\ell}(y)$  is the number density of photons inside the lepton, carrying a lepton-momentum fraction  $y$  ( $p_\gamma = yp_\ell$ ) and  $\sigma(\gamma p \rightarrow hX)$  is the cross section for the process  $\gamma p \rightarrow hX$  initiated by a *real* photon.

For the WW distribution we follow Ref. [201], adopting

$$f_{\gamma/\ell}(y) = \frac{\alpha_{em}}{2\pi} \frac{1 + (1-y)^2}{y} \left[ \ln \left( \frac{\mu^2}{y^2 m_\ell^2} \right) - 1 \right] + \mathcal{O}(\alpha^2), \quad (5.10)$$



where  $\alpha_{em}$  is as usual the electromagnetic coupling constant,  $\mu$  the factorisation scale and  $m_\ell$  the lepton mass. As this is not the only existent parametrisation for the WW distribution, we have also tried an alternative form, like the one proposed in Refs. [204–206] and used for SSA studies in Refs. [207, 208]. In both cases we have considered two choices of the factorisation scale, namely  $\mu = P_T$  or  $\mu = \sqrt{s}/2$ , and we observed no significant differences. So, in the following, all the results we present are calculated by using the form in Eq. (5.10) with  $\mu = P_T$ .

### 5.1.2 WEIZSÄCKER-WILLIAMS CONTRIBUTION TO $A_N$ FOR $\ell p^\dagger \rightarrow hX$ PROCESSES

Now, in order to calculate the WW contribution to  $A_N$ , based on the factorised ansatz (5.9), we start by adapting the formalism presented in Section 2.3.1 for the cross section, in the GPM framework, of the large- $P_T$  inclusive polarised process  $A(S_A) B(S_B) \rightarrow C X$  [127]. The master formula now reads [199]

$$\begin{aligned} \frac{E_h d\sigma_{WW}^{p(S) \ell \rightarrow hX}}{d^3\mathbf{P}_h} &= \sum_{acd} \sum_{\{\lambda\}} \int \frac{dx dy dz}{16\pi^2 x y z^2 s} \\ &\times d^2\mathbf{k}_\perp d^3\mathbf{p}_\perp \delta(\mathbf{p}_\perp \cdot \hat{\mathbf{p}}_c) J(p_\perp) \delta(\hat{s} + \hat{t} + \hat{u}) \\ &\times \rho_{\lambda_a \lambda'_a}^{a/p, S} \hat{f}_{a/p, S}(x, \mathbf{k}_\perp) \rho_{\lambda_\gamma \lambda'_\gamma}^{\gamma/\ell} f_{\gamma/\ell}(y) \\ &\times \hat{M}_{\lambda_c \lambda_d, \lambda_a \lambda_\gamma} \hat{M}_{\lambda'_c \lambda'_d, \lambda'_a \lambda'_\gamma}^* D_{\lambda_c, \lambda'_c}^{\lambda_h, \lambda'_h}(z, \mathbf{p}_\perp), \end{aligned} \quad (5.11)$$

where  $\{\lambda\}$  is a shorthand notation for the sum over all the helicities, and the whole expression can be written as usual by adopting the kernel  $\Sigma(S)$  as

$$d\sigma^{WW}(S) = \sum_{acd} \int \frac{dx dy dz}{16\pi^2 x y z^2 s} d^2\mathbf{k}_\perp d^3\mathbf{p}_\perp \delta(\mathbf{p}_\perp \cdot \hat{\mathbf{p}}_c) J(p_\perp) \delta(\hat{s} + \hat{t} + \hat{u}) \Sigma(S)^{a\gamma \rightarrow cd}. \quad (5.12)$$

We stress that in Eq. (5.11) we have consistently considered a collinear WW distribution, as properly defined for the case of a scattered lepton, and a photon, almost collinear with the initial lepton. Now  $a, c$  can be a quark (antiquark) or a gluon. Therefore, at variance with respect to the LO piece, also gluon TMDs are now involved.

The notation and the meaning of the quantities entering Eq. (5.11) are analogous to the one defined in Section 2.3.1 (see e.g. Eqs. (2.40)–(2.46) and Appendix B). It is worth noticing that the Mandelstam variables for the process  $a\gamma \rightarrow cd$  are defined using  $p_\gamma = yp_\ell$ , and that now we also have the helicity density matrix  $\rho_{\lambda_\gamma \lambda'_\gamma}^{\gamma/\ell}$  for photons inside an unpolarised lepton, whose explicit form is similar to the one for the gluon case (see Eq. (B.6)). The elementary processes are now  $q\gamma \rightarrow qg$  and  $g\gamma \rightarrow q\bar{q}$ , and the corresponding helicity amplitudes are related to the  $\hat{M}$ 's, defined in the proton-lepton c.m. frame, where the  $a\gamma \rightarrow cd$  processes are not planar. They can be expressed in terms of the corresponding canonical helicity amplitudes  $\hat{M}^0$ 's in the  $a\gamma$  c.m. using the relations in Eq. (B.11).

By performing the sum over the helicities, using the proper definition of the helicity density matrices for spin- $\frac{1}{2}$  and spin-1 partons, Eqs. (B.1) and (B.6), and exploiting the parity properties of the helicity amplitudes, Eq. (B.15), we obtain the following expressions for the

kernels  $\Sigma(S)^{a\gamma \rightarrow cd}$  [199]:

1.  $q\gamma \rightarrow qg$  processes

$$\begin{aligned} \Sigma(S) = \frac{1}{2} \hat{f}_{q/p,S}(x, \mathbf{k}_\perp) f_{\gamma/\ell}(y) \Big\{ D_{h/q}(z, p_\perp) \Big[ (|\hat{M}_1^0|^2 + |\hat{M}_2^0|^2) + P_z^q P_z^\gamma (|\hat{M}_1^0|^2 - |\hat{M}_2^0|^2) \Big] \\ - \Delta^N D_{h/q^\dagger}(z, p_\perp) \hat{M}_1^0 \hat{M}_2^0 \Big[ P_x^q \sin(\varphi_1 - \varphi_2 + \phi_q^h) - P_y^q \cos(\varphi_1 - \varphi_2 + \phi_q^h) \Big] \Big\}, \end{aligned} \quad (5.13)$$

where  $q$  can be either a quark or an antiquark and

$$|\hat{M}_1^0|^2 = -\frac{16}{3} g_s^2 e^2 e_q^2 \frac{\hat{s}}{\hat{u}}, \quad |\hat{M}_2^0|^2 = -\frac{16}{3} g_s^2 e^2 e_q^2 \frac{\hat{u}}{\hat{s}}, \quad \hat{M}_1^0 \hat{M}_2^0 = \frac{16}{3} g_s^2 e^2 e_q^2. \quad (5.14)$$

2.  $q\gamma \rightarrow gq$  processes

$$\begin{aligned} \Sigma(S) = \frac{1}{2} \hat{f}_{q/p,S}(x, \mathbf{k}_\perp) f_{\gamma/\ell}(y) \Big\{ D_{h/g}(z, p_\perp) \Big[ (|\hat{M}_1^0|^2 + |\hat{M}_3^0|^2) + P_z^q P_z^\gamma (|\hat{M}_1^0|^2 - |\hat{M}_3^0|^2) \Big] \\ + \Delta^N D_{h/\mathcal{T}_1^g}(z, p_\perp) \hat{M}_1^0 \hat{M}_3^0 \Big[ \mathcal{T}_1^\gamma \cos(\varphi_1 - \varphi_3 + 2\phi_g^h) + \mathcal{T}_2^\gamma \sin(\varphi_1 - \varphi_3 + 2\phi_g^h) \Big] \Big\}, \end{aligned} \quad (5.15)$$

where again  $q$  can be either a quark or an antiquark and

$$|\hat{M}_1^0|^2 = -\frac{16}{3} g_s^2 e^2 e_q^2 \frac{\hat{s}}{\hat{t}}, \quad |\hat{M}_3^0|^2 = -\frac{16}{3} g_s^2 e^2 e_q^2 \frac{\hat{t}}{\hat{s}}, \quad \hat{M}_1^0 \hat{M}_3^0 = \frac{16}{3} g_s^2 e^2 e_q^2. \quad (5.16)$$

3.  $g\gamma \rightarrow q\bar{q}$  processes

$$\begin{aligned} \Sigma(S) = \frac{1}{2} \hat{f}_{g/p,S}(x, \mathbf{k}_\perp) f_{\gamma/\ell}(y) D_{h/q}(z, p_\perp) \Big\{ \Big[ (1 - P_z^g P_z^\gamma) (|\hat{M}_2^0|^2 + |\hat{M}_3^0|^2) \Big] \\ + 2 \hat{M}_2^0 \hat{M}_3^0 \Big[ (\mathcal{T}_1^g \mathcal{T}_1^\gamma + \mathcal{T}_2^g \mathcal{T}_2^\gamma) \cos(\varphi_2 - \varphi_3) + (\mathcal{T}_1^g \mathcal{T}_2^\gamma - \mathcal{T}_2^g \mathcal{T}_1^\gamma) \sin(\varphi_2 - \varphi_3) \Big] \Big\}, \end{aligned} \quad (5.17)$$

where

$$|\hat{M}_2^0|^2 = 2 g_s^2 e^2 e_q^2 \frac{\hat{u}}{\hat{t}}, \quad |\hat{M}_3^0|^2 = 2 g_s^2 e^2 e_q^2 \frac{\hat{t}}{\hat{u}}, \quad \hat{M}_2^0 \hat{M}_3^0 = 2 g_s^2 e^2 e_q^2. \quad (5.18)$$

4.  $g\gamma \rightarrow \bar{q}q$  processes

These can be obtained from the  $g\gamma \rightarrow q\bar{q}$  processes by interchanging in the two above equations  $\hat{t}$  with  $\hat{u}$  (that is  $\hat{M}_2^0 \leftrightarrow \hat{M}_3^0$  and  $\varphi_2 \leftrightarrow \varphi_3$ ) and  $D_{h/q}$  with  $D_{h/\bar{q}}$ .

In the above equations  $g_s$  is the strong coupling constant,  $e^2 = 4\pi\alpha_{em}$  is the electromagnetic coupling,  $P_i^{q,g,\gamma}$  stand for the quark, gluon and photon polarisation vector components and  $\mathcal{T}_i^{g,\gamma}$  for the gluon and photon linear polarisation ones, while  $\varphi_i$  are the azimuthal phases of the helicity amplitudes (see Appendix B for more details).

With all these elements, we can now compute the WW contributions to  $A_N$ . By choosing  $\phi_S = \pi/2$  in the adopted reference frame, we have that the WW contributions appearing in Eq. (5.4) are

$$d\Delta\sigma^{\text{WW}} = \sum_{acd} \int \frac{dx dy dz}{16 \pi^2 x y z^2 s} d^2 \mathbf{k}_\perp d^3 \mathbf{p}_\perp \delta(\mathbf{p}_\perp \cdot \hat{\mathbf{p}}'_q) J(p_\perp) \delta(\hat{s} + \hat{t} + \hat{u}) [\Sigma(\uparrow) - \Sigma(\downarrow)]^{a\gamma \rightarrow cd} \quad (5.19)$$

$$2 d\sigma^{\text{WW}} = \sum_{acd} \int \frac{dx dy dz}{16 \pi^2 x y z^2 s} d^2 \mathbf{k}_\perp d^3 \mathbf{p}_\perp \delta(\mathbf{p}_\perp \cdot \hat{\mathbf{p}}'_q) J(p_\perp) \delta(\hat{s} + \hat{t} + \hat{u}) [\Sigma(\uparrow) + \Sigma(\downarrow)]^{a\gamma \rightarrow cd}, \quad (5.20)$$

where the sum over the partons is extended to

$$\begin{aligned} \sum_{acd} [\Sigma(\uparrow) \pm \Sigma(\downarrow)]^{a\gamma \rightarrow cd} &= [\Sigma(\uparrow) \pm \Sigma(\downarrow)]^{q\gamma \rightarrow qg} + [\Sigma(\uparrow) \pm \Sigma(\downarrow)]^{q\gamma \rightarrow gq} \\ &+ [\Sigma(\uparrow) \pm \Sigma(\downarrow)]^{\bar{q}\gamma \rightarrow \bar{q}g} + [\Sigma(\uparrow) \pm \Sigma(\downarrow)]^{\bar{q}\gamma \rightarrow g\bar{q}} \\ &+ [\Sigma(\uparrow) \pm \Sigma(\downarrow)]^{g\gamma \rightarrow q\bar{q}} + [\Sigma(\uparrow) \pm \Sigma(\downarrow)]^{g\gamma \rightarrow \bar{q}q}, \end{aligned} \quad (5.21)$$

with

$$\begin{aligned} [\Sigma(\uparrow) - \Sigma(\downarrow)]^{q\gamma \rightarrow qg} &= f_{\gamma/\ell}(y) \left\{ \frac{1}{2} \Delta^N f_{q/p^\uparrow}(x, k_\perp) \cos \phi \left[ |\hat{M}_1^0|^2 + |\hat{M}_2^0|^2 \right]^{q\gamma \rightarrow qg} D_{h/q}(z, p_\perp) \right. \\ &+ h_{1q}(x, k_\perp) \left[ \hat{M}_1^0 \hat{M}_2^0 \right]^{q\gamma \rightarrow qg} \Delta^N D_{h/q^\uparrow}(z, p_\perp) \cos(\phi' + \phi_q^h) \\ &\left. - \frac{k_\perp^2}{2M_p^2} h_{1T}^{\perp q}(x, k_\perp) \left[ \hat{M}_1^0 \hat{M}_2^0 \right]^{q\gamma \rightarrow qg} \Delta^N D_{h/q^\uparrow}(z, p_\perp) \cos(2\phi - \phi' - \phi_q^h) \right\}, \end{aligned} \quad (5.22)$$

$$\begin{aligned} [\Sigma(\uparrow) + \Sigma(\downarrow)]^{q\gamma \rightarrow gq} &= f_{\gamma/\ell}(y) f_{q/p}(x, k_\perp) \left[ |\hat{M}_1^0|^2 + |\hat{M}_2^0|^2 \right]^{q\gamma \rightarrow gq} D_{h/q}(z, p_\perp) \\ &- \frac{k_\perp}{M_p} h_1^{\perp q}(x, k_\perp) \left[ \hat{M}_1^0 \hat{M}_2^0 \right]^{q\gamma \rightarrow gq} \Delta^N D_{h/q^\uparrow}(z, p_\perp) \cos(\phi - \phi' - \phi_q^h), \end{aligned} \quad (5.23)$$

$$[\Sigma(\uparrow) - \Sigma(\downarrow)]^{q\gamma \rightarrow gq} = \frac{1}{2} f_{\gamma/\ell}(y) \Delta^N f_{q/p^\uparrow}(x, k_\perp) \cos \phi \left[ |\hat{M}_1^0|^2 + |\hat{M}_3^0|^2 \right]^{q\gamma \rightarrow gq} D_{h/g}(z, p_\perp), \quad (5.24)$$

$$[\Sigma(\uparrow) + \Sigma(\downarrow)]^{q\gamma \rightarrow gq} = f_{\gamma/\ell}(y) f_{q/p}(x, k_\perp) \left[ |\hat{M}_1^0|^2 + |\hat{M}_3^0|^2 \right]^{q\gamma \rightarrow gq} D_{h/g}(z, p_\perp), \quad (5.25)$$

$$[\Sigma(\uparrow) - \Sigma(\downarrow)]^{g\gamma \rightarrow q\bar{q}} = \frac{1}{2} f_{\gamma/\ell}(y) \Delta^N f_{g/p^\uparrow}(x, k_\perp) \cos \phi \left[ |\hat{M}_2^0|^2 + |\hat{M}_3^0|^2 \right]^{g\gamma \rightarrow q\bar{q}} D_{h/q}(z, p_\perp), \quad (5.26)$$

$$[\Sigma(\uparrow) + \Sigma(\downarrow)]^{g\gamma \rightarrow q\bar{q}} = f_{\gamma/\ell}(y) f_{g/p}(x, k_\perp) \left[ |\hat{M}_2^0|^2 + |\hat{M}_3^0|^2 \right]^{g\gamma \rightarrow q\bar{q}} D_{h/q}(z, p_\perp), \quad (5.27)$$

and once again in Eqs. (5.22)–(5.25)  $q$  can be either a quark or an antiquark, while for the  $g\gamma \rightarrow \bar{q}q$  channel one can use the last two relations replacing  $D_{h/q}$  with  $D_{h/\bar{q}}$ . In Eqs. (5.22) and (5.23) we have redefined  $\varphi_1 - \varphi_2 = \phi' - \phi$ , consistently, and in agreement, with the notation adopted in the LO expressions [196].

In Eqs. (5.22) and (5.24) we recognize the Sivers and Collins effects. Once again, as for the LO contributions, the terms involving the pretzelosity in Eq. (5.22) and the Boer-Mulders function in Eq. (5.23) are numerically negligible (even saturating their positivity bounds). On the other hand, having now access to gluon initiated partonic subprocesses, differently from the LO case in Eq. (5.26) we also have a potential contribution from the gluon Sivers function. Finally, notice that all contributions from linearly polarised gluons ( $\mathcal{T}^g$ ) appearing in Eqs. (5.15) and (5.17) disappear since they are coupled to linearly polarised photon ( $\mathcal{T}^\gamma$ ) distributions that are identically zero for an unpolarised initial lepton.

#### SSAs IN SINGLE-INCLUSIVE JET PRODUCTION AT LARGE TRANSVERSE MOMENTUM

Inclusive production of hadrons from lepton-proton collisions represents a helpful tool. In fact, its relative simplicity (in terms of partonic processes) with respect to the  $pp$  case is one of its advantages. This process probably becomes more important when taking into account inclusive jet production. Although more difficult to measure, this could be an invaluable tool to access the Sivers effect, as the lack of any fragmentation process forbids other contributions. In Ref. [196] this case was discussed and some results for a high-energy electron-nucleon collider were presented. In the same spirit we extended this analysis including the quasireal photon contribution. The relative expressions are easily obtainable from the case of inclusive hadron production by exploiting the replacement  $D_{h/q,g}(z, \mathbf{p}_\perp) \rightarrow \delta(1-z) \delta^2(\mathbf{p}_\perp)$ . For completeness, we report here the main results for the WW contribution, while the LO piece can be found in Ref. [196]. Starting from the master formula for the hadron case, Eq. (5.11), we can write the analogous one for inclusive jet production as

$$\begin{aligned} \frac{E_j d\sigma_{\text{WW}}^{(p,S) \ell \rightarrow \text{jet } X}}{d^3\mathbf{P}_j} &= \sum_{acd} \sum_{\{\lambda\}} \int \frac{dx dy}{16\pi^2 x y s} d^2\mathbf{k}_\perp \delta(\hat{s} + \hat{t} + \hat{u}) \\ &\times \rho_{\lambda_a \lambda'_a}^{a/p,S} \hat{f}_{a/p,S}(x, \mathbf{k}_\perp) \rho_{\lambda_\gamma \lambda'_\gamma}^{\gamma/\ell} f_{\gamma/\ell}(y) \hat{M}_{\lambda_c \lambda_d, \lambda_a \lambda_\gamma} \hat{M}_{\lambda_c \lambda_d, \lambda'_a \lambda'_\gamma}^*, \end{aligned} \quad (5.28)$$

while for the contributions to  $A_N(\text{jet})$  we have

$$d\Delta\sigma_{\text{jet}}^{\text{WW}} = \sum_{acd} \int \frac{dx dy}{16\pi^2 x y s} d^2\mathbf{k}_\perp \delta(\hat{s} + \hat{t} + \hat{u}) [\Sigma(\uparrow) - \Sigma(\downarrow)]_{\text{jet}}^{a\gamma \rightarrow cd} \quad (5.29)$$

$$2 d\sigma_{\text{jet}}^{\text{WW}} = \sum_{acd} \int \frac{dx dy}{16\pi^2 x y s} d^2\mathbf{k}_\perp \delta(\hat{s} + \hat{t} + \hat{u}) [\Sigma(\uparrow) + \Sigma(\downarrow)]_{\text{jet}}^{a\gamma \rightarrow cd}, \quad (5.30)$$

with Eq. (5.21) still valid also for inclusive jet production. Sums and differences of kernels are straightforward, since we can use the same expressions as given in Eqs. (5.22)–(5.27) replacing the fragmentation functions  $D_{h/q,g}(z, p_\perp)$  with 1 and  $\Delta^N D_{h/q^\uparrow}(z, p_\perp)$  with 0. In doing this, obviously, we are assuming that the jet coincides with a single final parton (further comments on such approximation will be made later on, at the end of the Chapter). Such

approximation guarantees that there is no fragmentation process and only the Siverts effect contributes to  $A_N$ . Hence, the inclusion of WW contribution to  $A_N$  (see Eq. (5.26)) renders this process a key one to directly access the poorly known gluon Siverts function.

### 5.1.3 PHENOMENOLOGICAL RESULTS AND COMPARISON WITH DATA

We now head to the presentation of our theoretical estimates of unpolarised cross sections and SSAs for  $\ell p \rightarrow hX$  collisions. Specifically, we will focus on inclusive pion production, and we will particularly examine the role of the WW contribution and its relevance with respect to the LO pieces. Moreover, we will discuss in some detail HERMES kinematics, for which transverse SSA data are available, and we will then give predictions for experiments at Jefferson Lab at 12 GeV, for COMPASS at CERN, and for the future Electron-Ion Collider. In this last case we will also show some estimates for inclusive jet production.

Before presenting our results, it is worth giving some comments on the adopted kinematical configuration with respect to usual experimental setups. For example, HERMES analysis [198] assumes the lepton to be moving along the positive  $Z_{\text{c.m.}}$  axis, so that we should consider the processes  $\ell p^\uparrow \rightarrow hX$ , rather than  $p^\uparrow \ell \rightarrow hX$ . In this reference frame the  $\uparrow$  ( $\downarrow$ ) direction, i.e. the polarisation direction, is still along the  $+Y_{\text{c.m.}}$  ( $-Y_{\text{c.m.}}$ ) axis and, keeping the usual definition of  $x_F = 2P_L/\sqrt{s}$ , where  $P_L$  is the longitudinal momentum of the final hadron, only the sign of  $x_F$  is reversed.

The azimuthal dependent cross section measured by HERMES is defined as [198]:

$$d\sigma = d\sigma_{UU}[1 + S_T A_{UT}^{\sin\psi} \sin\psi], \quad (5.31)$$

where

$$\sin\psi = \hat{S}_T \cdot (\hat{P}_T \times \hat{k}) \quad (5.32)$$

coincides with our  $\sin\phi_S$  of Eq. (5.3), as  $\mathbf{p}$  and  $\mathbf{k}$  (respectively, the proton and the lepton three-momenta) are opposite vectors in the lepton-proton c.m. frame and one has:

$$A_{UT}^{\sin\psi}(x_F, P_T) = A_N^{p^\uparrow \ell \rightarrow hX}(-x_F, P_T), \quad (5.33)$$

where  $A_N^{p^\uparrow \ell \rightarrow hX}$  is our SSA estimate, and  $A_{UT}^{\sin\psi}$  is the quantity measured by HERMES [198].

In the following, for convenience and to keep uniform the presentation of our results, we will show our predictions adopting the HERMES setup also for JLab and COMPASS experiments, while we keep the other configuration (with the proton moving along the positive  $Z_{\text{c.m.}}$  axis) for the future EIC, as it will allow us to emphasise the strong analogies with the transverse single-spin asymmetries observed in  $p^\uparrow p \rightarrow hX$  processes.

Moreover, a word of caution about the kinematical regions we will explore is in order. Notice that at relatively low  $P_T$ , around 1-2 GeV, due to the inclusion of intrinsic transverse momentum effects one or more of the partonic Mandelstam variables might become smaller than a typical hadronic scale. This configuration would then correspond to a situation where the propagator of the exchanged particle in the partonic scattering becomes soft. To avoid such region, following Ref. [125], we have introduced an infrared regulator mass ( $\mu_0 = 0.8$  GeV). Notice that the effect of introducing such a regulator is almost negligible in  $A_N$ , being ratio of cross sections. We have checked that shifting the partonic Mandelstam invariants by

this quantity squared or cutting them out below it gives similar results. Estimates will be then shown adopting the shifting procedure, that is:

$$\hat{s} \rightarrow \hat{s} + 2\mu_0^2, \quad \hat{t} \rightarrow \hat{t} - \mu_0^2, \quad \hat{u} \rightarrow \hat{u} - \mu_0^2. \quad (5.34)$$

Finally, a small disclaimer is necessary. In the following, the predictions we show have been calculated by adopting extractions for Sivers, transversity and Collins functions from some older analyses, following our work published in Ref. [199]. We will not use neither the latest Sivers fit presented in Section 3.2, nor the updated GSF extraction of Section 4.2.1. The results we will present are based on the so-called SIDIS1 [112, 163] and SIDIS2 [113, 209] extractions for the polarised quark TMDs (Sivers, transversity and Collins)<sup>1</sup>, and the GSF extraction of Ref. [186]. SIDIS1 and SIDIS2 sets differ for the adopted set of fragmentation functions, as we will see later. Surely, in future, it would be useful to check whether the latest extractions give the same results we are going to present. Nonetheless, we expect that the conclusions would not change that much, as the latest extracted functions are quite compatible with the older ones.

## PREDICTIONS FOR UNPOLARISED CROSS SECTIONS

Let us start by showing the predictions for the unpolarised cross sections at HERMES, JLab at 12 GeV, COMPASS and the future EIC. Here, we will particularly concentrate on the role of the WW contribution to the unpolarised cross section, i.e. the denominator of  $A_N$ , and we will try to address the question whether this effect could be visible by measuring unpolarised cross sections themselves.

As already mentioned, we adopted some former TMD fits for computing our predictions in [199]. In particular, for the computation of the unpolarised cross sections, we adopted the usual factorised expressions for the unpolarised PDFs and FFs, Eqs. (2.58) and (2.59), taking as unpolarised Gaussian widths  $\langle k_\perp^2 \rangle = 0.25 \text{ GeV}^2$  and  $\langle p_\perp^2 \rangle = 0.2 \text{ GeV}^2$  as extracted in Ref. [111]. Following the SIDIS1 and SIDIS2 extractions, as collinear functions we adopted the GRV98 LO PDF set [210], and the Kretzer [211] and DSS [148] LO sets for fragmentation functions. The reasons for this choice are the following: these sets were adopted in the extraction of the Sivers and Collins functions we used for the calculation of  $A_N$ ; they differ for the role of the gluon fragmentation function, that could have an impact on the WW contribution.

## HERMES

We start by presenting in Figs. 5.3 and 5.4 our estimates for the unpolarised cross sections at HERMES for  $\pi^+$  (left panels) and  $\pi^-$  (right panels) production at  $\sqrt{s} \simeq 7.25 \text{ GeV}$ , respectively at fixed  $x_F = 0.2$  as a function of  $P_T$ , and at fixed  $P_T = 1.4 \text{ GeV}$  as a function of  $x_F$ . The thin curves refer to the LO calculation, while the thick ones to the total (LO+WW) contribution. In particular, the blue dashed lines are obtained adopting the Kretzer set for the fragmentation functions, while the red solid lines with the DSS set.

One can immediatly notice that, while at LO there are almost no differences between the estimates based on the two FF sets, these become more significant when also the WW piece

---

<sup>1</sup>A test made with the more recent Sivers [118] and Collins [116] fits will be also shown.



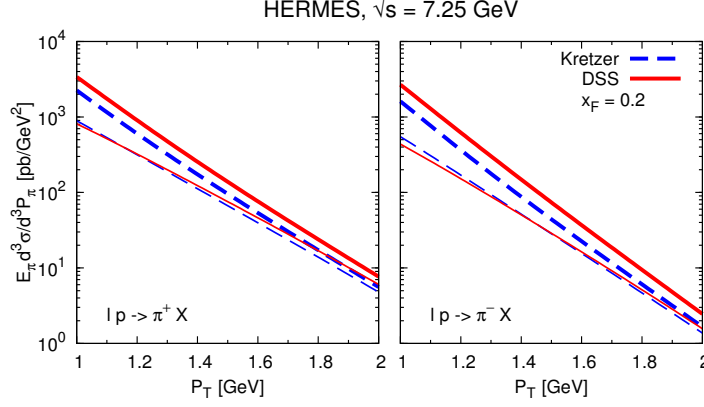


Figure 5.3: Estimates of the unpolarised cross sections at  $x_F = 0.2$  as a function of  $P_T$  for  $\pi^+$  (left panel) and  $\pi^-$  (right panel) production in  $\ell p \rightarrow \pi X$ , at HERMES,  $\sqrt{s} = 7.25$  GeV, adopting two sets for the fragmentation functions: Kretzer set (blue dashed lines) and DSS set (red solid lines). The thin curves represent the LO calculation, while the thick curves the total (LO+WW) result.

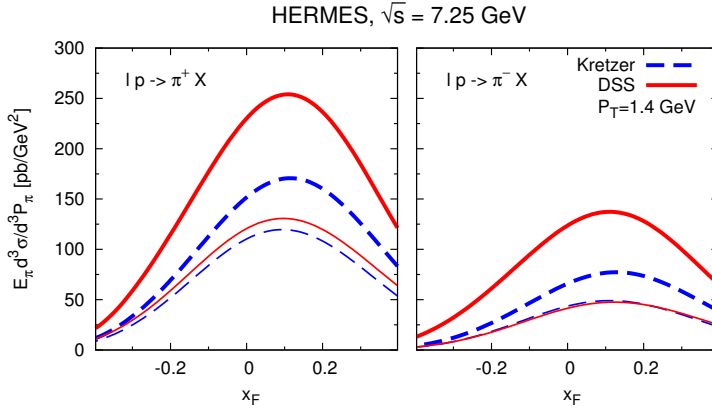


Figure 5.4: Estimates of the unpolarised cross sections at  $P_T = 1.4$  GeV as a function of  $x_F$  for  $\pi^+$  (left panel) and  $\pi^-$  (right panel) production in  $\ell p \rightarrow \pi X$ , at HERMES,  $\sqrt{s} = 7.25$  GeV. Curves have the same meaning as in Fig. 5.3.

is included. This is the effect of the much larger gluon fragmentation function in the DSS set with respect to the Kretzer one, that enters through the  $\gamma q \rightarrow gq$  partonic subprocess. Moreover, from Fig. 5.3 we note that the WW piece is more relevant for smaller  $P_T$  values, being almost three times bigger than the LO term around  $P_T = 1$  GeV. This behaviour is easily explained by checking the probed  $y$  values of the WW distribution, Eq. (5.10): we checked that, in this kinematical configuration, the lower the value of  $P_T$  is, the smaller value of  $y$  is probed, hence having an enhancement factor coming from the WW distribution. Furthermore, as one can see in Fig. 5.4, its contribution is strongly asymmetric in  $x_F$  (more than the LO term), being more important for (large) positive  $x_F$  values of the final hadron. This last feature could appear surprising, since in such a configuration the lepton undergoes, on average, a backward scattering, and one would expect a lesser role from quasireal photon exchange. On the other hand for large positive  $x_F$ , when the final hadron (as well as its parent parton  $c$ ) is produced in the *backward* proton hemisphere,  $|\hat{u}| \ll |\hat{t}|$ , where  $\hat{t} = (p_a - p_c)^2$  and  $\hat{u} = (p_\gamma - p_c)^2$  for the  $a\gamma \rightarrow cd$  process. This is the region favoured by the WW contribution with respect to the LO piece, since the latter goes like  $1/Q^2 \equiv 1/\hat{t}^2$ , while the former, in terms of the partonic cross section for the dominant subprocess  $q\gamma \rightarrow qg$  (see Eqs. (5.14) and (5.23)) goes like  $1/\hat{s}\hat{u}$ .



As seen in Section 3.1, at Jefferson Lab at 12 GeV a  $^3\text{He}$  target is used. Here, we consider the process  $\ell^3\text{He} \rightarrow \pi X$  and, adopting  $SU(2)$  symmetry, we show our estimates at the corresponding  $\sqrt{s} = 4.84 \text{ GeV}$  for the cross section *per nucleon*. More specifically, we plot

$$\frac{d^2\sigma}{dx_F dP_T} = \frac{2\pi P_T}{\sqrt{x_F^2 + x_T^2}} E_\pi \frac{d^3\sigma}{d^3P_\pi} \quad (5.35)$$

where  $x_T = 2P_T/\sqrt{s}$ .

Figs. 5.5 and 5.6 show the unpolarised cross sections for  $\pi^+$  (left panels) and  $\pi^-$  (right panels) production at  $\sqrt{s} \simeq 4.84 \text{ GeV}$ , respectively at fixed  $x_F = 0.2$  as a function of  $P_T$ , and at fixed  $P_T = 1.5 \text{ GeV}$  as a function of  $x_F$ . The curves retain the same meaning as for the HERMES kinematics. Same considerations as the HERMES case are still valid, and the only extra remark is that even the LO calculation gives sizeably different results adopting the two FF sets (see Fig. 5.6). We checked that this is driven by the more important role of the DSS FFs in the very large- $z$  region, as explored at this energies.

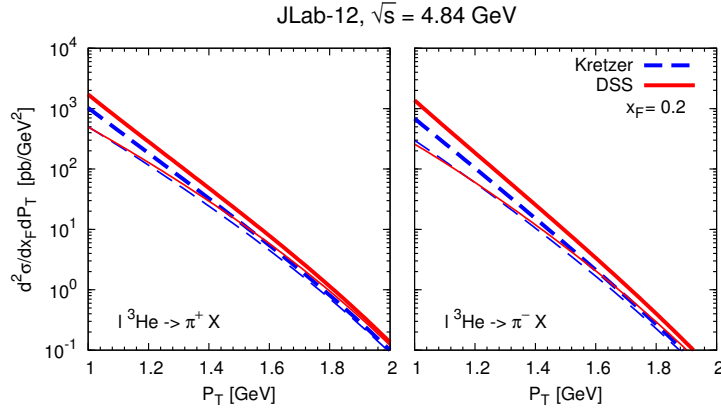


Figure 5.5: Estimates of the unpolarised cross sections *per nucleon* at  $x_F = 0.2$  as a function of  $P_T$  for  $\pi^+$  (left panel) and  $\pi^-$  (right panel) production in  $\ell^3\text{He} \rightarrow \pi X$ , at JLab-12,  $\sqrt{s} = 4.84 \text{ GeV}$ . Curves have the same meaning as in Fig. 5.3.

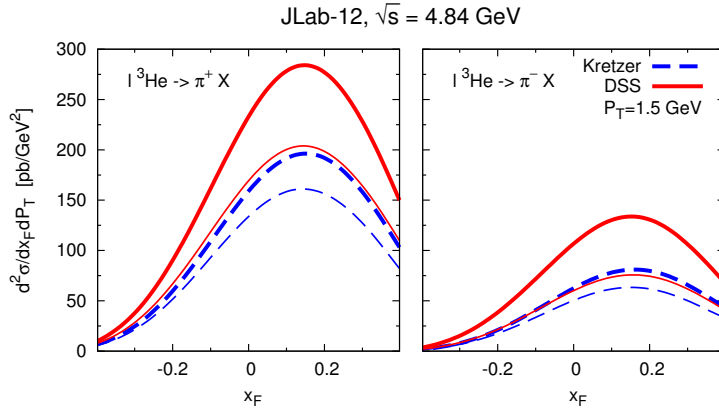


Figure 5.6: Estimates of the unpolarised cross sections *per nucleon* at  $P_T = 1.5 \text{ GeV}$  as a function of  $x_F$  for  $\pi^+$  (left panel) and  $\pi^-$  (right panel) production in  $\ell^3\text{He} \rightarrow \pi X$ , at JLab-12,  $\sqrt{s} = 4.84 \text{ GeV}$ . Curves have the same meaning as in Fig. 5.3.

## COMPASS

The COMPASS experiment uses a muon beam of lab-energy of 160 GeV, resulting in a c.m. energy  $\sqrt{s} = 17.4$  GeV. Following their setup, we use the c.m. pseudorapidity  $\eta$  of the produced hadron in the range  $-0.1 < \eta < 2$  (as covered by the COMPASS spectrometer). As for the HERMES configuration, pseudorapidity is counted as positive in the forward direction of the incident muon, and we have

$$\frac{d^2\sigma}{d\eta dP_T} = 2\pi P_T E_\pi \frac{d^3\sigma}{d^3P_\pi}. \quad (5.36)$$

Fig. 5.7 shows the unpolarised cross sections for  $\pi^+$  (left panel) and  $\pi^-$  (right panel) production at  $\sqrt{s} = 17.4$  GeV and fixed  $P_T = 2$  GeV as a function of  $\eta$ . The curves have the same meaning as in the previous figures. Differently from the former cases, the two FF sets give almost the same LO results. Moreover, the WW contribution, even if still important, appears here less relevant with respect to the HERMES configuration, resulting at most 65% (30%) of the LO term for  $\pi^-$  ( $\pi^+$ ), for the DSS set. Indeed, the muon mass is almost 200 times bigger than the electron mass, thus reducing the size of the logarithmic piece entering Eq. (5.10), partially cancelled by the finite term.

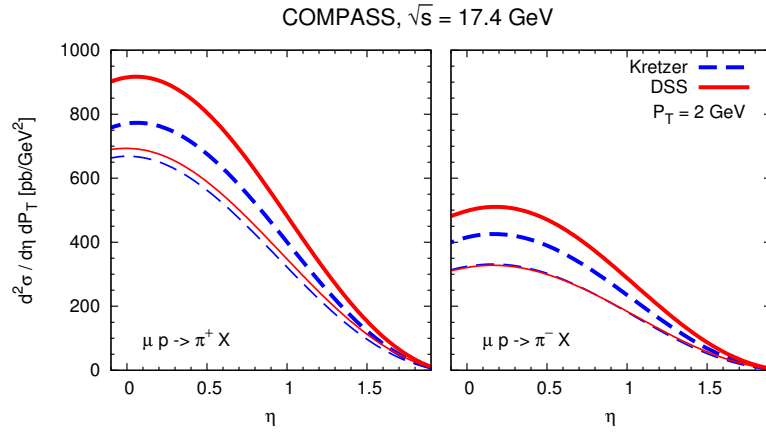


Figure 5.7: Estimates of the unpolarised cross sections at  $P_T = 2$  GeV as a function of  $\eta$  for  $\pi^+$  (left panel) and  $\pi^-$  (right panel) production in  $\mu p \rightarrow \pi X$ , at COMPASS,  $\sqrt{s} = 17.4$  GeV. Curves have the same meaning as in Fig. 5.3.

## ELECTRON-ION COLLIDER

The future EIC [76] will be an invaluable tool for TMD physics, and it would also allow us to study the cross section for single-inclusive pion production in  $ep$  collisions at very high energies, comparable to those reached in proton-proton reactions. In such a case, we prefer to adopt the configuration in which the proton moves along the positive  $Z_{\text{c.m.}}$  axis, defining  $x_F$  accordingly (more precisely,  $x_F > 0$  here will refer to the *forward* proton hemisphere). This choice will appear more natural and helpful in the context of the analysis of transverse single-spin asymmetries, Section 5.1.3, allowing an easier comparison with  $A_N$  measured in  $pp$  collisions. For the same reason we will consider neutral pion production.

Fig. 5.8 shows the predictions for the unpolarised cross sections for  $\pi^0$  production at  $\sqrt{s} = 100$  GeV, respectively at fixed  $P_T = 2$  GeV as a function of  $x_F$  (left panel) and at fixed  $x_F = 0.2$

as a function of  $P_T$  (right panel). The curves have again the same meaning as in Figs. 5.3–5.7. Once again, the two FF sets give almost the same LO results. On the other hand, here the WW contribution results much more relevant with respect to what happens at lower energies, being up to four times larger than the LO term at  $P_T = 2$  GeV. The reason is that at such large energies and not so large  $P_T$ , for  $x_F \geq 0$  one probes the small- $y$  region of the photon spectrum in the WW distribution, that behaves like  $1/y$ , while for  $x_F < 0$  (the backward region here) the WW partonic cross sections dominate the LO one, since  $|\hat{u}| \ll |\hat{t}|$ .

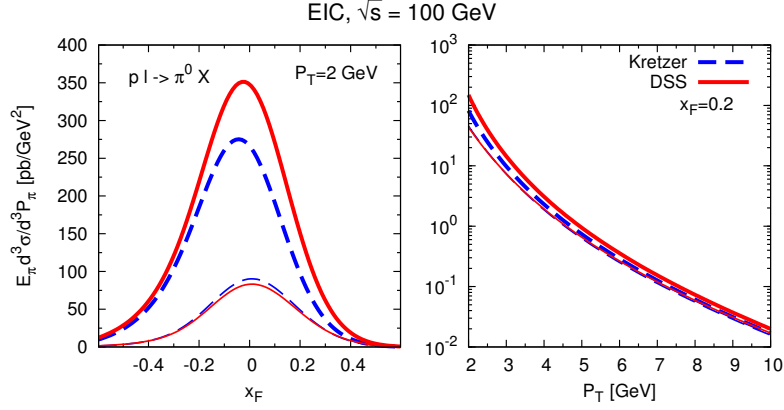


Figure 5.8: Estimates of the unpolarised cross sections in  $p \ell \rightarrow \pi^0 X$ , at EIC,  $\sqrt{s} = 100$  GeV, at  $P_T = 2$  GeV as a function of  $x_F$  (left panel) and at fixed  $x_F = 0.2$  as a function of  $P_T$  (right panel). Notice that  $x_F > 0$  here corresponds to the forward proton hemisphere. Curves have the same meaning as in Fig. 5.3.

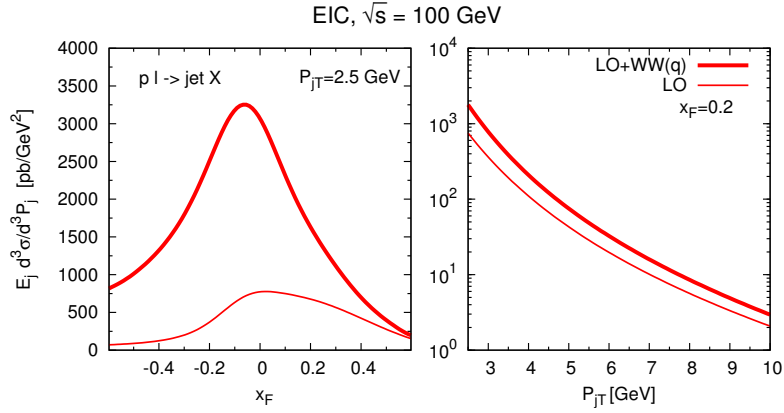


Figure 5.9: Estimates of the unpolarised cross sections in  $p \ell \rightarrow \text{jet } X$ , at EIC,  $\sqrt{s} = 100$  GeV at  $P_{jT} = 2.5$  GeV as a function of  $x_F$  (left panel) and at  $x_F = 0.2$  as a function of  $P_{jT}$  (right panel). Notice that  $x_F > 0$  here corresponds to the forward proton hemisphere. Thick (thin) curves refer to the LO+WW (LO) contribution.

At EIC, given the large energy available, the interesting study of inclusive jet production could be feasible. In Fig. 5.9 some estimates of the cross sections for jet production at fixed  $P_{jT} = 2.5$  GeV as a function of  $x_F = 2P_{jL}/\sqrt{s}$  (left panel) and at fixed  $x_F = 0.2$  as a function of  $P_{jT}$  (right panel) are plotted. The slightly larger  $P_{jT}$  value considered helps in keeping better under control potential infrared divergences in the hard elementary scattering. Even here the WW contribution heavily dominates the LO term over almost the full  $x_F$  range (with its characteristic asymmetric behaviour). Notice that in this case both at large positive and large negative  $x_F$  there is no dilution from the large- $z$  behaviour of fragmentation functions as happens in inclusive pion production.

After having seen in the previous Sections the impact of the WW contribution to the unpolarised cross sections, we can now focus on the study of the role of quasireal photon exchange in SSAs for inclusive particle production in  $\ell p$  collisions. To start with, we will make a comparison against the available data from the HERMES Collaboration [198].

Before showing the results, we comment again, and in more details, about the choice made on polarised TMDs fits. In our computations, we considered two different sets of the quark Sivers and Collins functions (the latter coupled to the transversity distribution), as previously obtained, within the GPM framework, in a series of papers from fits of SIDIS and  $e^+e^-$  data [112, 113, 163, 209]. We recall that these sets, besides some differences in the initial assumptions and in the data used for their extraction, differ in the choice of the collinear fragmentation functions. More precisely, for the so-called SIDIS1 [112, 163] fits the Kretzer FF set was adopted, while for the SIDIS2 fits [113, 209] the leading order DSS FF set was employed. Concerning the gluon Sivers function, still poorly determined, we adopted the first GSF extractions of Ref. [186]. Notice that these are obtained assuming a specific set for the quark Sivers functions, and therefore, for each “SIDIS” set, we will have an associated gluon Sivers function. As we largely pointed out in the past Chapters, it is worth to recall that the extractions of the quark and gluon Sivers functions (as well of the transversity distribution) are well constrained only up to  $x \simeq 0.3$ , as showed also for the latest fits (see e.g. Fig. 3.5 for the Sivers case).

In the following we will consider both the fully inclusive HERMES data, already discussed in Ref. [197], as well as the subsample of the so-called “anti-tagged” data (with no detection of the final lepton), for  $\ell p^\uparrow \rightarrow \pi X$  processes at large  $P_T$ . Since this process is inclusive, as we have seen in Section 2.2.2, in both cases only one large scale (needed for a perturbative calculation), the  $P_T$  of the final pion, is detected. To be sure to explore a safe, perturbative region, we only look at those data at  $P_T \geq 1$  GeV.

Finally, we recall that, at variance with SIDIS azimuthal asymmetries, where the Sivers and Collins effects can be accessed separately by looking at their corresponding azimuthal modulations (see Eq. (2.34)), here the two effects could contribute together and mix up. So, we will present for each SIDIS set the overall contribution, adding together the quark Sivers and Collins effects, for both the LO and the complete (LO+WW) calculation. For the latter, we will also show the overall statistical uncertainty bands given as the envelope of the uncertainties on the quark Sivers and Collins functions, obtained following the procedure described in Appendix A of Ref. [113]. For completeness, but with a word of caution, we have also computed the results obtained adding the contribution from the gluon Sivers function. In the following we will show them explicitly only for HERMES kinematics.

## HERMES: SSAs AND COMPARISON WITH DATA

Let us begin with the comparison against the available HERMES data. Fig. 5.10 presents our predictions for  $A_{UT}^{\sin\psi}$ , for inclusive  $\pi^+$  (upper panels) and  $\pi^-$  (lower panels) production, as a function of  $x_F$  at  $P_T = 1.1$  GeV, compared with the fully-inclusive HERMES data [198]. Notice that this is the only bin at relatively large  $P_T$  we could consider in our calculation. More precisely, we show the LO calculation, blue dashed lines, and the complete result adding the WW piece, red solid lines, adopting the quark Sivers and Collins functions from the SIDIS1

(left panels) and SIDIS2 (right panels) sets. The overall statistical uncertainty band is also shown. The green dot-dashed lines represent the total contribution including also the gluon Sivers effect.

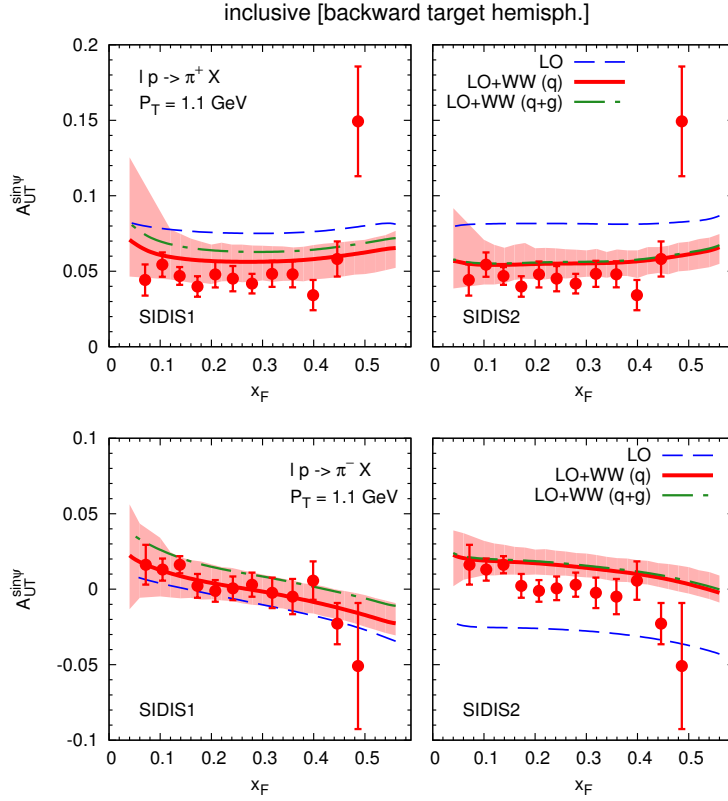


Figure 5.10: Theoretical estimates for  $A_{UT}^{\sin\psi}$  vs.  $x_F$  at  $\sqrt{s} \simeq 7.25 \text{ GeV}$  and  $P_T = 1.1 \text{ GeV}$  for inclusive  $\pi^+$  (upper panels) and  $\pi^-$  (lower panels) production in  $\ell p^\uparrow \rightarrow \pi X$  processes, compared with the fully inclusive HERMES data [198]. The SIDIS1 set (left panels) and the SIDIS2 set (right panels) for Sivers and Collins functions are considered. More precisely, we show both the LO (blue dashed lines) and LO+WW (red solid lines) quark contributions, as well as the total result including the gluon Sivers effect (green dot-dashed lines). The overall statistical uncertainty band, obtained following the procedure described in Appendix A of Ref. [113] is also shown.

Looking at Fig. 5.10, we can make the following remarks:

- the inclusion of the WW contribution that, in this kinematical region, dominates the unpolarised cross sections (see Figs. 5.3 and 5.4), improves significantly the agreement with the data;
- the Collins effect turned out to always be tiny or completely negligible (both in the LO and WW contributions);
- the differences between the predictions adopting the SIDIS1 and SIDIS2 sets are due to the distinct behaviour of the corresponding Sivers functions;
- the contribution coming from the GSF is almost negligible for the SIDIS2 set, while for the SIDIS1 set is relatively more important, reducing the agreement with the data. Nevertheless, it is important to point out that there is still a large uncertainty in the gluon Sivers function extraction in the large- $x$  region, as covered in such a kinematical configuration.

Fig. 5.11 shows, for the first time, our results for the anti-tagged category for  $A_{UT}^{\sin\psi}$ , compared against HERMES data [198], at fixed  $x_F = 0.2$  (that is the average value of the data set) as a function of  $P_T$ . Once again, we consider the inclusive  $\pi^+$  (upper panels) and  $\pi^-$  (lower panels) production cases, adopting the SIDIS1 (left panels) and SIDIS2 (right panels) sets for quark Sivers and Collins functions. The curves have the same meaning as for the fully inclusive case showed in Fig. 5.10.

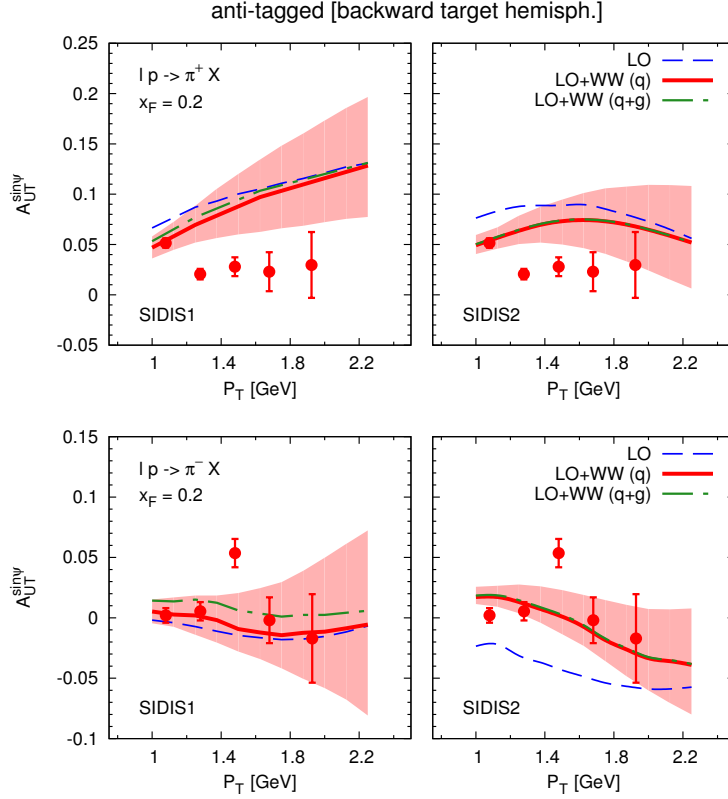


Figure 5.11: Theoretical estimates for  $A_{UT}^{\sin\psi}$  vs.  $P_T$  at  $\sqrt{s} \simeq 7.25$  GeV and  $x_F = 0.2$  for inclusive  $\pi^+$  (upper panels) and  $\pi^-$  (lower panels) production in  $\ell p^\dagger \rightarrow \pi X$  processes, compared with the anti-tagged HERMES data [198]. Curves have the same meaning as in Fig. 5.10.

From these results we can observe that, once again, the inclusion of the WW contribution leads to a very good improvement in describing the experimental measurements, even if some sizeable discrepancy for the  $\pi^+$  data remains. The gluon Sivers effect is negligible, except for the SIDIS 1 set in  $\pi^-$  production. Moreover, the wider uncertainty bands are due to the large- $x$  region probed at such moderate energies, where the current extractions of the Sivers function (that represent the dominant contribution to the SSAs) are still unconstrained.

#### SSAs AT JLAB

In the future, the 12 GeV upgrade of JLab will represent another valuable tool for TMD physics, especially for studying the large- $x$  region. Here, specifically, we focus on neutron target, that represent a complementary measure for HERMES data. Indeed, as we have seen in the case of the polarised quark TMD fits, Sections 3.2.2 and 3.3, the combined analysis of proton and neutron target events helps in understanding the flavour decomposition and the

role of the up and down quark contributions. The same would then happen having JLab  $A_N$  measurements on neutron target.

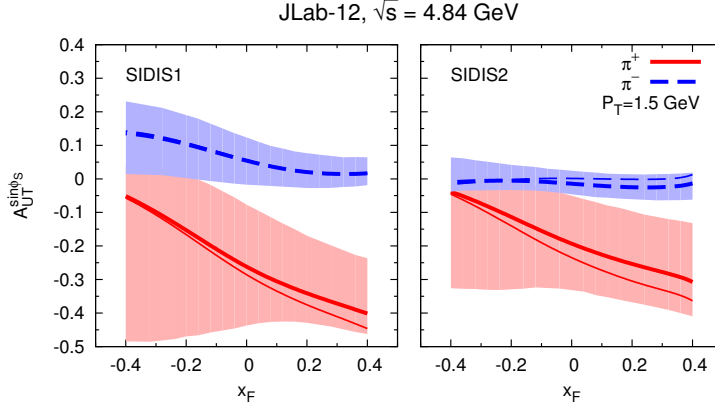


Figure 5.12: Theoretical estimates for  $A_{UT}^{\sin \phi_s}$  vs.  $x_F$  at  $\sqrt{s} \simeq 4.84$  GeV and  $P_T = 1.5$  GeV for inclusive  $\pi^+$  (red solid lines) and  $\pi^-$  (blue dashed lines) production, which will be measured at JLab operating on a polarised  $^3\text{He}$  (neutron) target, with a beam energy of 12 GeV. The thin curves refer to the LO calculation, while the thick ones to the full, LO+WW, estimates for the two sets for the quark Sivers and Collins functions: SIDIS1 (left panel) and SIDIS2 (right panel). The overall statistical uncertainty band, obtained following the procedure described in Appendix A of Ref. [113], is also shown.

Our estimates for the JLab SSAs,  $A_{UT}^{\sin \phi_s}$ , for inclusive pion production off polarised  $^3\text{He}$  (neutron) target are shown in Fig. 5.12 at fixed  $P_T = 1.5$  GeV as a function of  $x_F$ . Here, this somehow large  $P_T$  value has been chosen for uniformity with what discussed for the unpolarised cross section and because it allows to span a larger region in  $x_F$  (in particular its positive values). We recall that we keep adopting the HERMES configuration, with the incoming lepton moving along the positive  $Z_{\text{c.m.}}$  axis and plot  $A_{UT}^{\sin \phi_s} \equiv A_{UT}^{\sin \psi}$ . Particularly, we show for the SIDIS1 (left panel) and the SIDIS2 (right panel) the LO (thin lines) and the LO+WW (thick lines) calculation, displaying also the uncertainty bands for the total contribution. Moreover, we underline that the gluon Sivers effect is not included. We checked that, apart from the  $\pi^-$  production when adopting the SIDIS1 set, where it plays some role as in the HERMES case, its contribution is completely negligible. In most cases the full, LO+WW, estimates present the same behaviour, in size and sign, as the LO ones. Nonetheless one has to keep in mind that, with the DSS FF set for instance, the WW piece alone is about 50% (90%) of the LO contribution for  $\pi^+$  ( $\pi^-$ ) production in this kinematical region. Finally, the wider uncertainty bands are due to the large- $x$  region probed at such moderate energies, where the current extractions of the Sivers functions are still unconstrained.

## SSAs AT COMPASS

The COMPASS experiment is another place where  $A_N$  for inclusive pion production from polarised lepton-proton scattering could be surely measured. Here we present some predictions following their experimental setup. Fig. 5.13 shows  $A_{UT}^{\sin \phi_s}$  vs.  $x_F$  at  $\sqrt{s} \simeq 17.4$  GeV and  $P_T = 2$  GeV for inclusive  $\pi^+$  (red solid lines) and  $\pi^-$  (blue dashed lines) production in  $\mu p^\uparrow \rightarrow \pi X$  at COMPASS. The curves have the same meaning as in the previous figures. Here we expect the SSAs for  $\pi^+$  production to be sizeable, with quite narrow error bands. Consequently, COMPASS would surely represent a clear test for this approach. Again we observe that the inclusion of the WW contribution changes only slightly the LO estimates. This



is quite expectable, since  $A_N$  is built as a ratio, and the role of quasireal photon exchange is softened or balanced between numerator and denominator.

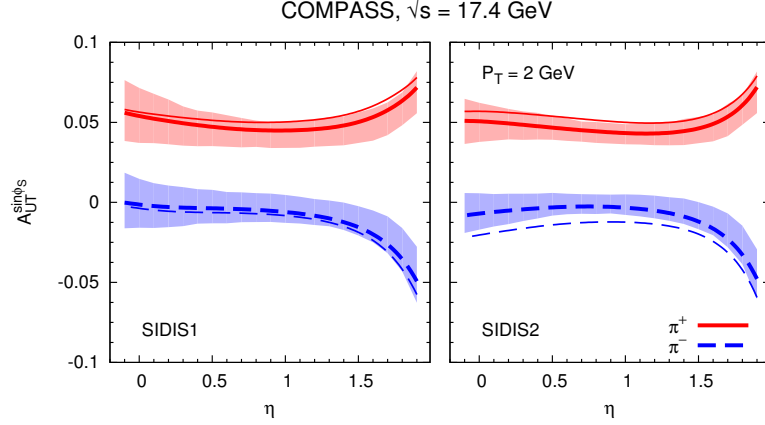


Figure 5.13: Theoretical estimates for  $A_{UT}^{\sin \phi_S}$  vs.  $x_F$  at  $\sqrt{s} \simeq 17.4$  GeV and  $P_T = 2$  GeV for inclusive  $\pi^+$  (red solid lines) and  $\pi^-$  (blue dashed lines) production in  $\mu p^\uparrow \rightarrow \pi X$  at COMPASS. Two sets for the quark Sivers and Collins functions have been adopted: SIDIS1 (left panel) and SIDIS2 (right panel). The overall statistical uncertainty band are also shown. Curves have the same meaning as in Fig. 5.12.

## SSAs AT THE FUTURE EIC

Once again, we stress that the future Electron-Ion Collider would be an unvaluable tool to explore transverse single-spin asymmetries in inclusive  $ep$  processes. Its high energy, 100 GeV, would allow to study both inclusive production of a pion or a jet. Moreover, it lies in the energy range where also  $A_N$  for  $p^\uparrow p \rightarrow \pi X$  processes is measured in hadron colliders like RHIC. So, in order to see whether some analogies between the  $\ell p$  and the  $pp$  cases could be observed at the EIC, it is more convenient to adopt the configuration where the polarised proton is moving along the positive  $Z_{c.m.}$  axis and positive  $x_F$  values correspond to the forward proton hemisphere. Of course, even in such configuration, it is also interesting to study the role of quasireal photon exchange at the future EIC.

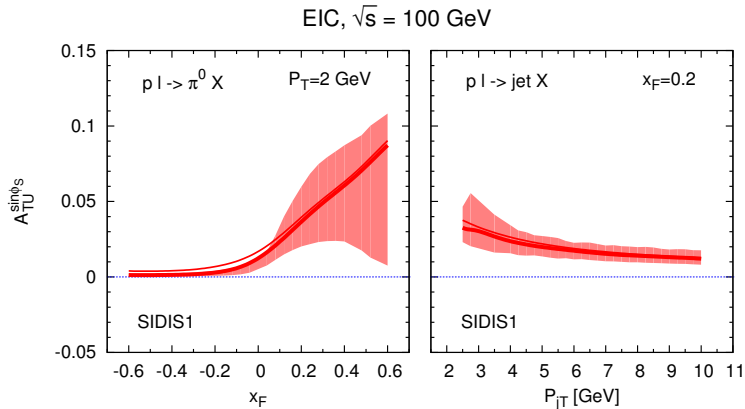


Figure 5.14: Theoretical estimates for  $A_{TU}^{\sin \phi_S}$  at  $\sqrt{s} = 100$  GeV as a function of  $x_F$  at  $P_T = 2$  GeV for inclusive  $\pi^0$  production (left panel) and as a function of  $P_{jT}$  at  $x_F = 0.2$  for inclusive jet production (right panel), adopting the SIDIS1 set for the quark Sivers and Collins functions. The overall statistical uncertainty bands, calculated according to the procedure described in Appendix A of Ref. [113], are also shown. Thick (thin) lines refer to the LO+WW (LO) calculation.

Fig. 5.14 shows our estimates at  $\sqrt{s} = 100$  GeV for  $A_{TU}^{\sin\phi_S} \equiv A_N$  for inclusive  $\pi^0$  production in  $p^\uparrow \ell \rightarrow \pi X$  vs.  $x_F$  at  $P_T = 2$  GeV (left panel) and for inclusive jet production vs.  $P_{jT}$  at  $x_F = 0.2$  (right panel), adopting the SIDIS1 set. This set indeed is the one that better reproduces the behaviour of  $A_N$  in  $p^\uparrow p \rightarrow \pi X$  processes (see for instance Ref. [212]) and that is consistent with the findings of a dedicated study performed in Ref. [213]. As in the previous figures, thick (thin) curves represent LO+WW (LO) contributions. Some comments are in order:

- we explicitly checked that the gluon Sivers effect (not shown) is completely negligible;
- the corresponding results for  $\pi^0$  as a function of  $P_T$ , not shown, are almost identical to those for inclusive jet production. The same is true for  $A_N$  for inclusive jet production as a function of  $x_F$ , not shown, almost identical to that for  $\pi^0$  production;
- as one can see the WW contribution does not change the LO behaviour. Again, this behaviour could be quite expected, as both contributions enter with the same structure in the single-spin asymmetry. This represent also a useful cross-check of the previous work, Ref. [197], for which we confirm all findings concerning the  $x_F$  behaviour. We only add the extra important information that, at such energies and  $P_T$  values, the WW piece is the *dominant* one in the unpolarised cross sections;
- quite interesting, the  $P_T$  behaviour, shown here for the first time, is almost flat (and seems to be measurable) up to very large  $P_T$  values. This is strongly analogous to what happens in  $p^\uparrow p \rightarrow \pi^0 X$  as measured for instance by the STAR Collaboration [214] and it would be another very important test of the full approach;
- the large error bands at large  $x_F$  reflects the still poor knowledge of the Sivers function in the large  $x$  region. This feature is still persistent also for latest fits (see Fig. 3.10). Future measurements at JLab could definitely help in this respect.

#### IMPACT OF SOME OF THE LATEST EXTRACTIONS OF THE SIVERS AND COLLINS FUNCTIONS

At the very last stage of the work we made in Ref. [199], a new extraction of the Sivers functions from the latest SIDIS data, the so-called “sign change fit” (referred to as “fit016” in Fig. 5.15), was released [118]. Together with the fit of the Collins and the transversity functions of Ref. [116], they represented at that time the most updated information on the relevant TMDs entering the analysis presented so far. So, it has been interesting to check whether these fits were confirming the good comparison with HERMES data.

Among the main features of these extractions it is useful to mention that:

- different Gaussian widths for the unpolarised TMDs, as extracted from SIDIS multiplicities from HERMES [114],  $\langle k_\perp^2 \rangle = 0.57 \text{ GeV}^2$  and  $\langle p_\perp^2 \rangle = 0.12 \text{ GeV}^2$  (to be compared with those used in SIDIS1 and SIDIS2 fits), along with the DSS LO FF set were used;
- the resulting size of the  $x$ -dependent part of the valence up and down Sivers distributions is reduced;
- a more flexible parametrisation of the Collins functions was adopted (i.e. the one used in Section 3.3 for the tests on the transversity and Collins fit) allowing for a more accurate extraction of their transverse momentum dependence;

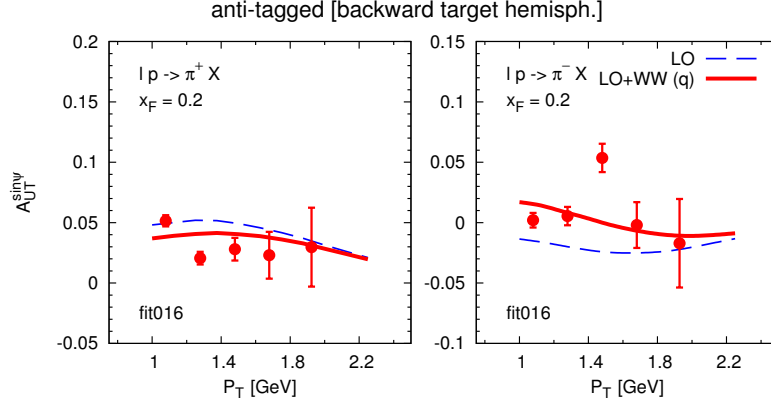


Figure 5.15: Theoretical estimates of the Sivers contribution to  $A_{UT}^{\sin\psi}$  vs.  $P_T$  at  $\sqrt{s} \simeq 7.25$  GeV and  $x_F = 0.2$  for inclusive  $\pi^+$  (left panel) and  $\pi^-$  (right panel) production in  $\ell p^\dagger \rightarrow \pi X$  processes, compared with the anti-tagged HERMES data [198] and adopting the quark Sivers functions of Ref. [118]. Curves have the following meaning: blue dashed lines for the LO and red solid lines for the LO+WW contributions.

- for the fit of the Sivers functions, the CTEQ611 parton distribution functions [146, 147] were used.

Bearing these elements in mind, we checked the impact of these new parametrisations on the description of HERMES data. We summarise here the main results:

- the Collins contribution is practically negligible for the fully inclusive dataset and tiny, but slightly improving the description, for the anti-tagged data category;
- while still confirming the good agreement with the fully inclusive data, the use of the new Sivers parametrisation reduces significantly the discrepancies between the theoretical predictions and the anti-tagged data for  $\pi^+$  production (slightly overestimated adopting the SIDIS1 and SIDIS2 sets, see Fig. 5.11, upper panels). This behaviour could be ascribed to the role of different values of the Gaussian widths, as recently studied in Ref. [215].

Fig. 5.15 presents the comparison of the new estimates calculated using the updated Sivers and Collins fits with the anti-tagged data. We can clearly notice that, even at LO, one gets a clear improvement in the description of  $\pi^+$  data, i.e. the ones to which our predictions had the less good comparison. Furthermore, no significant differences appear in the unpolarised cross sections, but the trend that sees the WW piece comparable to (or even dominating) the LO contribution is confirmed.

Analogous features show up also in the predictions for JLab and COMPASS kinematics: almost no differences appear in the unpolarised cross sections, while a reduction in size (almost a factor of two) of the SSAs for  $\pi^+$  production comes out. For  $A_N$  in  $\pi^0$  and jet production at EIC we find similar behaviours as those obtained adopting the SIDIS1 set (see Fig. 5.14), with a reduction of our estimates by a factor of two at fixed  $x_F$  vs.  $P_T$  and by a factor of about three at fixed  $P_T$  vs.  $x_F$ . In this last case we recall that one has to take into account the poor knowledge on the Sivers function in the large- $x$  region, that affects also the latest extractions.

## 5.2 CGI-GPM vs GPM: INCLUSIVE QUARKONIA AND PHOTON PRODUCTION IN POLARISED $pp$ PROCESSES

After having analysed a simpler inclusive process involving leptons, let us move on by showing predictions for inclusive production of hadron and photon in polarised  $pp$  collisions. Here, we will particularly concentrate on the inclusive production of a specific quarkonia, i.e. a bound state of a heavy quark-antiquark couple, the  $J/\psi$ , and on the inclusive production of a photon. Both of these processes are very sensitive to the gluon Sivvers effect, and also represent an interesting test for discriminating between different versions of the GPM, namely the traditional one and its colour gauge invariant extension introduced in Section 4.1. Also here, when available, we will compare our predictions against data. The predictions are calculated using the gluon Sivvers functions extracted within the GPM formalism and the ones estimated by the combined analysis of pion and  $D$ -meson production in the CGI-GPM approach, see Section 4.2.1 and Eq. (4.55), and Section 4.2.2 and Eq. (4.57) respectively.

Let us start with the inclusive  $J/\psi$  production case. In addition to the CGI-GPM approach, here we also adopt the so-called Colour Singlet Model (CSM), where the charm-anticharm pair forming the bound state is produced in the hard partonic scattering directly with the same quantum numbers as the  $J/\psi$ . Other possible  $J/\psi$  production mechanisms exist. We refer the reader to Ref. [216] for a recent review. As discussed in Ref. [110],  $A_N$  for  $J/\psi$  production is directly sensitive to the gluon Sivvers function and, within the CGI-GPM approach and the CSM, only the  $f$ -type distribution contributes to the Sivvers asymmetry. This is also expected, for instance, in  $ep$  scattering at LO, that represents another ideal tool to single out the  $f$ -type GSF [217]. In such a case, it turns out that the only contribution to  $A_N$  comes when the heavy quark pair is produced in a colour octet state (see also Ref. [218]).

Figs. 5.16 and 5.17 show a comparison of our estimates, evaluated adopting the so-called transverse mass,  $M_T^2 = M_{J/\psi}^2 + p_T^2$ , as factorisation scale, with PHENIX data [189] for  $A_N$  in  $p^\uparrow p \rightarrow J/\psi X$ . Particularly, in Fig. 5.16, left panel, we show the maximised ( $\mathcal{N}_g^{(f)}(x) = \pm 1$ ) contributions to  $A_N$  at fixed  $p_T = 1.65 \text{ GeV}$  as a function of  $x_F$ , both in the GPM (green dashed lines) and the CGI-GPM (red solid lines) approaches. Similarly to the  $D$ -meson production case (see Fig. 4.4, right panel), also in this case the integration over the Sivvers azimuthal phase strongly suppresses the asymmetry in the backward-rapidity region. In Fig. 5.16, right panel, we present our corresponding predictions based on the present analysis: GPM (green dashed line), CGI-GPM (red band:  $-0.01 \leq \mathcal{N}_g^{(f)} \leq 0.05$ ). Similarly, in Fig. 5.17 we show the corresponding estimates as a function of  $p_T$  at  $x_F = 0.1$  (left panel) and  $x_F = -0.1$  (right panel).

With the exception of the experimental point in the most backward rapidity region, data are compatible with zero and our estimates describe them fairly well. We underline that, in principle, by using a suitable  $x$ -dependent factor,  $\mathcal{N}_g^{(f)}(x)$  (e.g. something like  $N_g (1-x)^\beta$ , with  $N_g \simeq -1$  and a large  $\beta$ ), also the data points at  $x_F < 0$  could be accounted for. On the other hand, this would prevent a description of pion SSAs at small  $p_T$ , which require a strong suppression of the  $f$ -type GSF, in particular in the small- $x$  region (see Fig. 4.3, left panel). If  $J/\psi$  measurements would be confirmed even in future higher statistics samples, this would definitely represent a tension with the pion SSAs, at least within a TMD approach. In this respect, more data, on a wider kinematical range and with better statistics, would be very helpful.

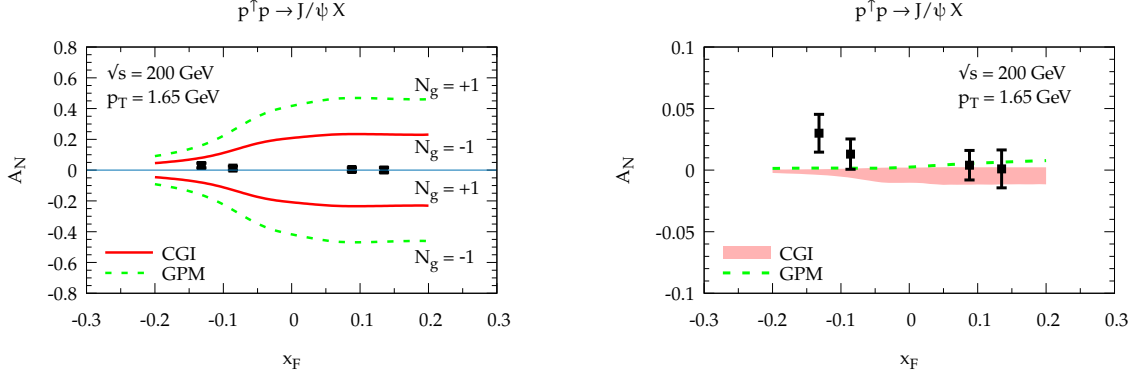


Figure 5.16:  $A_N$  for the process  $p^\uparrow p \rightarrow J/\psi X$  at  $\sqrt{s} = 200$  GeV and  $p_T = 1.65$  GeV as a function of  $x_F$ . Left panel: maximised  $A_N$  in the GPM (green dashed lines) and the CGI-GPM (red solid lines) approaches adopting  $|\mathcal{N}_g(x)| = 1$ . Right panel: estimates within the GPM (green dashed line) and the CGI-GPM approaches,  $f$ -type (red band), obtained adopting the GSFs from the present analysis (see Eqs. (4.55) and (4.57)). Data are from Ref. [189]. Notice the different scales in the two panels.

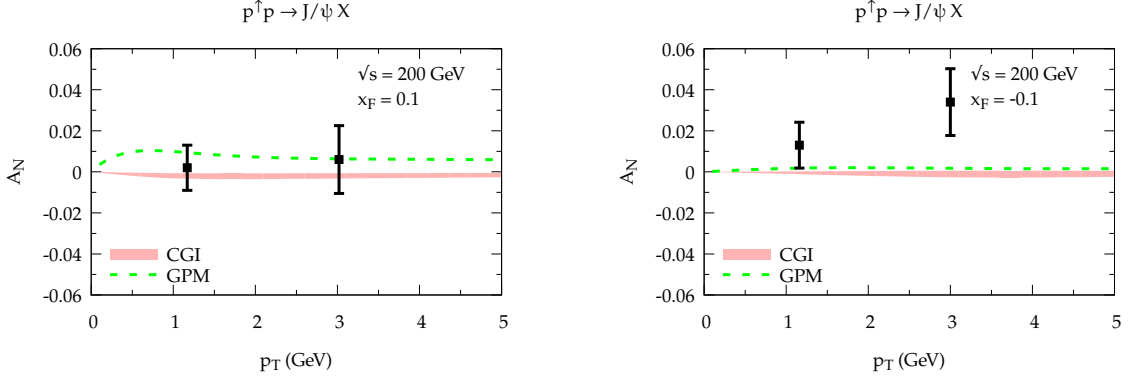


Figure 5.17: Estimates of  $A_N$  for the process  $p^\uparrow p \rightarrow J/\psi X$  at  $\sqrt{s} = 200$  GeV and  $x_F = +0.1$  (left panel) and  $x_F = -0.1$  (right panel) as a function of  $p_T$  in the GPM (green dashed line) and the CGI-GPM approaches (red band), adopting the GSFs as extracted in the present analysis (see Eqs. (4.55) and (4.57)). Data are from Ref. [189].

As the inclusive  $J/\psi$  production is a very interesting tool for studying the gluon Sivers effect, it is worth considering the corresponding analysis for  $A_N$  in  $J/\psi$  production for the kinematics reachable at LHC in the fixed target mode with a transversely polarised target (see the AFTER [78, 79] and LHCb [80, 81] proposals at CERN). In such a configuration one could probe even larger light-cone momentum fractions in the polarised proton, accessing the gluon TMDs in a very interesting and complementary region.

Fig. 5.18 presents our estimates for  $A_N$  for  $pp^\uparrow \rightarrow J/\psi X$  at  $\sqrt{s} = 115$  GeV, at fixed  $p_T = 2$  GeV, as a function of  $x_F$  (left panel) and at fixed rapidity  $y = -2$ , as a function of  $p_T$  (right panel). Notice that in such a configuration the backward rapidity region refers to the *forward* region for the polarised proton target. In particular, we show our predictions within the GPM (thick green dashed lines) and the CGI-GPM (red bands) approaches, together with the corresponding upper/lower positivity bounds (thin lines). As already largely mentioned throughout the past Chapters, we can again say that, from these results, we see that any further experimental information would be extremely useful.

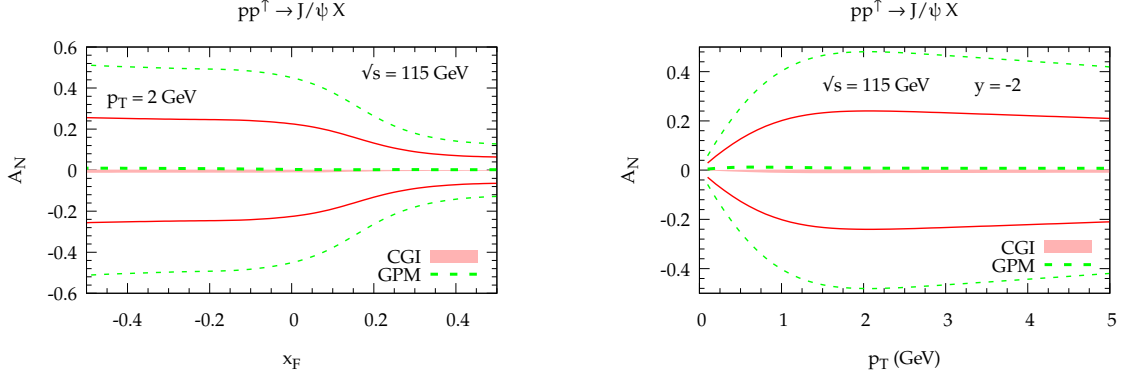


Figure 5.18:  $A_N$  for the process  $pp^\dagger \rightarrow J/\psi X$  at  $\sqrt{s} = 115 \text{ GeV}$  and  $p_T = 2 \text{ GeV}$  as a function of  $x_F$  (left panel) and at rapidity  $y = -2$  as a function of  $p_T$  (right panel). Notice that here negative rapidities correspond to the *forward* region for the polarised proton. Predictions are for the GPM (thick green dashed lines) and the CGI-GPM (red band) approaches (see Eqs. (4.55) and (4.57)). The corresponding maximised contributions for the GPM (thin green dashed lines) and the CGI-GPM (red solid lines) schemes are also shown.

Finally, we take a look to another interesting observable, i.e.  $A_N$  in  $p^\dagger p \rightarrow \gamma X$ . Also this process could give direct access to the gluon Sivers effect. We recall that this reaction can be studied both in the GPM and CGI-GPM approaches, as we have shown in Section 4.1.1, where we have given the complete expressions in the CGI-GPM scheme. Here, we present some estimates for both approaches, saturating their contribution as well as adopting the results of the phenomenological analysis presented in Sections 4.2.1 and 4.2.2. As in the case of inclusive  $\ell p$  scattering (see Section 5.1.3 and Eq. (5.34)), the estimates have been performed adopting  $\mu_0 = 0.8 \text{ GeV}$  as the value of the regulator for the Mandelstam variables. As explained in Section 2.3.1, this ensures avoiding infrared divergences in the propagators.

The most interesting regions are the same for the SSAs for  $\pi^0$  production, i.e. those at mid and slightly backward rapidity and not so large values of  $|x_F|$ . We concentrate on these regions because, at large negative values of  $x_F$ , the integration over the Sivers azimuthal phase washes out the effect. This would partially spoil the analysis proposed in Ref. [219], where the authors discussed this process as a clear tool to access the GSF, also in this kinematical region.

In the top panels of Fig. 5.19 we show the maximised contributions to  $A_N$  for inclusive  $\gamma$  production at  $x_F = 0$  (left) and  $x_F = -0.1$  (right). As one can see, the  $d$ -type term at  $x_F = 0$  is dynamically suppressed, as for the  $\pi^0$  production case: the reason is indeed the same, that is the partial cancellation between the hard  $gq \rightarrow \gamma q$  and  $g\bar{q} \rightarrow \gamma\bar{q}$  processes (see Eq. (4.27), second line). Indeed, this suppression is less pronounced at  $x_F = -0.1$ , where the unpolarised quark and anti-quark TMDs inside the unpolarised proton are probed at larger  $x$  values and therefore are not equally important. Furthermore, in the small  $p_T$  range (up to 3 GeV) the maximised estimates at  $x_F = -0.1$  are more suppressed with respect to those at  $x_F = 0$ : this is once again due to the integration over the Sivers azimuthal phase. Finally, lower panels of Fig. 5.19 show our estimates adopting the results discussed in the previous Chapter for GPM and CGI-GPM estimates. In all cases the values are very small and compatible with zero. Despite of this, a measure of  $A_N$  for direct photon production would be extremely important to test the consistency of the whole approach.



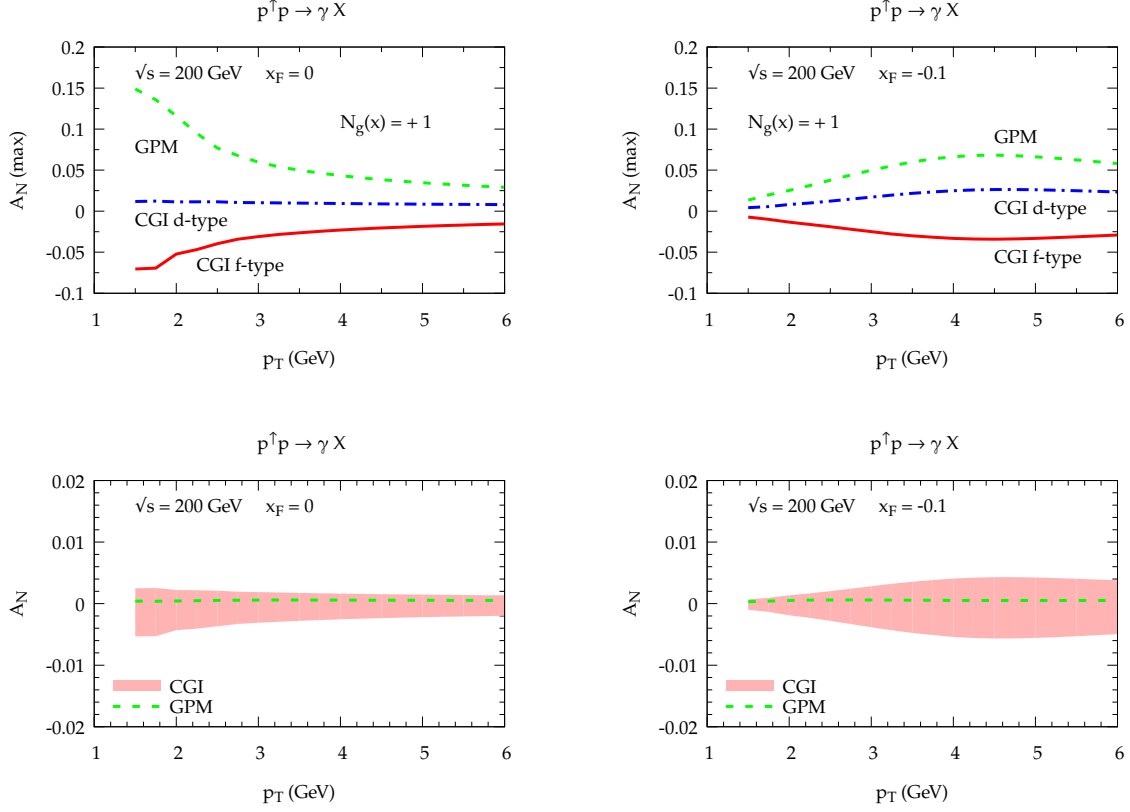


Figure 5.19: Estimates of  $A_N$  for the process  $p^\uparrow p \rightarrow \gamma X$  at  $\sqrt{s} = 200$  GeV as a function of  $p_T$  within the GPM and the CGI-GPM approaches. Upper panels: maximised contributions ( $N_g(x) = +1$ ) at  $x_F = 0$  (left) and  $x_F = -0.1$  (right); lower panels, estimates based on the present analysis (see Eqs. (4.55) and (4.57)): GPM (green dashed line), CGI-GPM (red band).

### 5.3 SUMMARY AND OUTLOOK

In this Chapter we have finally discussed some applications to single scale processes of the GPM (and the CGI-GPM) extractions of polarised TMDs. Specifically, in Section 5.1, we saw that, by considering the kinematical configuration in which the (unobserved) scattered lepton is almost collinear to the emitted photon, one can define a Weizsäcker-Williams distribution for the photon into the lepton, in analogy with the partonic distributions of quarks and gluons into nucleons. Moreover, by approximating the lepton as a source of real photons, we could write an ansatz for the WW contribution to transverse single-spin asymmetries for  $\ell p^\uparrow \rightarrow hX$  processes. Using then the new computed contribution, we were able to improve the descriptions of HERMES data, and for the first time we could consider the so-called “anti-tagged” data sample, the one dominated by quasireal photoproduction. In doing this, we have adopted a specific parametrisation for the WW distribution, the one in Eq. (5.10). It would be surely interesting to test some other distributions, maybe with different mathematical expressions. A word of caution should be used while thinking at a TMD WW distribution, as the definition of the leptonic PDF is strictly related to an integration over the “intrinsic” transverse momentum of the photon, thus leaving a pure collinear function.

Still in the context of the WW contribution to  $A_N$  for inclusive  $\ell p$  processes, we have also seen that a measurement of inclusive jet production could be feasible at the future EIC. This



would also allow to be sensitive to the gluon Sivers effect, whose corresponding TMD functions are, as largely shown in the previous Chapter, quite unknown. In studying the inclusive jet production, we have assumed that the jet coincides with the parton  $c$  produced in the  $a\gamma \rightarrow cd$  partonic subprocess. Such approximation is of course a leading order one. Surely, it would be interesting to extend this study by using jet functions, that have recently attracted a lot of interest in different approaches and for different processes (see e.g. Refs. [220–224]). Finally, regarding inclusive  $\ell p$  processes, it would be also very interesting to extend the study presented in this Chapter to the CGI-GPM approach. Again, such investigation would allow to add more details to the study of the poorly known gluon Sivers function.

The other topic we covered in this Chapter is the comparison between the GPM and the CGI-GPM in inclusive  $J/\psi$  and photon production from polarised  $pp$  processes. This, together with the GSFs study on  $D$ -meson production of Section 4.2.2, helped us to highlight the role of quarkonium associated observables, that can represent a very useful tool for TMD studies. Again, we have seen that a good description of the few existing experimental data-points is obtained for inclusive  $J/\psi$  production within both the GPM and the CGI-GPM approaches. Further measurements at existing and future experiments, especially for inclusive photon production, would certainly help in deepening our scarce knowledge on the gluon Sivers effect.

# 6

## A tool for quarkonia

In Chapters 4 and 5 we have seen that quarkonia represent another valuable tool for studying spin and polarisation effects. They especially represent a direct way to access gluon TMDs and so, eventually, they will be extremely useful to assess the gluon contribution to the nucleon spin. Before getting to the conclusion, we would like to present a work in the context of an upcoming project to which the author has contributed [225, 226]. So far, this work does not include any TMD-related part, but in the future it would be certainly suitable for TMD studies. Here, we would like to briefly introduce the preliminary results for this project, focussing on its quarkonia-related side.

### 6.1 THE NLOACCESS PROJECT

Let us start by introducing the NLOAccess project. This project is part of a broader European Union Horizon 2020 (H-2020) submission, *STRONG-2020*, that has been recently approved. *STRONG-2020* consists in a total of 32 Work Packages (WPs), and involves 44 institutions over 16 countries. Moreover, 7 Transnational Infrastructures will contribute to it: COSY, MAMI, ELSA, GSI, LNF, CERN and ECT\*.

*NLOAccess* is one of the WPs included in the *STRONG-2020* proposal. Its goal is to create a virtual, automated and online platform, that will give access to a collection of automated tools, generating scientific codes, thus allowing anyone to evaluate observables of scattering involving hadrons, such as production rates or kinematical properties. *Automation* and *versatility* are the key words of the project: indeed, there will be no need to pre-code any of the tools. For instance, this would allow a random user to request, for the first time, the computation of a specific reaction which nobody thought about before. Moreover, NLOAccess will be designed in such a way that any user would be able to test the code, demanding the NLOAccess servers to make the computation, so with no direct CPU cost on the user machine. Of course, if one user desires to download and use the code on its own computer, that would be feasible. So, in the way that NLOAccess will be designed, it would essentially results an online dynamical library.

NLOAccess is conceived in such a way that any code that could be compiled and executed via bash, i.e. the Unix terminal, could be added to the library. At the moment, two codes are planned to be part of NLOAccess:

- the MADGRAPH ensemble, heavily used by the high-energy physics community, extended in such a way to deal with meson and heavy-ion beams, and including its NLO version [227, 228];
- HELAC-Onia, a matrix element and event generator for heavy quarkonium physics [229, 230].

Although MADGRAPH is already available online, its web version is limited to LO calculations. The NLO computations are of course heavier, and their online implementation is under consideration. NLOAccess is likely to include it in future. At the moment, the only included code is HELAC-Onia, for which an online version already exists, as we will see in the next Section.

### WHY NLOACCESS?

As the time goes by, high energy physics moves towards higher and higher precision. This requires new tools for the research. These tools are often related to numerical computation. It is not a secret that, from the numerical point of view, the more one goes beyond leading order calculation, the more CPU power is in principle required. Indeed, simulations in high energy, nuclear and hadronic physics are often costly in terms of CPU and time consumption, especially because most of the time Monte Carlo computations are required. Moreover, different tools are necessary to pin down different problems. With respect to this, NLOAccess would then represent a very important tool to help future researches in high energy, nuclear and hadron physics, by offering an automated, virtual access to numerous tools and codes.

## 6.2 HELAC-ONIA AND ITS WEB REALISATION

In this Section we shortly take a look at HELAC-Onia and its web realisation. HELAC-Onia's first version has been first released back in January 2013, and was described in Ref. [229]. Its 2.0 version has then been published in Ref. [230]. This code is a matrix element and event generator for heavy quarkonium physics. It relies on an effective theory of QCD, the so-called Non-Relativistic QCD (NRQCD) framework [231] and on off-shell recursion relations [232] for calculating helicity amplitudes for general processes with  $n$  external legs.

For illustration, and without getting into details, we can say that within NRQCD factorisation one can write the cross section for inclusive production of a heavy quarkonium  $Q$  from  $pp$  scattering in a factorised form, with perturbative, short distance components and the nonperturbative, Long Distance Matrix Elements (LDMEs), as:

$$\sigma(pp \rightarrow Q + X) = \sum_{ij} \sum_n \int dx_1 dx_2 f_{i/p}(x_1) f_{j/p}(x_2) \hat{\sigma}(ij \rightarrow Q\bar{Q}[n] + X) \langle \mathcal{O}_n^Q \rangle \quad (6.1)$$

where

- $f_{i/p}(x_1) (f_{j/p}(x_2))$  is the collinear partonic distribution for the parton  $i$  ( $j$ ) into the first (second) proton in the initial state;
- $\hat{\sigma}(ij \rightarrow Q\bar{Q}[n] + X)$  is the short distance cross section for producing a heavy quark pair  $Q\bar{Q}$  into a specific Fock state  $n$ ;

- $n = {}^{2S+1}L_J^c$  represents the Fock state in the spectroscopic form, with  $S, L, J$  being the spin, orbital momentum and total angular momentum, respectively;  $c = 1, 8$  represent the colour state of the intermediate  $Q\bar{Q}$  pair (1 being colour-singlet – CS – and 8 being a colour-octet – CO – state);
- $\langle \mathcal{O}_n^Q \rangle$  is the LDME; their physical interpretation is, in analogy with fragmentation functions, a probability for a heavy quark pair in the Fock state  $n$  to evolve into a quarkonium  $Q$ .

LDMEs are usually estimated from phenomenological models and fitted from experimental data or calculated on the lattice (see e.g. Refs. [233–237]). As the number of Fock state  $n$  is infinite, we could have in principle an infinite number of LDMEs. What really happens is that, thanks to the power counting rules in NRQCD, there is only a finite amount of Fock state  $n$  for a given quarkonium  $Q$ . That is due to the fact that NRQCD calculations are limited to a specific order of  $v$ , the relative velocity of the heavy quark pair that forms the quarkonium, that represents, together with  $\alpha_s$ , one of the two expansion parameters of NRQCD.

All the details regarding HELAC-Onia can be found in Refs. [229, 230]. Here we limit ourselves in presenting the most interesting features of HELAC-Onia, that are:

- computations are made within the Standard Model, but the BSM extension is doable;
- different kinds of calculation are feasible, such as for instance multiple quarkonia production, event generation, yields vs polarisation, angular distributions of quarkonia decays;
- a reweighting method for estimating renormalisation/factorisation scale and PDF uncertainties is implemented;
- the code is interfaced with the widely used Les Houches Accord PDF library (LHAPDF) [238];
- interfaces with parton shower Monte Carlo programs, such PYTHIA 8 [239] for hadronic showers and QEDPS [240–243] for QED showers.

### 6.2.1 HELAC-ONIA WEB

As already mentioned, HELAC-Onia is one of the codes that will be part of the NLOAccess platform [225, 226]. To be more precise, the author contributed to the web realisation of HELAC-Onia, which is already online, and it is reachable at the address <https://nloaccess.in2p3.fr/H0>. HELAC-Onia is actually the first code available on NLOAccess, and its relative online platform is explicative of the objectives that NLOAccess has in terms of automation, versatility, and user-friendliness.

HELAC-Onia Web has been realised using *Flask*, a Python microframework<sup>1</sup>. This framework is very interesting, relatively easy and flexible to use. Indeed, by realising a simple Python application, that contains every route of the website (i.e. every single webpage) as a function, one can easily design a site capable of accomplish many different tasks. Flask

---

<sup>1</sup><https://flask.pocoo.org>



Figure 6.1: Schematic representation of the two-steps registration process for HELAC-Onia Web: 1. registration request, 2. e-mail address validation, 3. registration completion.

has several extensions, manages automatically the server side and is naturally designed for dealing with databases, e-mails, cloud storage, forms, login/logout management and many more things. All of this is also done by using modern safety and encryption measures, that guarantee the security of sensitive data.

## REGISTRATION PROCESS

For safety reason, the registration procedure to NLOAccess is realised in two different steps, as schematically depicted in Fig. 6.1. First of all, one has to request the registration via the link present on the HELAC-Onia website, providing then his/her e-mail address. Note that only institutional e-mail addresses (no Gmail or .com domains) are accepted. Then, one has to validate his/her own address via the confirmation link provided in an e-mail message. Finally, after the e-mail address validation, the user is redirected to the page for the completion of his/her registration to the NLOAccess platform.

After the registration is completed, the user is welcomed with another e-mail, that informs him/her of the account activation. In the same message he/she will find a link to a personal and encrypted *OwnCloud* (OC) folder. OwnCloud is an open source cloud file sharing, available at <https://owncloud.org/>. The OC folder is used to upload the results of any completed computation. Moreover, it is protected by a password, which is the *same* chosen by the user during the registration process.

## PROCESS GENERATION AND RUN MANAGEMENT

The process generation is also a quite simple procedure. Plenty of instructions and examples are present in Refs. [229, 230], but some tips and the HELAC-Onia syntax for quarkonia and SM particles are also illustrated on the website. The first way to launch a computation on the NLOAccess servers is represented by a classic file input. Either the user can input his/her own file, created following HELAC-Onia syntax, or either the file can be created online, with a guided procedure. The guided creation of the input file is, at the moment, in a preliminary version. An online guide is planned to be published in the near future. In broad terms, the basic structure of the input file is the following:

```

generate { process }
set { parameter }={ value }
:
launch
  
```

where the braces indicate that a value has to be inserted. The first line contains the process that the user wants to generate, and the value of process should be inserted following the

HELAC-Onia syntax. Then, after specifying the process, one can modify the default values of the parameters of HELAC-Onia itself, via the set command. Again, every parameter has a specific name defined into the HELAC-Onia code. There are several parameters that can be modified, that refers to many different features of the process and the code itself, such as:

- collisions parameters;
- theory parameters;
- variables for the Monte Carlo setup;
- PDFs related parameters;
- parameters governing kinematical cuts;
- quarkonium specific parameters (e.g. the values of different LDMEs);
- physical constants, both in the electroweak and in the QCD sector, (e.g.  $M_Z$  or  $M_W$ , the masses of the Z and W bosons, or the quarks mass).

Moreover, the kind of output can be specified (ROOT, Gnuplot, Top Drawer or Les Houces Event format are, at the moment, the available ones). After all the settings, one should put the launch command, in order to let HELAC-Onia run the computation.

An example of an input file could be the one for the production of a double  $J/\psi$  plus a gluon at the LHC at 14 TeV, that reads

```
generate p p > cc~(3S11) cc~(3S11) g
set energy_beam1 = 7.D3
set energy_beam2 = 7.D3
launch
```

where  $cc\sim(3S11)$  is the HELAC-Onia syntax for a  $J/\psi$ , and  $energy\_beam1$ ,  $energy\_beam2$  are the parameters (in GeV units) that control the energy of the two colliding proton beams.

Now, what about the results of a computation? As already mentioned, they are automatically collected by the system, and uploaded on the personal OC user folder. The user is also alerted via an e-mail notification, where the name of the new directory containing the results is indicated. Unless the user themselves have set some specific flag for the output to be false, the user will find the plots in .pdf format, ready to be seen.

Very recently, new functionalities, in a preliminary form, have been added to HELAC-Onia Web. These refer both to the runs. Now the users have in fact the possibility to see the run live status, i.e. how many jobs are running for a given requested process generation, and, if needed, to remove a given run. E-mail alerts are also used to inform the user whether a computation has failed. Moreover, the history of the past runs can be seen in the “run history” in the user menu.

All of this represent the automated procedure that HELAC-Onia Web offers to its users. Again, we stress that in doing this, the only effort that the user is required to make is to decide which process has to be generated, specifying, if desired, some settings. Then he/she

has just to wait for the results, and in going to see them he/she will find the plots, generated on the fly, and ready to be used. Of course, also the raw output is given, so that one could also make his/her own plots following their wished style. We underline that, since the OwnCloud system is used, one can also send a run on the website and, if the NLOAccess personal folder is synchronised on a personal device, the user will directly receive the results on his/her own device.

### 6.3 FUTURE DEVELOPEMENTS

The features presented so far represent of course the first preliminary form of NLOAccess. The STRONG-2020 project is starting now, so the work made up to now for NLOAccess is still at an embryonic stage. Nonetheless, HELAC-Onia Web is the first tool available on NLOAccess, and shows the features of a working online platform. As it is still at its early stages, it is important to understand what are the optimal functionalities that the users desire. So, the user's feedback is very important, and, at this stage, has a pivotal role in designing a user friendly platform. We encourage the users to send e-mails to the NLOAccess team, in order to have more points to work on and to improve.

Regarding future developements, while for the moment we refer the users to Refs. [229, 230], we hope to provide an online user guide. Moreover, we would like to have another page, with a minimal interface where some specific physical settings can be modified by the user. Hopefully, such interface will become available in the near future.



# 7

## Conclusions

By means of TMD distributions and fragmentation functions, polarisation phenomena and transverse momentum effects allow us to study, in the momentum space, the three-dimensional structure of the nucleons, as well as the hadroproduction mechanism. Since the early 1990s, TMD studies continuously gained more and more interest on both theoretical and experimental sides. In the meanwhile, phenomenology, the bridge connecting theory and experiment, advanced, and new ideas coming from the theory can now be tested against experimental data. Phenomenological extractions are now trying to push for embedding the TMD formalism in its full glory, and the study of single-spin asymmetries keeps being a fruitful field for testing TMD theory itself.

Although the huge effort made so far, it is useful to underline that, phenomenological extractions of (un)polarised TMDs are still at an early stage, especially if we compare them with the situation for collinear PDFs and FFs. A careful assessment of phenomenological results is so required to get more and more precise information on the distribution of partons inside the nucleons and, ultimately, the nucleon spin decomposition. In this spirit, we presented here some results about the extractions of polarised quark and gluons TMDs and their use in comparing theoretical predictions against existing experimental data.

As illustrated in Chapter 3, current data on Sivers asymmetry give us only partial information on the behaviour of the quark Sivers function. In fact, even by using a very simple parametrisation, one is able to obtain very good results in fitting it. Moreover, by carefully evaluating the uncertainties on the extracted function, we could underline the limited knowledge we still have on the Sivers function. Emphasis has been put on the outcome of different choices made on the chosen phenomenological model. As we have seen in Sections 3.2.1 and 3.2.2, letting some parameters to vary does not change the outcome of the fit, but allows to have a more faithful error estimation on the extracted function, especially when looking at the kinematical regions where data are scarce or absent.

With the same spirit, we could test whether any visible signal of scale dependence is present in the current data. Some hints of evolution for the  $u$ -quark Sivers function have been observed, while for the  $d$ -quark one the uncertainty is still too large to draw any definitive conclusion. New data from the COMPASS Collaboration on deuteron target could certainly help in this respect. Moreover, we expect that in future, both JLab data and EIC data will help in covering respectively high- and low- $x$  regions.

Relaxing some initial assumptions for transversity distribution allowed us to test whether its corresponding bound, the Soffer bound (SB), can be really observed in the SIDIS data. It turned out that, while for the  $u_v$  transversity function the situation is under control,  $d_v$  transversity seems to violate the SB. But, as explained in Section 3.3.2, statistically speaking  $d_v$  transversity fulfills its bound within the current uncertainty. At the same time, this seems to have a positive effect on calculating the tensor charges. In fact, the tension between phenomenological extractions and lattice calculation seems to ease, especially for the isovector tensor charge case. Again, having more experimental measurements would be certainly helpful.

While the situation for quark TMDs is becoming more and more promising, and although they represent a very appealing topic, polarised gluon TMDs are surely more difficult to study. In fact, even if they can be accessed at present colliders like the LHC, only few data-points are present for these kind of functions, such as the gluon Boer-Mulders or the gluon Sivers function. The former has been recently analysed in Refs. [75, 244] (the last work including TMD evolution), while the latter has been studied in Chapter 4, in the context of the GPM and its colour gauge invariant version, the CGI-GPM. This last model is very interesting for various reasons. For instance, it shows strong analogies with the collinear twist-3 formalism and, within this approach, one is also able to recover the predicted sign change of the Sivers function probed in SIDIS and Drell-Yan processes.

In Section 4.1 we have shown that, taking into account initial and final state interactions in a one-gluon exchange approximation, two independent GSFs emerge in CGI-GPM, the  $f$ - and  $d$ -type GSF (the name recalling the two different way in which colour can be neutralised). Then, in Section 4.2.2, we have been able to put the first constraints on the size of such functions, by means of analysing inclusive pion production data at midrapidity, together with the ones for  $\mu^\pm$  production from  $D$ -meson decay. Unfortunately, we cannot draw any definitive conclusion on the sign of the two GSFs, as we have found that two different combinations (see Eq. (4.57)) can give a satisfactory description of the data. Nonetheless, these first hints point to having an  $f$ -type GSF with opposite sign and different size with respect to the  $d$ -type one.

Phenomenological extractions then allowed us to compare our GPM predictions against existing data. Indeed, Chapter 5 covered two phenomenological studies. The first one regards a very interesting process,  $\ell p^\uparrow \rightarrow hX$ , representing a bridge between SIDIS and inclusive  $p^\uparrow p$  processes, and that could be tested at current experiments like COMPASS or future facilities such as the EIC. By using phenomenological extractions of the (quark and gluon) Sivers and Collins functions, we presented an updated work on the single-spin asymmetries in the aforementioned process, concentrating on the role of quasireal photon exchange. Under the Weizsäcker-Williams (WW) approximation, we could compute new contribution to  $A_N$ , obtaining a very nice description of inclusive HERMES data and, for the first time, describing (still with some discrepancies for  $\pi^+$  production), the so called anti-tagged data, the ones dominated by quasireal photon exchange. Such discrepancies result mitigated by more recent Sivers and Collins extractions. Predictions for ongoing and future experiments (JLab, COMPASS and the EIC) were also given. It turned out that, in some specific cases, while in the asymmetries this contribution is partially compensated by the ratio, the unpolarised cross section is dominated by the WW contribution.

The second phenomenological analysis presented in Chapter 5 completes the work on GPM and CGI-GPM estimates of the gluon Sivers function(s). By using the GSFs extracted within the GPM (Section 4.2.1) and CGI-GPM (Section 4.2.2), we compared our predictions for inclusive  $J/\psi$  to RHIC data, and we showed the ones for photon production in polarised  $pp$  processes. In doing this, we tried to see whether one could discriminate between the two versions of the GPM. No definitive conclusion could be drawn, but surely future experiment like the proposed ones at the LHC [78–81] would help in this respect.

Finally, in Chapter 6, a new project, at the moment not directly related to TMDs, has been presented. NLOAccess and HELAC-Onia Web are still at an embryonic state, but the potential of this project for helping research in hadron, nuclear and particle physics is quite high. Furthermore, quarkonia production studies represent a nice means to study gluon TMDs, and an extension of HELAC-Onia to such kind of studies would be certainly fruitful for the whole TMD community.

## OUTLOOK AND FUTURE DEVELOPEMENTS

Recalling that we have already given some outlooks and future developements at the end of every Chapter, we would like to stress again some points here.

The path to the comprehension of the three-dimensional structure of nucleons is not yet finished. So, every information that we can obtain from experimental data has to be weighted and carefully analysed. At the same time, it is useful to refine, when possible, phenomenological analyses. To this extent, in future phenomenological analyses, improving the error estimation method would be certainly helpful. Also, including more data containing information on Sivers, transversity and Collins function would surely help in improving the modelisation of such TMDs.

One example of possible improvements in TMD models is the inclusion of a kinematical dependence of TMD Gaussian widths. As recently showed by Belle Collaboration measurements [245], fragmentation function widths seem to depend on  $z$ , the collinear momentum fraction. It would not be certainly surprising to start including such effects in the phenomenological extractions of the widths and, consequently, of the polarised TMDs, as already done by Pavia group in the case of unpolarised TMDs extraction [119].

Phenomenological approaches can be improved as well. The CGI-GPM offers indeed a way to improve the GPM itself. A deeper understanding of such model could maybe help in understanding the analogies and the differences between different approaches, namely GPM and collinear twist-3, having so a broader point of view in interpreting results from single-spin asymmetries in inclusive processes.

The work presented here in this thesis helps in trying to take into account all the possible uncertainties and the impact of any choice in phenomenological analyses. The more we will better assess and reduce errors on the phenomenological extractions, the more we will understand about TMD effects in the existing data. In the medium/long term, a new Electron-Ion Collider would most likely be built, and future fixed-target experiments at the LHC could be developed. A careful, step by step, and down-to-earth approach in tackling TMD effects is then required to be ready when new and (hopefully) more precise data will come.



# Kinematics and helicity frames

Here we briefly give some details about the full  $\mathbf{k}_\perp$ -dependent kinematics and the helicity frames used in the context of the GPM.

## DETAILED $\mathbf{k}_\perp$ KINEMATICS

Following Appendix A of Ref. [127], we give a detailed account of the partonic kinematics with the inclusion of transverse momentum effects.

We recall that the hadronic reaction  $A B \rightarrow C X$  is considered in the  $AB$  center of mass frame, with  $A$  moving along the positive  $Z_{\text{c.m.}}$ -axis, and with the scattering plane fixed as the  $(XZ)_{\text{c.m.}}$  plane. All masses are neglected. The four-momenta of hadrons  $A, B, C$  are given by

$$p_A^\mu = \frac{\sqrt{s}}{2} (1, 0, 0, 1), \quad p_B^\mu = \frac{\sqrt{s}}{2} (1, 0, 0, -1), \quad p_C^\mu = (E_C, p_T, 0, p_L), \quad (\text{A.1})$$

with  $E_C = \sqrt{p_T^2 + p_L^2}$  and  $s = (p_A + p_B)^2$ .

For massless partons  $a, b$  inside hadrons  $A, B$  light-cone momentum fractions are introduced

$$x_a = \frac{p_a^+}{p_A^+} = \frac{p_a^0 + p_a^3}{p_A^0 + p_A^3}, \quad x_b = \frac{p_b^+}{p_B^+} = \frac{p_b^0 - p_b^3}{p_B^0 - p_B^3}, \quad (\text{A.2})$$

along with the transverse momenta  $\mathbf{k}_{\perp a}, \mathbf{k}_{\perp b}$ . Their four-momenta then read

$$\begin{aligned} p_a^\mu &= x_a \frac{\sqrt{s}}{2} \left( 1 + \frac{k_{\perp a}^2}{x_a^2 s}, \frac{2k_{\perp a}}{x_a \sqrt{s}} \cos \phi_a, \frac{2k_{\perp a}}{x_a \sqrt{s}} \sin \phi_a, 1 - \frac{k_{\perp a}^2}{x_a^2 s} \right), \\ p_b^\mu &= x_b \frac{\sqrt{s}}{2} \left( 1 + \frac{k_{\perp b}^2}{x_b^2 s}, \frac{2k_{\perp b}}{x_b \sqrt{s}} \cos \phi_b, \frac{2k_{\perp b}}{x_b \sqrt{s}} \sin \phi_b, -1 + \frac{k_{\perp b}^2}{x_b^2 s} \right), \end{aligned} \quad (\text{A.3})$$

where  $k_{\perp a, b} = |\mathbf{k}_{\perp a, b}|$  and  $\phi_{a, b}$  are the azimuthal angles of parton  $a, b$  three-momenta in the hadronic c.m. frame.

The four-momentum of the fragmenting parton  $c$  is given in terms of the observed hadron momentum  $p_C^\mu$ , of the light-cone momentum fraction  $z = p_C^+ / p_c^+$  and of the transverse momentum  $\mathbf{k}_{\perp C}$  of hadron  $C$  with respect to the parton  $c$  light-cone direction. In the hadronic c.m. frame,  $\mathbf{k}_{\perp C}$  is generally written as:

$$\mathbf{k}_{\perp C} = k_{\perp C} (\sin \theta_{k_{\perp C}} \cos \phi_{k_{\perp C}}, \sin \theta_{k_{\perp C}} \sin \phi_{k_{\perp C}}, \cos \theta_{k_{\perp C}}), \quad (\text{A.4})$$

and impose the orthogonality condition  $\mathbf{k}_{\perp C} \cdot \mathbf{p}_c = 0$  via the  $\delta$ -function  $\delta(\mathbf{k}_{\perp C} \cdot \hat{\mathbf{p}}_c)$ , where  $\hat{\mathbf{p}}_c$  is the unit vector along the direction of motion of parton  $c$ . The parton four-momentum,  $p_c^\mu = (E_c, \mathbf{p}_c)$ , can then be written as

$$\begin{aligned} \mathbf{p}_c &= \frac{E_c}{\sqrt{E_C^2 - k_{\perp C}^2}} (p_T - k_{\perp C} \sin \theta_{k_{\perp C}} \cos \phi_{k_{\perp C}}, -k_{\perp C} \sin \theta_{k_{\perp C}} \sin \phi_{k_{\perp C}}, p_L - k_{\perp C} \cos \theta_{k_{\perp C}}), \\ E_c &= \frac{E_C + \sqrt{E_C^2 - k_{\perp C}^2}}{2z}, \end{aligned} \quad (\text{A.5})$$

and the orthogonality condition  $\mathbf{k}_{\perp C} \cdot \mathbf{p}_c = 0$  implies

$$\begin{aligned} d^3 \mathbf{k}_{\perp C} \delta(\mathbf{k}_{\perp C} \cdot \hat{\mathbf{p}}_c) &= k_{\perp C} dk_{\perp C} d\theta_{k_{\perp C}} d\phi_{k_{\perp C}} \frac{\sqrt{E_C^2 - k_{\perp C}^2}}{p_T \sin \phi_{k_{\perp C}}^0} \\ &\times \left[ \delta(\phi_{k_{\perp C}} - \phi_{k_{\perp C}}^0) + \delta(\phi_{k_{\perp C}} - (2\pi - \phi_{k_{\perp C}}^0)) \right], \end{aligned} \quad (\text{A.6})$$

$$\cos \phi_{k_{\perp C}}^0 = \frac{k_{\perp C} - p_L \cos \theta_{k_{\perp C}}}{p_T \sin \theta_{k_{\perp C}}}, \quad 0 \leq \phi_{k_{\perp C}}^0 \leq \pi. \quad (\text{A.7})$$

This allows to perform directly the integration over  $\phi_{k_{\perp C}}$  (notice that there are two possible solutions to be considered).

The factor  $J(z, k_{\perp C})$  entering the master formula, Eq. (2.40), is the Jacobian factor connecting the parton  $c$  to hadron  $C$  invariant phase space, defined as

$$\frac{d^3 \mathbf{p}_c}{E_c} = \frac{1}{z^2} J(z, k_{\perp C}) \frac{d^3 \mathbf{p}_C}{E_C}. \quad (\text{A.8})$$

With intrinsic motion, for massless partons and hadrons, it takes the form of Eq. (2.43), while for collinear and massless particles reduces simply to  $J = 1$ .

With the expression of parton momenta given in Eqs. (A.3) and (A.5) one can calculate the partonic Mandelstam invariants:

$$\hat{s} = (p_a + p_b)^2 = x_a x_b s \left[ 1 - 2 \frac{k_{\perp a} k_{\perp b}}{x_a x_b s} \cos(\phi_a - \phi_b) + \frac{k_{\perp a}^2 k_{\perp b}^2}{x_a^2 x_b^2 s^2} \right], \quad (\text{A.9})$$

$$\hat{t} = (p_a - p_c)^2 = \frac{T}{z}, \quad \hat{u} = (p_b - p_c)^2 = \frac{U}{z}, \quad (\text{A.10})$$

$$\hat{s} \delta(\hat{s} + \hat{t} + \hat{u}) = z \delta \left( z + \frac{T + U}{\hat{s}} \right), \quad (\text{A.11})$$

where

$$\begin{aligned}
T = & -x_a \sqrt{s} \frac{E_C + \sqrt{E_C^2 - k_{\perp C}^2}}{2\sqrt{E_C^2 - k_{\perp C}^2}} \\
& \times \left\{ \left( 1 + \frac{k_{\perp a}^2}{x_a^2 s} \right) \sqrt{E_C^2 - k_{\perp C}^2} - \frac{2k_{\perp a}}{x_a \sqrt{s}} \cos \phi_a (p_T - k_{\perp C} \sin \theta_{k_{\perp C}} \cos \phi_{k_{\perp C}}) \right. \\
& \left. + \frac{2k_{\perp a}}{x_a \sqrt{s}} k_{\perp C} \sin \phi_a \sin \theta_{k_{\perp C}} \sin \phi_{k_{\perp C}} - \left( 1 - \frac{k_{\perp a}^2}{x_a^2 s} \right) (p_L - k_{\perp C} \cos \theta_{k_{\perp C}}) \right\} \quad (\text{A.12})
\end{aligned}$$

$$\begin{aligned}
U = & -x_b \sqrt{s} \frac{E_C + \sqrt{E_C^2 - k_{\perp C}^2}}{2\sqrt{E_C^2 - k_{\perp C}^2}} \\
& \times \left\{ \left( 1 + \frac{k_{\perp b}^2}{x_b^2 s} \right) \sqrt{E_C^2 - k_{\perp C}^2} - \frac{2k_{\perp b}}{x_b \sqrt{s}} \cos \phi_b (p_T - k_{\perp C} \sin \theta_{k_{\perp C}} \cos \phi_{k_{\perp C}}) \right. \\
& \left. + \frac{2k_{\perp b}}{x_b \sqrt{s}} k_{\perp C} \sin \phi_b \sin \theta_{k_{\perp C}} \sin \phi_{k_{\perp C}} + \left( 1 - \frac{k_{\perp b}^2}{x_b^2 s} \right) (p_L - k_{\perp C} \cos \theta_{k_{\perp C}}) \right\}. \quad (\text{A.13})
\end{aligned}$$

The phase space integrations must obey some constraints, originating from physical requests. Besides the trivial bounds  $0 < x_{a,b}, z < 1$ ,  $0 \leq \phi_{a,b} \leq 2\pi$  and  $0 \leq \theta_{k_{\perp C}} \leq \pi$ , is required that, even including intrinsic transverse momentum effects, *a*) each parton keeps moving along the same direction as its parent hadron,  $\mathbf{p}_{a(b)} \cdot \mathbf{p}_{A(B)} > 0$ , and *b*) the parton energy is not larger than the parent hadron energy,  $E_{a(b)} \leq E_{A(B)}$ . This implies the following bounds

$$k_{\perp a(b)} / \sqrt{s} < \min \left[ x_{a(b)}, \sqrt{x_{a(b)}(1 - x_{a(b)})} \right]. \quad (\text{A.14})$$

Analogously, for the fragmentation process  $c \rightarrow C + X$  we require  $\mathbf{p}_c \cdot \mathbf{p}_C > 0$  and  $E_c \leq E_C$  (both fulfilled by Eq. (A.5)), where the solution  $E_c = \left[ E_C - \sqrt{E_C^2 - k_{\perp C}^2} \right] / (2z)$  is consistently disregarded). The last constraint implies the following bound on  $k_{\perp C}$ , at fixed  $z$  values:

$$k_{\perp C} / E_C \leq 1 \quad (z \leq 1/2) \quad k_{\perp C} / E_C \leq 2\sqrt{z(1-z)} \quad (z > 1/2). \quad (\text{A.15})$$

Finally, by requiring  $|\cos \phi_{k_{\perp C}}^0| \leq 1$ , see Eq. (A.7), a further constraint on  $k_{\perp C}$  holds at fixed  $\theta_{k_{\perp C}}$ :

$$p_L \cos \theta_{k_{\perp C}} - p_T \sin \theta_{k_{\perp C}} \leq k_{\perp C} \leq p_L \cos \theta_{k_{\perp C}} + p_T \sin \theta_{k_{\perp C}}. \quad (\text{A.16})$$

## HELICITY FRAMES

Our physical observables are computed in the  $AB$  c.m. frame, with axes denoted by  $X_{\text{c.m.}}$ ,  $Y_{\text{c.m.}}$ ,  $Z_{\text{c.m.}}$ . The helicity frame of a particle with momentum  $\mathbf{p}$  along the direction  $\hat{\mathbf{p}} = (\sin \theta \cos \varphi, \sin \theta \sin \varphi, \cos \theta)$ , as defined in the hadronic frame, can be reached by performing

on the overall frame the rotations [129]

$$R(\varphi, \theta, 0) = R_{Y'}(\theta) R_{Z_{\text{c.m.}}}(\varphi). \quad (\text{A.17})$$

The first is a rotation by an angle  $\varphi$  around the  $Z_{\text{c.m.}}$ -axis and the second is a rotation by an angle  $\theta$  around the new  $Y'$ -axis, i.e. the axis obtained after the first rotation.

This results in the helicity frames with axes along the following directions (expressed in the hadronic frame):

$$\hat{X}_A = \hat{X}_{\text{c.m.}} \quad \hat{Y}_A = \hat{Y}_{\text{c.m.}} \quad \hat{Z}_A = \hat{Z}_{\text{c.m.}} \quad (\text{A.18})$$

for a hadron A moving along  $+\hat{Z}_{\text{c.m.}}$ ,

$$\hat{X}_B = \hat{X}_{\text{c.m.}} \quad \hat{Y}_B = -\hat{Y}_{\text{c.m.}} \quad \hat{Z}_B = -\hat{Z}_{\text{c.m.}} \quad (\text{A.19})$$

for a hadron B moving along  $-\hat{Z}_{\text{c.m.}}$ ,

$$\hat{x} = \hat{y} \times \hat{z} \quad \hat{y} = \frac{\hat{Z}_{\text{c.m.}} \times \hat{p}}{|\hat{Z}_{\text{c.m.}} \times \hat{p}|} = \hat{Z}_{\text{c.m.}} \times \hat{k}_\perp \quad \hat{z} = \hat{p} \quad (\text{A.20})$$

for a generic particle  $\mathbf{p}$ . Notice that  $\hat{k}_\perp$  is the unit transverse component (with respect to the  $Z_{\text{c.m.}}$ -direction) of  $\mathbf{p}$ , and that it lies in the  $(xz)$  plane.



# B

## Helicity formalism

Here we give some details about the quantities that appear in the helicity formalism. Specifically, we will take a look at the properties of the terms entering in the expression of the GPM master formula for  $A(S_A) + B(S_B) \rightarrow C + X$  processes, Eqs. (2.40) and (2.46), and for the parts appearing in the single-spin asymmetries coming from sum and difference of kernels with assigned polarisation, Eqs. (2.51)–(2.54). More details can be found in [126, 129].

### HELICITY DENSITY MATRICES

Let us start by briefly sketching the helicity density matrices for quark and gluon polarisations.

The helicity density matrix of quark  $a$  inside hadron  $A$  in a spin state  $S_A$  can be written in terms of the quark polarisation vector components,  $\mathbf{P}^a = (P_x^a, P_y^a, P_z^a) = (P_T^a \cos \phi_{s_a}, P_T^a \sin \phi_{s_a}, P_L^a)$ , as

$$\begin{aligned} \rho_{\lambda_a, \lambda'_a}^{a/A, S_A} &= \begin{pmatrix} \rho_{++}^a & \rho_{+-}^a \\ \rho_{-+}^a & \rho_{--}^a \end{pmatrix}_{A, S_A} = \frac{1}{2} \begin{pmatrix} 1 + P_z^a & P_x^a - iP_y^a \\ P_x^a + iP_y^a & 1 - P_z^a \end{pmatrix}_{A, S_A} \\ &= \frac{1}{2} \begin{pmatrix} 1 + P_L^a & P_T^a e^{-i\phi_{s_a}} \\ P_T^a e^{i\phi_{s_a}} & 1 - P_L^a \end{pmatrix}_{A, S_A}, \end{aligned} \quad (\text{B.1})$$

where the  $x$ ,  $y$  and  $z$  directions are meant in the helicity frame of parton  $a$ . The matrix elements satisfy the following general properties:

$$\rho_{++}^a + \rho_{--}^a = 1, \quad (\text{B.2})$$

$$\rho_{++}^a - \rho_{--}^a = P_z^a = P_L^a, \quad (\text{B.3})$$

$$2 \operatorname{Re} \rho_{-+}^a = 2 \operatorname{Re} \rho_{+-}^a = P_x^a = P_T^a \cos \phi_{s_a}, \quad (\text{B.4})$$

$$2 \operatorname{Im} \rho_{-+}^a = -2 \operatorname{Im} \rho_{+-}^a = P_y^a = P_T^a \sin \phi_{s_a}. \quad (\text{B.5})$$

Similarly to the quark case, the helicity density matrix for a massless spin 1 particle (e.g. a gluon) inside the hadron  $A$  in the spin state  $S_A$  is defined as

$$\begin{aligned}
\rho_{\lambda_g, \lambda'_g}^{g/A, S_A} &= \begin{pmatrix} \rho_{++}^g & \rho_{+-}^g \\ \rho_{-+}^g & \rho_{--}^g \end{pmatrix}_{A, S_A} = \frac{1}{2} \begin{pmatrix} 1 + P_z^g & \mathcal{T}_1^g - i\mathcal{T}_2^g \\ \mathcal{T}_1^g + i\mathcal{T}_2^g & 1 - P_z^g \end{pmatrix}_{A, S_A} \\
&= \frac{1}{2} \begin{pmatrix} 1 + P_{\text{circ}}^g & -P_{\text{lin}}^g e^{-2i\phi} \\ -P_{\text{lin}}^g e^{2i\phi} & 1 - P_{\text{circ}}^g \end{pmatrix}_{A, S_A}.
\end{aligned} \tag{B.6}$$

$P_{\text{circ}}^g$  corresponds to  $P_z^g$ , the gluon longitudinal polarisation, while the off-diagonal elements are related to the linear polarisation of the gluons in the  $(xy)$  plane at an angle  $\phi$  with respect to the  $x$ -axis. The  $x$ ,  $y$  and  $z$  axes refer to the standard gluon helicity frame, in which its momentum is  $p^\mu = (p, 0, 0, p)$ .  $P_{\text{lin}}^g$  is expressed in terms of the parameters  $\mathcal{T}_1^g$  and  $\mathcal{T}_2^g$ , which are closely related to the Stokes parameters used in classical optics; they play a role formally analogous to that of the  $x$  and  $y$ -components of the quark polarisation vector in the quark sector.

As in the quark case, the matrix elements of Eq. (B.6) satisfy some general relations:

$$\rho_{++}^g + \rho_{--}^g = 1, \tag{B.7}$$

$$\rho_{++}^g - \rho_{--}^g = P_z^g = P_{\text{circ}}^g, \tag{B.8}$$

$$2 \operatorname{Re} \rho_{-+}^g = 2 \operatorname{Re} \rho_{+-}^g = \mathcal{T}_1^g = -P_{\text{lin}}^g \cos 2\phi, \tag{B.9}$$

$$2 \operatorname{Im} \rho_{-+}^g = -2 \operatorname{Im} \rho_{+-}^g = \mathcal{T}_2^g = -P_{\text{lin}}^g \sin 2\phi. \tag{B.10}$$

## HELICITY AMPLITUDES

We now show some properties of the helicity amplitudes that enter in the expression of the GPM master formula. We recall that the amplitudes appearing in Eq. (2.40), the  $\hat{M}$ 's, are calculated in the *hadronic* c.m. frame. They are connected to the  $\hat{M}^0$ 's, the amplitudes in the *partonic* c.m. frame, by performing one boost and appropriate rotations, as described in full detail in [126]. These transformations induces nontrivial phases in the helicity amplitudes  $\hat{M}$ 's, due to the nonplanar kinematics of the partonic process. The relation between these helicity amplitudes and the canonical amplitudes  $\hat{M}^0$ , defined in the partonic  $ab \rightarrow cd$  c.m. frame, is

$$\begin{aligned}
\hat{M}_{\lambda_c \lambda_d, \lambda_a \lambda_b} &= \hat{M}_{\lambda_c \lambda_d, \lambda_a \lambda_b}^0 e^{-i(\lambda_a \xi_a + \lambda_b \xi_b - \lambda_c \xi_c - \lambda_d \xi_d)} \\
&\times e^{-i[(\lambda_a - \lambda_b) \tilde{\xi}_a - (\lambda_c - \lambda_d) \tilde{\xi}_c]} e^{i(\lambda_a - \lambda_b) \phi_c''},
\end{aligned} \tag{B.11}$$

with  $\xi_j, \tilde{\xi}_j$  ( $j = a, b, c, d$ ) and  $\phi_c''$  defined in Eqs. (35-42) of Ref. [126].

The parity properties of the canonical c.m. amplitudes  $\hat{M}^0$  are given by:

$$\begin{aligned}
\hat{M}_{-\lambda_c, -\lambda_d; -\lambda_a, -\lambda_b}^0 &= \eta_a \eta_b \eta_c \eta_d (-1)^{s_a + s_b - s_c - s_d} \\
&\times (-1)^{(\lambda_a - \lambda_b) - (\lambda_c - \lambda_d)} \hat{M}_{\lambda_c \lambda_d, \lambda_a \lambda_b}^0,
\end{aligned} \tag{B.12}$$

where  $\eta_i$  is the intrinsic parity factor for particle  $i$ . In the case of massless partons only three independent elementary amplitudes  $\hat{M}^0$  corresponding to the  $ab \rightarrow cd$  processes exists, and

appear in Eqs. (2.51)–(2.54). They are defined as

$$\hat{M}_{++;++} \equiv \hat{M}_1^0 e^{i\varphi_1}, \quad \hat{M}_{-+;-+} \equiv \hat{M}_2^0 e^{i\varphi_2}, \quad \hat{M}_{-+;+-} \equiv \hat{M}_3^0 e^{i\varphi_3}, \quad (\text{B.13})$$

where the + and – subscripts refer to (+1/2) and (–1/2) helicities for quarks, and to (+1) and (–1) helicities for gluons, and where

$$\hat{M}_{+,+;+,+}^0 \equiv \hat{M}_1^0, \quad \hat{M}_{-,+;-,-}^0 \equiv \hat{M}_2^0, \quad \hat{M}_{-,+;+,-}^0 \equiv \hat{M}_3^0. \quad (\text{B.14})$$

The phases  $\varphi_1$ ,  $\varphi_2$  and  $\varphi_3$  are given by replacing in Eq. (B.11) the appropriate value for the helicities  $\lambda_i$  ( $i = a, b, c, d$ ).

From Lorentz and rotational invariance properties [129] the following expressions that relates canonical amplitudes by exchanging the particles in the initial ( $a \leftrightarrow b$ ) or in the final state ( $c \leftrightarrow d$ ) hold:

$$\hat{M}_{\lambda_c \lambda_d, \lambda_b \lambda_a}^{0, ba \rightarrow cd}(\theta) = \hat{M}_{\lambda_c \lambda_d, \lambda_a \lambda_b}^{0, ab \rightarrow cd}(\pi - \theta) e^{-i\pi(\lambda_c - \lambda_d)}, \quad (\text{B.15})$$

$$\hat{M}_{\lambda_d \lambda_c, \lambda_a \lambda_b}^{0, ab \rightarrow dc}(\theta) = \hat{M}_{\lambda_c \lambda_d, \lambda_a \lambda_b}^{0, ab \rightarrow cd}(\pi - \theta) e^{-i\pi(\lambda_a - \lambda_b)}, \quad (\text{B.16})$$

where  $\theta$  is the scattering angle in the partonic c.m. frame.

#### “ $\Delta$ ” FUNCTIONS AND RELATIONS BETWEEN DIFFERENT NOTATIONS

Here we give the “ $\Delta$ ” functions appearing in Eqs. (2.51)–(2.54) in terms of the TMDs introduced in Section 2.1.

For the  $T$ -odd couple in the distribution sector, i.e. the Sivers and the Boer-Mulders functions, the following relations with the “ $\Delta$ ” functions appearing in the aforementioned equations holds [126]:

$$\begin{aligned} \Delta \hat{f}_{a/S_T}(x_a, \mathbf{k}_{\perp a}) &= -2 \frac{k_{\perp a}}{M} \sin(\phi_{S_A} - \phi_a) f_{1T}^{\perp}(x_a, k_{\perp a}) \\ &= \Delta^N f_{a/S_T}(x, k_{\perp a}) \end{aligned} \quad (\text{B.17})$$

$$\Delta \hat{f}_{S_y/A}^a(x_a, \mathbf{k}_{\perp a}) = -\frac{k_{\perp a}}{M} h_1^{\perp}(x_a, k_{\perp a}) = \Delta^N f_{S_y/A}(x, k_{\perp a}) \quad (\text{B.18})$$

where  $\phi_{S_A}$  is the azimuthal angle relative to the generic transverse polarisation direction  $\hat{\mathbf{P}}_A = (\cos \phi_{S_A}, \sin \phi_{S_A}, 0)$  and  $\phi_a$  is the azimuthal angle of  $\mathbf{k}_{\perp a}$  in the hadronic c.m. frame.

The other “ $\Delta$ ” functions, appearing in Eqs. (2.51) and (2.52), are related to combinations of transversity and Boer-Mulders functions:

$$\Delta \hat{f}_{S_x/S_T}(x_a, \mathbf{k}_{\perp a}) = \left[ h_{1T}(x_a, k_{\perp a}) + \frac{k_{\perp a}^2}{M^2} h_{1T}^{\perp}(x_a, k_{\perp a}) \right] \cos(\phi_{S_A} - \phi_a), \quad (\text{B.19})$$

$$\Delta \hat{f}_{S_y/S_T}(x_a, \mathbf{k}_{\perp a}) = -\frac{k_{\perp a}}{M} h_1^{\perp}(x_a, k_{\perp a}) + h_{1T}(x_a, k_{\perp a}) \sin(\phi_{S_A} - \phi_a). \quad (\text{B.20})$$

Finally, it is worth mentioning that the function  $\Delta\hat{f}_{s_y/S_Y}^a$ , can be decomposed in two terms, the Boer-Mulders one (independent of the hadron transverse polarisation) and another one that changes sign when the hadron polarisation direction is reversed:

$$\Delta\hat{f}_{s_y/S_Y}^a = \Delta\hat{f}_{s_y/A}^a + \Delta^{-}\hat{f}_{s_y/S_Y}^a, \quad (\text{B.21})$$

with

$$\Delta^{-}\hat{f}_{s_y/S_Y}^a \equiv \frac{1}{2} \left[ \Delta\hat{f}_{s_y/\uparrow}^a - \Delta\hat{f}_{s_y/\downarrow}^a \right]. \quad (\text{B.22})$$



# Colour projectors in CGI-GPM

As shown in Chapter 4, within the CGI-GPM one has to calculate modified hard factors, related to the  $f$ - and  $d$ -type GSFs, that embed the process dependence of the gluon Sivvers function. To do that, new colour factors have to be calculated, by means of colour projectors.

As discussed in Section 4.1, in the case of the gluon Sivvers function we have two different colour projectors, namely the antisymmetric and the symmetric one, defined as

$$\mathcal{T}_{ab}^c = \mathcal{N}_{\mathcal{T}}(T^c)_{ab}, \quad \mathcal{D}_{ab}^c = \mathcal{N}_{\mathcal{D}}(D^c)_{ab}, \quad (\text{C.1})$$

with  $a, b, c$  being colour indices and where the normalisation factors are related to inverse of traces of two (anti)symmetric structure constants of  $SU(N_c)$ , and are given by

$$\mathcal{N}_{\mathcal{T}} = \text{Tr}(T^c T^c)^{-1} = \frac{1}{N_c(N_c^2 - 1)}, \quad \mathcal{N}_{\mathcal{D}} = \text{Tr}(D^c D^c)^{-1} = \frac{N_c}{(N_c^2 - 4)(N_c^2 - 1)}. \quad (\text{C.2})$$

Another colour projector has been used in Refs. [109, 110], and is related to the quark case:

$$\mathcal{Q}_{ij}^c = \mathcal{N}_{\mathcal{Q}} t_{ij}^c, \quad \text{with} \quad \mathcal{N}_{\mathcal{Q}} = \frac{1}{\text{Tr}(t^c t^c)} = \frac{2}{N_c^2 - 1}. \quad (\text{C.3})$$

where  $t_{ij}^c$  are the generators of  $SU(N_c)$  in the fundamental representation. For completeness, the Feynman rules for the projectors are collected in Fig. C.1 [110]:

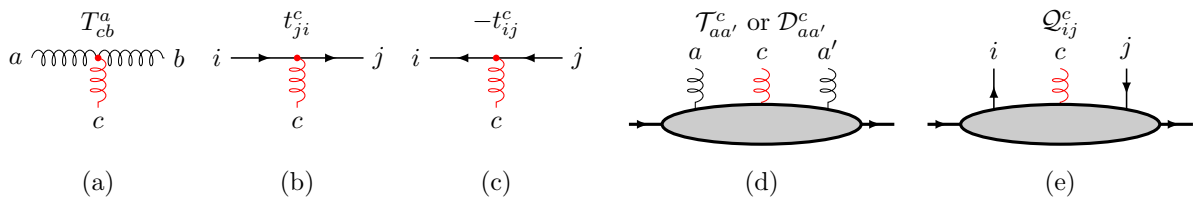


Figure C.1: CGI-GPM colour rules for the vertices involving an eikonal gluon with colour index  $c$ : (a) three-gluon, (b) quark-gluon and (c) antiquark-gluon. The colour projectors for the (d) gluon and the (e) quark Sivvers functions are shown as well.

# Acknowledgments

This three years have been the final part of a long ride at Cagliari University. There is a lot of people to whom I am grateful, and I would like to thank them again here.

First of all, I want to express my gratitude to my supervisors, Umberto D'Alesio and Francesco Murgia. I really appreciated your constant presence and help, and I am thankful for having allowed me to work with you. I also thank all the (past and present) members of the Cagliari hadron physics group: Cristian Pisano, Pieter Taels and Rajesh Sangem. I wish we had more time to work together. I also wish good luck to our PhD students, Marco Zaccheddu and Luca Maxia, for having a successful PhD and a bright future.

I am also very honored for having collaborated with the Torino group. I thank Mauro Anselmino and Maria Elena Boglione for their help and hospitality, and interesting discussions in several visits in Torino during these years. I am indebtely grateful to Osvaldo Gonzalez, that helped me a lot in developing a large part of the work present in this thesis. Thanks also to Alessandro Bacchetta, Marco Radici and all the Pavia group for very stimulating discussions during my visit in Pavia and during SarWors. Thanks to Andrea Signori as well, for the discussions we had in Philadelphia and during last year in the US.

During these three years I had the opportunity to travel abroad quite often, and to work with several well-recognised researchers in different corners of the world. I am not but thankful to Daniel Boer, Jean-Philippe Lansberg and Alexei Prokudin for their hospitality, supervision and help throughout my visits in their institutions, and also to all the people that welcomed and helped me at IPN Orsay, VSI Groningen and Penn State Berks. Special mention to Leonard Gamberg, who has been really helpful during my visit at Penn State Berks. I am also very grateful to the thesis referees, Daniel Boer and Werner Vogelsang. Your comments, observations and suggestions that have helped me to further improve this thesis.

Everyday life in the department has been full of work and interaction with other students and researchers, and has been fueled with a lot of nice memories. Many thanks to my PhD colleagues: Andrea, Angelo, Davide, Elisa, Paola, Qingqian. During these three years, we grew together, sharing thoughts, experiences, and helping each other. I hope that our future, regardless of what we will decide to do, will be happy, satisfying and successful for all of us. Thanks to all the colleagues and friends I met abroad, especially to Juan, Florent, Simone and Lucia, and the GGI friends, along with I had a wonderful time in Firenze: Ale, Andre, Fotis, Giò, Dott. Pobbe, Ste and Zhengwen. Thanks also to Tuvi, Ed, Deddu, Franci, Valerio and all the others Cagliari friends and colleagues (the list is very very long). Special mention for a friend, now also sister-in-law, who supported me a lot during these years. Thank you Frà!

Grazie a mamma e papà: il vostro supporto è sempre stato (e sempre sarà) importantissimo, e senza di voi non sarei mai potuto arrivare fino a qua. Vi voglio bene. Grazie anche alle zie, gli zii, cugine e cugini, a Lucia, Luigino, Claudia e Fabrizio. E grazie anche a vecchi e nuovi amici, specialmente a Pippo, Ele e Andre.

Finally, I can express nothing but love for my lovely wife Giulia. Your love and support make me stronger, and you make me feel very lucky. I am nothing but delighted to share my life with you, and I wish our future will be as bright as possible.

# References

- [1] M. Gell-Mann. *Nonleptonic weak decays and the eightfold way*. Phys. Rev. Lett., **12**:155–156, 1964. doi: 10.1103/PhysRevLett.12.155.  $\hookrightarrow$  page 1
- [2] M. Gell-Mann. *A Schematic Model of Baryons and Mesons*. Phys. Lett., **8**:214–215, 1964. doi: 10.1016/S0031-9163(64)92001-3.  $\hookrightarrow$  page 1
- [3] G. Zweig. *An SU(3) model for strong interaction symmetry and its breaking; Version 1*. Technical Report CERN-TH-401, CERN, Geneva, Jan 1964. URL <http://cds.cern.ch/record/352337>.  $\hookrightarrow$  page 1
- [4] G. Zweig. *An SU(3) model for strong interaction symmetry and its breaking. Version 2*. In D. B. Lichtenberg and S. P. Rosen, editors, *Developments in the quark theory of hadrons, vol. 1. 1964 - 1978*, pages 22–101. 1964.  $\hookrightarrow$  page 1
- [5] R. P. Feynman. *Very high-energy collisions of hadrons*. Phys. Rev. Lett., **23**:1415–1417, 1969. doi: 10.1103/PhysRevLett.23.1415. [,494(1969)].  $\hookrightarrow$  page 1
- [6] J. D. Bjorken and E. A. Paschos. *Inelastic electron proton and gamma proton scattering, and the structure of the nucleon*. Phys. Rev., **185**:1975–1982, 1969. doi: 10.1103/PhysRev.185.1975.  $\hookrightarrow$  page 1
- [7] E. D. Bloom *et al.* *High-energy inelastic ep scattering at 6-degrees and 10-degrees*. Phys. Rev. Lett., **23**:930–934, 1969. doi: 10.1103/PhysRevLett.23.930.  $\hookrightarrow$  page 1
- [8] M. Breidenbach *et al.* *Observed behavior of highly inelastic electron-Proton scattering*. Phys. Rev. Lett., **23**:935–939, 1969. doi: 10.1103/PhysRevLett.23.935.  $\hookrightarrow$  page 1
- [9] N. Cabibbo. *Unitary Symmetry and Leptonic Decays*. Phys. Rev. Lett., **10**:531–533, 1963. doi: 10.1103/PhysRevLett.10.531. [,648(1963)].  $\hookrightarrow$  page 1
- [10] M. Kobayashi and T. Maskawa. *CP Violation in the Renormalizable Theory of Weak Interaction*. Prog. Theor. Phys., **49**:652–657, 1973. doi: 10.1143/PTP.49.652.  $\hookrightarrow$  page 1
- [11] R. Brandelik *et al.* *Evidence for Planar Events in  $e^+e^-$  Annihilation at High-Energies*. Phys. Lett., **86B**:243–249, 1979. doi: 10.1016/0370-2693(79)90830-X.  $\hookrightarrow$  page 1
- [12] D. P. Barber *et al.* *Discovery of Three Jet Events and a Test of Quantum Chromodynamics at PETRA Energies*. Phys. Rev. Lett., **43**:830, 1979. doi: 10.1103/PhysRevLett.43.830.  $\hookrightarrow$  [see prev. ref.]
- [13] C. Berger *et al.* *Evidence for Gluon Bremsstrahlung in  $e^+e^-$  Annihilations at High-Energies*. Phys. Lett., **86B**:418–425, 1979. doi: 10.1016/0370-2693(79)90869-4.  $\hookrightarrow$  [see prev. ref.]
- [14] W. Bartel *et al.* *Observation of Planar Three Jet Events in  $e^+e^-$  Annihilation and Evidence for Gluon Bremsstrahlung*. Phys. Lett., **91B**:142–147, 1980. doi: 10.1016/0370-2693(80)90680-2.  $\hookrightarrow$  page 1



- [15] D. J. Gross and F. Wilczek. *Ultraviolet Behavior of Nonabelian Gauge Theories*. Phys. Rev. Lett., **30**:1343–1346, 1973. doi: 10.1103/PhysRevLett.30.1343. [,271(1973)].  
↪ page 2
- [16] H. D. Politzer. *Reliable Perturbative Results for Strong Interactions?* Phys. Rev. Lett., **30**: 1346–1349, 1973. doi: 10.1103/PhysRevLett.30.1346. [,274(1973)]. ↪ page 2
- [17] M. Tanabashi *et al.* *Review of Particle Physics*. Phys. Rev., **D98**(3):030001, 2018. doi: 10.1103/PhysRevD.98.030001. ↪ page 2
- [18] V. N. Gribov and L. N. Lipatov. *Deep inelastic ep scattering in perturbation theory*. Sov. J. Nucl. Phys., **15**:438–450, 1972. [Yad. Fiz.15,781(1972)]. ↪ pages 3, 35, 75
- [19] G. Altarelli and G. Parisi. *Asymptotic freedom in parton language*. Nucl. Phys., **B126**: 298–318, 1977. doi: 10.1016/0550-3213(77)90384-4. ↪ [see prev. ref.]
- [20] Y. L. Dokshitzer. *Calculation of the structure functions for Deep Inelastic Scattering and  $e^+e^-$  annihilation by perturbation theory in Quantum Chromodynamics*. Sov. Phys. JETP, **46**:641–653, 1977. [Zh. Eksp. Teor. Fiz.73,1216(1977)]. ↪ pages 3, 35, 75
- [21] J. Ashman *et al.* *A measurement of the spin asymmetry and determination of the structure function  $g_1$  in Deep Inelastic muon-proton Scattering*. Phys. Lett., **B206**:364, 1988. doi: 10.1016/0370-2693(88)91523-7. [,340(1987)]. ↪ page 3
- [22] A. Airapetian *et al.* *Single-spin asymmetries in semi-inclusive deep-inelastic scattering on a transversely polarized hydrogen target*. Phys. Rev. Lett., **94**:012002, 2005. doi: 10.1103/PhysRevLett.94.012002. ↪ page 3
- [23] V. Y. Alexakhin *et al.* *First measurement of the transverse spin asymmetries of the deuteron in semi-inclusive deep inelastic scattering*. Phys. Rev. Lett., **94**:202002, 2005. doi: 10.1103/PhysRevLett.94.202002. ↪ page 3
- [24] E. S. Ageev *et al.* *A new measurement of the Collins and Sivers asymmetries on a transversely polarised deuteron target*. Nucl. Phys., **B765**:31–70, 2007. doi: 10.1016/j.nuclphysb.2006.10.027. ↪ page 3
- [25] L. Dick *et al.* *Spin effects in the inclusive reactions  $\pi^\pm p^\uparrow \rightarrow \pi^\pm$  Anything at 8-GeV/c*. Phys. Lett., **57B**:93–96, 1975. doi: 10.1016/0370-2693(75)90252-X. ↪ page 3
- [26] R. D. Klem *et al.* *Measurement of asymmetries of inclusive pion production in proton proton interactions at 6-GeV/c and 11.8-GeV/c*. Phys. Rev. Lett., **36**:929–931, 1976. doi: 10.1103/PhysRevLett.36.929. ↪ [see prev. ref.]
- [27] W. H. Dragoset *et al.* *Asymmetries in inclusive proton-nucleon scattering at 11.75-GeV/c*. Phys. Rev., **D18**:3939–3954, 1978. doi: 10.1103/PhysRevD.18.3939. ↪ page 3
- [28] D. L. Adams *et al.* *Comparison of spin asymmetries and cross-sections in  $\pi^0$  production by 200-GeV polarized anti-protons and protons*. Phys. Lett., **B261**:201–206, 1991. doi: 10.1016/0370-2693(91)91351-U. ↪ page 3
- [29] D. L. Adams *et al.* *Analyzing power in inclusive  $\pi^+$  and  $\pi^-$  production at high  $x_F$  with a 200 GeV polarized proton beam*. Phys. Lett., **B264**:462–466, 1991. doi: 10.1016/0370-2693(91)90378-4. ↪ page 19

- [30] D. L. Adams *et al.* *Large  $x_F$  spin asymmetry in  $\pi^0$  production by 200-GeV polarized protons.* Z. Phys., **C56**:181–184, 1992. doi: 10.1007/BF01555512.  $\hookrightarrow$  [see prev. ref.]
- [31] A. Bravar *et al.* *Single spin asymmetries in inclusive charged pion production by transversely polarized anti-protons.* Phys. Rev. Lett., **77**:2626–2629, 1996. doi: 10.1103/PhysRevLett.77.2626.  $\hookrightarrow$  page 3
- [32] J. Adams *et al.* *Cross-sections and transverse single spin asymmetries in forward neutral pion production from proton collisions at  $\sqrt{s} = 200$  GeV.* Phys. Rev. Lett., **92**:171801, 2004. doi: 10.1103/PhysRevLett.92.171801.  $\hookrightarrow$  page 3
- [33] J. Adams *et al.* *Forward neutral pion production in  $p+p$  and  $d+Au$  collisions at  $\sqrt{s} = 200$  GeV.* Phys. Rev. Lett., **97**:152302, 2006. doi: 10.1103/PhysRevLett.97.152302.  $\hookrightarrow$  [see prev. ref.]
- [34] S. S. Adler *et al.* *Mid-rapidity neutral pion production in proton proton collisions at  $\sqrt{s} = 200$  GeV.* Phys. Rev. Lett., **91**:241803, 2003. doi: 10.1103/PhysRevLett.91.241803.  $\hookrightarrow$  [see prev. ref.]
- [35] S. S. Adler *et al.* *Measurement of transverse single-spin asymmetries for mid-rapidity production of neutral pions and charged hadrons in polarized  $p+p$  collisions at  $\sqrt{s} = 200$  GeV.* Phys. Rev. Lett., **95**:202001, 2005. doi: 10.1103/PhysRevLett.95.202001.  $\hookrightarrow$  [see prev. ref.]
- [36] I. Arsene *et al.* *Production of mesons and baryons at high rapidity and high  $P_T$  in proton-proton collisions at  $\sqrt{s} = 200$  GeV.* Phys. Rev. Lett., **98**:252001, 2007. doi: 10.1103/PhysRevLett.98.252001.  $\hookrightarrow$  [see prev. ref.]
- [37] B. I. Abelev *et al.* *Forward neutral pion Transverse Single Spin Asymmetries in  $p + p$  collisions at  $\sqrt{s} = 200$  GeV.* Phys. Rev. Lett., **101**:222001, 2008. doi: 10.1103/PhysRevLett.101.222001.  $\hookrightarrow$  page 19
- [38] I. Arsene *et al.* *Single Transverse Spin Asymmetries of Identified Charged Hadrons in Polarized  $p+p$  Collisions at  $\sqrt{s} = 62.4$  GeV.* Phys. Rev. Lett., **101**:042001, 2008. doi: 10.1103/PhysRevLett.101.042001.  $\hookrightarrow$  [see prev. ref.]
- [39] L. Adamczyk *et al.* *Transverse Single-Spin Asymmetry and Cross-Section for  $\pi^0$  and  $\eta$  Mesons at Large Feynman- $x$  in Polarized  $p + p$  Collisions at  $\sqrt{s} = 200$  GeV.* Phys. Rev., **D86**:051101, 2012. doi: 10.1103/PhysRevD.86.051101.  $\hookrightarrow$  [see prev. ref.]
- [40] A. Adare *et al.* *Measurement of transverse-single-spin asymmetries for midrapidity and forward-rapidity production of hadrons in polarized  $p + p$  collisions at  $\sqrt{s} = 200$  and 62.4 GeV.* Phys. Rev., **D90**(1):012006, 2014. doi: 10.1103/PhysRevD.90.012006.  $\hookrightarrow$  pages 3, 19, 74, 76, 77, 82
- [41] J. C. Collins, D. E. Soper, and G. F. Sterman. *Transverse momentum distribution in Drell-Yan pair and  $W$  and  $Z$  boson production.* Nucl. Phys., **B250**:199–224, 1985. doi: 10.1016/0550-3213(85)90479-1.  $\hookrightarrow$  pages 4, 13
- [42] J. C. Collins, D. E. Soper, and G. F. Sterman. *Factorization for short distance hadron-hadron scattering.* Nucl. Phys., **B261**:104–142, 1985. doi: 10.1016/0550-3213(85)90565-6.  $\hookrightarrow$  pages 4, 19

- [43] X.-D. Ji, J.-P. Ma, and F. Yuan. *QCD factorization for spin-dependent cross sections in DIS and Drell-Yan processes at low transverse momentum*. Phys.Lett.B, **597**:299–308, 2004. doi: 10.1016/j.physletb.2004.07.026.  $\hookrightarrow$  page 4
- [44] C. Rogers, T and P. J. Mulders. *No generalized TMD-factorization in hadro-production of high transverse momentum hadrons*. Phys. Rev., **D81**:094006, 2010. doi: 10.1103/PhysRevD.81.094006.  $\hookrightarrow$  [see prev. ref.]
- [45] J. C. Collins. *Foundations of perturbative QCD*. Camb. Monogr. Part. Phys. Nucl. Phys. Cosmol., **32**:1–624, 2011.  $\hookrightarrow$  page 19
- [46] S. M Aybat, J. C. Collins, J.-W. Qiu, and T. C. Rogers. *The QCD Evolution of the Sivers Function*. Phys. Rev., **D85**:034043, 2012. doi: 10.1103/PhysRevD.85.034043.  $\hookrightarrow$  pages 49, 50
- [47] M. G. Echevarria, A. Idilbi, and I. Scimemi. *Factorization theorem for Drell-Yan at low  $q_T$  and transverse momentum distributions on-the-light-cone*. JHEP, **07**:002, 2012. doi: 10.1007/JHEP07(2012)002.  $\hookrightarrow$  [see prev. ref.]
- [48] S. M. Aybat and T. C. Rogers. *TMD parton distribution and fragmentation functions with QCD evolution*. Phys. Rev., **D83**:114042, 2011. doi: 10.1103/PhysRevD.83.114042.  $\hookrightarrow$  [see prev. ref.]
- [49] M. G. Echevarria, A. Idilbi, and I. Scimemi. *Soft and collinear factorization and transverse momentum dependent parton distribution functions*. Phys. Lett., **B726**:795–801, 2013. doi: 10.1016/j.physletb.2013.09.003.  $\hookrightarrow$  [see prev. ref.]
- [50] M. G. Echevarria, A. Idilbi, A. Schäfer, and I. Scimemi. *Model-independent evolution of transverse momentum dependent distribution functions (TMDs) at NNLL*. Eur. Phys. J., **C73**(12):2636, 2013. doi: 10.1140/epjc/s10052-013-2636-y.  $\hookrightarrow$  [see prev. ref.]
- [51] I. Scimemi and A. Vladimirov. *Analysis of vector boson production within TMD factorization*. Eur. Phys. J., **C78**(2):89, 2018. doi: 10.1140/epjc/s10052-018-5557-y.  $\hookrightarrow$  [see prev. ref.]
- [52] I. Scimemi and A. Vladimirov. *Systematic analysis of double-scale evolution*. JHEP, **08**:003, 2018. doi: 10.1007/JHEP08(2018)003.  $\hookrightarrow$  [see prev. ref.]
- [53] I. Scimemi. *A short review on recent developments in TMD factorization and implementation*. Adv. High Energy Phys., **2019**:3142510, 2019. doi: 10.1155/2019/3142510.  $\hookrightarrow$  pages 4, 13
- [54] S. J. Brodsky, D. S. Hwang, and I. Schmidt. *Final state interactions and single spin asymmetries in semiinclusive deep inelastic scattering*. Phys. Lett., **B530**:99–107, 2002. doi: 10.1016/S0370-2693(02)01320-5.  $\hookrightarrow$  page 4
- [55] S. J. Brodsky, D. S. Hwang, and I. Schmidt. *Initial state interactions and single spin asymmetries in Drell-Yan processes*. Nucl. Phys., **B642**:344–356, 2002. doi: 10.1016/S0550-3213(02)00617-X.  $\hookrightarrow$  [see prev. ref.]
- [56] J. C. Collins. *Leading twist single transverse-spin asymmetries: Drell-Yan and deep inelastic scattering*. Phys. Lett., **B536**:43–48, 2002. doi: 10.1016/S0370-2693(02)01819-1.  $\hookrightarrow$  pages 10, 11
- [57] A. V. Belitsky, X. Ji, and F. Yuan. *Final state interactions and gauge invariant parton distributions*. Nucl. Phys., **B656**:165–198, 2003. doi: 10.1016/S0550-3213(03)00121-4.  $\hookrightarrow$  [see prev. ref.]

- [58] D. Boer, P. J. Mulders, and F. Pijlman. *Universality of  $T$  odd effects in single spin and azimuthal asymmetries*. Nucl. Phys., **B667**:201–241, 2003. doi: 10.1016/S0550-3213(03)00527-3.  $\hookrightarrow$  pages 12, 47
- [59] C. J. Bomhof, P. J. Mulders, and F. Pijlman. *The Construction of gauge-links in arbitrary hard processes*. Eur. Phys. J., **C47**:147–162, 2006. doi: 10.1140/epjc/s2006-02554-2.  $\hookrightarrow$  [see prev. ref.]
- [60] D. Boer, P. J. Mulders, C. Pisano, and J. Zhou. *Asymmetries in Heavy Quark Pair and Dijet Production at an EIC*. JHEP, **08**:001, 2016. doi: 10.1007/JHEP08(2016)001.  $\hookrightarrow$  pages 4, 8, 63
- [61] A. Bacchetta, G. Bozzi, M. Radici, M. Ritzmann, and A. Signori. *Effect of flavor-dependent partonic transverse momentum on the determination of the  $W$  boson mass in hadronic collisions*. Phys. Lett., **B788**:542–545, 2019. doi: 10.1016/j.physletb.2018.11.002.  $\hookrightarrow$  page 4
- [62] V. Cirigliano, J. Jenkins, and M. Gonzalez-Alonso. *Semileptonic decays of light quarks beyond the Standard Model*. Nucl. Phys., **B830**:95–115, 2010. doi: 10.1016/j.nuclphysb.2009.12.020.  $\hookrightarrow$  pages 4, 8, 59
- [63] T. Bhattacharya, V. Cirigliano, S. D. Cohen, A. Filipuzzi, M. Gonzalez-Alonso, M. L. Graesser, R. Gupta, and H.-W. Lin. *Probing novel scalar and tensor interactions from (ultra)cold neutrons to the LHC*. Phys. Rev., **D85**:054512, 2012. doi: 10.1103/PhysRevD.85.054512.  $\hookrightarrow$  [see prev. ref.]
- [64] A. Courtoy, S. Baeßler, M. González-Alonso, and S. Liuti. *Beyond-Standard-Model tensor interaction and hadron phenomenology*. Phys. Rev. Lett., **115**:162001, 2015. doi: 10.1103/PhysRevLett.115.162001.  $\hookrightarrow$  pages 4, 8, 59
- [65] R. D. Field and R. P. Feynman. *Quark elastic scattering as a source of high transverse momentum mesons*. Phys. Rev., **D15**:2590–2616, 1977. doi: 10.1103/PhysRevD.15.2590.  $\hookrightarrow$  page 6
- [66] R. P. Feynman, R. D. Field, and G. C. Fox. *A quantum chromodynamic approach for the large transverse momentum production of particles and jets*. Phys. Rev., **D18**:3320, 1978. doi: 10.1103/PhysRevD.18.3320. [739(1978)].  $\hookrightarrow$  page 6
- [67] M. E. Peskin and D. V. Schroeder. *An Introduction to quantum field theory*. Addison-Wesley, Reading, USA, 1995. ISBN 9780201503975, 0201503972. URL <http://www.slac.stanford.edu/~mpeskin/QFT.html>.  $\hookrightarrow$  page 7
- [68] R. L. Jaffe. *Spin, twist and hadron structure in deep inelastic processes*. In *The spin structure of the nucleon. Proceedings, International School of Nucleon Structure, 1st Course, Erice, Italy, August 3-10, 1995*, pages 42–129, 1996.  $\hookrightarrow$  page 7
- [69] D. W. Sivers. *Single Spin production Asymmetries from the hard scattering of point-like constituents*. Phys. Rev., **D41**:83, 1990. doi: 10.1103/PhysRevD.41.83.  $\hookrightarrow$  page 7
- [70] D. W. Sivers. *Hard scattering scaling laws for single spin production asymmetries*. Phys. Rev., **D43**:261–263, 1991. doi: 10.1103/PhysRevD.43.261.  $\hookrightarrow$  page 7
- [71] D. Boer and P. J. Mulders. *Time reversal odd distribution functions in lepton production*. Phys. Rev., **D57**:5780–5786, 1998. doi: 10.1103/PhysRevD.57.5780.  $\hookrightarrow$  pages 7, 9

- [72] G. A. Miller. *Densities, parton distributions, and measuring the non-spherical shape of the nucleon*. Phys. Rev., **C76**:065209, 2007. doi: 10.1103/PhysRevC.76.065209.  $\hookrightarrow$  page 7
- [73] J. Soffer. *Positivity constraints for spin dependent parton distributions*. Phys. Rev. Lett., **74**: 1292–1294, 1995. doi: 10.1103/PhysRevLett.74.1292.  $\hookrightarrow$  page 7
- [74] D. Boer and C. Pisano. *Impact of gluon polarization on Higgs boson plus jet production at the LHC*. Phys. Rev., **D91**(7):074024, 2015. doi: 10.1103/PhysRevD.91.074024.  $\hookrightarrow$  pages 8, 63
- [75] J.-P. Lansberg, C. Pisano, F. Scarpa, and M. Schlegel. *Pinning down the linearly-polarised gluons inside unpolarised protons using quarkonium-pair production at the LHC*. Phys. Lett., **B784**:217–222, 2018. doi: 10.1016/j.physletb.2018.08.004, 10.1016/j.physletb.2019.01.057. [Erratum: Phys. Lett.B791,420(2019)].  $\hookrightarrow$  pages 8, 116
- [76] A. Accardi *et al.* *Electron Ion Collider: the next QCD frontier*. Eur. Phys. J., **A52**(9):268, 2016. doi: 10.1140/epja/i2016-16268-9.  $\hookrightarrow$  pages 8, 32, 33, 44, 61, 95
- [77] C. Pisano, D. Boer, S. J. Brodsky, M. G. A. Buffing, and P. J. Mulders. *Linear polarization of gluons and photons in unpolarized collider experiments*. JHEP, **10**:024, 2013. doi: 10.1007/JHEP10(2013)024.  $\hookrightarrow$  pages 8, 63
- [78] S. J. Brodsky, F. Fleuret, C. Hadjidakis, and J. P. Lansberg. *Physics Opportunities of a Fixed-Target Experiment using the LHC Beams*. Phys. Rept., **522**:239–255, 2013. doi: 10.1016/j.physrep.2012.10.001.  $\hookrightarrow$  pages 8, 105, 117
- [79] C. Hadjidakis *et al.* *A fixed-target programme at the LHC: physics case and projected performances for heavy-ion, hadron, spin and astroparticle studies*. , 2018. URL <http://arxiv.org/abs/arXiv:1807.00603>.  $\hookrightarrow$  pages 63, 105
- [80] C. A. Aidala *et al.* *The LHCSpin project*. , 2019. URL <http://arxiv.org/abs/arXiv:1901.08002>.  $\hookrightarrow$  pages 63, 105
- [81] E. Steffens, V. Carassiti, G. Ciullo, P. Di Nezza, P. Lenisa, L. L. Pappalardo, and A. Vasilyev. *Design consideration on a polarized gas target for the LHC*. In *23rd International Symposium on Spin Physics (SPIN 2018) Ferrara, Italy, September 10-14, 2018*, 2019.  $\hookrightarrow$  pages 8, 105, 117
- [82] J. C. Collins. *Fragmentation of transversely polarized quarks probed in transverse momentum distributions*. Nucl. Phys., **B396**:161–182, 1993. doi: 10.1016/0550-3213(93)90262-N.  $\hookrightarrow$  pages 9, 10
- [83] P. J. Mulders and R. D. Tangerman. *The Complete tree level result up to order  $1/Q$  for polarized deep inelastic lepton production*. Nucl. Phys., **B461**:197–237, 1996. doi: 10.1016/S0550-3213(96)00648-7, 10.1016/0550-3213(95)00632-X. [Erratum: Nucl. Phys.B484,538(1997)].  $\hookrightarrow$  page 9
- [84] A. Signori. *Flavor and Evolution Effects in TMD Phenomenology*. PhD thesis, Vrije U., Amsterdam, 2016. URL [http://www.nikhef.nl/pub/services/biblio/theses\\_pdf/thesis\\_A\\_Signori.pdf](http://www.nikhef.nl/pub/services/biblio/theses_pdf/thesis_A_Signori.pdf).  $\hookrightarrow$  pages 9, 27
- [85] A. Bacchetta, M. Boglione, A. Henneman, and P. J. Mulders. *Bounds on transverse momentum dependent distribution and fragmentation functions*. Phys. Rev. Lett., **85**:712–715, 2000. doi: 10.1103/PhysRevLett.85.712.  $\hookrightarrow$  pages 9, 12



- [86] U. D'Alesio and F. Murgia. *Azimuthal and Single Spin Asymmetries in Hard Scattering Processes*. Prog. Part. Nucl. Phys., **61**:394–454, 2008. doi: 10.1016/j.pnpnp.2008.01.001.   
↪ pages 9, 10, 11, 21, 26
- [87] V. Barone, F. Bradamante, and A. Martin. *Transverse-spin and transverse-momentum effects in high-energy processes*. Prog. Part. Nucl. Phys., **65**:267–333, 2010. doi: 10.1016/j.pnpnp.2010.07.003.   
↪ pages 9, 10, 11, 19
- [88] L. Adamczyk *et al.* *Measurement of the transverse single-spin asymmetry in  $p^\uparrow + p \rightarrow W^\pm / Z^0$  at RHIC*. Phys. Rev. Lett., **116**(13):132301, 2016. doi: 10.1103/PhysRevLett.116.132301.   
↪ pages 10, 33
- [89] M. Aghasyan *et al.* *First measurement of transverse-spin-dependent azimuthal asymmetries in the Drell-Yan process*. Phys. Rev. Lett., **119**(11):112002, 2017. doi: 10.1103/PhysRevLett.119.112002.   
↪ pages 10, 33, 44
- [90] A. Metz. *Gluon-exchange in spin-dependent fragmentation*. Phys. Lett., **B549**:139–145, 2002. doi: 10.1016/S0370-2693(02)02899-X.   
↪ page 11
- [91] J. C. Collins and A. Metz. *Universality of soft and collinear factors in hard-scattering factorization*. Phys. Rev. Lett., **93**:252001, 2004. doi: 10.1103/PhysRevLett.93.252001.   
↪ page 11
- [92] D. Boer, R. Jakob, and P. J. Mulders. *Asymmetries in polarized hadron production in  $e^+e^-$  annihilation up to order  $1/Q$* . Nucl. Phys., **B504**:345–380, 1997. doi: 10.1016/S0550-3213(97)00456-2.   
↪ pages 11, 52
- [93] A. V. Efremov and O. V. Teryaev. *On spin effects in quantum chromodynamics*. Sov. J. Nucl. Phys., **36**:140, 1982. [Yad. Fiz.36,242(1982)].   
↪ pages 12, 14
- [94] A. V. Efremov and O. V. Teryaev. *The transversal polarization in quantum chromodynamics*. Sov. J. Nucl. Phys., **39**:962, 1984. [Yad. Fiz.39,1517(1984)].   
↪ [see prev. ref.]
- [95] A. V. Efremov and O. V. Teryaev. *QCD asymmetry and polarized hadron structure functions*. Phys. Lett., **150B**:383, 1985. doi: 10.1016/0370-2693(85)90999-2.   
↪ [see prev. ref.]
- [96] J.-W. Qiu and G. F. Sterman. *Single transverse spin asymmetries*. Phys. Rev. Lett., **67**:2264–2267, 1991. doi: 10.1103/PhysRevLett.67.2264.   
↪ [see prev. ref.]
- [97] J.-W. Qiu and G. F. Sterman. *Single transverse spin asymmetries in hadronic pion production*. Phys. Rev., **D59**:014004, 1999. doi: 10.1103/PhysRevD.59.014004.   
↪ pages 12, 14
- [98] L. Gamberg, Z.-B. Kang, D. Pitonyak, and A. Prokudin. *Phenomenological constraints on  $A_N$  in  $p^\uparrow p \rightarrow \pi X$  from Lorentz invariance relations*. Phys. Lett., **B770**:242–251, 2017. doi: 10.1016/j.physletb.2017.04.061.   
↪ page 12
- [99] M. Burkardt. *Quark correlations and single spin asymmetries*. Phys. Rev., **D69**:057501, 2004. doi: 10.1103/PhysRevD.69.057501.   
↪ page 12
- [100] M. Burkardt. *Sivers mechanism for gluons*. Phys. Rev., **D69**:091501, 2004. doi: 10.1103/PhysRevD.69.091501.   
↪ page 12
- [101] A. V. Efremov, K. Goeke, S. Menzel, A. Metz, and P. Schweitzer. *Sivers effect in semi-inclusive DIS and in the Drell-Yan process*. Phys. Lett., **B612**:233–244, 2005. doi: 10.1016/j.physletb.2005.03.010.   
↪ page 12

- [102] A. Schafer and O. V. Teryaev. *Sum rules for the T - odd fragmentation functions*. Phys. Rev., **D61**:077903, 2000. doi: 10.1103/PhysRevD.61.077903.  $\hookrightarrow$  page 12
- [103] A. Bacchetta, U. D'Alesio, M. Diehl, and C. Andy Miller. *Single-spin asymmetries: The Trento conventions*. Phys. Rev. , **D70**:117504, 2004. doi: 10.1103/PhysRevD.70.117504.  $\hookrightarrow$  pages 13, 15
- [104] G. L. Kane, J. Pumplin, and W. Repko. *Transverse quark polarization in large- $p_T$  reactions,  $e^+e^-$  jets, and leptonproduction: a test of QCD*. Phys. Rev. Lett., **41**:1689, 1978. doi: 10.1103/PhysRevLett.41.1689.  $\hookrightarrow$  pages 14, 19, 20
- [105] J.-W. Qiu and G. F. Sterman. *Single transverse spin asymmetries in direct photon production*. Nucl. Phys., **B378**:52–78, 1992. doi: 10.1016/0550-3213(92)90003-T.  $\hookrightarrow$  page 14
- [106] C. Kouvaris, J.-W. Qiu, W. Vogelsang, and F. Yuan. *Single transverse-spin asymmetry in high transverse momentum pion production in pp collisions*. Phys. Rev., **D74**:114013, 2006. doi: 10.1103/PhysRevD.74.114013.  $\hookrightarrow$  page 18
- [107] K. Kanazawa, Y. Koike, A. Metz, and D. Pitonyak. *Transverse single-spin asymmetries in  $p^\uparrow p \rightarrow \gamma X$  from quark-gluon-quark correlations in the proton*. Phys. Rev., **D91**(1):014013, 2015. doi: 10.1103/PhysRevD.91.014013.  $\hookrightarrow$  [see prev. ref.]
- [108] K. Kanazawa, Y. Koike, A. Metz, and D. Pitonyak. *Towards an explanation of transverse single-spin asymmetries in proton-proton collisions: the role of fragmentation in collinear factorization*. Phys. Rev., **D89**(11):111501, 2014. doi: 10.1103/PhysRevD.89.111501.  $\hookrightarrow$  pages 14, 18
- [109] L. Gamberg and Z.-B. Kang. *Process dependent Sivers function and implication for single spin asymmetry in inclusive hadron production*. Phys. Lett. , **B696**:109–118, 2011. doi: 10.1016/j.physletb.2010.11.066.  $\hookrightarrow$  pages 14, 63, 64, 67, 68, 69, 70, 81, C.1
- [110] U. D'Alesio, F. Murgia, C. Pisano, and P. Taels. *Probing the gluon Sivers function in  $p^\uparrow p \rightarrow J/\psi X$  and  $p^\uparrow p \rightarrow D X$* . Phys. Rev., **D96**(3):036011, 2017. doi: 10.1103/PhysRevD.96.036011.  $\hookrightarrow$  pages 14, 63, 64, 68, 69, 70, 72, 74, 76, 78, 79, 104, C.1
- [111] M. Anselmino, M. Boglione, U. D'Alesio, A. Kotzinian, F. Murgia, and A. Prokudin. *The Role of Cahn and Sivers effects in deep inelastic scattering*. Phys. Rev., **D71**:074006, 2005. doi: 10.1103/PhysRevD.71.074006.  $\hookrightarrow$  pages 14, 26, 35, 75, 92
- [112] M. Anselmino, M. Boglione, U. D'Alesio, A. Kotzinian, F. Murgia, and A. Prokudin. *Extracting the Sivers function from polarized SIDIS data and making predictions*. Phys. Rev., **D72**:094007, 2005. doi: 10.1103/PhysRevD.72.094007, 10.1103/PhysRevD.72.099903. [Erratum: Phys. Rev.D72,099903(2005)].  $\hookrightarrow$  pages 92, 97
- [113] M. Anselmino, M. Boglione, U. D'Alesio, A. Kotzinian, S. Melis, F. Murgia, A. Prokudin, and C. Turk. *Sivers effect for pion and kaon production in Semi-Inclusive Deep Inelastic Scattering*. Eur. Phys. J., **A39**:89–100, 2009. doi: 10.1140/epja/i2008-10697-y.  $\hookrightarrow$  pages 35, 36, 43, 58, 77, 92, 97, 98, 100, 101
- [114] M. Anselmino, M. Boglione, J. O. Gonzalez Hernandez, S. Melis, and A. Prokudin. *Unpolarised Transverse Momentum Dependent Distribution and Fragmentation Functions from SIDIS Multiplicities*. JHEP, **04**:005, 2014. doi: 10.1007/JHEP04(2014)005.  $\hookrightarrow$  pages 26, 32, 35, 36, 56, 102



- [115] M. G. Echevarria, A. Idilbi, Z.-B. Kang, and I. Vitev. *QCD Evolution of the Sivers Asymmetry*. Phys. Rev., **D89**:074013, 2014. doi: 10.1103/PhysRevD.89.074013.  $\hookrightarrow$  page 42
- [116] M. Anselmino, M. Boglione, U. D'Alesio, J. O. Gonzalez Hernandez, S. Melis, F. Murgia, and A. Prokudin. *Collins functions for pions from SIDIS and new  $e^+e^-$  data: a first glance at their transverse momentum dependence*. Phys. Rev., **D92**(11):114023, 2015. doi: 10.1103/PhysRevD.92.114023.  $\hookrightarrow$  pages 26, 52, 54, 55, 56, 57, 58, 92, 102
- [117] M. Boglione and A. Prokudin. *Phenomenology of transverse spin: past, present and future*. Eur. Phys. J., **A52**(6):154, 2016. doi: 10.1140/epja/i2016-16154-6.  $\hookrightarrow$  [see prev. ref.]
- [118] M. Anselmino, M. Boglione, U. D'Alesio, F. Murgia, and A. Prokudin. *Study of the sign change of the Sivers function from STAR Collaboration W/Z production data*. JHEP, **04**:046, 2017. doi: 10.1007/JHEP04(2017)046.  $\hookrightarrow$  pages 26, 28, 35, 42, 43, 46, 92, 102, 103
- [119] A. Bacchetta, F. Delcarro, C. Pisano, M. Radici, and A. Signori. *Extraction of partonic transverse momentum distributions from semi-inclusive deep-inelastic scattering, Drell-Yan and Z-boson production*. JHEP, **06**:081, 2017. doi: 10.1007/JHEP06(2017)081, 10.1007/JHEP06(2019)051. [Erratum: JHEP06,051(2019)].  $\hookrightarrow$  pages 27, 32, 117
- [120] M. Boglione, U. D'Alesio, C. Flore, and J. O. Gonzalez-Hernandez. *Assessing signals of TMD physics in SIDIS azimuthal asymmetries and in the extraction of the Sivers function*. JHEP, **07**:148, 2018. doi: 10.1007/JHEP07(2018)148.  $\hookrightarrow$  pages 14, 35, 44, 62
- [121] A. Bacchetta, M. Diehl, K. Goeke, A. Metz, P. J. Mulders, and M. Schlegel. *Semi-inclusive deep inelastic scattering at small transverse momentum*. JHEP, **02**:093, 2007. doi: 10.1088/1126-6708/2007/02/093.  $\hookrightarrow$  pages 16, 18
- [122] S. Bastami et al. *Semi-Inclusive Deep Inelastic Scattering in Wandzura-Wilczek-type approximation*. JHEP, **06**:007, 2019. doi: 10.1007/JHEP06(2019)007.  $\hookrightarrow$  pages 17, 18, 28, 30, 55
- [123] J. C. Collins. *Hard scattering in QCD with polarized beams*. Nucl. Phys., **B394**:169–199, 1993. doi: 10.1016/0550-3213(93)90105-X.  $\hookrightarrow$  page 19
- [124] M. Anselmino, Mariaelena Boglione, and F. Murgia. *Single spin asymmetry for  $p^\uparrow p \rightarrow \pi X$  in perturbative QCD*. Phys. Lett., **B362**:164–172, 1995. doi: 10.1016/0370-2693(95)01168-P.  $\hookrightarrow$  page 20
- [125] U. D'Alesio and F. Murgia. *Parton intrinsic motion in inclusive particle production: unpolarized cross sections, single spin asymmetries and the Sivers effect*. Phys. Rev., **D70**:074009, 2004. doi: 10.1103/PhysRevD.70.074009.  $\hookrightarrow$  pages 21, 91
- [126] M. Anselmino, M. Boglione, U. D'Alesio, E. Leader, and F. Murgia. *Parton intrinsic motion: suppression of the Collins mechanism for transverse single spin asymmetries in  $p^\uparrow p \rightarrow \pi X$* . Phys. Rev., **D71**:014002, 2005. doi: 10.1103/PhysRevD.71.014002.  $\hookrightarrow$  pages 22, B.1, B.2, B.3
- [127] M. Anselmino, M. Boglione, U. D'Alesio, E. Leader, S. Melis, and F. Murgia. *The general partonic structure for hadronic spin asymmetries*. Phys. Rev., **D73**:014020, 2006. doi: 10.1103/PhysRevD.73.014020.  $\hookrightarrow$  pages 20, 23, 85, 87, A.1
- [128] M. Anselmino, M. Boglione, U. D'Alesio, S. Melis, F. Murgia, E. R. Nocera, and A. Prokudin. *General Helicity Formalism for Polarized Semi-Inclusive Deep Inelastic Scattering*. Phys. Rev., **D83**:114019, 2011. doi: 10.1103/PhysRevD.83.114019.  $\hookrightarrow$  pages 21, 35

- [129] E. Leader. *Spin in particle physics*. Camb. Monogr. Part. Phys. Nucl. Phys. Cosmol., **15**: pp.1–500, 2011.  $\hookrightarrow$  pages 22, A.4, B.1, B.3
- [130] J. C. Collins, A. V. Efremov, K. Goeke, S. Menzel, A. Metz, and P. Schweitzer. *Sivers effect in semi-inclusive deeply inelastic scattering*. Phys. Rev., **D73**:014021, 2006. doi: 10.1103/PhysRevD.73.014021.  $\hookrightarrow$  page 26
- [131] P. Schweitzer, T. Teckentrup, and A. Metz. *Intrinsic transverse parton momenta in deeply inelastic reactions*. Phys. Rev., **D81**:094019, 2010. doi: 10.1103/PhysRevD.81.094019.  $\hookrightarrow$  [see prev. ref.]
- [132] A. Signori, A. Bacchetta, M. Radici, and G. Schnell. *Investigations into the flavor dependence of partonic transverse momentum*. JHEP, **11**:194, 2013. doi: 10.1007/JHEP11(2013)194.  $\hookrightarrow$  pages 26, 27
- [133] A. Bacchetta, D. Boer, M. Diehl, and P. J. Mulders. *Matches and mismatches in the descriptions of semi-inclusive processes at low and high transverse momentum*. JHEP, **08**:023, 2008. doi: 10.1088/1126-6708/2008/08/023.  $\hookrightarrow$  page 27
- [134] J. Dudek *et al.* *Physics opportunities with the 12 GeV upgrade at Jefferson Lab*. Eur. Phys. J., **A48**:187, 2012. doi: 10.1140/epja/i2012-12187-1.  $\hookrightarrow$  page 32
- [135] C. Adolph *et al.* *Sivers asymmetry extracted in SIDIS at the hard scales of the Drell-Yan process at COMPASS*. Phys. Lett., **B770**:138–145, 2017. doi: 10.1016/j.physletb.2017.04.042.  $\hookrightarrow$  pages 32, 33, 44, 45, 46, 47
- [136] A. Airapetian *et al.* *Observation of the Naive-T-odd Sivers Effect in Deep-Inelastic Scattering*. Phys. Rev. Lett., **103**:152002, 2009. doi: 10.1103/PhysRevLett.103.152002.  $\hookrightarrow$  pages 33, 36, 43
- [137] M. Alekseev *et al.* *Collins and Sivers asymmetries for pions and kaons in muon-deuteron DIS*. Phys. Lett., **B673**:127–135, 2009. doi: 10.1016/j.physletb.2009.01.060.  $\hookrightarrow$  pages 33, 34, 36, 43, 44, 56
- [138] X. Qian *et al.* *Single Spin Asymmetries in charged pion production from Semi-Inclusive Deep Inelastic Scattering on a transversely polarized  $^3\text{He}$  target*. Phys. Rev. Lett., **107**:072003, 2011. doi: 10.1103/PhysRevLett.107.072003.  $\hookrightarrow$  pages 33, 34, 36, 43, 44
- [139] J. Friedrich, O. Denisov, and A. Vorobyev. *Addendum to the COMPASS-II Proposal*. Technical Report CERN-SPSC-2017-034. SPSC-P-340-ADD-1, CERN, Geneva, 2018. URL <http://cds.cern.ch/record/2286954>.  $\hookrightarrow$  pages 34, 44
- [140] A. Airapetian *et al.* *Effects of transversity in deep-inelastic scattering by polarized protons*. Phys. Lett., **B693**:11–16, 2010. doi: 10.1016/j.physletb.2010.08.012.  $\hookrightarrow$  pages 34, 56
- [141] A. Airapetian *et al.* *Azimuthal distributions of charged hadrons, pions, and kaons produced in deep-inelastic scattering off unpolarized protons and deuterons*. Phys. Rev., **D87**(1):012010, 2013. doi: 10.1103/PhysRevD.87.012010.  $\hookrightarrow$  page 34
- [142] C. Adolph *et al.* *Collins and Sivers asymmetries in muonproduction of pions and kaons off transversely polarised protons*. Phys. Lett., **B744**:250–259, 2015. doi: 10.1016/j.physletb.2015.03.056.  $\hookrightarrow$  pages 34, 44, 46, 56
- [143] R. Seidl *et al.* *Measurement of azimuthal asymmetries in inclusive production of hadron pairs in  $e^+e^-$  annihilation at  $\sqrt{s} = 10.58$  GeV*. Phys. Rev., **D78**:032011,

2008. doi: 10.1103/PhysRevD.78.032011,10.1103/PhysRevD.86.039905. [Erratum: Phys. Rev.D86,039905(2012)].  $\hookrightarrow$  pages 34, 52, 56
- [144] J. P. Lees *et al.* *Measurement of Collins asymmetries in inclusive production of charged pion pairs in  $e^+e^-$  annihilation at BABAR.* Phys. Rev., **D90**(5):052003, 2014. doi: 10.1103/PhysRevD.90.052003.  $\hookrightarrow$  pages 34, 52, 56
- [145] M. Ablikim *et al.* *Measurement of azimuthal asymmetries in inclusive charged dipion production in  $e^+e^-$  annihilations at  $\sqrt{s} = 3.65$  GeV.* Phys. Rev. Lett., **116**(4):042001, 2016. doi: 10.1103/PhysRevLett.116.042001.  $\hookrightarrow$  pages 34, 52, 56, 57
- [146] J. Pumplin, D. R. Stump, J. Huston, H.-L. Lai, Pavel M. Nadolsky, and W.-K. Tung. *New generation of parton distributions with uncertainties from global QCD analysis.* JHEP, **07**:012, 2002. doi: 10.1088/1126-6708/2002/07/012.  $\hookrightarrow$  pages 35, 75, 103
- [147] D. Stump, J. Huston, J. Pumplin, W.-K. Tung, H.-L. Lai, S. Kuhlmann, and J.-F. Owens. *Inclusive jet production, parton distributions, and the search for new physics.* JHEP, **10**:046, 2003. doi: 10.1088/1126-6708/2003/10/046.  $\hookrightarrow$  pages 35, 103
- [148] D. de Florian, R. Sassot, and M. Stratmann. *Global analysis of fragmentation functions for pions and kaons and their uncertainties.* Phys. Rev., **D75**:114010, 2007. doi: 10.1103/PhysRevD.75.114010.  $\hookrightarrow$  pages 35, 75, 92
- [149] F. James and M. Roos. *Minuit: a system for function minimization and analysis of the parameter errors and correlations.* Comput. Phys. Commun., **10**:343–367, 1975. doi: 10.1016/0010-4655(75)90039-9.  $\hookrightarrow$  pages 36, 57
- [150] Z.-B. Kang and J.-W. Qiu. *Evolution of twist-3 multi-parton correlation functions relevant to single transverse-spin asymmetry.* Phys. Rev., **D79**:016003, 2009. doi: 10.1103/PhysRevD.79.016003.  $\hookrightarrow$  pages 47, 48
- [151] W. Vogelsang and F. Yuan. *Next-to-leading order calculation of the Single Transverse Spin Asymmetry in the Drell-Yan process.* Phys. Rev., **D79**:094010, 2009. doi: 10.1103/PhysRevD.79.094010.  $\hookrightarrow$  [see prev. ref.]
- [152] V. M. Braun, A. N. Manashov, and B. Pirnay. *Scale dependence of twist-three contributions to single spin asymmetries.* Phys. Rev., **D80**:114002, 2009. doi: 10.1103/PhysRevD.80.114002,10.1103/PhysRevD.86.119902. [Erratum: Phys. Rev.D86,119902(2012)].  $\hookrightarrow$  [see prev. ref.]
- [153] Z.-B. Kang and J.-W. Qiu. *QCD evolution of naive-time-reversal-odd parton distribution functions.* Phys. Lett., **B713**:273–276, 2012. doi: 10.1016/j.physletb.2012.06.021.  $\hookrightarrow$  page 47
- [154] M. Anselmino, M. Boglione, and S. Melis. *A Strategy towards the extraction of the Sivers function with TMD evolution.* Phys. Rev., **D86**:014028, 2012. doi: 10.1103/PhysRevD.86.014028.  $\hookrightarrow$  pages 47, 49
- [155] G. P. Salam and J. Rojo. *A Higher Order Perturbative Parton Evolution Toolkit (HOPPET).* Comput. Phys. Commun., **180**:120–156, 2009. doi: 10.1016/j.cpc.2008.08.010.  $\hookrightarrow$  pages 47, 56
- [156] A. Prokudin. private communication, 2018.  $\hookrightarrow$  page 47

- [157] S. M. Aybat, A. Prokudin, and T. C. Rogers. *Calculation of TMD evolution for Transverse Single Spin Asymmetry measurements*. Phys. Rev. Lett., **108**:242003, 2012. doi: 10.1103/PhysRevLett.108.242003.  $\hookrightarrow$  page 49
- [158] M. Boglione, J. O. Gonzalez-Hernandez, S. Melis, and A. Prokudin. *A study on the interplay between perturbative QCD and CSS/TMD formalism in SIDIS processes*. JHEP, **02**:095, 2015. doi: 10.1007/JHEP02(2015)095.  $\hookrightarrow$  page 49
- [159] M. Boglione, J. Collins, L. Gamberg, J. O. Gonzalez-Hernandez, T. C. Rogers, and N. Sato. *Kinematics of Current Region Fragmentation in Semi-Inclusive Deeply Inelastic Scattering*. Phys. Lett., **B766**:245–253, 2017. doi: 10.1016/j.physletb.2017.01.021.  $\hookrightarrow$  [see prev. ref.]
- [160] J. Collins, L. Gamberg, A. Prokudin, T. C. Rogers, N. Sato, and B. Wang. *Relating Transverse Momentum Dependent and collinear factorization theorems in a generalized formalism*. Phys. Rev., **D94**(3):034014, 2016. doi: 10.1103/PhysRevD.94.034014.  $\hookrightarrow$  [see prev. ref.]
- [161] E. Moffat, W. Melnitchouk, T. C. Rogers, and N. Sato. *What are the low- $Q$  and large- $x$  boundaries of collinear QCD factorization theorems?* Phys. Rev., **D95**(9):096008, 2017. doi: 10.1103/PhysRevD.95.096008.  $\hookrightarrow$  [see prev. ref.]
- [162] M. Boglione, A. Dotson, L. Gamberg, S. Gordon, J. O. Gonzalez-Hernandez, A. Prokudin, T. C. Rogers, and N. Sato. *Mapping the Kinematical Regimes of Semi-Inclusive Deep Inelastic Scattering*. arXiv e-prints, art. arXiv:1904.12882, Apr 2019.  $\hookrightarrow$  page 49
- [163] M. Anselmino, M. Boglione, U. D’Alesio, A. Kotzinian, F. Murgia, A. Prokudin, and C. Turk. *Transversity and Collins functions from SIDIS and  $e^+e^-$  data*. Phys. Rev., **D75**:054032, 2007. doi: 10.1103/PhysRevD.75.054032.  $\hookrightarrow$  pages 52, 54, 57, 92, 97
- [164] M. Anselmino, M. Boglione, U. D’Alesio, S. Melis, F. Murgia, and A. Prokudin. *Simultaneous extraction of transversity and Collins functions from new SIDIS and  $e^+e^-$  data*. Phys. Rev., **D87**:094019, 2013. doi: 10.1103/PhysRevD.87.094019.  $\hookrightarrow$  pages 52, 57, 58
- [165] D. de Florian, R. Sassot, M. Stratmann, and W. Vogelsang. *Extraction of spin-dependent parton densities and their uncertainties*. Phys. Rev., **D80**:034030, 2009. doi: 10.1103/PhysRevD.80.034030.  $\hookrightarrow$  pages 56, 58
- [166] P. M. Nadolsky, H.-L. Lai, Q.-H. Cao, J. Huston, J. Pumplin, D. Stump, W.-K. Tung, and C.-P. Yuan. *Implications of CTEQ global analysis for collider observables*. Phys. Rev., **D78**:013004, 2008. doi: 10.1103/PhysRevD.78.013004.  $\hookrightarrow$  pages 56, 58
- [167] D. de Florian, R. Sassot, M. Epele, R. J. Hernández-Pinto, and M. Stratmann. *Parton-to-Pion Fragmentation Reloaded*. Phys. Rev., **D91**(1):014035, 2015. doi: 10.1103/PhysRevD.91.014035.  $\hookrightarrow$  page 56
- [168] T. Hahn. *CUBA: a library for multidimensional numerical integration*. Comput. Phys. Commun., **168**:78–95, 2005. doi: 10.1016/j.cpc.2005.01.010.  $\hookrightarrow$  page 57
- [169] M. Radici and A. Bacchetta. *First extraction of transversity from a global analysis of electron-proton and proton-proton data*. Phys. Rev. Lett., **120**(19):192001, 2018. doi: 10.1103/PhysRevLett.120.192001.  $\hookrightarrow$  page 59



- [170] C. Alexandrou. *Novel applications of Lattice QCD: Parton Distributions, proton charge radius and neutron electric dipole moment*. EPJ Web Conf., **137**:01004, 2017. doi: 10.1051/epjconf/201713701004.  $\hookrightarrow$  page 59
- [171] W. Vogelsang. *Next-to-leading order evolution of transversity distributions and Soffer’s inequality*. Phys. Rev., **D57**:1886–1894, 1998. doi: 10.1103/PhysRevD.57.1886.  $\hookrightarrow$  page 61
- [172] D. Boer, C. Lorcé, C. Pisano, and J. Zhou. *The gluon Sivers distribution: status and future prospects*. Adv. High Energy Phys., **2015**:371396, 2015. doi: 10.1155/2015/371396.  $\hookrightarrow$  pages 63, 64
- [173] U. D’Alesio, L. Gamberg, Z.-B. Kang, F. Murgia, and C. Pisano. *Testing the process dependence of the Sivers function via hadron distributions inside a jet*. Phys. Lett., **B704**: 637–640, 2011. doi: 10.1016/j.physletb.2011.09.067.  $\hookrightarrow$  page 63
- [174] U. D’Alesio, F. Murgia, and C. Pisano. *Probing TMDs through azimuthal distributions of pions inside a jet in hadronic collisions*. Phys. Part. Nucl., **45**:110–112, 2014. doi: 10.1134/S1063779614010225.  $\hookrightarrow$  page 63
- [175] U. D’Alesio, C. Flore, F. Murgia, C. Pisano, and P. Tael. *Unraveling the Gluon Sivers Function in hadronic collisions at RHIC*. Phys. Rev., **D99**(3):036013, 2019. doi: 10.1103/PhysRevD.99.036013.  $\hookrightarrow$  pages 63, 66, 67, 68, 69, 70, 72, 74
- [176] Z.-B. Kang, J.-W. Qiu, W. Vogelsang, and F. Yuan. *Accessing tri-gluon correlations in the nucleon via the single spin asymmetry in open charm production*. Phys. Rev., **D78**:114013, 2008. doi: 10.1103/PhysRevD.78.114013.  $\hookrightarrow$  pages 64, 65, 67
- [177] Z.-B. Kang and J.-W. Qiu. *Single transverse-spin asymmetry for D-meson production in semi-inclusive deep inelastic scattering*. Phys. Rev., **D78**:034005, 2008. doi: 10.1103/PhysRevD.78.034005.  $\hookrightarrow$  pages 64, 65, 67
- [178] D. Binosi and L. Theussl. *JaxoDraw: A Graphical user interface for drawing Feynman diagrams*. Comput. Phys. Commun., **161**:76–86, 2004. doi: 10.1016/j.cpc.2004.05.001.  $\hookrightarrow$  pages 64, 65
- [179] D. Binosi, J. C. Collins, C. Kaufhold, and L. Theussl. *JaxoDraw: A Graphical user interface for drawing Feynman diagrams. Version 2.0 release notes*. Comput. Phys. Commun., **180**: 1709–1715, 2009. doi: 10.1016/j.cpc.2009.02.020.  $\hookrightarrow$  pages 64, 65
- [180] X.-D. Ji. *Gluon correlations in the transversely polarized nucleon*. Phys. Lett., **B289**:137–142, 1992. doi: 10.1016/0370-2693(92)91375-J.  $\hookrightarrow$  page 65
- [181] B. L. Ioffe, V. S. Fadin, and L. N. Lipatov. *Quantum chromodynamics: perturbative and nonperturbative aspects*, volume 30. Cambridge Univ. Press, 2010. ISBN 9781107424753, 9780521631488, 9780511717444. doi: 10.1017/CBO9780511711817. URL <http://www.cambridge.org/de/knowledge/isbn/item2710695>.  $\hookrightarrow$  page 66
- [182] C. J. Bomhof and P. J. Mulders. *Gluonic pole cross-sections and single spin asymmetries in hadron-hadron scattering*. JHEP, **02**:029, 2007. doi: 10.1088/1126-6708/2007/02/029.  $\hookrightarrow$  pages 67, 68, 71
- [183] C. J. Bomhof. *Azimuthal spin asymmetries in hadronic processes*. PhD thesis, Vrije U., Amsterdam, 2007.  $\hookrightarrow$  pages 67, 68

- [184] C. Pisano, U. D'Alesio, C. Flore, F. Murgia, and P. Tael. *Process dependence of the gluon Sivers function in inclusive pp collisions: theory*. In *23rd International Symposium on Spin Physics (SPIN 2018) Ferrara, Italy, September 10-14, 2018*, 2019.  $\hookrightarrow$  pages 68, 69
- [185] R. M. Godbole, A. Kaushik, A. Misra, and S. Padval. *Probing the Gluon Sivers Function through direct photon production at RHIC*. *Phys. Rev.*, **D99**(1):014003, 2019. doi: 10.1103/PhysRevD.99.014003.  $\hookrightarrow$  page 70
- [186] U. D'Alesio, F. Murgia, and C. Pisano. *Towards a first estimate of the gluon Sivers function from  $A_N$  data in pp collisions at RHIC*. *JHEP*, **09**:119, 2015. doi: 10.1007/JHEP09(2015)119.  $\hookrightarrow$  pages 74, 76, 92, 97
- [187] M. Anselmino, U. D'Alesio, S. Melis, and F. Murgia. *Constraints on the gluon Sivers distribution via transverse single spin asymmetries at mid-rapidity in  $p^\uparrow p \rightarrow \pi^0 X$  processes at RHIC*. *Phys. Rev.*, **D74**:094011, 2006. doi: 10.1103/PhysRevD.74.094011.  $\hookrightarrow$  pages 74, 76
- [188] C. Aidala *et al.* *Cross section and transverse single-spin asymmetry of muons from open heavy-flavor decays in polarized p+p collisions at  $\sqrt{s} = 200$  GeV*. *Phys. Rev.*, **D95**(11):112001, 2017. doi: 10.1103/PhysRevD.95.112001.  $\hookrightarrow$  pages 76, 78, 79, 80, 82
- [189] C. Aidala *et al.* *Single-spin asymmetry of  $J/\psi$  production in  $p + p$ ,  $p + Al$ , and  $p + Au$  collisions with transversely polarized proton beams at  $\sqrt{s_{NN}} = 200$  GeV*. *Phys. Rev.*, **D98**(1):012006, 2018. doi: 10.1103/PhysRevD.98.012006.  $\hookrightarrow$  pages 76, 104, 105
- [190] U. D'Alesio, F. Murgia, and C. Pisano. *Azimuthal asymmetries for hadron distributions inside a jet in hadronic collisions*. *Phys. Rev.*, **D83**:034021, 2011. doi: 10.1103/PhysRevD.83.034021.  $\hookrightarrow$  page 77
- [191] J. Bok (PHENIX Coll.). private communication, 2019.  $\hookrightarrow$  page 79
- [192] Y. Koike and S. Yoshida. *Probing the three-gluon correlation functions by the single spin asymmetry in  $p^\uparrow p \rightarrow DX$* . *Phys. Rev.*, **D84**:014026, 2011. doi: 10.1103/PhysRevD.84.014026.  $\hookrightarrow$  page 80
- [193] Y. Koike. *Single transverse spin asymmetry in  $p^\uparrow p \rightarrow \pi X$  and  $ep^\uparrow \rightarrow \pi X$* . *Nucl. Phys.*, **A721**:364–367, 2003. doi: 10.1016/S0375-9474(03)01070-4.  $\hookrightarrow$  page 83
- [194] L. Gamberg, Z.-B. Kang, A. Metz, D. Pitonyak, and A. Prokudin. *Left-right spin asymmetry in  $\ell N^\uparrow \rightarrow hX$* . *Phys. Rev.*, **D90**(7):074012, 2014. doi: 10.1103/PhysRevD.90.074012.  $\hookrightarrow$  page 83
- [195] Z.-B. Kang, A. Metz, J.-W. Qiu, and J. Zhou. *Exploring the structure of the proton through polarization observables in  $\ell p \rightarrow \text{jet}X$* . *Phys. Rev.*, **D84**:034046, 2011. doi: 10.1103/PhysRevD.84.034046.  $\hookrightarrow$  page 83
- [196] M. Anselmino, M. Boglione, U. D'Alesio, S. Melis, F. Murgia, and A. Prokudin. *Single spin asymmetries in  $\ell p \rightarrow hX$  processes: a test of factorization*. *Phys. Rev.*, **D81**:034007, 2010. doi: 10.1103/PhysRevD.81.034007.  $\hookrightarrow$  pages 83, 84, 85, 90
- [197] M. Anselmino, M. Boglione, U. D'Alesio, S. Melis, F. Murgia, and A. Prokudin. *Single Spin Asymmetries in  $\ell p^\uparrow \rightarrow hX$  processes and TMD factorisation*. *Phys. Rev.*, **D89**(11):114026, 2014. doi: 10.1103/PhysRevD.89.114026.  $\hookrightarrow$  pages 83, 85, 86, 97, 102

- [198] A. Airapetian *et al.* *Transverse target single-spin asymmetry in inclusive electroproduction of charged pions and kaons.* Phys. Lett., **B728**:183–190, 2014. doi: 10.1016/j.physletb.2013.11.021.  $\hookrightarrow$  pages 83, 91, 97, 98, 99, 103
- [199] U. D’Alesio, C. Flore, and F. Murgia. *Transverse single-spin asymmetries in  $\ell p^\uparrow \rightarrow h X$  within a TMD approach: role of quasi-real photon exchange.* Phys. Rev., **D95**(9):094002, 2017. doi: 10.1103/PhysRevD.95.094002.  $\hookrightarrow$  pages 84, 87, 88, 92, 102
- [200] U. D’Alesio, C. Flore, and F. Murgia. *Quasi-real photon contribution to  $A_N$  in  $\ell p^\uparrow \rightarrow \pi X$  within a TMD approach.* PoS, **QCDEV2016**:002, 2017. doi: 10.22323/1.284.0002.  $\hookrightarrow$  page 84
- [201] P. Hinderer, M. Schlegel, and W. Vogelsang. *Single-inclusive production of hadrons and jets in lepton-nucleon scattering at NLO.* Phys. Rev., **D92**(1):014001, 2015. doi: 10.1103/PhysRevD.92.014001, 10.1103/PhysRevD.93.119903. [Erratum: Phys. Rev.D93,no.11,119903(2016)].  $\hookrightarrow$  page 86
- [202] C. F. von Weizsacker. *Radiation emitted in collisions of very fast electrons.* Z. Phys., **88**:612–625, 1934. doi: 10.1007/BF01333110.  $\hookrightarrow$  page 86
- [203] E. J. Williams. *Nature of the high-energy particles of penetrating radiation and status of ionization and radiation formulae.* Phys. Rev., **45**:729–730, 1934. doi: 10.1103/PhysRev.45.729.  $\hookrightarrow$  page 86
- [204] S. J. Brodsky, T. Kinoshita, and H. Terazawa. *Two photon mechanism of particle production by high-energy colliding beams.* Phys. Rev., **D4**:1532–1557, 1971. doi: 10.1103/PhysRevD.4.1532.  $\hookrightarrow$  pages 86, 87
- [205] H. Terazawa. *Two photon processes for particle production at high-energies.* Rev. Mod. Phys., **45**:615–662, 1973. doi: 10.1103/RevModPhys.45.615.  $\hookrightarrow$  [see prev. ref.]
- [206] B. A. Kniehl. *Elastic  $ep$  scattering and the Weizsacker-Williams approximation.* Phys. Lett., **B254**:267–273, 1991. doi: 10.1016/0370-2693(91)90432-P.  $\hookrightarrow$  pages 86, 87
- [207] R. M. Godbole, A. Misra, A. Mukherjee, and V. S. Rawoot. *Sivers effect and transverse single spin ssymmetry in  $e + p^\uparrow \rightarrow e + J/\psi + X$ .* Phys. Rev., **D85**:094013, 2012. doi: 10.1103/PhysRevD.85.094013.  $\hookrightarrow$  page 87
- [208] R. M. Godbole, A. Misra, A. Mukherjee, and V. S. Rawoot. *Transverse single spin asymmetry in  $e + p^\uparrow \rightarrow e + J/\psi + X$  and transverse momentum dependent evolution of the Sivers function.* Phys. Rev., **D88**(1):014029, 2013. doi: 10.1103/PhysRevD.88.014029.  $\hookrightarrow$  page 87
- [209] M. Anselmino, M. Boglione, U. D’Alesio, A. Kotzinian, F. Murgia, A. Prokudin, and S. Melis. *Update on transversity and Collins functions from SIDIS and  $e^+e^-$  data.* Nucl. Phys. Proc. Suppl., **191**:98–107, 2009. doi: 10.1016/j.nuclphysbps.2009.03.117.  $\hookrightarrow$  pages 92, 97
- [210] M. Glück, E. Reya, and A. Vogt. *Dynamical parton distributions revisited.* Eur. Phys. J., **C5**:461–470, 1998. doi: 10.1007/s100529800978, 10.1007/s100520050289.  $\hookrightarrow$  page 92
- [211] S. Kretzer. *Fragmentation functions from flavour-inclusive and flavour-tagged  $e^+e^-$  annihilations.* Phys. Rev., **D62**:054001, 2000.  $\hookrightarrow$  page 92
- [212] M. Boglione, U. D’Alesio, and F. Murgia. *Single spin asymmetries in inclusive hadron production from semiinclusive DIS to hadronic collisions: Universality and phenomenology.* Phys. Rev., **D77**:051502, 2008. doi: 10.1103/PhysRevD.77.051502.  $\hookrightarrow$  page 102



- [213] M. Anselmino, M. Boglione, U. D'Alesio, S. Melis, F. Murgia, and A. Prokudin. *Sivers effect and the single spin asymmetry  $A_N$  in  $p^\uparrow p \rightarrow hX$  processes*. Phys. Rev., **D88**(5): 054023, 2013. doi: 10.1103/PhysRevD.88.054023.  $\hookrightarrow$  page 102
- [214] G. Igo. *New STAR transverse spin results*. AIP Conf. Proc., **1523**(1):188–193, 2013. doi: 10.1063/1.4802147.  $\hookrightarrow$  page 102
- [215] M. Anselmino, M. Boglione, U. D'Alesio, F. Murgia, and A. Prokudin. *Role of transverse momentum dependence of unpolarized parton distribution and fragmentation functions in the analysis of azimuthal spin asymmetries*. Phys. Rev., **D98**(9):094023, 2018. doi: 10.1103/PhysRevD.98.094023.  $\hookrightarrow$  page 103
- [216] J.-P. Lansberg. *New observables in inclusive production of quarkonia*. arXiv e-prints, art. arXiv:1903.09185, Mar 2019.  $\hookrightarrow$  page 104
- [217] A. Mukherjee and S. Rajesh.  *$J/\psi$  production in polarized and unpolarized ep collision and Sivers and  $\cos 2\phi$  asymmetries*. Eur. Phys. J., **C77**(12):854, 2017. doi: 10.1140/epjc/s10052-017-5406-4.  $\hookrightarrow$  page 104
- [218] A. Bacchetta, D. Boer, C. Pisano, and P. Tael. *Gluon TMDs and NRQCD matrix elements in  $J/\psi$  production at an EIC*. arXiv e-prints, art. arXiv:1809.02056, Sep 2018.  $\hookrightarrow$  page 104
- [219] I. Schmidt, J. Soffer, and J.-J. Yang. *Transverse single spin asymmetries in photon production*. Phys. Lett., **B612**:258–262, 2005. doi: 10.1016/j.physletb.2005.03.008.  $\hookrightarrow$  page 106
- [220] R. Bain, Y. Makris, and T. Mehen. *Transverse Momentum Dependent fragmenting jet functions with applications to quarkonium production*. JHEP, **11**:144, 2016. doi: 10.1007/JHEP11(2016)144.  $\hookrightarrow$  page 108
- [221] D. Gutierrez-Reyes, I. Scimemi, W. J. Waalewijn, and L. Zoppi. *Transverse momentum dependent distributions with jets*. Phys. Rev. Lett., **121**(16):162001, 2018. doi: 10.1103/PhysRevLett.121.162001.  $\hookrightarrow$  [see prev. ref.]
- [222] D. Gutierrez-Reyes, I. Scimemi, W. J. Waalewijn, and L. Zoppi. *Studying transverse momentum distributions with jets at  $N^3$ LL*. In *27th International Workshop on Deep Inelastic Scattering and Related Subjects (DIS 2019) Torino, Italy, April 8-12, 2019*, 2019.  $\hookrightarrow$  [see prev. ref.]
- [223] D. Gutierrez-Reyes, Y. Makris, V. Vaidya, I. Scimemi, and L. Zoppi. *Probing Transverse-Momentum Distributions with groomed jets*. arXiv e-prints, art. arXiv:1907.05896, 2019.  $\hookrightarrow$  [see prev. ref.]
- [224] M. G. A. Buffing, Z.-B. Kang, K. Lee, and X. Liu. *A transverse momentum dependent framework for back-to-back photon+jet production*. arXiv e-prints, art. arXiv:1812.07549, Dec 2018.  $\hookrightarrow$  page 108
- [225] C. Flore. Talk at Quarkonia as Tools 2019: Aussois, France, 2019. URL <https://indico.cern.ch/event/745939/contributions/3246227/>.  $\hookrightarrow$  pages 109, 111
- [226] C. Flore. Talk at 2<sup>nd</sup> LHCb Heavy Ion Workshop: Chia, Italy, 2019. URL <https://agenda.infn.it/event/18734/contributions/98749/>.  $\hookrightarrow$  pages 109, 111
- [227] J. Alwall et al. *The automated computation of tree-level and next-to-leading order differential cross sections, and their matching to parton shower simulations*. JHEP, **07**:079, 2014. doi: 10.1007/JHEP07(2014)079.  $\hookrightarrow$  page 110

- [228] R. Frederix, S. Frixione, V. Hirschi, D. Pagani, H.-S. Shao, and M. Zaro. *The automation of next-to-leading order electroweak calculations*. JHEP, **07**:185, 2018. doi: 10.1007/JHEP07(2018)185.  $\hookrightarrow$  page 110
- [229] H.-S. Shao. *HELAC-Onia: An automatic matrix element generator for heavy quarkonium physics*. Comput. Phys. Commun., **184**:2562–2570, 2013. doi: 10.1016/j.cpc.2013.05.023.  $\hookrightarrow$  pages 110, 111, 112, 114
- [230] H.-S. Shao. *HELAC-Onia 2.0: an upgraded matrix-element and event generator for heavy quarkonium physics*. Comput. Phys. Commun., **198**:238–259, 2016. doi: 10.1016/j.cpc.2015.09.011.  $\hookrightarrow$  pages 110, 111, 112, 114
- [231] G. T. Bodwin, E. Braaten, and G. P. Lepage. *Rigorous QCD analysis of inclusive annihilation and production of heavy quarkonium*. Phys. Rev., **D51**:1125–1171, 1995. doi: 10.1103/PhysRevD.55.5853,10.1103/PhysRevD.51.1125. [Erratum: Phys. Rev.D55,5853(1997)].  $\hookrightarrow$  page 110
- [232] F. A. Berends and W. T. Giele. *Recursive Calculations for Processes with  $n$  Gluons*. Nucl. Phys., **B306**:759–808, 1988. doi: 10.1016/0550-3213(88)90442-7.  $\hookrightarrow$  page 110
- [233] G. T. Bodwin, H. S. Chung, D. Kang, J. Lee, and C. Yu. *Improved determination of color-singlet nonrelativistic QCD matrix elements for  $S$ -wave charmonium*. Phys. Rev., **D77**:094017, 2008. doi: 10.1103/PhysRevD.77.094017.  $\hookrightarrow$  page 111
- [234] R. Sharma and I. Vitev. *High transverse momentum quarkonium production and dissociation in heavy ion collisions*. Phys. Rev., **C87**(4):044905, 2013. doi: 10.1103/PhysRevC.87.044905.  $\hookrightarrow$  [see prev. ref.]
- [235] K.-T. Chao, Y.-Q. Ma, H.-S. Shao, K. Wang, and Y.-J. Zhang.  *$J/\psi$  polarization at hadron colliders in Nonrelativistic QCD*. Phys. Rev. Lett., **108**:242004, 2012. doi: 10.1103/PhysRevLett.108.242004.  $\hookrightarrow$  [see prev. ref.]
- [236] G. T. Bodwin, H. S. Chung, U-R. Kim, and J. Lee. *Fragmentation contributions to  $J/\psi$  production at the Tevatron and the LHC*. Phys. Rev. Lett., **113**(2):022001, 2014. doi: 10.1103/PhysRevLett.113.022001.  $\hookrightarrow$  [see prev. ref.]
- [237] H.-F. Zhang, Z. Sun, W.-L. Sang, and R. Li. *Impact of  $\eta_c$  hadroproduction data on charmonium production and polarization within NRQCD framework*. Phys. Rev. Lett., **114**(9):092006, 2015. doi: 10.1103/PhysRevLett.114.092006.  $\hookrightarrow$  page 111
- [238] A. Buckley *et al.* *LHAPDF6: parton density access in the LHC precision era*. Eur. Phys. J., **C75**:132, 2015. doi: 10.1140/epjc/s10052-015-3318-8.  $\hookrightarrow$  page 111
- [239] T. Sjostrand, S. Mrenna, and P. Z. Skands. *A Brief Introduction to PYTHIA 8.1*. Comput. Phys. Commun., **178**:852–867, 2008. doi: 10.1016/j.cpc.2008.01.036.  $\hookrightarrow$  page 111
- [240] K. Kato and T. Munehisa. *Double cascade scheme for QCD jets in  $e^+e^-$  annihilation*. Phys. Rev., **D39**:156, 1989. doi: 10.1103/PhysRevD.39.156.  $\hookrightarrow$  page 111
- [241] J. Fujimoto, Y. Shimizu, and T. Munehisa. *Monte Carlo approach to radiative processes in  $e^+e^-$  annihilation*. Prog. Theor. Phys., **90**:177–186, 1993. doi: 10.1143/PTP.90.177.  $\hookrightarrow$  [see prev. ref.]

- [242] J. Fujimoto, Y. Shimizu, and T. Munehisa. *Monte Carlo approach to radiative corrections in Bhabha scattering*. Prog. Theor. Phys., **91**:333–340, 1994. doi: 10.1143/ptp/91.2.333, 10.1143/PTP.91.333.  $\hookrightarrow$  [see prev. ref.]
- [243] T. Munehisa, J. Fujimoto, Y. Kurihara, and Y. Shimizu. *Improved QEDPS for radiative corrections in  $e^+e^-$  annihilation*. Prog. Theor. Phys., **95**:375–388, 1996. doi: 10.1143/PTP.95.375.  $\hookrightarrow$  page 111
- [244] F. Scarpa, D. Boer, M. G. Echevarria, J.-P. Lansberg, C. Pisano, and M. Schlegel. *Studies of gluon TMDs and their evolution using quarkonium-pair production at the LHC*. arXiv e-prints, art. arXiv:1909.05769, Sep 2019.  $\hookrightarrow$  page 116
- [245] R. Seidl *et al.* *Transverse momentum dependent production cross sections of charged pions, kaons and protons produced in inclusive  $e^+e^-$  annihilation at  $\sqrt{s} = 10.58$  GeV*. Phys. Rev., **D99**(11):112006, 2019. doi: 10.1103/PhysRevD.99.112006.  $\hookrightarrow$  page 117